Raising the Roof: Extending the Met Office's Unified Model into the Mesosphere and Lower Thermosphere

Griffith, Matthew

Award date:
2021

Awarding institution:
University of Bath

Raising the Roof: Extending the Met Office's Unified Model into the Mesosphere and Lower Thermosphere

submitted by

Matthew James GRIFFITH

for the degree of *Doctor of Philosophy*

of the

University of Bath

Department of Mathematical Sciences

August 2021

Declaration of any previous Submission of the Work

The material presented here for examination for the award of a higher degree by research has not been incorporated into a submission for another degree.

. . . . . .

Matthew James GRIFFITH

Declaration of Authorship

I am the author of this thesis, and the work described therein was carried out by myself personally.

. . . . . .

Matthew James GRIFFITH

Summary

In this thesis, we extend the UK Met Office's Unified Model into the Mesosphere and Lower Thermosphere (MLT), and validate the realism of the model by comparison to meteor radar observations and other high-top atmospheric models. This thesis therefore "raises the roof" of current weather forecasting at the Met Office.

The first goal of this thesis is to stabilise the previously unstable Extended Unified Model (ExUM). We perform a thorough and systematic analysis of the UM with an extended upper boundary, and show that the incorrect assumption of Local Thermodynamic Equilibrium (LTE) in the MLT is the primary driver of the model instability. The implementation of a temperature relaxation, or "nudging", scheme to replace the radiation scheme above 70 km stabilises the model with upper boundaries of 100, 120 and 135 km.

The second goal of this thesis is to validate the realism of the modelled fields produced by the ExUM in the MLT. Comparisons are made with meteor-radar observations as well as with other atmospheric models and observational datasets of this region. These show that the ExUM has a good natural capability to model the MLT, but that developments to the model's physical schemes – such as the non-orographic gravity wave and chemistry schemes – are required in this region to obtain more realistic fields.

The work performed in this thesis gives insight into the work required to successfully extend an atmospheric model into the MLT and lays the foundation for the future development of a Whole Atmosphere UM.

Contents

Chapter 1

Abstract

Whole Atmosphere Models (WAMs) have the capability to revolutionise not only weather and climate forecasting of the lower atmosphere, but also space weather forecasting to protect humans from harmful solar activity. This type of model has gained particular scientific interest over the last three decades, with many modelling and experimental studies illustrating the importance of a coupled atmospheric model. Despite this, it is still unclear as to what is the ideal formulation for a WAM and which atmospheric features must be prioritised in such a model. To aid the analysis and development of such models, the extension of the UK Met Office's Unified Model (UM) into the Mesosphere and Lower Thermosphere (MLT; 50-120 km) is a key strategic goal of the Met Office. By doing this, we shall "raise the roof" of current weather forecasting at the Met Office and allow study of the interaction between Earth and space weather. By extending an already established model, we can gain insight into key factors in the development of high-top atmosphere models, and test hypotheses on which atmospheric phenomena are most important for modelling the MLT.

The goal of this thesis is to stabilise the currently unstable Extended Unified Model (ExUM) and validate the realism of the model by comparison to meteor radar observations, and other high-top atmospheric models. This model has applications both in scientific research (in this thesis and elsewhere) and as a potential future whole atmosphere model to be used by the Met Office Space Weather Operations Centre. We will start by examining the current state of whole atmosphere modelling, in order to understand properties which are critical in accurately modelling the upper atmosphere. With this in mind, we can then perform a thorough and systematic analysis of the UM with an extended upper boundary. We will demonstrate that care needs to be taken in ensuring that assumptions made in the lower atmosphere are still valid when moving to the upper atmosphere – the incorrect assumption of Local Thermodynamic Equilibrium (LTE) in the MLT will be shown to be the primary driver of the model instability. We will propose a stopgap solution to this problem, namely a temperature relaxation or "nudging" scheme which replaces the radiation scheme above 70 km. With this we show that indeed the assumption of LTE in the MLT was the primary driver of model instability and that with this nudging scheme, the model can run in a stable manner with upper boundaries of 100, 120 and 135 km.

Having stabilised the model, we next validate the output of the ExUM. For example, in Chapter 6 of the thesis, we will compare the output of the model with meteor radar observations and in Chapter 7 we make comparisons with other atmospheric models and observational datasets of this region. These provide the first results of the capability of the ExUM to model atmospheric winds and tides in the MLT. We will show that the ExUM has a good natural capability to model the MLT, but that there is room for improvement in the model physics in this region. Throughout this interdisciplinary research, we will push the capabilities of the Met Office's UM and develop new points for comparison and discussion in the field of whole atmosphere modelling, and lay the foundations for the development of a Whole Atmosphere UM in the future. Therefore the outcomes of this thesis will not only influence modelling of the MLT at the Met Office, but also within the community of whole atmosphere modelling as a whole, guiding further study into this type of model.

Chapter 2

Introduction

2.1. Overview

An important focus of many weather forecasting organisations is the development of a complete coupled Sun-to-Earth modelling system in order to ultimately develop a fully coupled system (e.g. Tóth et al., 2005). The national weather service of the United Kingdom, the Met Office, therefore also has this strategic goal. A first step to this is developing a whole atmosphere model - namely one that stretches up to heights of up to c. 600 km above the surface. This is important not only from a perspective of furthering scientific research, but also since a whole atmosphere model provides many important forecasting benefits. For example, this type of model can provide enhanced forecasting of space weather, and hence provide useful information ahead of time to safeguard human lives and resources from the effects of the Sun on the Earth system (e.g. Bothmer and Daglis, 2007). The forecasting of this region is important for real world applications such as radio communication, satellite drag calculation and Global Navigation Satellite System Positioning, Navigation and Timing (GNSS PNT). These can all be influenced by atmospheric waves in the upper atmosphere, and so modelling this region can help mitigate potential disruption to these systems.

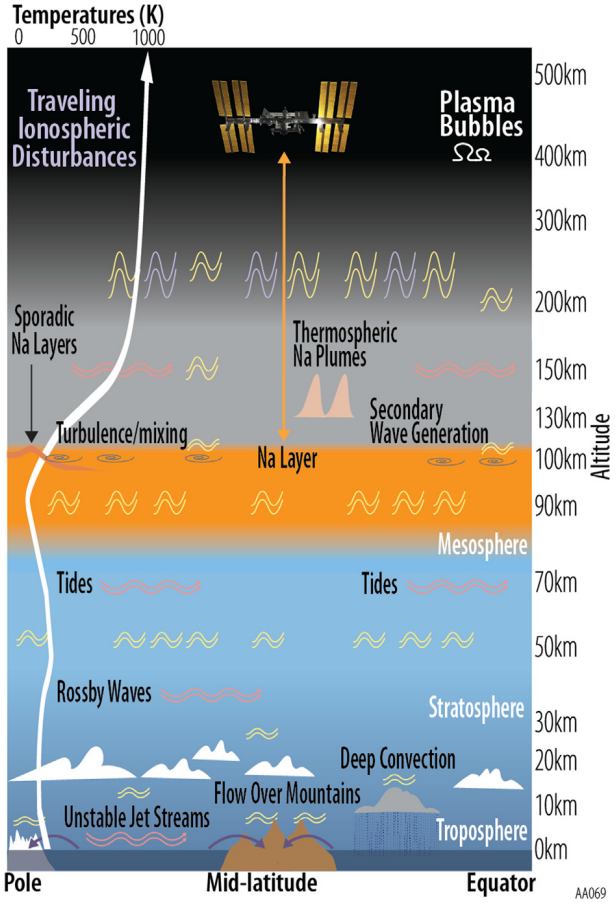

Figure 2-1: *Examples of some important middle and upper atmosphere coupling processes including atmospheric tides. From Janches et al. (2019).*

Such a model can incorporate many important coupling processes, such as those in Figure 2-1. Notably, large scale oscillations of the atmosphere – called *atmospheric tides* (discussed more in Chapters 6 and 7) – are critical in coupling the lower and upper atmosphere (e.g., Pogoreltsev et al., 2007). Hence, the benefit here is twofold. A more accurate model of the lower atmosphere can be produced by including the upper atmosphere, and vice versa. Atmospheric tides propagate upwards, growing roughly exponentially with height because of the corresponding exponential decrease of the background density. Hence, these waves become particularly large in the Mesosphere and Lower Thermosphere (MLT), with associated influences on the ionosphere and thermosphere at higher altitudes including an influence on the transport of chemical species (e.g., Jones Jr et al., 2014). The lower atmosphere is therefore an important driving factor in upper atmosphere variability (Akmaev, 2011), and thus any space weather forecast must include these factors so that affected users can obtain a more comprehensive picture of upper atmosphere variations and the consequent implications for their use case. In turn, energetic particle precipitation (EPP) and changes in solar radiation associated with the solar cycle can also impact the troposphere. EPP events can lead to changes in MLT and stratospheric NOx and ozone concentrations which can modulate polar surface air temperatures by affecting the radiative budget with consequent effect on atmospheric circulation patterns (e.g., Seppälä et al., 2009; Päivärinta et al., 2013). Ineson et al. (2011) show the impact of solar minimum and solar maximum on Northern Hemisphere winter surface temperatures via changes to the North Atlantic Oscillation. Further, tidal winds in the upper atmosphere act to filter the field of atmospheric waves, and consequently modulate the forcing of the global atmospheric circulation (e.g., Fritts and Alexander, 2003).

The Met Office's weather and climate model – the Unified Model (UM) (discussed more in Chapter 3.2) – currently has an upper boundary at 85 km. Attempts to increase the height of this upper boundary have thus far been unsuccessful. Initial runs of the UM with an increased model lid height performed by Harry (2015) became unstable and crashed unless considerable damping was used. These runs tested the UM with both 100 and 120 km model lids, with experiments focused on tuning parameters to obtain the longest run time possible. In particular, the cause and nature of the instability remained undiagnosed.

New UM chemistry and radiation schemes to supply appropriate radiative forcing in the MLT were not ready at the time of performing this research. In addition, the non-orographic gravity wave parameterisation scheme has not been optimised for use above the mesopause.

In the case that the model can be extended, it must be verified that the fields produced by the model are realistic and that various key properties of the upper atmosphere are captured. In particular, the wind fields are an important indicator of realistic atmospheric circulation, and thus an important question is - are the wind fields produced by the new ExUM physically realistic in the extended region? Further, one must examine the properties of the model to determine if it is producing realistic fields in a manner that is consistent with observations and other modelling studies. In particular, the spatial and temporal characteristics of the tides produced by the model must be examined in order to validate their accuracy.

The aim of this research is to extend the Unified Model into the Mesosphere and Lower Thermosphere and validate the realism of the model output using meteor radar observations, with a particular focus on winds and tides and their decomposition into

migrating and non-migrating modes. The thesis can be split into two parts.

The first part of the thesis is devoted to building a stable Extended Unified Model appropriate for giving an accurate representation of the Mesosphere and Lower Thermosphere. To do this, we perform an analysis of the unstable extension of the Unified Model with an upper boundary at 100 km, looking at key diagnostics to determine the cause of the model instability. Consequently, we produce a new nudging scheme to a climatological temperature profile for the MLT which successfully stabilises the ExUM. Satisfied that the model produced was now stable, we tested this stability by refining the vertical mesh as well as increasing the upper boundary to heights of 120 and 135 km. With this, we are able to investigate the functionality of the model under different regimes and suggest model configurations for future studies.

The second part of the thesis is focused on comparing the ExUM developed in the first part with meteor radar observations and with other modelling studies, with the focus of determining the realism of the fields produced by the newly developed model. Based on the fact that a key driver of atmospheric flow in the MLT is atmospheric tides, we put particular weight on examining the properties of tides produced by the model with those given by meteor radar observations. In the first case study examining the ExUM, we observe that the model has a reasonable capability to produce winds and tides that are comparable to meteor radar observations, but with significant differences in the detail. The simplified nature of the global temperature profile used for the nudging scheme makes it necessary to improve the scheme for continued use, and so we develop this to be a function of both month and latitude. With this we examine the structure of the migrating and non-migrating modes present in the model, and show that the ExUM has a good capability for producing non-migrating modes which have been shown to be important in other modelling studies, such as the large amplitude DE3 which has been proposed to account for the striking zonal wavenumber-four wave structure observed in the equatorial ionospheric anomaly and equatorial electrojet (Hagan et al., 2007).

The work in this thesis has led to a published review commentary (Jackson et al., 2019) and three original papers led by the author of this thesis (one published (Griffith et al., 2020), one accepted (Griffith et al., 2021) and one submitted (Griffith and Mitchell, 2021)). The author of this thesis has also been involved as a co-author for a related paper (Jackson et al., 2020). This is summarised in Table 2.1.

Title	**Year**	**Contribution**	**Status**
Future directions for whole atmosphere modeling: Developments in the context of space weather. (DOI: 10.1029/2019SW002267)	2019	Co-Author	Published
The Space Weather Atmosphere Models and Indices (SWAMI) Project: Overview and First Results. (DOI: 10.1051/swsc/2020019)	2020	Co-Author	Published
Stable Extension of the UM into the MLT. (DOI: 10.1051/swsc/2020018)	2020	Lead Author	Published
Winds and Tides of the Extended UM in the MLT Validated with Meteor Radar Observations. (DOI: 10.5194/angeo-39-487-2021)	2021	Lead Author	Published
Analysis of Migrating and Non-Migrating Tides of the Extended UM in the MLT.	2021	Lead Author	In Review

Table 2.1: *A summary showing the papers produced involving the author of this thesis.*

The review is presented in Chapter 4 and provides a commentary on the current state of whole atmosphere modelling, discussing important considerations and the models which are at the forefront of current study in this field. This chapter does not include original results, but provides a good introduction to the field of whole atmosphere modelling. The remainder of the thesis presents three original papers formulated by the author of this thesis, which are presented following the "Alternative Thesis Format" or in the style of Thesis by Publication. Namely, Chapters 5 - 7 each comprise of one of the published/submitted manuscripts. In each Chapter, we provide a short introduction and conclusion to place the work in the context of the thesis. Chapter 8 then provides some final conclusions, discussing the results of the work in the broader setting of whole atmosphere modelling and an outlook on directions for future research.

2.2. Summary of original papers

Chapter 5 – Stable Extension of the Unified Model into the Mesosphere and Lower Thermosphere

In this chapter we successfully produce a stable extension of the UM into the MLT, as a first step towards a whole atmosphere model. The pre-existing instability is examined and narrowed down to the model's radiation scheme - its assumption of Local Thermodynamic Equilibrium (LTE) is broken in the MLT. We subsequently address this issue by relaxation to a climatological temperature profile in this region. This provides a stable extended UM which can be used as a developmental tool for further examination of the model performance. We then build on the success of the nudging implementation by testing the model at an improved vertical resolution. Initial attempts to address this problem with a 3 km vertical resolution and a 100 km lid were successful, and we hence use this model for its validation in Chapter 6. Refining the vertical resolution to 1.5 km makes the model becomes unstable due to large horizontal and vertical wind velocities. However, increasing the vertical damping coefficient, which damps vertical velocities near the upper boundary, allows a successful year long climatology to be produced with these model settings. With the goal of a whole atmosphere model we also experiment with an increased upper boundary height. Increasing the upper model boundary to 120 and 135 km also leads to stable simulations. However, a 3 km resolution must be used and it is necessary to further increase the vertical damping coefficient.

The author's contribution in particular was in performing the model runs to extract results from the unstable and stable model; producing the nudging scheme and vertical level sets used in the model; preparation of all figures; and leading the authoring of the manuscript.

Chapter 6 – Winds and Tides of the Extended Unified Model in the Mesosphere and Lower Thermosphere Validated with Meteor Radar Observations

In this chapter we present the first study of winds & tides from the new stable extension of the Unified Model (ExUM) developed in Chapter 5. We make a comparison against meteor radar observations of winds and tides from 2006 between 80 and 100 km over two radar stations – Rothera (68° S, 68° W) and Ascension Island (8° S, 14° W). These locations are chosen to study tides in two very different tidal regimes – the equatorial regime, where the diurnal (24 hour) tide dominates, and the polar regime, where the semi-diurnal (12 hour) tide dominates. We also discuss the results of the model in the context of other atmospheric models such as those discussed in Chapter 4. The results of this study illustrate that the ExUM is capable of reproducing atmospheric winds and tides that capture many of the key characteristics seen in meteor radar

observations, such as zonal & meridional wind maxima and minima, the increase in tidal amplitude with increasing height, and the decrease in tidal phase with increasing height. In particular, in the equatorial regime, some essential characteristics of the background winds, tidal amplitudes and tidal phases are well captured, but with significant differences in detail. In the polar regime, the difference is more pronounced. The ExUM zonal background winds in austral winter are primarily eastward rather than westward, and in austral summer are larger than observed above 90 km. The ExUM tidal amplitudes here are in general consistent with observed values, but are also larger than observed values above 90 km in austral summer. The tidal phases are generally well replicated in this regime. We propose that the bias in background winds in the polar regime is a consequence of the lack of in-situ gravity wave generation to generate eastward fluxes in the MLT. The results of this study indicate that the ExUM has a good natural capability for modelling atmospheric winds and tides in the MLT, but that there is room for improvement in physical parameterisations in this region such as the simplified nudging scheme which we develop further in Chapter 7.

The author's contribution in particular was in performing the model runs for comparison with meteor radar data; performing the tidal analysis on the model and radar data; preparation of all figures; and leading the authoring of the manuscript.

Chapter 7 – Tidal Analysis of the Extended Unified Model

In this chapter we refine the features of the ExUM developed in Chapter 5 to make the model more robust up to the lower boundary of the ionosphere at around 110 km, based on some of the observations made in Chapter 6. This includes an improved nudging profile with seasonal and latitudinal dependency, as well as a physically derived vertical resolution, which allows us to strike a balance between resolving physically significant waves and computational efficiency. We also place the lid at 120 km but only use output below c. 110 km, where the lack of a modelled ionosphere is still reasonable. With this in place and with the improvement of the non-orographic gravity wave parameterisation scheme in mind, we perform an analysis of the spatial tidal components present in the modelled winds. We place a particular focus on the non-migrating (not sun-following) modes of the atmospheric tides present in the model, analysing their magnitude and seasonal variability. We also present the latitudinal and short-term variability of these modes together with that of the migrating modes. The results of this study show that the ExUM is in general consistent with other high-top models and observational datasets. In particular, the non-migrating tidal modes in the ExUM have notable magnitudes across a large number of spatial modes, with significant short term variability. The migrating modes reproduce the expected latitudinal variation, such as the bimodal structure with tropical peaks in the diurnal zonal wind tide. However, the characteristics of the tides differ even across the relatively small number of studies considered and therefore it is necessary to see what effects the non-orographic gravity wave parameterisation has on the magnitudes and structure of the tides in order to confirm that it is appropriate for the MLT. We make recommendations of further studies which can be performed to help improve this scheme for the MLT, building on the suggestions made in Chapter 6, such as using a latitudinally varying source spectrum, as well as tuning the scheme for the MLT rather than to give a realistic Quasi-Biennial Oscillation (QBO).

The author's contribution in particular was in performing the model runs for comparison with meteor radar data; implementing improvements to the model's nudging scheme and vertical level set; performing the non-

migrating tidal analysis on the model data; preparation of all figures; and leading the authoring of the manuscript.

Chapter 3

Background

We now introduce a few key concepts which provide useful background knowledge to the chapters which follow.

3.1. Atmospheric structure

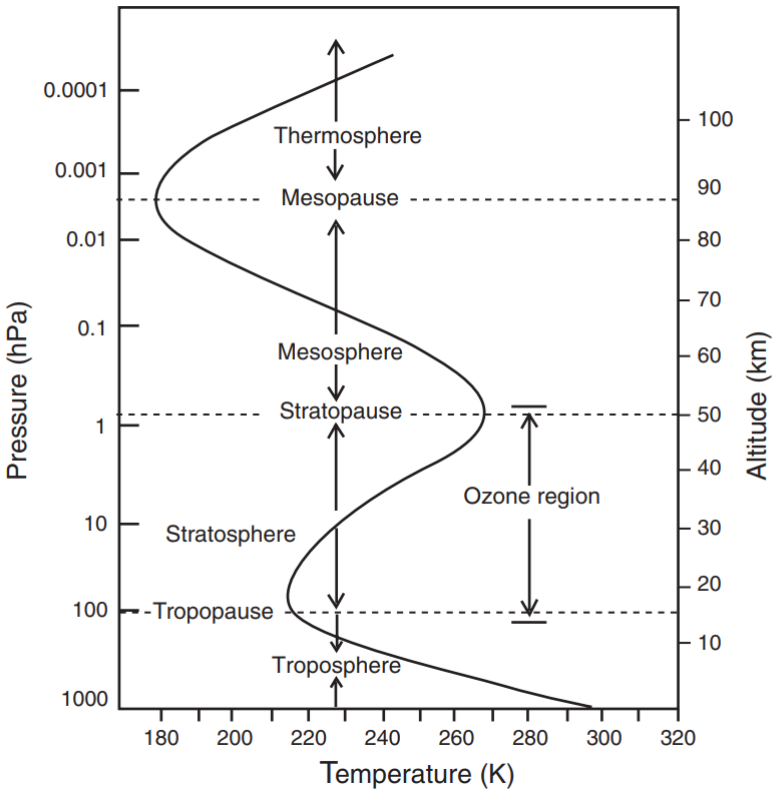

Figure 3-1: *Thermal structure of the Earth's atmosphere up to 120 km.*

The atmosphere can be categorised based on its thermal structure, which splits the atmosphere into four primary vertical regions, as in Figure 3-1. These are the troposphere, stratosphere, mesosphere and thermosphere, split based on the temperature extrema observed between each region.

The mesosphere and lower thermosphere (MLT) describes the region containing the boundary between the Earth's atmosphere and outer space, ranging from around 50-120 km. The fact that the MLT contains this boundary means it is a region of particular scientific interest, but is also therefore challenging to represent accurately in atmospheric models. For example, this region is where vertically propagating atmospheric waves, in particular atmospheric tides (discussed more in 3.4), can reach peak amplitudes – the exponential decrease with increasing height in the background density corresponds to an exponential increase in a wave's amplitude. This results in the wave becoming dynamically unstable leading to "wave breaking" with consequent momentum deposition into the upper layers of the atmosphere. This greatly influences the atmospheric circulation in this region (e.g., Immel et al., 2006). The MLT also

contains the lower part of the ionosphere which introduces additional influences on the dynamics of this region due to the electric field and its variation (as discussed in Chapter 4). Changes in the electric field modify Joule heating, which in turn modifies atmospheric temperature and wind. Thus, the dynamics shift from that of a neutral atmosphere to one that is also driven by electrical and magnetic forcing. The chemical composition of the atmosphere also changes greatly within the MLT. The atmosphere is well mixed below the turbopause (c. 105 km), but above this, diffusive separation means that the atmospheric composition is organised by molecular weight and hence it is this that determines the dynamics. Furthermore, because of the increasing effect of the ionosphere, the chemistry becomes dominated by ion chemistry, rather than by compound chemistry as is the case in the lower atmosphere (e.g., Plane et al., 2015). Investigations into the model chemistry are beyond the scope of this thesis, and work to develop this aspect of the model was performed by Chris Kelly at the University of Leeds (Kelly, 2020).

3.2. The Unified Model

The Met Office's Unified Model is a General Circulation Model (GCM), modelling the weather and climate of the atmosphere. It is split into two main sections; the first contains the *dynamical core*, which describes the evolution of resolved atmospheric fluid dynamical processes by numerically solving the Euler equations of motion governing atmospheric flow; and the second is made up of *physical parameterisations*, which attempt to describe parts of atmospheric physics not captured by the governing equations, such as solar radiation and sub-grid scale gravity waves (see e.g. Walters et al. (2019) for an idea on the formulation of the Unified Model).

3.2.1 Dynamical core

The current dynamical core (ENDGame; Wood et al., 2014) solves the non-hydrostatic, fully compressible deep-atmosphere equations of motion on a rotating sphere using a semi-implicit semi-Lagrangian formulation. The primary prognostic variables used are the three-dimensional wind components, virtual dry potential temperature, the Exner function of pressure and dry density, whilst moisture prognostics are advected as free tracers (further details on these variables is given below). The discretised equations are solved using an iterative implicit method – more details of which can also be found in Wood et al. (2014). Importantly this is in a non-hydrostatic framework which allows for vertical acceleration and hence accurate high resolution forecasting.

In vector form, these governing equations (for a perfect gas) are

$$\frac{D\mathbf{u}}{Dt} + 2\boldsymbol{\Omega} \times \mathbf{u} = -c_p\theta\nabla\pi + \mathbf{g} + \mathbf{S}^{\mathbf{u}}, \tag{3.1}$$

$$\frac{D\theta}{Dt} = S^{\theta}, \tag{3.2}$$

$$\frac{D\rho}{Dt} + \rho\nabla \cdot \mathbf{u} = 0, \tag{3.3}$$

$$\pi^{(1-\kappa)/\kappa} = \left(\frac{R}{p_0}\right)\rho\theta, \tag{3.4}$$

$$\frac{D\mathbf{x}}{Dt} = \mathbf{u}, \tag{3.5}$$

which represent the conservation of momentum (3.1), the first law of thermodynam-

ics (3.2), the conservation of mass or continuity equation (3.3), the equation of state (3.4) and the kinematic equation (3.5), which is included in anticipation of the semi-Lagrangian discretisation (as introduced later in this Section).

The variables introduced are:

- $\mathbf{x}$, the chosen coordinate system (e.g. cartesian or spherical polar);
- $\mathbf{u} = (u, v, w)^T$, the 3 dimensional vector of velocities;
- $\mathbf{\Omega}$, the Earth's angular velocity vector;
- c_p, the specific heat at constant pressure for air;
- c_v, the specific heat at constant volume for air;
- θ, the potential temperature;
- π, the Exner function of atmospheric pressure p,
- g, the apparent gravitational vector, being the sum of actual gravity and the centrifugal force;
- $\mathbf{S^u} = (S^u, S^v, S^w)$ & S^θ, external forcing terms which are approximated by various parameters. These terms are estimated in the parameterisation section of the model (c.f. Section 3.2.2);
- ρ, the atmospheric density;
- $\kappa \equiv R/c_p$, where $R \equiv c_p - c_v$ is the difference of specific heats; and
- p_0, the reference atmospheric pressure, usually taken at mean sea level.

The chosen model variables have useful properties when it comes to modelling atmospheric flow. The potential temperature θ of a parcel of fluid at pressure p is the temperature that the parcel would attain if adiabatically[1] brought to the reference atmospheric pressure p_0. It is given by

$$\theta \equiv T \left(\frac{p_0}{p} \right)^\kappa .$$

The potential temperature acts as a useful metric of atmospheric stability. Under normal, stably stratified conditions, the potential temperature increases with height, so that its derivative with respect to height is strictly positive, and vertical motions are suppressed (Fritts and Rastogi, 1985). If it is strictly negative, the atmosphere is unstable to vertical motions. This gives a good indicator for when convection is likely, which can then be introduced dynamically through the parametrised terms $\mathbf{S^u}$ and S^θ.

Additionally, the Exner function of pressure π, which can be viewed as a non-dimensionalised form of atmospheric pressure, is defined as

$$\pi \equiv \left(\frac{p}{p_0} \right)^\kappa = \frac{T}{\theta},$$

where T is absolute temperature. As can be seen, this gives a very simple relationship between the Exner pressure and potential temperature. It is also useful as it removes

[1] That is, without loss of heat or matter to the surroundings, with energy only being lost to the surroundings as work.

a $1/\rho$ multiplier in the pressure gradient term, replacing it with a θ multiplier, which varies much more slowly with height.

Finally, the material or Lagrangian derivative (applied to a vector component-wise) is given by

$$\frac{D}{Dt}(\cdot) \equiv \frac{\partial}{\partial t}(\cdot) + \mathbf{u} \cdot \nabla(\cdot). \tag{3.6}$$

Several other intricacies and modifications including equations for the various phases of moisture travelling within an air parcel are implemented in the UM, but are not discussed here.

There are a few important observations regarding (3.1) - (3.5) that should be made:

- The equations do not make the shallow-atmosphere approximation in that the full terms relating to the Coriolis acceleration involving $\mathbf{\Omega}$ are retained. Without this approximation, the model is therefore referred to as a *deep-atmosphere* model.

- The equations do not make the hydrostatic approximation and are hence *non-hydrostatic*. This assumption allows the vertical propagation of wave motions through the atmosphere, and is particularly important as the model resolution becomes finer and the hydrostatic approximation is no longer valid. The hydrostatic approximation states that complete balance exists between the force of gravity and the pressure force, namely, with a z vertical coordinate, that

  $$\frac{\partial p}{\partial z} = \rho g.$$

  This inhibits vertical wave motion and it is this that influences the choice of a height based vertical coordinate in the Met Office's UM which therefore allows vertical wave motion in a non-hydrostatic framework.

- The dynamical core does not specify a particular coordinate system; it is coded with respect to a generalised coordinate system and a generalised metric. Thus, the model is able to be used for many different purposes, for many spatial scales and for many time scales. Contrasting scenarios such as a climate model running over the course of decades on a coarse grid or a weather model running over the course of days on a fine grid are both able to be run under the same model. This unifies the entire modelling framework without the need for several models serving different purposes, which gives the model it's name - the *Unified* Model.

- The external forcing terms $\mathbf{S^u} = (S^u, S^v, S^w)$ and S^θ include many of the complex phenomena that occur in the atmosphere. These terms are determined by various parameterisation schemes in the model, which attempt to capture what is dropped when the numerical method is applied to the equations. Thus, in every time step of the model, the governing equations are solved using the numerical method, and then the parametrisation schemes are implemented to update these forcing terms in every time step. There are a large number of elements to capture, and consequently a large number of schemes - we focus on and describe a few of these in Section 3.2.2.

In order to solve (3.1) - (3.5), the Met Office's UM (as well as many other models) uses a semi-implicit semi-Lagrangian method which combines a semi-implicit time integration, with a semi-Lagrangian advection scheme in space (e.g., Temperton and Staniforth, 1987; Melvin et al., 2010; Wood et al., 2014; Benacchio and Wood, 2016).

The equations are then discretised spatially on an Arakawa C grid (first used in Arakawa and Lamb (1977)) in the horizontal and a Charney-Phillips grid (first used in Charney and Phillips (1953)) in the vertical. These discretisations can be seen in Figure 3-2.

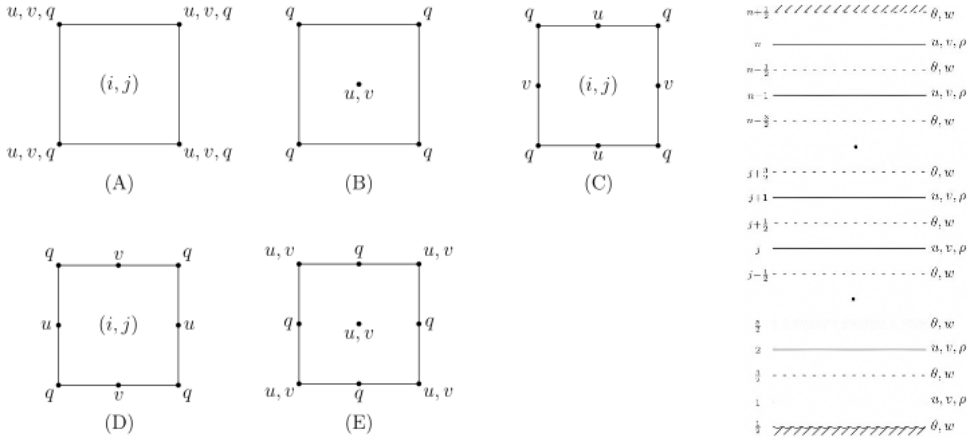

Figure 3-2: *The grids used in the spatial discretisation in the horizontal (left, grid (C)) and the vertical (right) in the UM.*

The difference between each of the grids is in the placement of variables. They can either be collocated (e.g. grid (A)), staggered (e.g. grid (C)) or a mix of the two (e.g. grid (B)). The Arakawa C grid and Charney-Phillips grid are chosen to optimise natural oscillations and to avoid producing computational modes, hence improving the stability of the model. These computational modes can occur when quantities within the model equations are computed using collocated variables, and so the choice of which variables to collocate and which to stagger is based on the governing equations for the system.

There are many stability mechanisms used within the dynamics section of the model to account for problems introduced by the numerical discretisation (e.g., Thuburn and Staniforth, 2004; Rivest et al., 1994). Such problems and numerical schemes introduced to help resolve them are discussed in Chapter 5, Section 2.2.

The parametrised terms $\mathbf{S^u}$ and S^θ are solved for outside of the ENDGame scheme. We describe the general structure and a few specific schemes in the next section.

3.2.2 Physical parameterisations

There are many atmospheric processes which are not included in the dynamical equations of the model or operate on much smaller length scales than those used in the dynamical scheme, and are therefore not resolved on the numerical grid. This is where the physical parameterisation section of the model comes in. The atmospheric physics section of the model adds these parameterisations to account for atmospheric processes not included in the dynamical equations and therefore complete the atmospheric model. There are a large number of parameterised processes within the model, and they are detailed in (Walters et al., 2019).

The radiation scheme simulates the effect of the Sun on the Earth's atmosphere, parameterising incoming short wavelength radiation and outgoing long wavelength radiation, based on the scheme of Edwards and Slingo (1996). The chemistry scheme

models the effects of airborne molecules and aerosols and their transport interactively. It couples with the radiation scheme to provide appropriate heating/cooling to give the expected atmospheric temperature structure. Some of the details of both of these schemes are discussed in Chapter 5, Section 2.1, in preparation for modifying the schemes and introducing a new radiation scheme for the work in Chapters 6 and 7.

The method employed in the UM to account for sub-grid scale non-orographic gravity waves is the Ultra Simple Spectral Parameterisation (USSP) of Warner and McIntyre (2001). It treats non-orographic gravity waves with non-zero phase speeds which are unable to be resolved by the model. This is important as the model has too coarse a resolution to represent large portions of the gravity wave spectrum. The approach, with further modifications by Scaife et al. (2002) imposes gravity wave saturation via an empirical, observationally derived criterion (e.g. Tsuda et al. (1991)) that limits the growth of the vertical wave number spectrum of the gravity wave field. It launches an unsaturated spectrum from a level close to the surface and imposes a homogeneous (location invariant) total vertical flux of horizontal wave pseudomomentum[2]. The spectrum uses a characteristic vertical wavelength peak of 4.3 km and parameterises vertical wavelengths up to a maximum of 20 km. The amplitude of the spectrum is chosen to give momentum deposition and, hence, a QBO in the model that is realistic, whilst also decelerating the extratropical jets in the mesosphere in a realistic manner.

This scheme requires specification of a source spectrum for the non-orographic gravity waves, with the assumption of a globally uniform source. This is necessary for computational efficiency, but is poorly constrained by observations due to the sporadic nature of middle atmosphere non-orographic gravity waves (e.g., Fritts and Alexander, 2003). In fact, in a recent study by Yiğit et al. (2021), they showed that the use of a latitudinally varying GW source spectrum can have a significant impact on middle atmosphere circulation, with consequent important effect on the diurnal tides in the MLT.

Moreover, it is worth reiterating that the USSP as used in the UM was designed, and primarily tuned, to obtain more realistic stratospheric features such as the QBO rather than to give appropriate forcing in the MLT. Hence, it is likely that additional work is necessary to improve the representation of gravity waves in the MLT. This topic represents a key part of our discussion in Chapters 6 and 7, where we recommend specific improvements which can be made to the USSP, as well as further studies which can be carried out to improve its accuracy in the MLT.

3.3. High-Top and Whole Atmosphere Models

A whole atmosphere model is an atmospheric model that extends from the ground up to the limits of the Earth's atmosphere at around 600 km. This is therefore a model which must combine a model of the neutral atmosphere and a model of the ionosphere. A discussion on aspects of their development can be found in Chapter 4, with a list of current state-of-the-art whole atmosphere models.

A "high-top" model generally extends the upper boundary of an atmospheric model into the thermosphere and may or may not include a modelled ionosphere. This represents a first step towards a whole atmosphere model. A detailed summary of current non-mechanistic high-top models can be found in Chapter 6, with reference to how the Extended Unified Model produced in Chapter 5 compares within this context.

[2]The vertical wave numbers representing the horizontal momentum stored in a vertically propagating gravity wave.

3.4. Atmospheric Tides

Atmospheric solar thermal tides are global-scale oscillations with a period exactly equal to one day or an integer fraction of one day. The solar thermal tides (hereafter, simply "tides") are excited primarily by the diurnal cycle in the solar heating of water vapour and ozone in the troposphere and stratosphere and the release of latent heat in deep tropospheric convection. An important distinction in considering the tides is the difference between the migrating and non-migrating modes. The migrating tides are Sun-synchronous - i.e., they follow the apparent westward motion of the Sun around the Earth. These tides must therefore have zonal wavenumbers equal to the number of cycles of the tide per day. In contrast, the non-migrating tides are not Sun-synchronous and include modes that propagate eastwards as well as westwards and that can have zonal wavenumbers not equal to the number of cycles of the tide per day.

Detailed reviews on migrating and non-migrating tides and their important influence on dynamics in the MLT can be found in the introduction to Chapters 6 and 7.

Chapter 4

A Commentary on the State of Whole Atmosphere Modeling

This chapter provides a commentary on the current state of whole atmosphere modelling and recent developments, with particular a focus on space weather. It gives useful background as to what must be considered when producing a model with an extended upper boundary, and hence provides useful context for the rest of the thesis. This joint work was produced with David R. Jackson, Tim J. Fuller-Rowell, Dan J. Griffin, Christopher W. Kelly, Daniel R. Marsh, and Maria-Theresia Walach and was published in *Space Weather* as an open access publication (Jackson et al., 2019).

4.1. Outline of the Article

This article presents a commentary on the current state of whole atmosphere modelling with the key finding that any model of the upper atmosphere now needs to have some representation of the lower atmosphere. This commentary was produced based on the discussion and presentations at the Whole Atmosphere Modelling Workshop in Madrid in 2018, hosted by Deimos.

The work begins by introducing space weather forecasting and how whole atmosphere models – which model the atmosphere from the ground to around 600 km – are a key part of this given the importance of atmosphere-ionosphere coupling.

Three existing models are then summarised, leading to a discussion on what the key building blocks are for good whole atmosphere models, including the dynamical core, radiation and chemistry schemes, ionospheric dynamics and atmospheric observations.

This informs future research directions, such as comparing models with hydrostatic and non-hydrostatic dynamical cores, as well as developing a verification strategy and methodology for future models.

Appendix 6B: Statement of Authorship

This declaration concerns the article entitled:			
Future Directions for Whole Atmosphere Modeling: Developments in the Context of Space Weather			
Publication status (tick one) **Draft manuscript** ☐ **Submitted** ☐ **In review** ☐ **Accepted** ☐ **Published** X			
Publication details (reference)	Journal: Space Weather Authors: David R. Jackson, Tim J. Fuller-Rowell, Dan J. Griffin, Matthew J. Griffith, Christopher W. Kelly, Daniel R. Marsh, and Maria-Theresia Walach		
Copyright status (tick the appropriate statement) I hold the copyright for this material X Copyright is retained by the publisher, but I have been given permission to replicate the material here ☐			
Candidate's contribution to the paper (provide details, and also indicate as a percentage)	The largest portion of the work for this article was performed by David R. Jackson (40%). All other authors contributed equally (12%). The formulation of ideas and design of methodology was performed equally by all authors (17%) The presentation of the content was performed equally by all authors (17%) The author's contribution in particular was to aid in the gathering of information for the commentary at the Whole Atmosphere Modelling Workshop; to write up a portion of the gathered information, as well as helping with proofing of the final document.		
Statement from Candidate	This paper reports on original research I conducted during the period of my Higher Degree by Research candidature.		
Signed	Matthew J. GRIFFITH	**Date**	06/08/2021

Last update: Feb 2019

AGU100 ADVANCING EARTH AND SPACE SCIENCE

Space Weather

COMMENTARY
10.1029/2019SW002267

Key Points:
- We have reached a paradigm shift, where any self-respecting space weather model of the upper atmosphere now needs to have some representation of the lower atmosphere
- Further model developments are required in several key areas, including dynamical cores and the improved representation of gravity waves
- A road map of future actions is presented to ensure good progress continues to be made; this includes the development of a multi-model verification strategy

Correspondence to:
D. R. Jackson,
david.jackson@metoffice.gov.uk

Citation:
Jackson, D. R., Fuller-Rowell, T. J., Griffin, D. J., Griffith, M. J., Kelly, C. W., Marsh, D. R., & Walach, M.-T. (2019). Future directions for whole atmosphere modeling: Developments in the context of space weather. *Space Weather*, *17*, 1342–1350. https://doi.org/10.1029/2019SW002267

Received 31 MAY 2019
Accepted 24 AUG 2019
Accepted article online 30 AUG 2019
Published online 11 SEP 2019

Future Directions for Whole Atmosphere Modeling: Developments in the Context of Space Weather

David R. Jackson[1], Tim J. Fuller-Rowell[2], Dan J. Griffin[1], Matthew J. Griffith[3], Christopher W. Kelly[4], Daniel R. Marsh[4,5], and Maria-Theresia Walach[6]

[1]Met Office, Exeter, UK, [2]CIRES, University of Colorado, Boulder, CO, USA, [3]Department of Mathematical Sciences, University of Bath, Bath, UK, [4]School of Earth and Environment, University of Leeds, Leeds, UK, [5]National Center for Atmospheric Research, Boulder, CO, USA, [6]Department of Physics, Lancaster University, Lancaster, UK

Abstract Coupled Sun-to-Earth models represent a key part of the future development of space weather forecasting. With respect to predicting the state of the thermosphere and ionosphere, there has been a recent paradigm shift; it is now clear that any self-respecting model of this region needs to include some representation of forcing from the lower atmosphere, as well as solar and geomagnetic forcing. Here we assess existing modeling capability and set out a road map for the important next steps needed to ensure further advances. These steps include a model verification strategy, analysis of the impact of nonhydrostatic dynamical cores, and a cost-benefit analysis of model chemistry for weather and climate applications.

Plain Language Summary Numerical models that comprehensively simulate the region between the Sun and the Earth represent a key part of the future development of space weather forecasting. With respect to predicting the Earth's upper atmosphere, there has been a recent paradigm shift; it is now clear that any self-respecting model of this region needs to include some representation of impacts from below (the lower atmosphere) as well as from above (solar variability and the effects of solar wind fluctuations). Here we assess existing modeling capability and set out a road map for the important next steps needed to ensure further advances. These steps include a strategy for checking the accuracy of the models, an analysis of the impact of methods chosen to represent upper atmosphere dynamics, and an assessment of the relative benefits of comprehensive (but expensive) and simplified (but inexpensive) model representations of upper atmosphere chemistry.

1. Introduction

We are at the stage in the development of operational space weather forecasts where individual models of components of the Sun-to-Earth domain (including the ionosphere and the thermosphere) are beginning to be coupled together. Such a coupled modeling system, constrained by assimilation of near real time observations, has the potential to provide considerably better forecasts than currently available. It is clear that representing the impact of, for example, a coronal mass ejection, across the whole Sun-to-Earth domain can potentially improve forecasts in the ionosphere. The potential for improved forecasts has already been demonstrated for parts of the Sun-to-Earth system. For example, coupling a global magnetosphere model with an inner magnetosphere drift physics model considerably improves forecasts of geomagnetic storms (Liemohn et al., 2018) and improved representation of the thermosphere leads to improved ionospheric evolution (e.g., Chartier et al., 2013). In addition, there is a strong connection between the lower atmosphere state and the ionosphere that was highlighted initially by Immel et al. (2006) and demonstrated in later modeling studies (e.g., Pedatella et al., 2016). Furthermore, data assimilation (DA) schemes are already used for operational ionosphere models (e.g., Schunk et al., 2016), and experimental systems show that assimilation can improve model initial conditions in the thermosphere (e.g., Murray et al., 2015), the magnetosphere (e.g., Merkin et al., 2016), and the heliosphere (e.g., Lang & Owenst, 2019).

However, it is also becoming increasingly apparent that, in addition to correctly specifying this space weather forcing, thermosphere and ionosphere forecasts can also benefit from an accurate representation of coupling from within and below. The motivation for a whole atmosphere model (i.e., a model that extends from the ground up to the exobase) is thus twofold:

1. Recent research (e.g., Chartier et al., 2013, 2016; Hsu et al., 2014) has shown that no matter how accurately one represents the current ionospheric state, the quality of the subsequent ionospheric forecasts crucially depends on the ability to also represent the thermosphere and its evolution.
2. Both the ionosphere and thermosphere are sensitive to forcing from the lower atmosphere. The seminal paper by Immel et al. (2006) indicated connections between tidal patterns in the lower thermosphere and the *F* region ionosphere and noted that the tidal structure was linked to patterns of convection in the equatorial troposphere. Furthermore, numerous papers (e.g., Goncharenko, Chau, et al., 2010, Goncharenko, Coster, et al., 2010; Liu & Roble, 2002; McDonald et al., 2018; Pedatella et al., 2012) have shown how planetary wave forcing, specifically via stratospheric sudden warmings (SSWs), can affect lower thermospheric tides and thus the ionosphere.

Akmaev (2011) reviewed whole atmosphere models at a time when these models were quite new and our understanding of the links between the lower and upper atmosphere was developing. A Whole Atmosphere Modelling Workshop was held in Tres Cantos, Spain in June 2018 and a strong consensus emerged: the need to have some representation of the lower atmosphere in space weather models of the upper atmosphere. This is highly significant for the continued development of whole atmosphere models. In this commentary we review existing models, how their building blocks can be further developed, and how we can use observations (via DA and verification) to confront the model simulations and potentially produce improved forecasts.

2. Existing Models

There are three current whole atmosphere space weather models:

1. The Whole Atmosphere Model (WAM; Akmaev et al., 2008; Fuller-Rowell et al., 2008) is based on the U.S. National Weather Service Numerical Weather prediction model and extends from the surface to around 600 km. It is being combined with a separate ionosphere model Ionosphere Plasmasphere Electrodynamics (Maruyama et al., 2016) to produce a coupled model of the ionosphere and neutral atmosphere. WAM represents both the mean state and tides in the thermosphere well (e.g., Lieberman et al., 2013, show good agreement with diurnal and time mean Challenging Mini Satellite Payload winds). The pattern of changes seen in ionospheric vertical plasma drift and Total Electron Content (TEC; which occur in response to SSW forcing from below) agrees well with observations (e.g., Wang et al., 2014).
2. The Whole Atmosphere Community Climate Model with thermosphere and ionosphere extension (WACCM-X; Liu et al., 2010; Liu et al., 2018) is focused primarily on climate time scales (in contrast to WAM, which is focused on weather forecast time scales). With a comparable altitude range to WAM, it has a much more detailed representation of neutral and ion chemistry. Liu et al. (2018) report that in WACCM-X the amplitudes and seasonal variations of atmospheric tides in the mesosphere and lower thermosphere (MLT), equatorial ionosphere anomaly structures and storm time ionospheric behavior are all in good agreement with observations.
3. The Ground to topside model of the Atmosphere and Ionosphere for Aeronomy (GAIA) combines neutral atmosphere, ionospheric, and electrodynamic models. The neutral model covers the entire atmosphere from the Earth's surface up to the top of the thermosphere and contains a comprehensive range of physical parametrizations (e.g., Fujiwara & Miyoshi, 2010). Jin et al. (2012) show the ability of GAIA to model the impact of an SSW on migrating tides and the associated ionospheric response, with in general good agreement shown with Sounding of the Atmosphere using Broadband Emission and Constellation Observing System for Meteorology, Ionosphere, and Climate observations.

For clarification, weather models focus on short forecast time scales (often less than 10 days) and use as fine a resolution as possible in order to represent meteorological features such as weather fronts. Since forecast quality will depend on initial conditions, weather models must be initialized using DA. Coupling to other models (such as an ocean model) is usually not required on forecast time scales, and the need to run quickly in near real time precludes the use of such coupled models, and it is necessary to use fast, less-complex representations of physics and chemistry. Climate models are run for long forecast time scales such as annual or multidecadal periods and so generally have coarser resolutions than weather models. Coupling to comprehensive models of the Earth system (chiefly ocean and atmospheric chemistry models) is required to

represent long-term variability and climate change. For the specific case of whole atmosphere models, WAM and WACCM do not completely meet the description given above (e.g., WACCM can run at a finer horizontal resolution than WAM), but the WAM chemistry scheme is simple and designed for fast weather forecasts, whereas the WACCM chemistry scheme is considerably more complex, and it can be coupled to an ocean model. This enables WACCM to be used in activities like the Coupled Model Intercomparison Project 5, studying, for example, climate change from 1850 (Marsh et al., 2013) and climate impacts associated with long-term ozone change (Eyring et al., 2013).

3. Building Blocks for Better Models

3.1. Dynamics—Gravity Waves and Dynamical Formulation

The representation of gravity waves is very important for accurate modeling of the thermosphere. They are the prime driver of the middle atmosphere circulation and affect tidal amplitudes and thus can influence the mechanisms connecting the lower atmosphere with the thermosphere and ionosphere (see, e.g., Yiğit et al., 2016). Furthermore, accurate simulation of medium and small-scale traveling ionospheric disturbances (MSTIDs) and associated ionospheric plasma bubbles that impact precision application of Global Navigation Satellite System data require the ability to represent subgrid-scale gravity waves in whole atmosphere models. This information on MSTIDs could be input into existing tools for estimating Global Navigation Satellite System positioning error from TIDs (e.g., Lejeune et al., 2012). Gravity waves also play an important role in the transport of chemical constituents, which is discussed in more detail later.

Liu et al. (2014) ran a fine-resolution (0.25° × 0.25° horizontal, 0.1 scale height vertical) version of WACCM to demonstrate the simulation and impact of gravity waves up to around 100 km. However, it is not clear whether such resolutions are needed at higher levels in the thermosphere. Miyoshi et al. (2018) showed that a GAIA simulation with a resolution of 1° × 1° produces fluctuations in electron density with length scales less than around 1,000 km and periods of less than around 2 hr, which are in good agreement with observations and which are not seen in a coarser resolution (2.5° × 2.5°) simulation. The fluctuations reported by Miyoshi et al. are attributed to TIDs that are excited by secondary gravity waves. These waves typically have horizontal wavelengths of around 100 km to several 1,000s of kilometers (Vadas & Crowley, 2010). This also appears consistent with Gardner and Schunk (2011), who indicated observed gravity waves in the thermosphere typically have horizontal scales of around 100–500 km. Furthermore, at altitudes above around 110-km molecular viscosity and thermal conduction strongly influence gravity wave filtering and dissipation, as opposed to winds and wave breaking lower in the atmosphere (see, e.g., Vadas & Fritts, 2005). Accordingly, lower atmosphere gravity wave parametrization schemes may not be appropriate in the thermosphere. Schemes that specifically focus on parameterizing gravity waves in the thermosphere (e.g., Yiğit et al., 2008) could be adopted for coarse horizontal resolution whole atmosphere model simulations.

Presently, WAM, WACCM-X, and GAIA use hydrostatic dynamical cores. The dynamical core solves the governing fluid and thermodynamic equations in the model on resolved scales, while parametrizations represent subgrid-scale processes and other processes not included in the dynamical core such as radiative transfer (Thuburn, 2008). Certainly for some applications, such as satellite drag, the hydrostatic approximation appears adequate (see, e.g., Bruinsma et al., 2018), but there is still a need to identify the impact on model results that may arise from nonhydrostatic processes. For some applications that require accurate representation of the wave fluctuations (such as radio wave propagation in the bottomside *F* region for HF applications), the hydrostatic approximation may be inappropriate in the thermosphere, and adoption of nonhydrostatic (non-H) dynamical cores appears to be a logical next step. The hydrostatic approximation breaks in the presence of large vertical accelerations (e.g., Curry & Webster, 1998), and using a non-H dynamical core may affect the modeled gravity wave spectrum, particularly when applied at fine horizontal resolution. High-frequency waves with horizontal wavelength less than $4\pi H$ (where H is scale height) should be treated nonhydrostatically (Akmaev, 2011). For example, Eckermann et al. (2016) showed observations of gravity waves that had propagated from the surface to the lower thermosphere with vertical velocities of several tens of meters per second. They concluded that these waves must be nonhydrostatic, since if they were hydrostatic, they would have broken in the troposphere or lower stratosphere rather than propagating higher. Therefore, selection of a non-H dynamical core can affect the modeled gravity wave spectrum in the MLT, and thus the simulation of MSTIDs. A fine horizontal resolution is required to represent such

waves in the first place, and, given that whole atmosphere models currently have resolutions of ~100 to 200 km, the case for using non-H cores at such resolutions is not yet well made. Three new whole atmosphere models are being developed, which use non-H cores: the Navy Global Environmental Model (NAVGEM; e.g., McCormack et al., 2017), the Met Office Extended Unified Model (UM) and WAM, where the current dynamical core is being replaced with the Geophysics Fluid Dynamics Laboratory Finite-Volume on a Cubed-Sphere (FV3) non-H core (Ullrich et al., 2017). In addition, Borchert et al. (2018) report on work to extend the ICOsahedral Non-hydrostatic general circulation model up to 150-km altitude. NAVGEM and the UM have the option to switch between hydrostatic and non-H formulations, and both these models could play key roles in evaluating the importance of non-H cores in whole atmospheric models.

There can also be issues with the robustness of non-H dynamical cores in the thermosphere. Griffin and Thuburn (2018) showed that the UM required the addition of molecular viscosity and diffusion in order to realistically stabilize artificial wave growth, as this viscosity has a significant damping effect in the thermosphere. Another challenge arises above the turbopause (around 105 km) where diffusive separation means that air parcels are no longer turbulently mixed and the molecular weight of a species determines its dynamical evolution. Therefore, ideally, each species should have its own set of dynamical equations that need to be solved. The molecular diffusion is also affected by variable gravity, which in turn modifies atmospheric scale heights. Thus, there is a need to reformulate the dynamical core to properly model the individual species, as well as a need to add a correction to the thermal equation.

3.2. Radiation and Chemistry

Accurate radiation and chemistry schemes are needed throughout the whole atmosphere model domain, most obviously in the MLT where the radiation scheme calculates the absorption of solar radiation that drive the large rise in temperature with height there. This means that radiation schemes need to include the far ultraviolet, extreme ultraviolet, and soft X-ray spectral ranges that are usually ignored in lower atmosphere models. In the MLT, heating from exothermic reactions becomes important (especially during polar night) and must be accounted for to correctly simulate the thermal structure. Quenching of $O(^1D)$ is a large source of heating throughout the MLT, above 100-km ion reactions, and reactions involving atomic nitrogen are significant sources of heat, and below 100 km O_x and HO_x reactions are the dominant producers of chemical heating (Marsh et al., 2007). In addition, above the midmesosphere, local thermodynamic equilibrium (LTE) schemes need to be replaced by non-LTE formulations, since both near infrared heating and infrared cooling are overestimated by the LTE schemes. The Fomichev non-LTE parametrization (Fomichev & Blanchet, 1995; Fomichev et al., 1998; Ogibalov & Fomichev, 2003) is the only scheme currently available for Earth GCMs. Its formulation is based on recent atmospheric conditions, and it lacks the adaptability to be used for climate change experiments. The UM's radiation scheme is being extended to include far ultraviolet and extreme ultraviolet wavelengths. The scheme is highly flexible, with the option of being run using different spectral resolutions. In future it could be further modified to include a more comprehensive representation of non-LTE heating, possibly based on a scheme developed for Mars (López-Valverde & López-Puertas, 1994), which potentially represents a considerable improvement on the Fomichev scheme. Since the scheme is also publically available, it could be a highly important community resource for future collaborative whole atmosphere model development.

While only relatively few major chemical reactions are sufficient to adequately represent the large rise in temperature in the MLT (Marsh et al., 2007), other challenges remain. Below 85 km the atmospheric chemistry is dominated by compounds, and above 100 km by ion chemistry. Particularly interesting chemistry exists in between, where atoms including highly reactive hydrogen and oxygen atoms are in abundance, with maximum mixing ratios observed at around 85 and 90–95 km, respectively (Plane et al., 2015). WACCM simulations of metal layers originating from the ablation of meteoroids in the MLT give good model agreement with data at midlatitudes but show worse agreement at high latitudes. For example, for Fe chemistry Feng et al. (2013) show that the model significantly overestimates winter Fe and underestimates summer Fe compared to observations from three Antarctic ground-based lidars. This implies that the model vertical transport of chemical species may be significantly underestimated. A possible issue is that global models cannot capture transport associated with small-scale gravity waves, and adding diffusion terms to account for this does help with reducing the large bias. Observations of MLT chemistry are sparse, and thus, there is great scope for new observations to significantly improve our knowledge of the interaction

between chemistry and transport. For example, recent observations made by the Atmospheric Chemistry Experiment indicate nitrous oxide (N_2O) is being produced in the MLT (Sheese et al., 2016). N_2O is a precursor of odd nitrogen (NO_x), which destroys stratospheric ozone. A new chemical source of N_2O has been successfully added to WACCM by Kelly et al. (2018). Model simulations were able to capture the observed N_2O layer and well replicate seasonal variations near the poles. Recent studies have also highlighted the importance of radiation and chemistry schemes working together to produce the strong NO cooling, which is observed in the immediate aftermath of geomagnetic storm time thermospheric heating (e.g. Knipp et al., 2017) .

3.3. Ionosphere and Electrodynamics

The coupling between the thermosphere and ionosphere is important, as mentioned above, in ensuring a more accurate evolution of the ionospheric state. Fang et al. (2013) performed an intercomparison of a range of ionospheric models. It is clear that the thermosphere/ionosphere coupling was modeled better when the models employed a fully consistent representation of the electrodynamics. This led to the development of the Ionosphere Plasmasphere Electrodynamics model, which includes the following requirements: It represents the ionosphere globally with similar resolution to the neutral atmospheric model (WAM) it is coupled to; it uses self-consistent electrodynamics for quiet and storm time dynamo processes; it uses a coupling infrastructure.

Also important is an accurate representation of the electric field and its variation. There are limitations with current empirical electric field models, such as those developed by Heelis et al. (1982) and Weimer (2005). These are climatological in nature, but more observations are required to capture the electric field variability. The introduction of Super Dual Auroral Radar Network (SuperDARN) data crucially adds extra observations poleward of 40^o geomagnetic latitude (as well as providing observations at lower latitudes), and the deviation of SuperDARN high-latitude electric fields from the average ionospheric state shows the importance of accounting for the prior evolution of the ionospheric state. M.-T. Walach (presentation available at http://www.research.lancs.ac.uk/portal/en/activities/characterising-and-understanding-temporal-variability-in-ionospheric-flows-using-superdarn-data(21f8f287-e085-4418-8a1c-387d597ef2f0).html) used SuperDARN data to show that greater solar wind corresponds to greater variability in convection and is currently investigating the drivers of this variability in more detail. Use of SuperDARN observations in the Canadian Ionosphere and Atmosphere Model (Martynenko et al., 2014) allows detailed features in the plasma density distribution to be reproduced, especially in the topside ionosphere at high latitudes. Data from the Assimilative Mapping of Ionospheric Electrodynamics can be used to assimilate multiple data sources (SuperDARN) for testing in whole atmosphere models. The electric field model chosen also influences modeled Joule heating, and it is important to continue to confront empirical model-based estimates with observations (e.g., Billett et al., 2018).

3.4. Observations for DA and Model Verification

DA is important in attempting to ensure the model state is constrained to be close to the true atmospheric state and has been applied extensively in WACCM-X, WAM, and NAVGEM. DA in WACCM-X is done using an ensemble Kalman filter while the NAVGEM DA system is a hybrid of 4D-Var and an ensemble Kalman Filter. The ensemble Kalman Filter (Evensen, 1994) is a combination of a Kalman Filter (which evolves the state and estimate covariance as new observations arrive) and Monte Carlo estimation methods (the full estimate covariance matrix is explicitly evolved using an ensemble—sample of evolved states). The NAVGEM system has been shown to add a lot of value in the thermosphere. As an example, in Figure 1 the observed Wave Number 4 structure in TEC is best reproduced when the NAVGEM model thermosphere is forced by 3-hourly analyses; forcing by 6-hourly analyses is less accurate. A major challenge is that the models cover a large altitude range, so waves can grow exponentially, and to maintain model stability with DA, more damping is often added to deal with spurious small-scale waves. A consequence of this approach is that while model dynamics and chemical transport are improved, it is at the cost of the tidal amplitudes being too weak. To add to the challenge in the upper atmosphere, data are sparse, and processes act on shorter time scales than in the lower atmosphere. Provision of considerably more near real-time observations of the upper atmosphere, particularly of the thermosphere, is vital if we are to exploit DA in order to produce improved model forecasts.

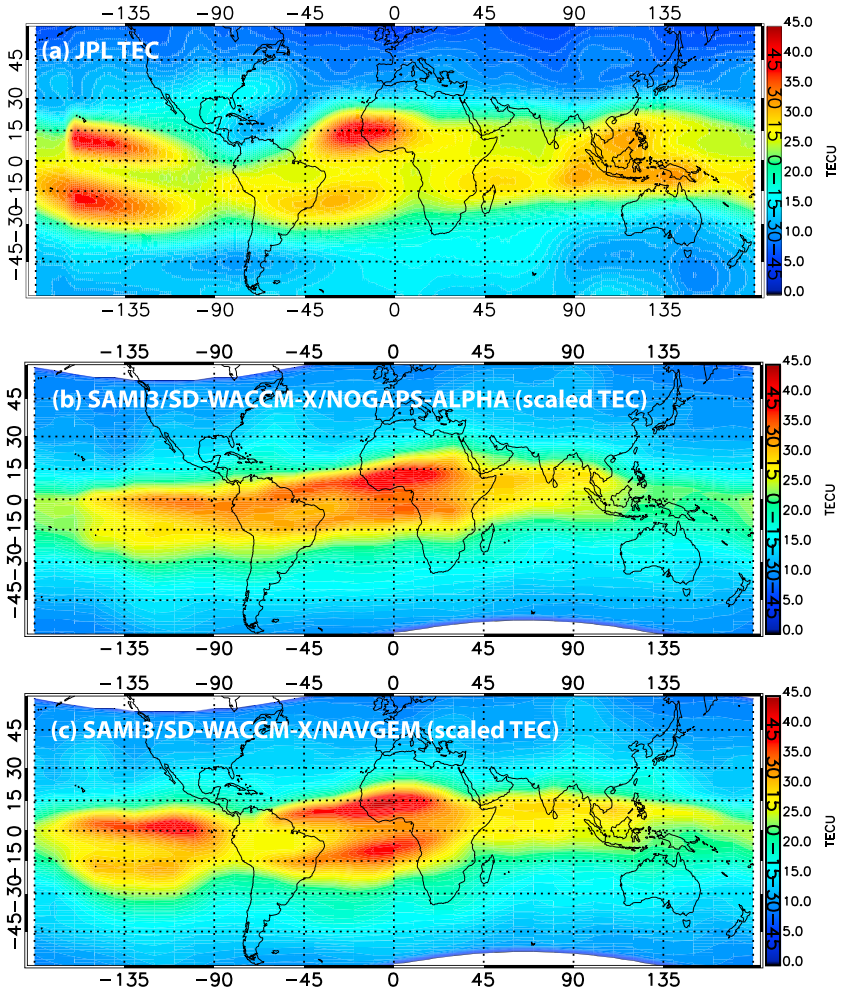

Figure 1. (a) Jet Propulsion Laboratory (JPL) global ionospheric map of total electron content (TEC) on 12 January 2010 shown at constant local time of 13:00 LT. (b) /NOGAPS-ALPHA simulation of TEC. (c) Navy Global Environmental Model (NAVGEM) simulation of TEC. The simulated TEC is scaled by a factor of 0.7 (from McDonald et al., 2018). WACCM = Whole Atmosphere Community Climate Model.

To compound the lack of observations, the instruments that produce many of the upper atmosphere observations used in the DA schemes (e.g., Sounding of the Atmosphere using Broadband Emission, and MLS, the Microwave Limb Sounder) are well past their nominal mission lifetimes, and no follow-on programs are planned. Furthermore, these instruments only observe up to the lower thermosphere and observations higher in the thermosphere are extremely sparse. The QB50 Cubesat project (e.g., Gill et al., 2013) focused on the building and launching of instruments to measure thermospheric neutral density, but with little or no attention given to coordination and reception of data. However, the constellation of Cubesats used could be a pathfinder for a future operational observations system, with the critical proviso that this constellation would need to be underpinned by associated systems for near real time data reception and cross-calibration of data. In addition, new data from the Global-scale Observations of the Limb and Disk mission will help address the paucity of thermospheric data. The planned assimilation of Global-scale Observations of the Limb and Disk O/N2 observations into WAM could test the assumption that temperature is a key variable for the initialization of upper atmosphere models. Since O/N2 plays a key role as a diagnostic of thermospheric transport, it is possible that future DA schemes could instead use O/N2 as a primary control variable.

Model verification using existing data has proved invaluable. However, there is a need for a consistent model verification strategy, and in particular community-wide agreement on which metrics to compare—this could include basic seasonal variability, tide amplitudes and variability, TEC, and the magnitude of the solar

semidiurnal migrating tide. An important consideration is to understand which observations are trusted and therefore should be used to validate model output, and there are benefits in an Intergovernmental Panel on Climate Change style model intercomparison, and a cooperative approach. An example is Coupled Model Intercomparison Project 5 (Taylor et al., 2012), in which an agreed set of experiments addressing major gaps in understanding was run using multiple models, and output data were formatted in a common way and made freely available via data portals. Empirical models may not be ideal for use as a level of comparison, and we suggest the employment of a more general model comparison system, for example, as implemented in the International Land Model Benchmarking Project (Collier et al., 2018).

4. Future Research Directions and Activities

Based on the discussions throughout the workshop, the following road map for future collaboration was agreed:

1. Compare existing hydrostatic models to understand impacts of dynamical formulation (also interactions with chemistry, the ionosphere, and radiation)
2. Comparison of non-H and hydrostatic dynamical cores to assess impact of non-H cores (and whether non-H is even needed at coarser resolution)
3. Assess numerical cost/benefit of comprehensive chemistry schemes designed for climate applications (e.g., WACCM) against simpler schemes designed for near-real time operational use (e.g., as used in WAM)
4. Development of a verification strategy and methodology, which is required to underpin the above three actions. Clearly, it makes sense to make links with other activities to guide our future actions. These include the Committee on Space Research International Space Weather Action Team and the Community Coordinated Modeling Center Space Weather Modeling Capabilities Assessment (Scherliess et al., 2019).

Of course, other issues that were discussed at the workshop (such as near real time availability of observations and DA) are very important, but the first focus here is on assessment and developing the whole atmosphere models themselves.

There was a further suggestion that the joint development of parametrizations would be

incredibly useful in unifying parametrization strategy across multiple models. The International Space Science Institute has a good setup for accomplishing verification with data, and this setting would be helpful for deciding a verification strategy. To monitor progress, it was also agreed to organize a follow up workshop in mid-2020.

Acknowledgments
AcknowledgementsWe thank Fabrizio Sassi (Naval Research Laboratory) for supplying Figure 1. No data were generated for use in this manuscript.

References

Akmaev, R. A. (2011). Whole atmosphere modeling: Connecting terrestrial and space weather. *Reviews of Geophysics*, *49*, RG4004. https://doi.org/10.1029/2011RG000364

Akmaev, R. A., Fuller-Rowell, T. J., Wu, F., Forbes, J. M., Zhang, X., Anghel, A. F., et al. (2008). Tidal variability in the lower thermosphere: Comparison of Whole Atmosphere Model (WAM) simulations with observations from TIMED. *Geophysical Research Letters*, *35*, L03810. https://doi.org/10.1029/2007GL032584

Billett, D. D., Grocott, A., Wild, J. A., Walach, M.-T., & Kosch, M. J. (2018). Diurnal variations in global Joule heating morphology and magnitude due to neutral winds. *Journal of Geophysical Research: Space Physics*, *123*, 2398–2411. https://doi.org/10.1002/2017JA025141

Borchert, S., Zhou, G., Baldauf, M., Schmidt, H., Zängl, G., & Reinert, D. (2018). The upper-atmosphere extension of the ICON general circulation model. *Geoscientific Model Development Discussion*, 1–50. https://doi.org/10.5194/gmd-2018-289

Bruinsma, S., Sutton, E., Solomon, S. C., Fuller-Rowell, T., & Fedrizzi, M. (2018). Space weather modeling capabilities assessment: Neutral density for orbit determination at low Earth orbit. *Space Weather*, *16*, 1806–1816. https://doi.org/10.1029/2018SW002027

Chartier, A. T., Jackson, D. R., & Mitchell, C. N. (2013). A comparison of the effects of initializing different thermosphere-ionosphere model fields on storm time plasma density forecasts. *Journal of Geophysical Research: Space Physics*, *118*, 7329–7337. https://doi.org/10.1002/2013JA019034

Chartier, A. T., Matsuo, T., Anderson, J. L., Collins, N., Hoar, T. J., Lu, G., et al. (2016). Ionospheric data assimilation and forecasting during storms. *Journal of Geophysical Research: Space Physics*, *121*, 764–778. https://doi.org/10.1002/2014JA020799

Collier, N., Hoffman, F. M., Lawrence, D. M., Keppel-Aleks, G., Koven, C. D., Riley, W. J., et al. (2018). The International Land Model Benchmarking (ILAMB) system: Design, theory, and implementation. *Journal of Advances in Modeling Earth Systems*, *10*, 2731–2754. https://doi.org/10.1029/2018MS001354

Curry, J. A., & Webster, P. J. (1998). *Thermodynamics of atmospheres & oceans*, *International Geophysics Series* (Vol. 65). London: Academic Press.

Eckermann, S. D., Broutman, D., Ma, J., Doyle, J. D., Pautet, P., Taylor, M. J., et al. (2016). Dynamics of orographic gravity waves observed in the mesosphere over the Auckland Islands during the Deep Propagating Gravity Wave Experiment (DEEPWAVE). *Journal of the Atmospheric Sciences*, *73*(10), 3855–3876. https://doi.org/10.1175/JAS-D-16-0059.1

Evensen, G. (1994). Sequential data assimilation with a nonlinear quasi-geostrophic model using Monte Carlo methods to forecast error statistics. *Journal of Geophysical Research*, *99*, 10,143–10,162. https://doi.org/10.1029/94JC00572

Eyring, V., Arblaster, J. M., Cionni, I., Sedláček, J., Perlwitz, J., Young, P. J., et al. (2013). Long-term ozone changes and associated climate impacts in CMIP5 simulations. *Journal of Geophysical Research: Atmospheres*, *118*, 5029–5060. https://doi.org/10.1002/jgrd.50316

Fang, T.-W., Anderson, D., Fuller-Rowell, T. J., Akmaev, R., Codrescu, M., Millward, G., et al. (2013). Comparative studies of theoretical models in the equatorial ionosphere. In J. D. Huba (Ed.), *Modeling the Ionosphere-Thermosphere*, Geophys. Monogr. Ser. (Vol. 201, pp. 133–144). Washington, DC: American Geophysical Union.

Feng, W., Marsh, D. R., Chipperfield, M. P., Janches, D., Höffner, J., Yi, F., & Plane, J. M. C. (2013). A global atmospheric model of meteoric iron. *Journal of Geophysical Research: Atmospheres*, *118*, 9456–9474. https://doi.org/10.1002/jgrd.50708

Fomichev, V. I., & Blanchet, J.-P. (1995). Development of the new CCC/GCM radiation model for extension into the Middle Atmosphere. *Atmosphere-Ocean*, *33*(3), 513–529. https://doi.org/10.1080/07055900.1995.9649543

Fomichev, V. I., Blanchet, J.-P., & Turner, D. S. (1998). Matrix parameterization of the 15 μm CO 2 band cooling in the middle and upper atmosphere for variable CO 2 concentration. *Journal of Geophysical Research*, *103*(D10), 11,505–11,528. https://doi.org/10.1029/98JD00799

Fujiwara, H., & Miyoshi, Y. (2010). Morphological features and variations of temperature in the upper thermosphere simulated by a whole atmosphere GCM. *Annales de Geophysique*, *28*(2), 427–437. https://doi.org/10.5194/angeo-28-427-2010

Fuller-Rowell, T. J., Akmaev, R. A., Wu, F., Anghel, A. F., Maruyama, N., Anderson, D. N., et al. (2008). Impact of terrestrial weather on the upper atmosphere. *Geophysical Research Letters*, *35*, L09808. https://doi.org/10.1029/2007GL032911

Gardner, L. C., & Schunk, R. W. (2011). Large-scale gravity wave characteristics simulated with a high-resolution global thermosphere-ionosphere model. *Journal of Geophysical Research*, *116*, A06303. https://doi.org/10.1029/2010JA015629

Gill, E., Sundaramoorthy, P., Bouwmeester, J., Zandbergen, B., & Reinhard, R. (2013). Formation flying within a constellation of nano-satellites: The QB50 mission. *Acta Astronautica*, *82*(1), 110–117. https://doi.org/10.1016/j.actaastro.2012.04.029

Goncharenko, L., Chau, J., Liu, H.-L., & Coster, A. J. (2010). Unexpected connections between the stratosphere and ionosphere. *Geophysical Research Letters*, *37*, L10101. https://doi.org/10.1029/2010GL043125

Goncharenko, L., Coster, A. J., Chau, J., & Valladares, C. (2010). Impact of sudden stratospheric warmings on equatorial ionization anomaly. *Journal of Geophysical Research*, *115*, A00G07. https://doi.org/10.1029/2010JA015400

Griffin, D. J., & Thuburn, J. (2018). Numerical effects on vertical wave propagation in deep-atmosphere models. *Quarterly Journal of The Royal Meteorological Society*, *144*(711), 567–580.

Heelis, R. A., Lowell, J. K., & Spiro, R. W. (1982). A model of the high-latitude ionospheric convection pattern. *Journal of Geophysical Research*, *87*(A8), 6339–6345. https://doi.org/10.1029/JA087iA08p06339

Hsu, C. T., Matsuo, T., Wang, W., & Liu, J. Y. (2014). Effects of inferring unobserved thermospheric and ionospheric state variables by using an Ensemble Kalman Filter on global ionospheric specification and forecasting. *Journal of Geophysical Research: Space Physics*, *119*, 9256–9267. https://doi.org/10.1002/2014JA020390

Immel, T. J., Sagawa, E., England, S. L., Henderson, S. B., Hagan, M. E., Mende, S. B., et al. (2006). The control of equatorial ionospheric morphology by atmospheric tides. *Geophysical Research Letters*, *33*, L15108. https://doi.org/10.1029/2006GL026161

Jin, H., Miyoshi, Y., Pancheva, D., Mukhtarov, P., Fujiwara, H., & Shinagawa, H. (2012). Response of migrating tides to the stratospheric sudden warming in 2009 and their effects on the ionosphere studied by a whole atmosphere-ionosphere model GAIA with COSMIC and TIMED/SABER observations. *Journal of Geophysical Research*, *117*, A10323. https://doi.org/10.1029/2012JA017650

Kelly, C. W., Chipperfield, M. P., Plane, J. M. C., Feng, W., Sheese, P. E., Walker, K. A., & Boone, C. D. (2018). An explanation for the nitrous oxide layer observed in the mesopause region. *Geophysical Research Letters*, *45*, 7818–7827. https://doi.org/10.1029/2018GL078895

Knipp, D. J., Pette, D. V., Kilcommons, L. M., Isaacs, T. L., Cruz, A. A., Mlynczak, M. G., et al. (2017). Thermospheric nitric oxide response to shock-led storms. *Space Weather*, *15*, 325–342. https://doi.org/10.1002/2016SW001567

Lang, M., & Owens, M. J. (2019). A variational approach to data assimilation in the solar wind. *Space Weather*, *17*, 59–83. https://doi.org/10.1029/2018SW0018

Lejeune, S., Wautelet, G., & Warnant, R. (2012). Ionospheric effects on relative positioning within a dense GPS network. *GPS Solutions*, *16*(1), 105–116. https://doi.org/10.1007/s10291-011-0212-1

Lieberman, R. S., Akmaev, R. A., Fuller-Rowell, T. J., & Doornbos, E. (2013). Thermospheric zonal mean winds and tides revealed by CHAMP. *Geophysical Research Letters*, *40*, 2439–2443. https://doi.org/10.1002/grl.50481

Liemohn, M., Ganushkina, N. Y., De Zeeuw, D. L., Rastaetter, L., Kuznetsova, M., Welling, D. T., et al. (2018). Real-time SWMF at CCMC: Assessing the Dst output from continuous operational simulations. *Space Weather*, *16*, 1583–1603. https://doi.org/10.1029/2018SW001953

Liu, H.-L., Bardeen, C. G., Foster, B. T., Lauritzen, P., Liu, J., Lu, G., et al. (2018). Development and validation of the Whole Atmosphere Community Climate Model with thermosphere and ionosphere extension (WACCM-X 2.0). *Journal of Advances in Modeling Earth Systems*, *10*, 381–402. https://doi.org/10.1002/2017MS001232

Liu, H.-L., Foster, B. T., Hagan, M. E., McInerney, J. M., Maute, A., Qian, L., et al. (2010). Thermosphere extension of the Whole Atmosphere Community Climate Model. *Journal of Geophysical Research*, *115*, A12302. https://doi.org/10.1029/2010JA015586

Liu, H.-L., McInerney, J. M., Santos, S., Lauritzen, P. H., Taylor, M. A., & Pedatella, N. M. (2014). Gravity waves simulated by high-resolution Whole Atmosphere Community Climate Model. *Geophysical Research Letters*, *41*, 9106–9112. https://doi.org/10.1002/2014GL062468

Liu, H.-L., & Roble, R. G. (2002). A study of a self-generated stratospheric sudden warming and its mesospheric–lower thermospheric impacts using the coupled TIME-GCM/CCM3. *Journal of Geophysical Research*, *107*(D23), 4695. https://doi.org/10.1029/2001JD001533

López-Valverde, M. A., & López-Puertas, M. (1994). A non-local thermodynamic equilibrium radiative transfer model for infrared emissions in the atmosphere of Mars. 1: Theoretical basis and nighttime populations of vibrational levels. *Journal of Geophysical Research*, *99*(E6), 13,093–13,115. https://doi.org/10.1029/94JE00635

Marsh, D. R., Garcia, R. R., Kinnison, D. E., Boville, B. A., Sassi, F., Solomon, S. C., & Matthes, K. (2007). Modeling the whole atmosphere response to solar cycle changes in radiative and geomagnetic forcing. *Journal of Geophysical Research*, *112*, D23306. https://doi.org/10.1029/2006JD008306

Marsh, D. R., Mills, M. J., Kinnison, D. E., & Lamarque, J.-F. (2013). Climate Change from 1850 to 2005 Simulated in CESM1(WACCM). *Journal of Climate*, *26*(19), 7372–7391. https://doi.org/10.1175/JCLI-D-12-00558.1

Martynenko, O. V., Fomichev, V. I., Semeniuk, K., Beagley, S. R., Ward, W. E., McConnell, J. C., & Namgaladze, A. A. (2014). Physical mechanisms responsible for forming the 4-peak longitudinal structure of the 135.6 nm ionospheric emission: First results from the Canadian IAM. *Journal of Atmospheric and Solar - Terrestrial Physics*, *120*, 51–61. https://doi.org/10.1016/j.jastp.2014.08.014

Maruyama, N., Sun, Y.-Y., Richards, P. G., Middlecoff, J., Fang, T.-W., Fuller-Rowell, T. J., et al. (2016). A new source of the midlatitude ionospheric peak density structure revealed by a new Ionosphere-Plasmasphere model. *Geophysical Research Letters*, *43*, 2429–2435. https://doi.org/10.1002/2015GL067312

McCormack, J. P., Hoppel, K., Kuhl, D., de Wit, R., Stober, G., Espy, P., et al. (2017). Comparison of mesospheric winds from a high-altitude meteorological analysis system and meteor radar observations during the boreal winters of 2009–2010 and 2012–2013. *Journal of Atmospheric and Solar - Terrestrial Physics*, *154*, 132–166. https://doi.org/10.1016/j.jastp.2016.12.007

McDonald, S. E., Sassi, F., Tate, J., McCormack, J., Kuhl, D. D., Drob, D. P., et al. (2018). Impact of non-migrating tides on the low latitude ionosphere during a sudden stratospheric warming event in January 2010. *Journal of Atmospheric and Solar-Terrestrial Physics*, *171*, 188–200. https://doi.org/10.1016/j.jastp.2017.09.012

Merkin, V. G., Kondrashov, D., Ghil, M., & Anderson, B. J. (2016). Data assimilation of low-altitude magnetic perturbations into a global magnetosphere model. *Space Weather*, *14*, 165–184. https://doi.org/10.1002/2015SW001330

Miyoshi, Y., Jin, H., Fujiwara, H., & Shinagawa, H. (2018). Numerical study of traveling ionospheric disturbances generated by an upward propagating gravity wave. *Journal of Geophysical Research: Space Physics*, *123*, 2141–2155. https://doi.org/10.1002/2017JA025110

Murray, S. A., Henley, E. M., Jackson, D. R., & Bruinsma, S. L. (2015). Assessing the performance of thermospheric modeling with data assimilation throughout solar cycles 23 and 24. *Space Weather*, *13*, 220–232. https://doi.org/10.1002/2015SW001163

Ogibalov, V. P., & Fomichev, V. I. (2003). Parameterization of solar heating by the near IR CO2 bands in the mesosphere. *Advances in Space Research*, *32*(5), 759–764. https://doi.org/10.1016/S0273-1177(03)80069-8

Pedatella, N. M., Fang, T.-W., Jin, H., Sassi, F., Schmidt, H., Chau, J. L., et al. (2016). Multimodel comparison of the ionosphere variability during the 2009 sudden stratosphere warming. *Journal of Geophysical Research: Space Physics*, *121*, 7204–7225. https://doi.org/10.1002/2016JA022859

Pedatella, N. M., Liu, H.-L., Richmond, A. D., Maute, A., & Fang, T.-W. (2012). Simulations of solar and lunar tidal variability in the mesosphere and lower thermosphere during sudden stratosphere warmings and their influence on the low-latitude ionosphere. *Journal of Geophysical Research*, *117*, A08326. https://doi.org/10.1029/2012JA017858

Plane, J. M. C., Feng, W., & Dawkins, E. C. M. (2015). The mesosphere and metals: Chemistry and changes. *Chemical Reviews*, *115*(10), 4497–4541. https://doi.org/10.1021/cr500501m

Scherliess, L., Tsagouri, I., Yizengaw, E., Bruinsma, S., Shim, J. S., Coster, A., & Retterer, J. M. (2019). The International Community Coordinated Modeling Center space weather modeling capabilities assessment: Overview of ionosphere/thermosphere activities. *Space Weather*, *17*, 527–538. https://doi.org/10.1029/2018SW002036

Schunk, R. W., Scherliess, L., Eccles, V., Gardner, L. C., Sojka, J. J., Zhu, L., et al. (2016). Space weather forecasting with a Multimodel Ensemble Prediction System (MEPS). *Radio Science*, *51*, 1157–1165. https://doi.org/10.1002/2015RS005888

Sheese, P. E., Walker, K. A., Boone, C. D., Bernath, P. F., & Funke, B. (2016). Nitrous oxide in the atmosphere: First measurements of a lower thermospheric source. *Geophysical Research Letters*, *43*, 2866–2872. https://doi.org/10.1002/2015GL067353

Taylor, K. E., Stouffer, R. J., & Meehl, G. A. (2012). An overview of CMIP5 and the experiment design. *Bulletin of the American Meteorological Society*, *93*(4), 485–498. https://doi.org/10.1175/BAMS-D-11-00094.1

Thuburn, J. (2008). Some conservation issues for the dynamical cores of NWP and climate models. *Journal of Computational Physics*, *227*(7), 3715–3730. https://doi.org/10.1016/j.jcp.2006.08.016

Ullrich, P. A., Jablonowski, C., Kent, J., Lauritzen, P. H., Nair, R., Reed, K. A., et al. (2017). DCMIP2016: a review of non-hydrostatic dynamical core design and intercomparison of participating models. *Geoscientific Model Development*, *10*(12), 4477–4509. https://doi.org/10.5194/gmd-10-4477-2017

Vadas, S. L., & Crowley, G. (2010). Sources of the traveling ionospheric disturbances observed by the ionospheric TIDDBIT sounder near Wallops Island on October 30, 2007. *Journal of Geophysical Research*, *115*, A07324. https://doi.org/10.1029/2009JA015053

Vadas, S. L., & Fritts, D. C. (2005). Thermospheric responses to gravity waves: Influences of increasing viscosity and thermal diffusivity. *Journal of Geophysical Research*, *110*, D15103. https://doi.org/10.1029/2004JD005574

Wang, H., Akmaev, R. A., Fang, T.-W., Fuller-Rowell, T. J., Wu, F., Maruyama, N., & Iredell, M. D. (2014). First forecast of a sudden stratospheric warming with a coupled whole-atmosphere/ionosphere model IDEA. *Journal of Geophysical Research: Space Physics*, *119*, 2079–2089. https://doi.org/10.1002/2013JA019481

Weimer, D. (2005). Improved ionospheric electrodynamic models and application to calculating Joule heating rates. *Journal of Geophysical Research*, *110*, A05306. https://doi.org/10.1029/2004JA010884

Yiğit, E., Aylward, A. D., & Medvedev, A. S. (2008). Parameterization of the effects of vertically propagating gravity waves for thermosphere general circulation models: Sensitivity study. *Journal of Geophysical Research*, *113*, D19106. https://doi.org/10.1029/2008JD010135

Yiğit, E., Koucká Knížová, P., Georgieva, K., & Ward, W. (2016). A review of vertical coupling in the Atmosphere–Ionosphere system: Effects of waves, sudden stratospheric warmings, space weather, and of solar activity. *Journal of Atmospheric and Solar-Terrestrial Physics*, *141*, 1–12. https://doi.org/10.1016/j.jastp.2016.02.011

4.2. Conclusions

We present the outcomes obtained from discussions and presentations at the Whole Atmosphere Modelling Workshop in Madrid in 2018, hosted by Deimos.

Current whole atmosphere models are summarised, aiding discussion on the key building blocks for whole atmosphere models.

The commentary concludes that we have reached a paradigm shift, with it now being crucial to include modelling of the lower atmosphere when attempting to represent upper atmospheric motion.

It was noted that the adoption of non-hydrostatic dynamical cores for use in whole atmosphere models is a logical next step, due to the fact that the hydrostatic approximation breaks in the presence of large vertical accelerations. However, it is likely that these dynamical cores will need to be reformulated to properly model individual species in the thermosphere.

Furthermore, it is clear that model developments are required in several areas to appropriately model the upper atmosphere, such as radiation and chemistry schemes, the representation of gravity waves as well as the representation of the ionosphere and electrodynamics.

Finally, the importance of model verification was also indicated. There is a recognised need for a consistent model verification strategy with community-wide agreement on which metrics to compare. This also feeds in to unifying the development of parameterisation schemes across multiple models for better comparison, highlighting the importance of collaboration between model developers to strengthen all whole atmosphere models.

Chapter 5

Stable Extension of the Unified Model into the Mesosphere and Lower Thermosphere

This chapter is devoted to identifying and rectifying the instability on raising the upper boundary of the Met Office's Unified Model and testing subsequent increased extensions. This is motivated by the goal of inspecting the model fields produced by the Extended Unified Model in the MLT which we perform in Chapters 6 and 7. This joint work was produced with David R. Jackson, Daniel J. Griffin and Christopher J. Budd and was published in the *Journal of Space Weather and Space Climate* as an open access publication (Griffith et al., 2020).

5.1. Outline of the Article

This article presents the first stable extension of the UM into the MLT.

We first introduce whole atmosphere models, the UM, and the issues faced on extending the Met Office's model into the MLT.

In Section 2, the Unified Model is described in more detail. The radiation scheme is described, highlighting the assumption of Local Thermodynamic Equilibrium (LTE) which is made, and which breaks down above around 65 km. The chemistry scheme is also described, and it is noted that at the time of performing this research, it did not include the relevant exothermic reactions important for the large increase in temperature seen in the lower thermosphere. Thus, it must be switched off and is replaced by monthly zonal mean profiles to represent important missing atmospheric constituents. Due to its importance as a significant heat source in the stratosphere, profiles for atmospheric ozone are provided to retain this effect in the model. Finally, relevant stability mechanisms are discussed which can be used to damp large velocities near the upper boundary. These include the model sponge layer, the model halos and numerical stabilisation, the latter of which is not used due to its detrimental effect on the accuracy of the model fields throughout the entire model domain.

In Section 3, the diagnosis of the instability is detailed. Firstly the model setup is described, which encompasses adding three more levels in the vertical to take the upper boundary from 85 to 100 km. Following this, the results from the extended model are analysed, and indicate large winds at the poles occurring in a seasonal manner. This points the investigation towards the radiation scheme, which is found to have erroneously large values at the summer pole. These values are found to be in line with those produced when the LTE assumption is used in the lower thermosphere, and so it is this erroneous assumption which is found to be causing the observed high wind speeds and consequent instability observed in the extended model.

In Section 4, the scheme used to resolve the instability is described. At the time of performing this research, a non-LTE radiation scheme for use in the model was under development. Thus, an interim solution of relaxation – or "nudging" – to an analytic temperature profile is added to the model to see if this resolves the instability – it was certainly not clear that the false assumption in the radiation scheme was the only cause of instability in the model. With the nudging scheme in place, and the erroneous values from the radiation scheme zeroed above around 70 km, a stable extension of the

UM was successfully produced, with the polar instability removed. A brief comparison to data was performed, with the observation made that further developments were necessary for realistic modelling in the MLT.

Finally, in Section 5, we build on the success of the stable extension of the model, and experiment with the vertical resolution and height of the model upper boundary. We trial both 3 km and 1.5 km vertical resolutions in the MLT – resolutions informed by a half and a quarter of the atmospheric scale height at around 100 km – and find that the 3 km resolution requires no change to the vertical damping coefficient, whereas the 1.5 km resolution requires an increase to the standard value. With the upper boundary height increased to both 120 km and 135 km, the 1.5 km resolution is too unstable and the nudged model could not be run with this vertical resolution, even for short periods of time. The 3 km resolution is successful in producing stable model runs using these raised upper boundaries with increases to the model halo and vertical damping coefficient.

Appendix 6B: Statement of Authorship

This declaration concerns the article entitled:			
Stable Extension of the Unified Model into the Mesosphere and Lower Thermosphere			
Publication status (tick one) **Draft manuscript** ☐ **Submitted** ☐ **In review** ☐ **Accepted** ☐ **Published** X			
Publication details (reference)	Journal: Space Weather and Space Climate Authors: Matthew J. Griffith, David R. Jackson, Daniel J. Griffin and Chris J. Budd		
Copyright status (tick the appropriate statement) I hold the copyright for this material X Copyright is retained by the publisher, but I have been given permission to replicate the material here ☐			
Candidate's contribution to the paper (provide details, and also indicate as a percentage)	The bulk of the work for this article was performed by the author of the thesis (80%). The formulation of ideas and design of methodology was performed equally by all authors (25%) The experimental work was entirely performed by the author of this thesis. The bulk of the presentation of the content was performed by the author of the thesis (80%) The author's contribution in particular was in performing the model runs to extract results from the unstable and stable model; produce the nudging scheme and vertical level sets used in the model; preparation of all figures; and leading the authoring of the manuscript with some contribution from all authors.		
Statement from Candidate	This paper reports on original research I conducted during the period of my Higher Degree by Research candidature.		
Signed	Matthew J. GRIFFITH	**Date**	06/08/2021

Last update: Feb 2019

J. Space Weather Space Clim. 2020, **10**, 19

https://doi.org/10.1051/swsc/2020018

JSWSC

Available online at:
www.swsc-journal.org

Topical Issue - Scientific Advances from the European Commission H2020 projects on Space Weather

RESEARCH ARTICLE OPEN ACCESS

Stable extension of the unified model into the mesosphere and lower thermosphere

Matthew J. Griffith[1,*], David R. Jackson[2], Daniel J. Griffin[2], and Chris J. Budd[1]

[1] University of Bath, Department of Mathematics, Bath BA2 7AY, United Kingdom
[2] Met Office, Fitzroy Rd, Exeter EX1 3PB, United Kingdom

Received 2 December 2019 / Accepted 10 April 2020

Abstract – A coupled Sun-to-Earth model is the goal for accurate forecasting of space weather. A key component of such a model is a whole atmosphere model – a general circulation model extending from the ground into the upper atmosphere – since it is now known that the lower atmosphere also drives variability and space weather in the upper atmosphere, in addition to solar variability. This objective motivates the stable extension of The Met Office's Unified Model (UM) into the Mesosphere and Lower Thermosphere (MLT), acting as a first step towards a whole atmosphere model.

At the time of performing this research, radiation and chemistry schemes that are appropriate for use in the MLT had not yet been implemented. Furthermore, attempts to run the model with existing parameterizations and a raised upper boundary led to an unstable model with inaccurate solutions. Here, this instability is examined and narrowed down to the model's radiation scheme – its assumption of Local Thermodynamic Equilibrium (LTE) is broken in the MLT. We subsequently address this issue by relaxation to a climatological temperature profile in this region. This provides a stable extended UM which can be used as a developmental tool for further examination of the model performance.

The standard vertical resolution used in the UM above 70 km is too coarse (approx. 5 km) to represent waves that are important for MLT circulation. We build on the success of the nudging implementation by testing the model at an improved vertical resolution. Initial attempts to address this problem with a 3 km vertical resolution and a 100 km lid were successful, but on increasing the resolution to 1.5 km the model becomes unstable due to large horizontal and vertical wind velocities. Increasing the vertical damping coefficient, which damps vertical velocities near the upper boundary, allows a successful year long climatology to be produced with these model settings. With the goal of a whole atmosphere model we also experiment with an increased upper boundary height. Increasing the upper model boundary to 120 and 135 km also leads to stable simulations. However, a 3 km resolution must be used and it is necessary to further increase the vertical damping coefficient.

This is highly promising initial work to raise the UM into the MLT, and paves the way for the development of a whole atmosphere model.

1 Introduction

An important focus of many weather forecasting organisations is the development of a complete Sun-to-Earth model in order to enhance forecasting of space weather, and ultimately develop a fully coupled system describing the Earth's atmosphere (e.g. Tóth et al., 2005). This is particularly since it is now known that the lower atmosphere is an important driving factor in variability and space weather in the upper atmosphere, in addition to solar variability (Akmaev, 2011). It is for this reason that the Met Office wishes to extend its weather and climate model, the Unified Model (UM), into the upper atmosphere (above 85 km).

One of the Met Office's long term aims to achieve this fully coupled system is the development of the UM into a whole atmosphere model (e.g. Akmaev, 2011; Jackson et al., 2019) – namely one that simulates the Earth's atmosphere from the surface up to the exobase (≈ 600 km). Such a model is crucial in obtaining accurate prediction of the upper atmosphere as the model resolution increases (e.g. Immel et al., 2006; Yue et al., 2016). This is due to the influence of vertically propagating atmospheric waves, in particular tides, that grow roughly exponentially with height because of the corresponding exponential decrease of the background density. Hence, these waves become particularly large in the Mesosphere and Lower

*Corresponding author: m.j.griffith@bath.ac.uk

Thermosphere (MLT), with associated influences on the ionosphere and thermosphere at higher altitudes.

Energetic particle precipitation (EPP) and changes in solar radiation associated with the solar cycle can also impact the troposphere. EPP events can lead to changes in MLT and stratospheric NOx and ozone concentrations which can modulate polar surface air temperatures by affecting the radiative budget with consequent effect on atmospheric circulation patterns (e.g. Seppälä et al., 2009; Päivärinta et al., 2013). Ineson et al. (2011) indicates the impact of solar minimum and solar maximum on Northern Hemisphere winter surface temperatures via changes to the North Atlantic Oscillation.

Thus, these waves are influential in atmospheric dynamics at all heights, and so their inclusion is important not only as drivers of upper atmosphere circulation, but also in terms of improving accuracy for current lower atmosphere models.

The forecasting of this region is important for real world applications such as radio communication, satellite drag calculation and Global Navigation Satellite System Positioning, Navigation and Timing (GNSS PNT). These can all be influenced by atmospheric waves in the MLT, and so modelling this region can help mitigate the potential disruption to these systems.

Initial runs of the UM with an increased model lid height performed by Harry (2015) became unstable and crashed unless considerable damping was used. These runs tested the UM with both 100 and 120 km model lids, with experiments focused on tuning parameters to obtain the longest run time possible. In particular, the cause and nature of the instability remained undiagnosed.

These initial results relied on changes in damping using an implicit weighting parameter α (described later) and changes to the time step Δt to produce model runs which were not reliably stable. Both of these modifications are undesirable for an accurate and efficient model. Increasing the implicit weighting parameter α damps out high frequency wave components globally and thus degrades the solution over the entire model domain, whilst decreasing the time step Δt leads to a more costly model which is impractical for real world application. The choices made in this research are made with these factors in mind, and are discussed further in Section 2.2.3.

Here, we advance the development of a whole atmosphere model by investigating the instability when the model lid is raised into the MLT, raising the roof of the current 85 km lid. This is achieved by first investigating the output produced using a raised upper boundary of 100 km and considering key prognostic variables such as winds and temperature, as well as diagnostic variables such as short wave radiative heating.

This series of diagnostic tests yielded the important result that the instability is not a result of numerical errors, but is the result of an incorrect application of the parameterization schemes in the MLT, where their physical approximation is no longer valid. By a careful inspection of the parameterization schemes, the cause of the instability was shown to lie in the use of the Local Thermodynamic Equilibrium (LTE) assumption used in the radiation scheme.

New UM chemistry and radiation schemes to supply appropriate radiative forcing in the MLT were not ready at the time of performing this research. Here, we wish to circumvent these delays and press ahead with our aim of producing a stable extended UM. We achieve this by switching off the UM chemistry and radiation schemes (the latter above 70 km in altitude only) and relaxing the model to a prescribed climatological temperature profile. This relaxation approximates the impact of the omitted radiation and chemistry and follows the approach used in other atmospheric models (e.g. Telford et al., 2008).

The non-orographic gravity wave forcing scheme was also suspected to be poorly optimised for the high atmosphere. This scheme is based on the Ultra Simple Spectral Parameterization (USSP) developed by Warner & McIntyre (2001). Several runs comparing the model with this scheme on and off were performed. In agreement with the results of Harry (2015), experimentation revealed that the scheme did not have a large impact on the stability of the UM. Thus, this scheme is left unchanged throughout. The scheme will undoubtedly need modifications to provide accurate non-orographic gravity wave forcing in the MLT, but we do not discuss this in this paper.

The layout of the remainder of this paper is as follows. Section 2 contains a description of the UM and a discussion of parts of the model particularly relevant when considering the instability in the extended model. The instability is diagnosed in Section 3 and is consequently resolved in Section 4 using relaxation to a climatological temperature profile. Further extensions to this stable "nudged" model are made in Section 5 and finally conclusions are drawn along with ideas for future work in Section 6.

2 Background

2.1 The Unified Model

As in any General Circulation Model (GCM), the UM is split into two core sections, one that describes atmospheric dynamics (the dynamical core) and one that describes atmospheric physics (parameterizations). The original UM is documented by Cullen (1993). A new dynamical core was introduced in the early 2000s (Davies et al., 2005) and the UM's current dynamical core, ENDGame, is described by Wood et al. (2014).

The ENDGame dynamical core solves the non-hydrostatic, fully compressible deep-atmosphere equations of motion on a rotating sphere using a semi-implicit semi-Lagrangian formulation. The primary prognostic variables of the three-dimensional wind components, virtual dry potential temperature, Exner pressure and dry density are used whilst moisture prognostics are advected as free tracers. Importantly this non-hydrostatic framework allows for vertical acceleration; an important consideration in the forcing of vertical winds, which are typically larger in the upper atmosphere than those seen in the lower atmosphere. The discretised equations are solved using an iterative implicit method – more details of which can also be found in Wood et al. (2014).

The model discretisation is split up into horizontal and vertical components. We fix the horizontal resolution at 1.25°N × 1.875°E, or the so called N96 resolution.[1] In the vertical, an 85-level set labelled L85 is used, which has 50 levels below 18 km, 35 levels above this and a model lid 85 km above sea

[1] The integer N represents the maximum number of zonal 2 grid-point waves that can be represented – so N96 can represent 96 such waves.

level. This level specification follows a roughly exponential distribution in that the level depth exponentially increases with increase in height. We will add more levels to raise the upper boundary and investigate whether this level specification is appropriate for accurate modelling of the MLT in Section 5.

There are many atmospheric processes which operate on smaller length scales than those used in the dynamical scheme, and therefore are not resolved on the numerical grid. Furthermore, some physical processes such as radiation are not represented in the equations of motion used in the UM. Such processes are therefore approximated within the atmospheric physics section of the model by parameterization. These parameterizations are key to obtaining realistic and useful forecasts for the operational model, and their addition to the dynamics provides a reasonably complete description of the atmosphere.

Amongst these parameterizations, it is the radiation and chemistry scheme which are most relevant for this paper, and thus we outline their parameterization here.

2.1.1 The radiation scheme

The purpose of the radiation scheme, which is based on the work of Edwards & Slingo (1996), is to simulate the effect of the Sun on the Earth's atmosphere. It parameterizes the effect of incoming short wavelength (0.2–0.5 μm) radiation and the subsequent emission of long wavelength radiation (>3 μm) into space, along with the redistribution of heat within the atmosphere.

In order to do this, radiative fluxes (i.e. the amount of energy transferred by incoming solar radiation per unit area per unit time) are calculated and are modelled as upward and downward fluxes of energy relative to a model grid point. From these fluxes, quantities such as atmospheric heating rates are derived, which can then be used to influence the model.

Also captured are the effects of various radiative processes, such as the absorption and emission of radiation by various airborne molecules. In particular, absorption of short wave (SW) and long wave (LW) radiation by various atmospheric constituents must be considered, as this is important in achieving the correct atmospheric temperature structure.

However, the current implementation of the radiation scheme makes the assumption of LTE – the condition under which matter emits radiation based on its intrinsic properties and its temperature, uninfluenced by the magnitude of any incident radiation. This assumption breaks down above ≈ 65 km (Fomichev et al., 2004). In addition, the radiation scheme does not consider wavelengths less than 0.2 μm, which are significant for radiative heating (see e.g. Chamberlain & Hunten, 1987) and to drive exothermic heating from chemical reactions in the MLT. Both of these factors make the current radiation scheme unsuited for use in the MLT. We diagnose this problem in Section 3 and address the consequent stability issues with the introduction of a relaxation scheme to a climatological temperature profile in Section 4.

2.1.2 The chemistry scheme

The UKCA (United Kingdom Chemistry and Aerosols; Morgenstern et al., 2009 and O'Connor et al., 2014) is a framework that encompasses several atmospheric chemistry and aerosol schemes, which is broadly referred to as the chemistry scheme. These schemes are responsible for modelling the effects of airborne molecules and aerosols, and their transport, interactively. They also account for the interaction of these particles with other parameterization schemes such as the radiation scheme described above.

However, the UKCA does not currently[2] include the relevant reactions above the 85 km model lid height. Chemical heating from exothermic reactions is key for the large increase in temperature with altitude seen in the lower thermosphere (see e.g. Marsh et al., 2007). However, these reactions are not currently represented in the UKCA, nor are their corresponding photolysis rates included in the radiation scheme. Thus, the chemistry scheme is switched off and in its place, monthly zonal mean profiles are provided to represent important missing atmospheric constituents. Due to its importance as a significant heat source in the stratosphere, profiles for atmospheric ozone are provided to retain this effect in the model. The various atmospheric aerosols in the model primarily influence only tropospheric dynamics, and so these are switched off in the extended upper boundary runs.

2.2 Stability mechanisms in the Unified Model

2.2.1 Model damping/sponge layer

In atmospheric models, it is often necessary to add a damping or sponge layer to the upper boundary of the model in order to prevent spurious reflection of vertically propagating waves from the model lid, and resulting numerical instabilities. These occur due to the no-flow (or zero vertical velocity) upper boundary condition which results in a rigid, reflecting lid.

It is also necessary to add damping at the poles to deal with numerical instabilities caused by the clustering of points due to the latitude-longitude grid, see e.g. Thuburn & Staniforth (2004).

In the UM, these instabilities are dealt with by adding a simple damping term $-\mu w$ to the forcing term of the vertical wind (w) equation – see Wood et al. (2014) for an in depth explanation of how it is incorporated into the model setup.

As an example, μ can be defined as a height dependent function[3] $\mu = \mu(z)$ so that the sponge is implemented gradually from the base of the sponge layer z_B until the top of the model z_{TOP}, namely

$$\mu(z) = \begin{cases} 0\,, & \text{if } z < z_B \\ \bar{\mu}\sin^2\left[\frac{\pi}{2}\left(\frac{z-z_B}{z_{TOP}-z_B}\right)\right], & \text{if } z_B \le z \le z_{TOP}, \end{cases}$$

where $\bar{\mu} \in [0, 1]$ is the vertical damping coefficient which can be tuned according to the application to increase/decrease the strength of the sponge layer – the default value is $\bar{\mu} = 0.05\ \mathrm{s}^{-1}$.

This example however does not incorporate the latitudinal variation that can also be added to the sponge layer to introduce damping around the problematic polar regions. The form of the sponge layer implemented in the default configuration of the

[2] Development of the UKCA model to include better representation of the atmosphere above 85 km is work currently being undertaken by Christopher W. Kelly et al. at the University of Leeds.

[3] In the model this function is actually defined in terms of the terrain-following coordinate $\eta \in [0,1]$. However for simplicity we describe the sponge layer in terms of physical height z here.

UM provides damping of strength $\bar{\mu}$ towards the upper boundary of the model domain, as well as providing damping of strength $2\bar{\mu}$ at the poles for all altitudes. This is depicted for a 100 km model lid in Figure 1.

This parameter $\bar{\mu}$ can be tuned appropriately to deal with larger vertical velocities at the upper boundary as the upper boundary height and number of vertical levels increase. The downside to increasing μ in this way is that it introduces artificial damping. However, this damping is highly localised to the model top and poles, and so is favourable to applying the numerical damping discussed in Section 2.2.3.

As well as this, it is already used in the standard UM, and so it is natural to include it in our experiments with an extended upper boundary. We will see that the damping must be increased in order to stabilise the model with the finer vertical resolutions and greater upper boundary heights used in Section 5.

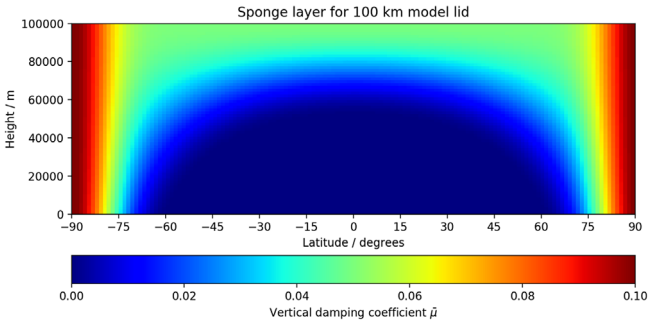

Fig. 1. The default sponge layer with vertical damping coefficient $\bar{\mu} = 0.05\ s^{-1}$ and 100 km model lid. The sponge layer can be seen to be at $\bar{\mu} = 0.05\ s^{-1}$ for most latitudes and for high altitudes but is doubled at the polar latitudes for all altitudes to help numerical stability in this area.

2.2.2 Model halos

The UM is parallelised for use on a large high performance computer. The model domain is consequently split up across separate processors; each processor has access to a limited latitude-longitude square on its main CPU grid. The halo or ring of neighbouring grid points is then put in place to account for advection outside this region.

However, if the horizontal wind is large enough, the advection scheme will try to access data that is very far away from the arrival point and outside this additional halo. If this occurs, then the model fails with a halo error. For global model runs, this problem only occurs in the North-South wind direction – the periodic structure in the East-West direction allows data to be communicated from one processor to another whenever necessary for East-West winds. A schematic of this problem can be seen in Figure 2.

This halo can be extended in order to deal with larger wind speeds, with some impact on computational efficiency. However, this importantly does not affect the model solution, and is a necessary additional expense to deal with the larger wind speeds encountered on raising the model lid (see for example those observed in Fig. 1 of Hedin et al., 1991). We will see that the extension of this halo is also necessary with the finer vertical resolutions and greater upper boundary heights used in Section 5.

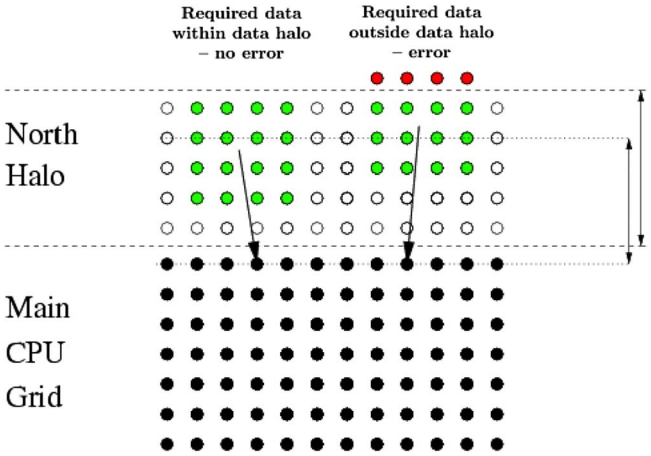

Fig. 2. Schematic illustrating the halo error. On the right hand side of the figure, the advection scheme can be seen trying to access data that is outside of the halo region which causes an error. The halo size can be increased to accommodate the larger winds present in the upper atmosphere.

2.2.3 Numerical stabilisation

The model can also be stabilised more directly by adjusting the implicit weighting parameter α as well as the time step Δt. This implicit weighting parameter (or off-centring parameter) is used in the approximation made in the semi-implicit semi-Lagrangian discretization – discussed in Wood et al. (2014) and in further detail in e.g. Rivest et al. (1994). However, both of these options are detrimental to the model as a whole.

Making the model more implicit by increasing the implicit weighting parameter α improves the stability of the model by introducing more implicit damping into the model. However, it therefore also decreases the accuracy of the entire solution because waves (in particular their high-frequency components) are artificially damped throughout the whole atmosphere, without physical motivation.

Decreasing the time step Δt allows the model to cope better with larger wind speeds, as the advection scheme then advects less per time step. However, this is only really a viable solution for research purposes. For use as an operational forecasting model, the run time must be kept short to achieve timely forecasts. This is an important motivation for retaining a larger time step.

We favour the more tailored approaches discussed above and avoid changing α and Δt for the extended UM experiments.

3 Diagnosing the instability

We start with the standard General Atmosphere (GA) 7.0 configuration of the UM as described in Walters et al. (2017), with the standard 85 km lid. We begin by raising the model lid to 100 km in order to determine the nature of the instability causing the model to crash. To do this, we undertake an

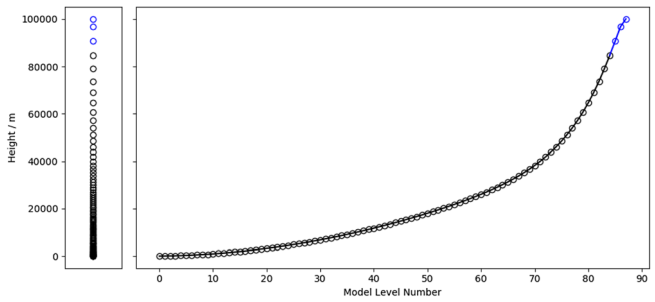

Fig. 3. Vertical level sets for the standard model height (black) and those added for the raised model height (blue). Two levels are added conforming to the 85 km level distribution, whilst the final is placed at 100 km.

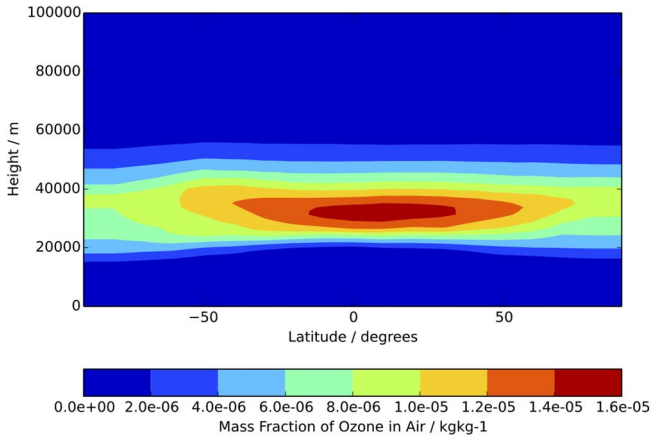

Fig. 4. A zonal mean profile produced to prescribe the initial configuration of atmospheric ozone for the 100 km model lid. Its inclusion is important in order to represent the correct vertical temperature structure (via radiative heating).

empirical analysis of model runs of the UM using different configurations.

3.1 Extended model setup

The changes that are made to the aforementioned standard GA7.0 configuration of the UM are summarised below

1. The model chemistry scheme is entirely switched off – this is not yet configured to work above 85 km.
2. Atmospheric aerosols are switched off and ozone background files are switched on, accounting for the lack of the chemistry scheme.
3. The model upper boundary is raised from 85 to 100 km.

Otherwise, we conserve as many model features as possible in order to appropriately compare the output to that of the 85 km model. For the latter of these points, a new vertical level set is provided that extends the 85 vertical levels in the 85 km model up to 88 vertical levels in the 100 km model. We adhere to the default level spacing to add an additional two levels, and then add the final level at 100 km. A comparison of the two sets of vertical levels can be seen in Figure 3.

This level spacing – where the levels increase in depth according to an approximately exponential distribution – is chosen with the lower atmosphere in mind; the majority of levels are placed in this region and the vertical resolution at the top of the model is much larger – nearing 6 km. To diagnose the cause of the aforementioned instability, we keep this model level spacing so as to keep the first 85 km of the model domain the same and provide a good comparison between the configurations. However, to obtain a model that resolves appropriate wave scales in the MLT, we must have a finer vertical resolution. We will investigate different vertical level sets that are better suited to achieving this objective in Section 5.1.

As discussed previously, monthly zonal mean profiles are prescribed for atmospheric ozone, which are extended to have an upper boundary at 100 km. An example profile for June is depicted in Figure 4.

Finally, it is important to note that in all cases, the experimental runs are performed multiple times in order to validate the consistency of the output.

3.2 Extended model results

We summarise the runs performed using the extended UM in Table 1.

In both model runs, an error related to the North-South advection scheme is produced and causes the model to crash. This means that the prognostic variables related to a grid point have been advected further than the data halo for the given grid point. This is indicative of excessive wind speeds in the model. This instability is localised in space and time. We proceed to investigate these abnormal wind speeds in order to determine their cause.

To do this, we consider the September model run, which crashed in the following December, therefore running with no issues and normal model fields for several thousand model time steps. We subsequently plot instantaneous westerly (u) and southerly (v) winds at the last time step before the model crash.

The problem arises over the South Pole of the model. Thus, we take a stereographic plot over this pole, as well as a slice through the atmosphere at this most southerly latitude circle (i.e at 89.375°S for u wind and 90°S for v wind). This can be seen in Figure 5. Here, the greatly excessive wind speeds are evident, on the order of 600 m/s for the u wind and 400 m/s for the v wind. This is in comparison to u winds of at most 90 m/s in e.g. Swinbank & Ortland (2003) and v winds of at most 100 m/s in e.g. Hedin et al. (1991). The problematic winds can also be seen to be constrained to the uppermost model level.

The same phenomenon is observed for the March model run which crashes in the following June, but with the problem occurring around the North Pole.

It is evident therefore that the problematic model winds occur in the summer season for a particular hemisphere. Namely, in the southern hemisphere summer (December) for a September start date and the northern hemisphere summer (June) for a March start date. We deduce that the problem is therefore a seasonal one.

At this stage, it is important to consider that the instability could be numerical in nature. On increasing the model upper boundary, larger density perturbations associated with

Table 1. A summary showing the model runs performed for the investigation, with its corresponding crash date and location.

	Run start date	Run crash date	Location of high wind speeds causing crash
Sep Model Run	September 1988	December 1988	Southern hemisphere (restricted to pole)
Mar Model Run	March 1988	June 1988	Northern hemisphere (restricted to pole)

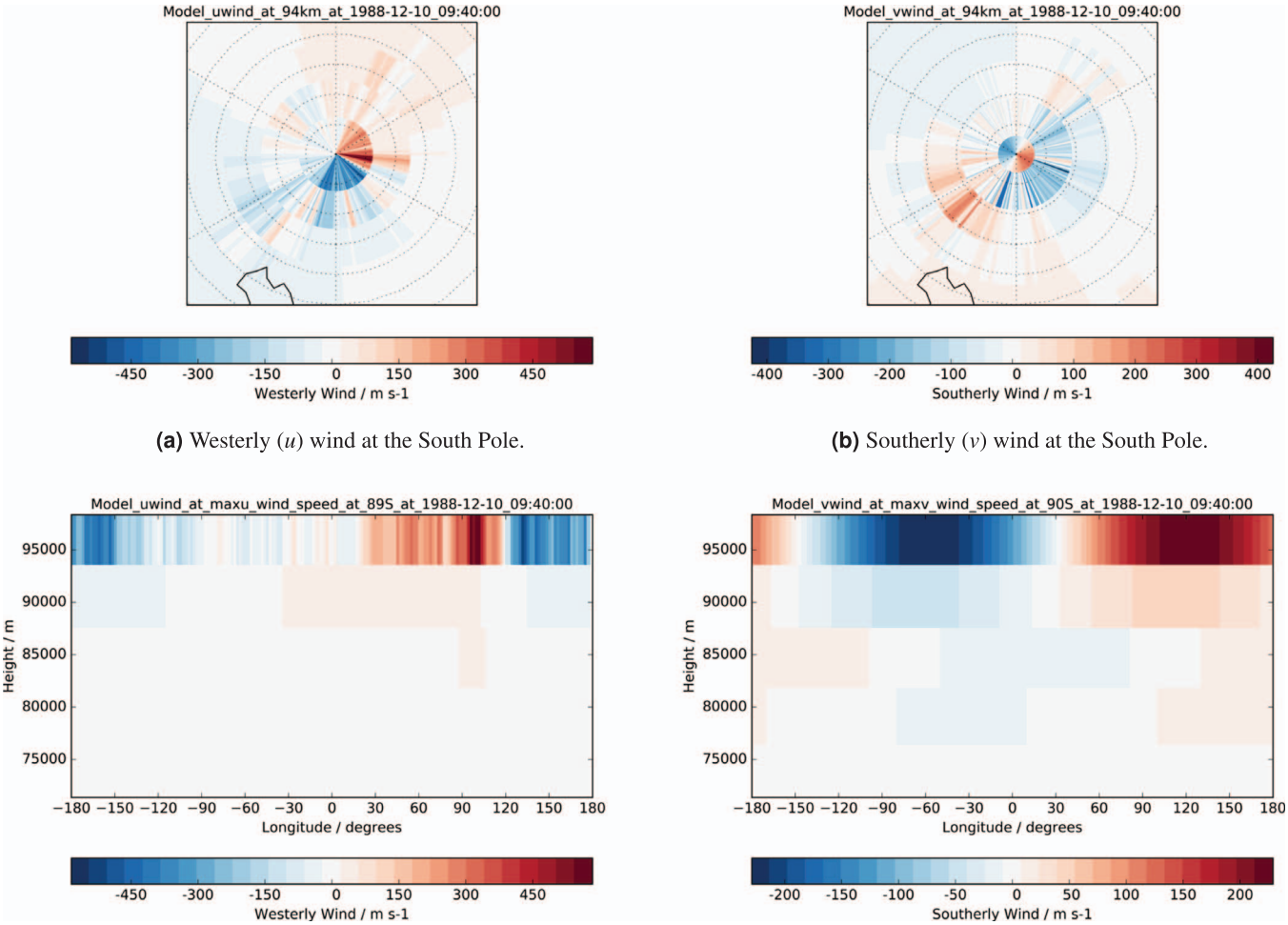

(a) Westerly (u) wind at the South Pole.

(b) Southerly (v) wind at the South Pole.

(c) Westerly (u) wind at $\approx 90^{\circ}$S.

(d) Southerly (v) wind at $\approx 90^{\circ}$S.

Fig. 5. Modelled wind in the 100 km September model run at the time step before the model crash. Stereographic plots at the uppermost model level (a) and (b). Plots of the wind at the southernmost latitude circle (c) and (d). This makes evident the abnormally high wind speeds causing the model to crash.

exponential wave growth are introduced which could cause the underlying numerical scheme to become unstable. However, the long run times of the model and the seasonal pattern of the crash dates indicate that the observed instability is dominated by problems in the physical schemes used in the model.

It is also pertinent to observe that this instability is local in nature. A global instability is more likely to be caused by problems in the dynamical core of the model, whereas a local instability is more illustrative of a problem with localised forcing provided by the parameterization schemes in the model. We indeed see localised instabilities, which consistently occur in the polar regions of the model.

Both of these factors mean we are confident in excluding numerical issues as the cause of the instability in the first instance. We therefore focus our investigation on the seasonal forcing provided by the radiation scheme – which we already suspect will have problems when extended to the MLT.

The radiation scheme provides the solar energy input responsible for seasonal weather variations. Hence, we look at the SW radiation provided by the radiation scheme which governs this input of energy through heating.

We plot the zonal mean of instantaneous SW radiative heating at the last time step before the model crashes for both start dates in Figure 6. The heating from the ozone layer is evident in

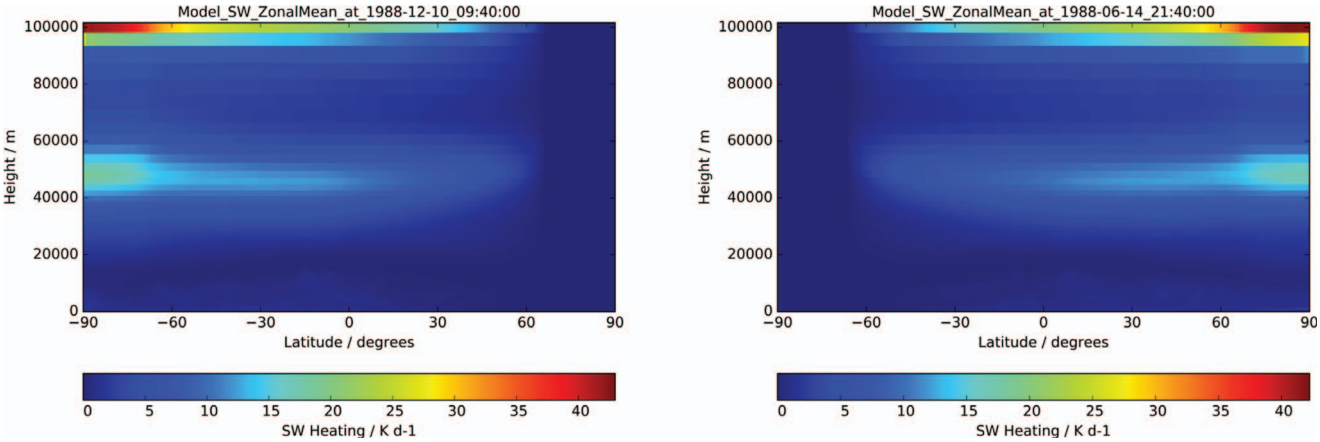

(a) Zonal mean of the SW radiative heating for the model run starting in September and crashing in December.

(b) Zonal mean of the SW radiative heating for the model run starting in March and crashing in June.

Fig. 6. Plots illustrating the issue evident with the SW radiation produced by the radiation scheme. We see abnormal values in exactly the regions where the high wind speeds occur in the previously discussed model runs. (a) Zonal mean of the SW radiative heating for the model run starting in September and crashing in December. (b) Zonal mean of the SW radiative heating for the model run starting in March and crashing in June.

the summer hemisphere of both figures, but more pertinent are the abnormal values at the top of the model. The values are focused in the summer pole of the uppermost layer; exactly the region where the problematic winds were previously observed. Thus, we deduce that it is this incorrect SW radiative forcing that is driving the high polar wind speeds and ultimately therefore causing the observed instability in the UM with a raised upper boundary.

The observed SW radiative heating is in fact in keeping with LTE. However, this assumption is no longer valid in the MLT, as is demonstrated in Figure 7.

We strongly suspect that it is indeed the assumption of LTE that is leading to the observed instability in the UM, and that non-LTE (NLTE) effects must be considered when extending the upper boundary to the MLT.

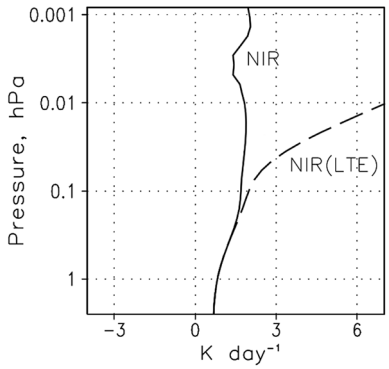

Fig. 7. Total heating due to solar energy absorption in the near-IR CO_2 (NIR) bands. This illustrates the difference in heating in K day^{-1} when the Local Thermodynamic Equilibrium (LTE) approximation is made. This approximation breaks down at around 0.1 hPa (approx. 65 km) as can be seen. After Fomichev et al. (2004).

4 Resolving the instability

The introduction of a NLTE radiation scheme is an important step towards a whole atmosphere model. However, such a scheme was not ready at the time of performing this research. In the meantime, it is important to verify that the radiative forcing is the sole cause of the observed instability, and not one of several factors. We confirm this by verifying that with appropriate radiative forcing in the upper atmosphere, the model is stable under the current 100 km model configuration.

To supply appropriate radiative forcing for the upper atmosphere without access to the NLTE radiation scheme, it is necessary to develop the model to account for NLTE effects which become prevalent in the MLT. Thus, an interim solution of relaxation – or "nudging" – to an analytic temperature profile is added to the model to confirm that the extended UM is stable under corrected forcing. We shall refer to the model with this nudging included as the nudged model.

4.1 Nudged model setup

The erroneous radiation scheme is replaced at high altitudes by relaxation to a temperature profile based on climatology. The scheme begins to drift away from LTE at around 65–70 km, and so it is from 70 km and above that the scheme is replaced. For simplicity, this profile is globally uniform and varies only with height so that $T_{\mathrm{PROFILE}} = T_{\mathrm{PROFILE}}(z)$. This is sufficient as an interim solution before the introduction of the full NLTE radiation scheme.

This relaxation acts to push – or "nudge" – the temperature field from the model dynamics toward the chosen temperature profile, over a given timescale. This timescale τ is chosen as

to allow some variation about this profile, so that the dynamics of the model can also influence the temperature field.

More concretely, the nudged temperature field is computed in an additional step after each dynamics step as

$$T_{\mathrm{NUDGED}} = \alpha_{\mathrm{NP}} T_{\mathrm{PROFILE}} + (1 - \alpha_{\mathrm{NP}}) T_{\mathrm{DYN}},$$

where T_{NUDGED} is the nudged temperature field, T_{PROFILE} is the chosen analytic profile, T_{DYN} is the temperature field computed by the dynamics and $\alpha_{\mathrm{NP}} = k\Delta t/\tau$ is the nudging parameter. The timescale τ is chosen to be 24 hours, in keeping with work by Song et al. (2018). Here, using a hydrostatic model, a physical reasoning was used to determine appropriate relaxation timescales for a high atmosphere model being nudged to data. They found that between 8, 24 and 40 h timescales, the 24 h gave the most reasonable model fields and conservation properties out of the three options. Thus, this informed our choice of using τ as 24 h. Finally, $k \in [0, 1]$ is the nudging ramp parameter – this gives a smoothed transition to the nudging as it is introduced at 70 km.

The temperature profile T_{PROFILE} used is based on climatological and satellite data so that

- Between 70 and 86 km the profile is based on the US Standard Atmosphere (USSA) (COESA, 1976).
- Between 86 and 119.7 km the profile is based on the Committee on Space Research (COSPAR) International Reference Atmosphere (CIRA) (Fleming et al., 1990).
- Above 119.7 km the temperature asymptotes to a selected exobase temperature (here 1000 K).

This leads to the expression given in Equation (1) for this profile

See Equation (1) *at the bottom of the page*

where

$$\sigma(z) = \frac{(z - z_{\mathrm{CIRA-top}})(R_{\oplus} + z_{\mathrm{CIRA-top}})}{(z + R_{\oplus})}$$

with the radius of the Earth denoted $R_{\oplus}$ and with the following parameter values:

• $T_{70\mathrm{km}} = 219.6$ K	• $\Gamma_{\mathrm{THERMO}} = 1.875 \times 10^{-5}$	• $z_{\mathrm{USSA-bottom}} = 70$ km
• $T_{\mathrm{exobase}} = 1000$ K	• $\Gamma_{\mathrm{CIRA}} = 9.727 \times 10^{-4}$	• $z_{\mathrm{USSA-top}} = 86$ km
• $T_{\mathrm{CIRA-top}} = 369.8$ K	• $\Gamma_{\mathrm{MESO}} = 2 \times 10^{-3}$	• $z_{\mathrm{Tmin-CIRA}} = 93.3$ km
		• $z_{\mathrm{CIRA-top}} = 119.7$ km

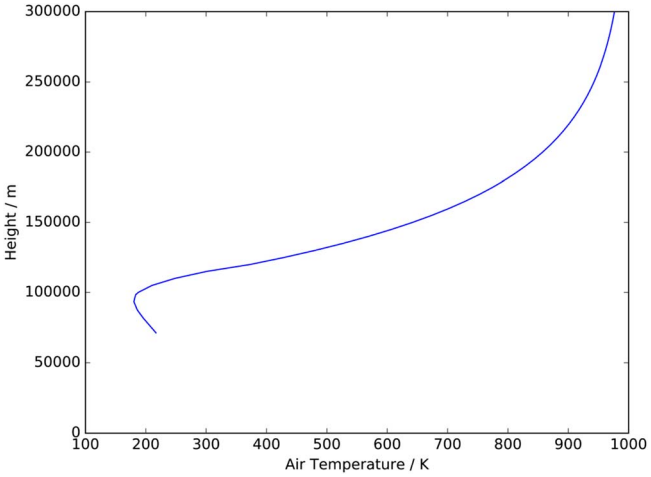

Fig. 8. Temperature profile used for the relaxation of the temperature field.

The T values represent temperatures, the Γ values represent lapse rates and the z values represent heights, all at locations indicated by the subscripts. Note in particular the exobase temperature at 1000 K. In reality this can vary from 700 to 1600 K dependent on the solar cycle. This parameter can be easily tuned but is just set to a typical value here, given that the upper boundaries considered are much lower than the exobase.

The resulting profile is plotted in Figure 8. The main features of the profile are that it lapses linearly up to ≈ 93 km, then is quadratic to ≈ 120 km (including the mesopause temperature minimum) and finally asymptotes towards the exobase temperature.

Importantly, the chosen temperature profile shows good agreement with the standard 85 km model temperatures at 70 km, where the nudging is introduced, as can be seen in Figure 9. This therefore minimises the possibility of discontinuities in the temperature field in the area of transition.

Finally the erroneous values from the radiation scheme are zeroed above 70 km. This removes the erroneous forcing that was evident in Figure 6.

4.2 Nudged model results

We now perform the same model runs as in Section 3.2 using the nudged model. Now the model differs from the standard GA7.0 configuration of the UM in the following ways:

$$T_{\mathrm{PROFILE}}(z) = \begin{cases} T_{70\ \mathrm{km}} - \Gamma_{\mathrm{MESO}}(z - z_{\mathrm{USSA-bottom}}) & , \text{if } 70 \le z \le 86\,\mathrm{km} \\ T_{70\mathrm{km}} - \Gamma_{\mathrm{MESO}}(z_{\mathrm{USSA-top}} - z_{\mathrm{USSA-bottom}}) & \\ \qquad -\Gamma_{\mathrm{CIRA}}(z - z_{\mathrm{USSA-top}}) & , \text{if } 86 < z \le 93.3\,\mathrm{km} \\ T_{70\mathrm{km}} - \Gamma_{\mathrm{MESO}}(z_{\mathrm{USSA-top}} - z_{\mathrm{USSA-bottom}}) & \\ \qquad -\Gamma_{\mathrm{CIRA}}(z - z_{\mathrm{USSA-top}}) & \\ \qquad +(3 \times 10^{-7})(z - z_{\mathrm{Tmin-CIRA}})^2 & , \text{if } 93.3 < z \le 119.7\,\mathrm{km} \\ T_{\mathrm{exobase}} - (T_{\mathrm{exobase}} - T_{\mathrm{CIRA-top}}) \exp(-\Gamma_{\mathrm{THERMO}}\sigma(z)) & , \text{if } z > 119.7\,\mathrm{km} \end{cases} \quad (1)$$

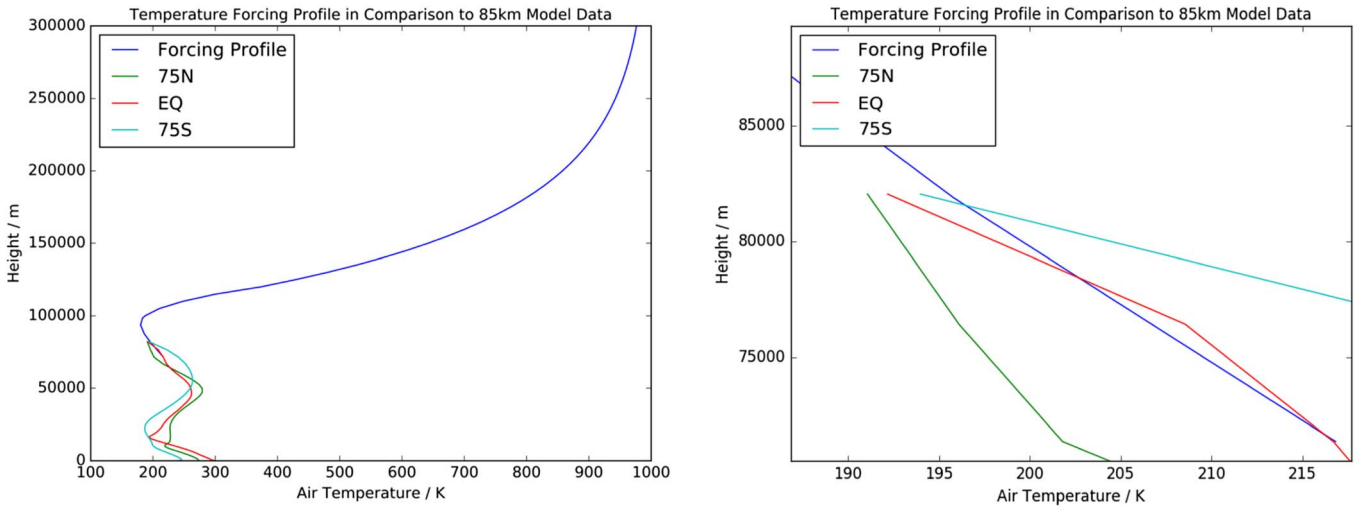

Fig. 9. Comparison of the 85 km temperature field for various latitudes and the forcing profile (a), with pertinent area zoomed in (b). Good agreement between the two is seen.

1. The model chemistry scheme is entirely switched off – this is not yet configured to work above 85 km.
2. Atmospheric aerosols are switched off and ozone background files are switched on, accounting for the lack of the chemistry scheme.
3. The model upper boundary is raised from 85 to 100 km.
4. The forcing from the radiation scheme is zeroed above 70 km.
5. The temperature field above 70 km is nudged towards a prescribed climatological temperature profile.

Importantly, with this in place, the model is consequently stable for both start dates and can be run for several years without the appearance of the instability observed in Section 3. In Figure 10, we plot instantaneous u and v winds produced using the September nudged model run for comparison with the winds from the initial extended model run in Figure 5. These are plotted at the same model time as previously, namely the December crash date of the initial extended model. We also plot the winds in the same manner – stereographic plots over the South Pole, as well as a slice through the atmosphere at the most southerly latitude circle (at around 90°S).

In comparing the two figures, it is evident that the instability in the polar region has been removed, with the resultant winds of a much more reasonable order of magnitude; the 400–600 m/s winds are no longer evident and the unphysical winds of opposite signs in neighbouring grid cells are also removed. The winds are also much more on par with the magnitudes seen in Swinbank & Ortland (2003) and Hedin et al. (1991).

We also see that the excessive SW radiative heating has been removed in Figure 11.

These results indicate that the LTE assumption in the radiation scheme is indeed responsible for the model instability with a lid at 100 km and importantly, we are able to conclude that there are no additional factors causing instability with the current configuration – such as problems resulting from the polar singularity of the latitude-longitude numerical discretisation.

We would now like to build on this stable configuration and extend the model further to different vertical resolutions and upper boundary heights. However, it is first diligent to compare important model fields with the 85 km model to illustrate that the nudging is not having a detrimental effect on the modelled fields in the lower atmosphere.

To do this, we compare climatological fields rather than the instantaneous fields presented previously. Thus, we present monthly mean zonal mean plots for westerly (u) wind, vertical (w) wind and temperature from the nudged model. These are plotted for December in the second column of Figure 12 and for June in the second column of Figure 13. They are compared to fields from the 85 km model in the first column of the respective figures.

We observe good consistency of the model fields for both December in Figure 12 and June in Figure 13 up to around 70 km where the nudging is implemented. At this height, there is evidence of the globally uniform approximation of the temperature field in comparing plot **(i)** with plot **(j)** in both figures at around 70 km. Here, we observe temperature changes on the order of 10–20 K at the summer poles in both figures. However, this is to be expected given the simplified physical approximation made in the temperature profile. We reiterate that the nudging is put in place to observe if the model is consequently stable rather than as a permanent solution – the more physically accurate NLTE radiation scheme and the updated UKCA chemistry scheme will address this issue.

We comment on the other plots in this figure (with different vertical resolutions) in Section 5.1.

At this stage, we also make a preliminary comparison with data in order to test the realism of the nudged model – in reality given the simplified physical approximations made we expect the model to drift away from realistic values.

We compare climatologies for monthly mean zonal mean westerly (u) wind and temperature for the 100 km lid model run against data. We use the 3 km vertical resolution 94 level configuration which will be developed in Section 5 for comparison, given the finer structure observed in the model fields. The wind data used for comparison is the Upper Atmosphere Research Satellite (UARS) Reference Atmosphere Project (URAP) (Swinbank & Ortland, 2003). The temperature data used for comparison is from the Earth Observing System

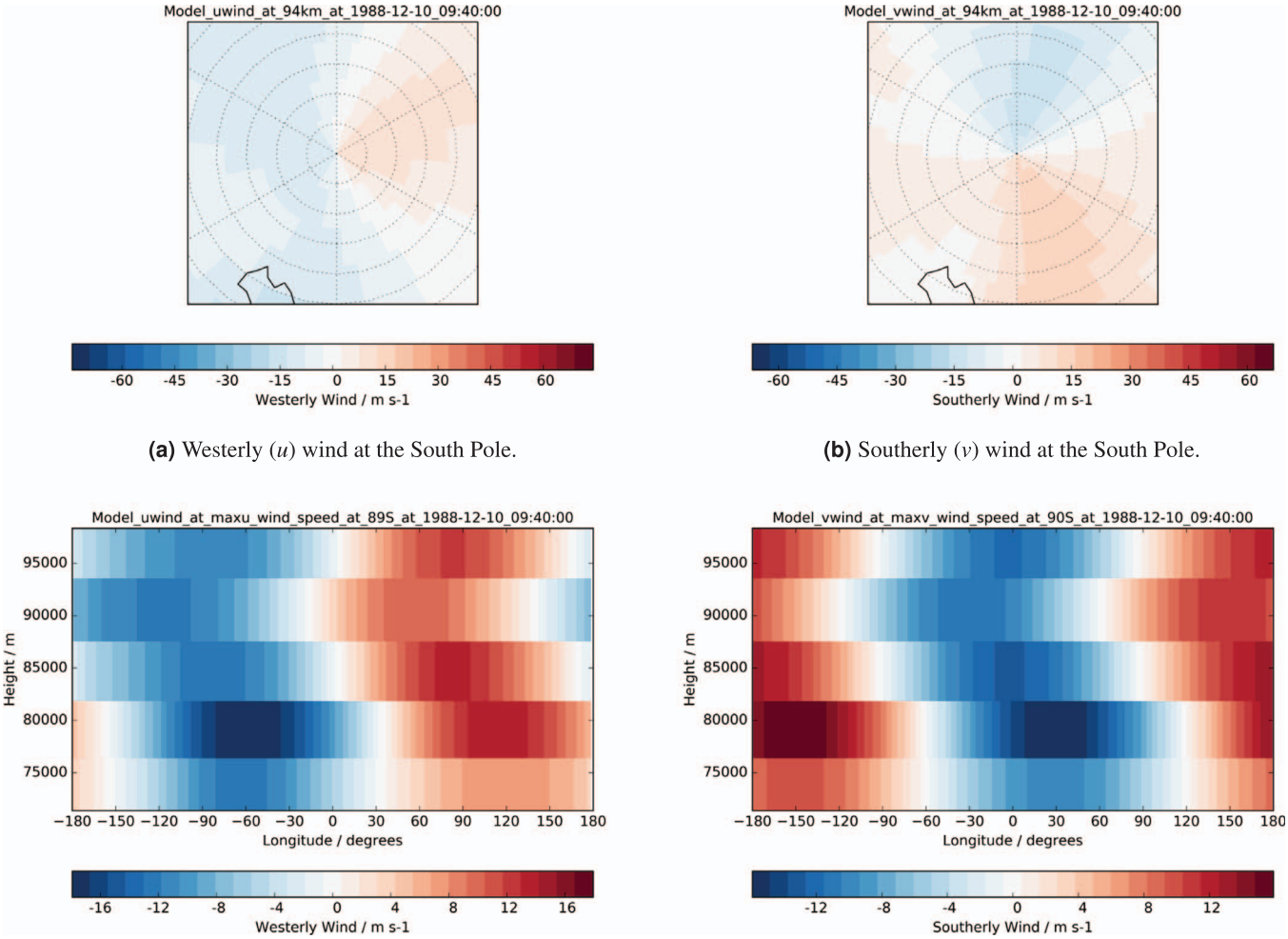

(a) Westerly (u) wind at the South Pole.

(b) Southerly (v) wind at the South Pole.

(c) Westerly (u) wind at $\approx 90^\circ$S.

(d) Southerly (v) wind at $\approx 90^\circ$S.

Fig. 10. Modelled wind in the 100 km September model run with the nudging scheme in place. Stereographic plots at the uppermost model level (a) and (b). Plots of the wind at the southernmost latitude circle (c) and (d). We see the removal of the anomalous wind speeds present previously by comparison with Figure 5.

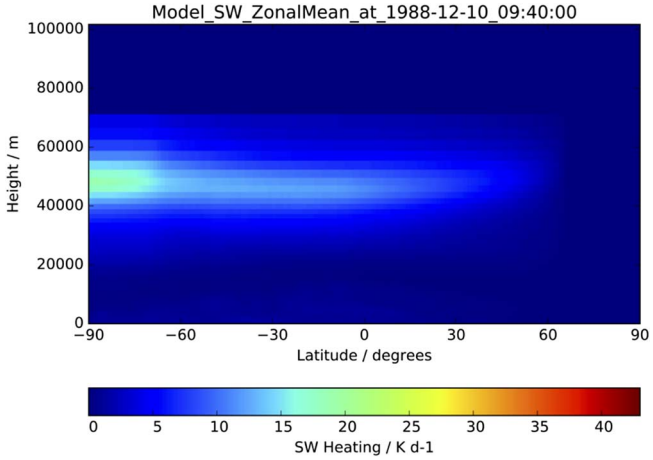

Fig. 11. SW radiation showing zeroed field above 70 km.

Microwave Limb Sounder (EOS MLS) on the Aura satellite (Waters et al., 2006). The data is recorded on pressure levels and we make an approximate conversion to height using $z = -H \ln(p/p_0)$, with p_0 = 1000 hPa and H = 7200 m.

We plot the climatologies and data for December in Figure 14 and for June in Figure 15. A more in depth comparison to data will come as the model is improved further in the MLT.

A slight temperature gradient towards the summer pole is seen at around 90 km in the modelled temperature, indicative of a cold summer mesopause. This is however less pronounced than the cold summer mesopause in the MLS data, but is encouraging given the simplified physics. It is also worth noting that there are also doubts in the robustness of the MLS data at low pressures (e.g. Schwartz et al., 2008), meaning that the cold summer mesopause is not necessarily as cold as indicated by the MLS data, but is certainly colder than the model currently predicts. In the model winds, the summer-time westerly

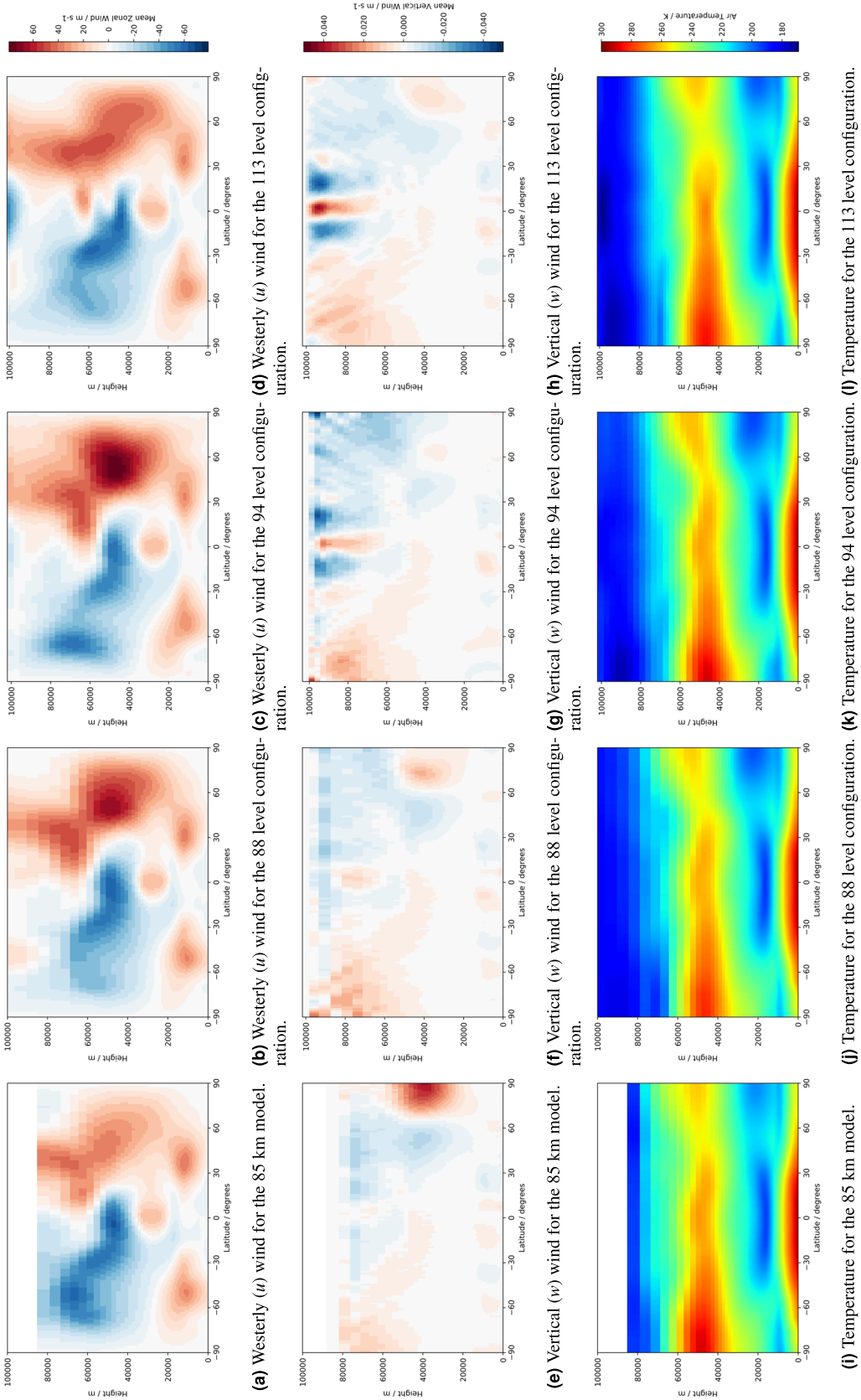

(a) Westerly (u) wind for the 85 km model. **(b)** Westerly (u) wind for the 88 level configuration. **(c)** Westerly (u) wind for the 94 level configuration. **(d)** Westerly (u) wind for the 113 level configuration.

(e) Vertical (w) wind for the 85 km model. **(f)** Vertical (w) wind for the 88 level configuration. **(g)** Vertical (w) wind for the 94 level configuration. **(h)** Vertical (w) wind for the 113 level configuration.

(i) Temperature for the 85 km model. **(j)** Temperature for the 88 level configuration. **(k)** Temperature for the 94 level configuration. **(l)** Temperature for the 113 level configuration.

Fig. 12. Zonal mean monthly mean climatologies in December of westerly (u) wind (top), vertical (w) wind (middle) and temperature (bottom) comparing the original 85 km model with the 88, 94 and 113 level configurations.

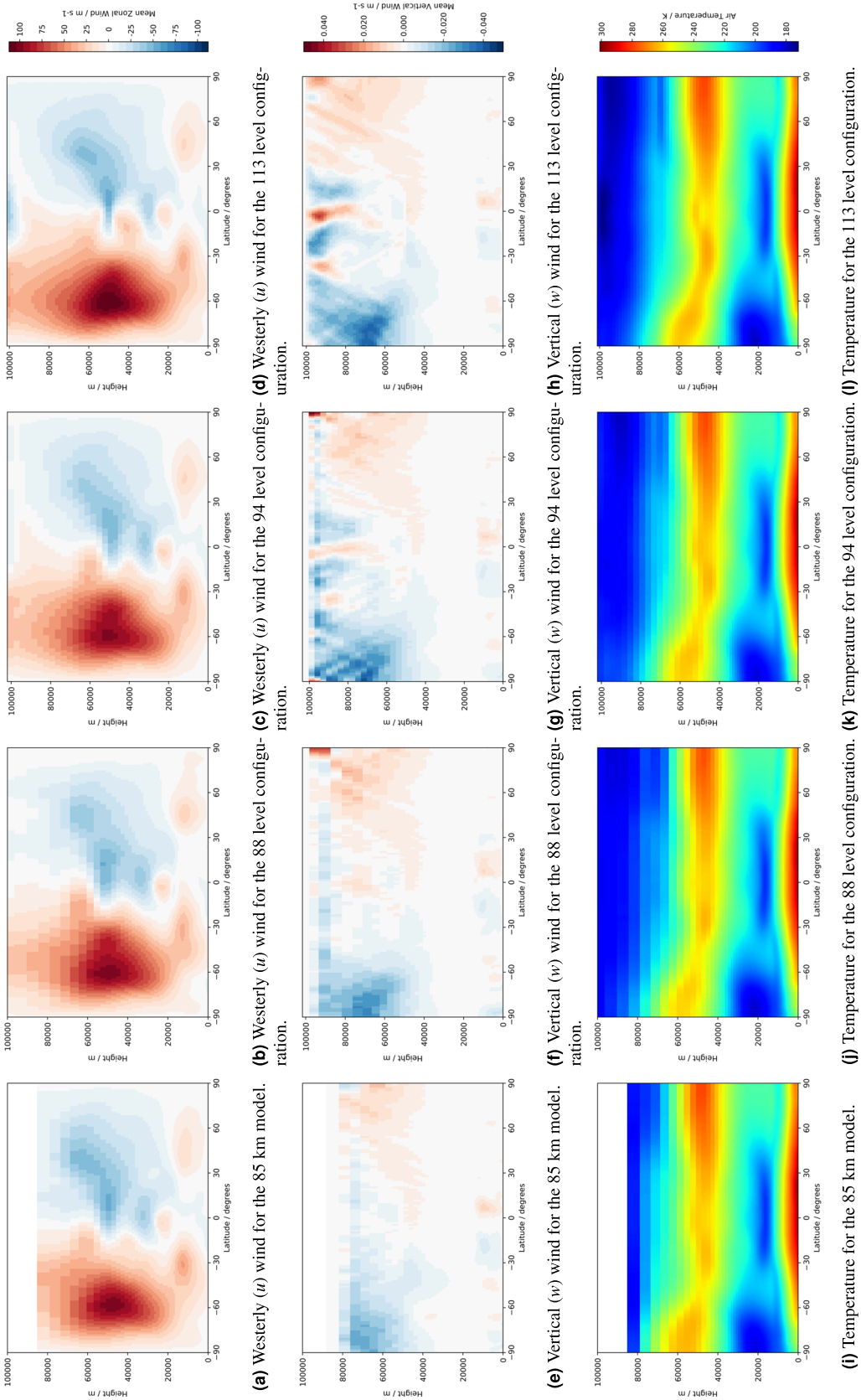

(a) Westerly (u) wind for the 85 km model. **(b)** Westerly (u) wind for the 88 level configuration. **(c)** Westerly (u) wind for the 94 level configuration. **(d)** Westerly (u) wind for the 113 level configuration.

(e) Vertical (w) wind for the 85 km model. **(f)** Vertical (w) wind for the 88 level configuration. **(g)** Vertical (w) wind for the 94 level configuration. **(h)** Vertical (w) wind for the 113 level configuration.

(i) Temperature for the 85 km model. **(j)** Temperature for the 88 level configuration. **(k)** Temperature for the 94 level configuration. **(l)** Temperature for the 113 level configuration.

Fig. 13. Zonal mean monthly mean climatologies in June of westerly (u) wind (top), vertical (w) wind (middle) and temperature (bottom) comparing the original 85 km model with the 88, 94 and 113 level configurations.

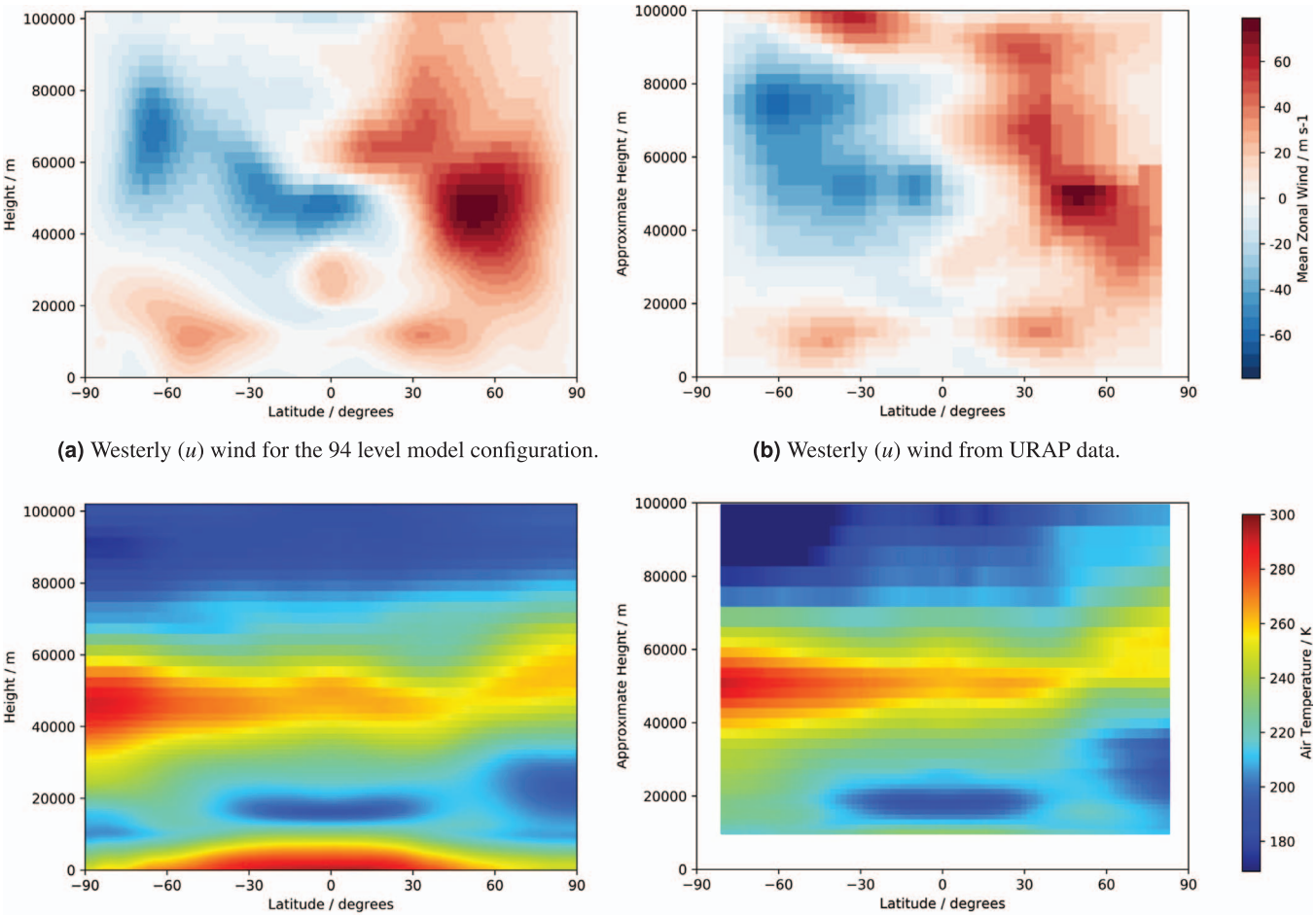

(a) Westerly (u) wind for the 94 level model configuration.

(b) Westerly (u) wind from URAP data.

(c) Temperature for the 94 level model configuration.

(d) Temperature from MLS data.

Fig. 14. Zonal mean monthly mean climatologies in December of westerly (u) wind (top) and temperature (bottom). These are compared to URAP data for zonal wind and MLS data for temperature. The approximate height is calculated using a scale height of H = 7200 m.

mesospheric jet is not present at 90 km when compared to the URAP data, however this is to be expected given the lack of a strong temperature gradient provided by a cold summer mesopause.

It is evident therefore that the model still requires several additions before being able to produce realistic dynamics in the MLT. However, as a developmental tool the nudging has served its purpose in that it has stabilised the model for this configuration, and has in fact given evidence of producing more complex dynamics, even with its simplified setup. Furthermore, implementation of the correct radiative and chemical forcing will hence provide a complete and stable model of the mesosphere and lower thermosphere up to 100 km.

5 Extending the nudged model

With a stable model produced up to 100 km, we can now extend this new configuration in order to more appropriately model atmospheric waves in the MLT as well model greater atmospheric heights. To this end, we investigate changes to both the vertical resolution and the height of the model upper boundary.

We discuss the implementation of these extensions and analyse the model fields produced with them in place.

5.1 Experimentation with vertical resolution

The standard model vertical level set is set up so that model levels increase in height with each new level introduced, so that at the upper boundary of the 88 level model configuration, the vertical level height is approximately 6 km (cf. Fig. 3). However, this resolution is not appropriate to accurately represent vertically propagating gravity waves in the MLT; these waves are significant carriers of energy and momentum in the upper atmosphere and are important contributors to general circulation in the MLT – see for example Becker & Vadas (2018).

To see why this resolution is not sufficient in the MLT, we must consider the model scale height H. This can be related to the atmospheric temperature so that $H = R_{\text{dry}}T(z)/g(z)$, where R_{dry} is the gas constant for dry air[4] and $g(z)$ is the acceleration due to gravity as a function of height above the surface z. This is given by $g(z) = g_0 R_\oplus^2/(R_\oplus + z)^2$, where g_0 is the

[4] This is a reasonable assumption above the troposphere for order of magnitude calculations.

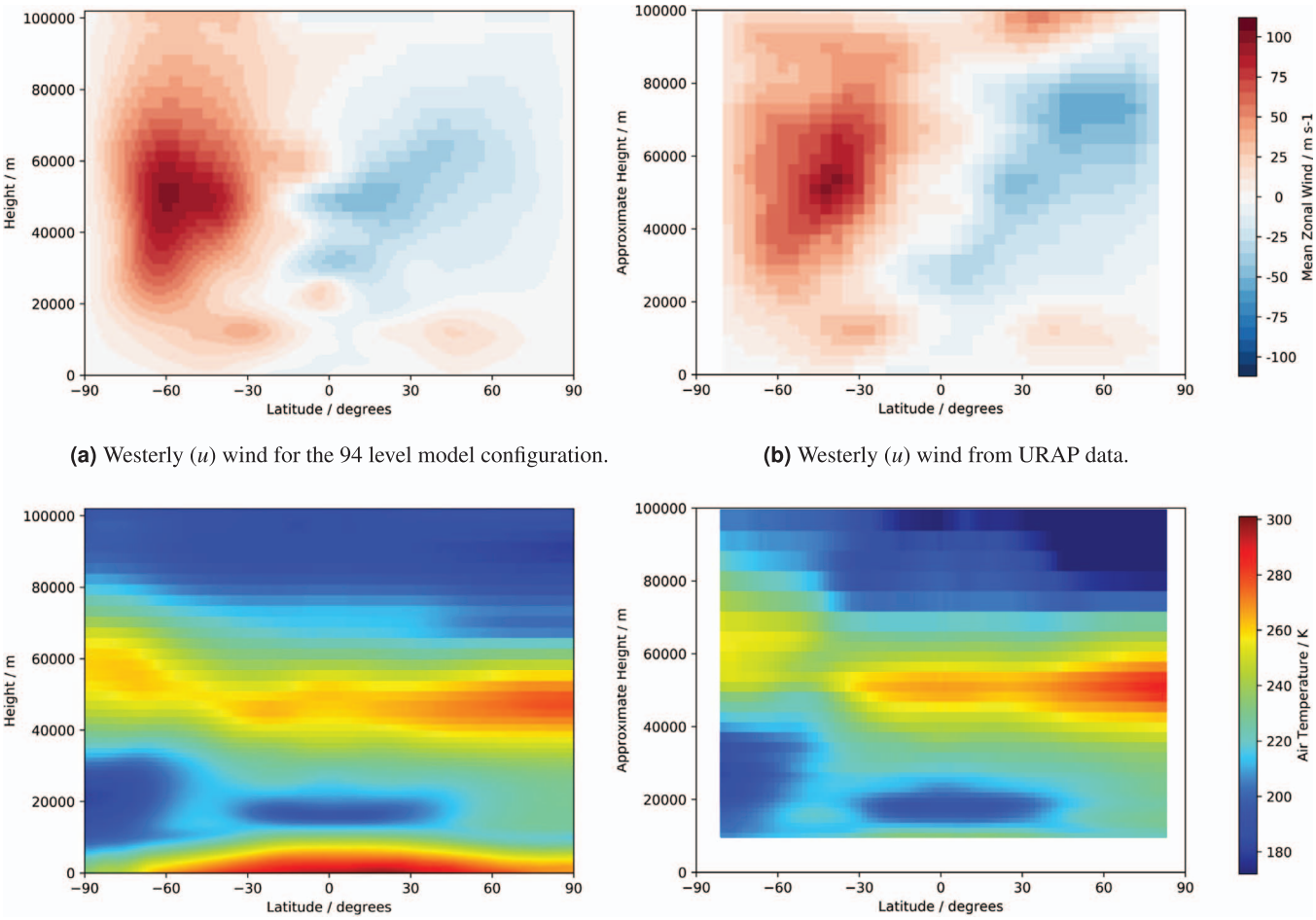

(a) Westerly (u) wind for the 94 level model configuration.

(b) Westerly (u) wind from URAP data.

(c) Temperature for the 135 km model lid.

(d) Temperature from MLS data.

Fig. 15. Zonal mean monthly mean climatologies in June of westerly (u) wind (top) and temperature (bottom). These are compared to URAP data for zonal wind and MLS data for temperature. The approximate height is calculated using a scale height of $H = 7200$ m.

acceleration due to gravity at sea level and $R_\oplus$ is the radius of the Earth. This quantity dictates the height for which the atmospheric pressure drops by a factor e at a given temperature.

In order to accurately model vertical wavenumbers in atmospheric dispersion relations – see Griffin & Thuburn (2018) for a more in depth explanation – the vertical resolution must be finer than this scale height. Thus we must make our choice of vertical resolution based on the scale height H so as to be able to resolve these waves. To do this, we plot this scale height as a function of altitude in Figure 16. Since we would like the grid to be finer than the scale height H, we also plot $H/2$ and $H/4$ for comparison – these would give two and four vertical levels per scale height respectively. The temperature field used in the calculation of the scale height is the same as that used in the nudging – namely as shown in Figure 8.

This informs our choice of vertical level heights. With a vertical level height of 1.5 km, we place approximately four vertical levels per scale height. This resolution will give an accurate representation of waves throughout the MLT.

However, this fine resolution leads to concerns regarding consequent numerical instability in the vertical motion as well as computational cost. We therefore also consider a vertical level height of 3 km. This gives approximately two vertical levels per scale height in the MLT and is a good middle ground; some finer vertical wave scales are resolved and the computational cost incurred of resolving at a much finer scale is reduced.

In theory the vertical resolution could increase after around 100 km in keeping with the corresponding increase in scale height. This would make the model less costly and less prone to numerical instability as the model is extended up into the thermosphere. However this is not investigated in this paper and will be the subject of further research on the extended UM.

These two new vertical level sets are shown in Figure 17, and we proceed to test the model using these vertical level sets.

5.1.1 3 km vertical resolution

We first experiment with the vertical level set that has a maximal vertical resolution of 3 km. To do this, we set up the vertical levels so that the model levels increase in depth as before, up until they near 3 km. We then fix the vertical level height at this value. This yields a 94 level configuration going up to a height of 102 km – this can be seen in Figure 17.

With this vertical level set and the nudging scheme employed as in Section 4.1, we observe no effect on the stability of the model and once more have a stable model with the lid at approximately 102 km.[5] The model is able to run for several years with no issues.

In this paper, we focus on climatological mean fields rather than instantaneous or short term fields used to examine finer atmospheric features such as atmospheric tides. This is because our priority here is model stability, and improving the realism of the UM in the MLT will be the subject of future research. The mean fields provide a good starting point to examine the fields produced by the nudged UM.

Thus, we compare climatologies for monthly mean zonal mean westerly (u) wind, vertical (w) wind and temperature for the 88 and 94 level configuration. We plot this for December in Figure 12 and for June in Figure 13, with column 2 and column 3 in both figures showing the 88 and 94 level configurations respectively.

In particular, we observe the same general structure in the model fields but with some finer scale vertical features evident towards the upper boundary with the 94 level configuration.

The primary goal here is stability and it is encouraging that no additional model changes such as modification of the sponge layer are necessary for the model to run with the new 94 level configuration. We will see that for a finer vertical resolution, additional modifications are necessary to stabilise the model.

5.1.2 1.5 km vertical resolution

We now experiment with a vertical level set that has a maximal vertical resolution of 1.5 km. The construction is as in Section 5.1.1 but using 1.5 km as the maximal depth – this can be seen in Figure 17. This yields a 113 level configuration going up to a height of around 101 km.

With this configuration, and the nudging implemented as in Section 4.1, the model does not initially run successfully, and crashes due to excessive wind speeds in the North-South and vertical directions.

To combat each of these issues, we make two modifications.

Firstly, we adjust the halo region (cf. Sect. 2.2.2) to account for the larger wind speeds in the lower thermosphere. In order to maximise the wind speeds that the model can cope with, we set the halo region to its maximum permitted size. This will allow for significantly larger wind speeds in the North-South direction. Thus, any further issues with N-S halos must be put down to unphysical winds developing elsewhere in the model.

Secondly we adjust the sponge layer of the model, as described in Section 2.2. To do this we shall increase the value of the vertical damping coefficient $\bar{\mu}$ to damp out large vertical velocities near the model upper boundary until the model is able to run. However, despite this targeted damping, we wish to avoid over damping modelled vertical velocities. Thus, we use as low a value as possible so that the model is consequently stable.

Adding an extended halo gives a stable model run with a vertical damping coefficient of $\bar{\mu} = 0.3\ \mathrm{s}^{-1}$. As in Section 5.1.1, we compare the 88 level climatologies to the corresponding climatologies for the new 113 level configuration. Climatologies for December are shown in Figure 12, and for June in Figure 13, with column 2 and column 4 in both figures showing the 88 and 113 level configurations respectively.

Here, many finer scale vertical and horizontal features become evident from about 40 km upwards where the 1.5 km resolution begins. For example, looking at the westerly (u) wind there appears to be more structure in the equatorial winds in the upper stratosphere and mesosphere. This suggests possible impacts on the Semiannual Oscillation (SAO) (e.g. Shepherd et al., 2006), but more detailed study is required to confirm this. In the vertical (w) wind, the appearance of an equatorial upwelling is apparent, but this is likely an effect of the upper boundary of the model. It is evident therefore that this finer resolution does indeed give more features in the model fields. By adjusting the halo region and increasing the vertical damping coefficient, we are able to achieve a stable model with this finer vertical resolution.

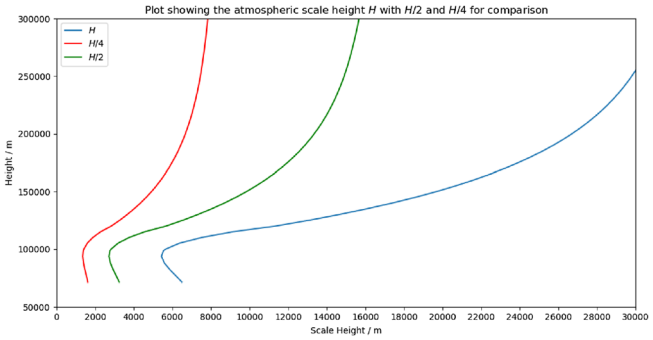

Fig. 16. Plot illustrating the scale height of the upper atmosphere H. We require multiple vertical levels per scale height and thus $H/2$ and $H/4$ are also plotted to illustrate the vertical level height necessary to have 2 and 4 vertical levels per scale height respectively.

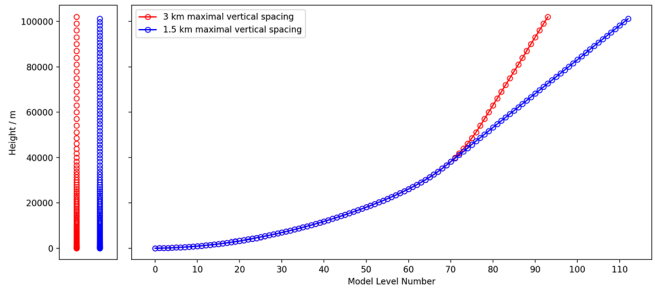

Fig. 17. Vertical level sets for the 3 km maximal vertical spacing (red) and the 1.5 km maximal vertical spacing (blue). These give approximately 2 and 4 vertical levels per scale height in the MLT respectively.

5.2 Experimentation with the height of the model upper boundary

Now that experiments with resolution have been performed, we look to extend the upper boundary of the model to greater heights to evaluate the performance of the model in preparation for its use as a whole atmosphere model. In the medium term, this will be done by coupling the extended atmospheric model

[5] The lid is placed at 102 km to avoid a change in vertical level height for the last level.

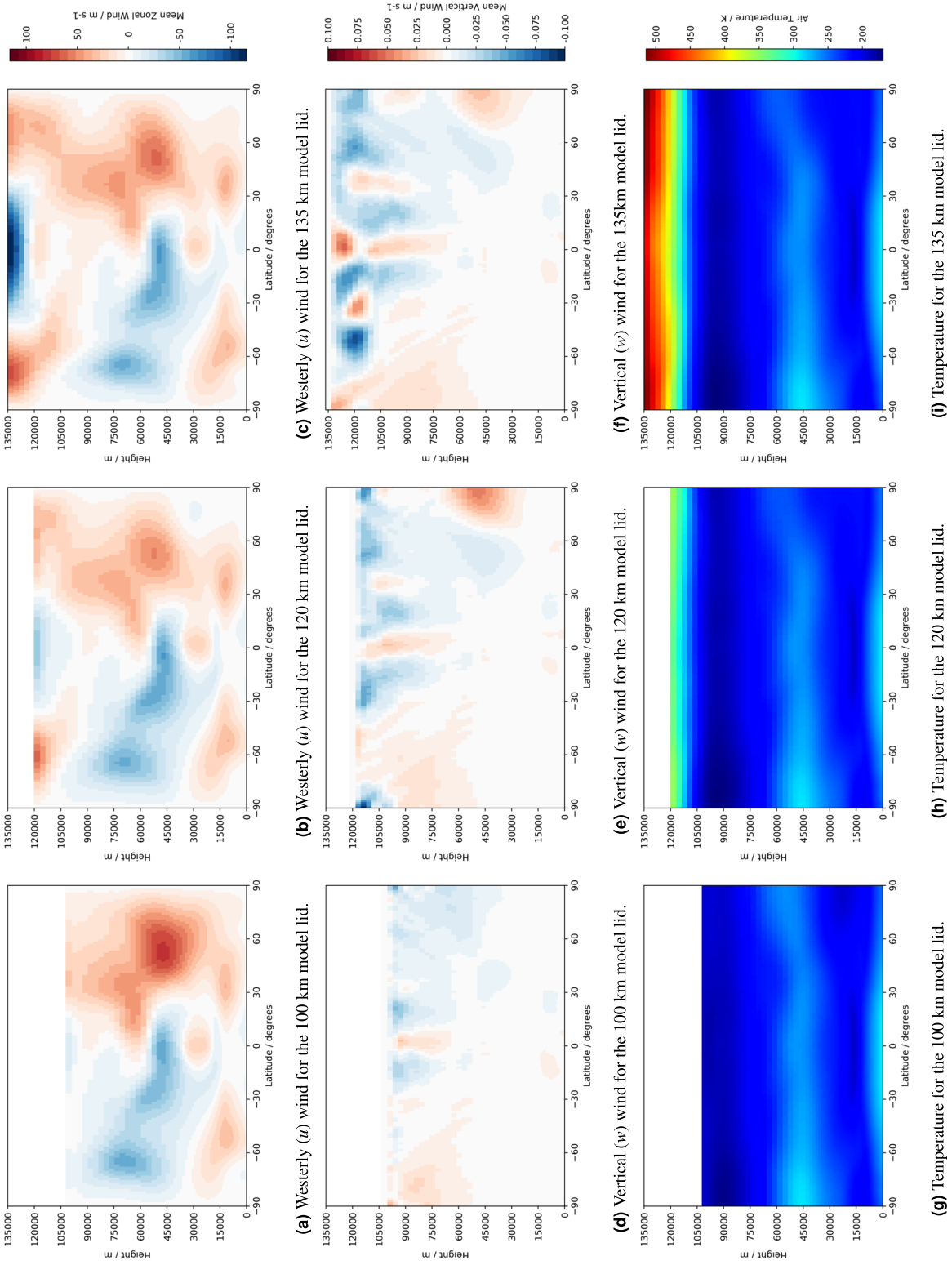

Fig. 18. Zonal mean monthly mean climatologies in December of westerly (u) wind (top), vertical (w) wind (middle) and temperature (bottom) comparing the nudged 100 km model run with the successful 120 and 135 km lid model runs.

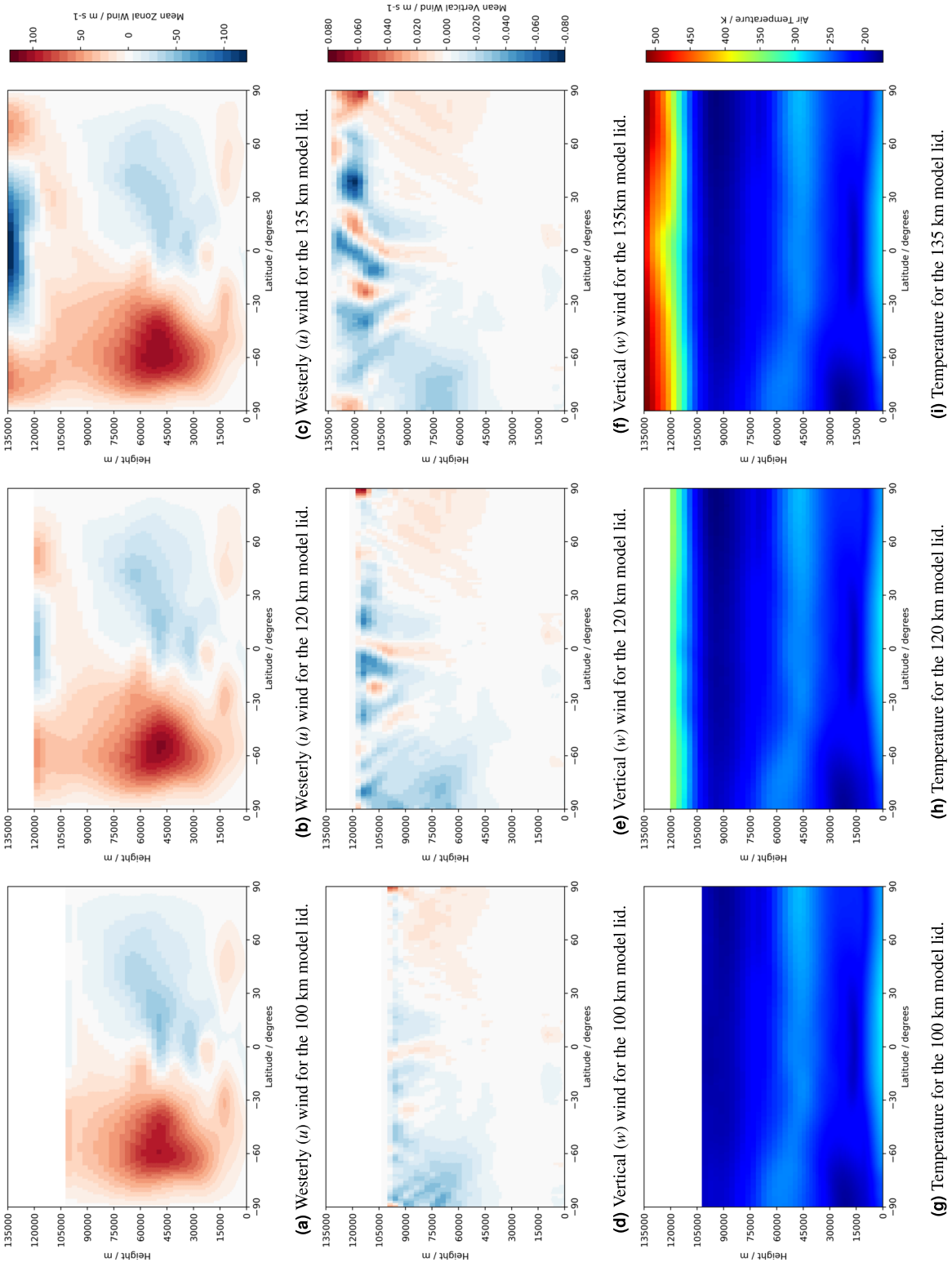

Fig. 19. Zonal mean monthly mean climatologies in June of westerly (u) wind (top), vertical (w) wind (middle) and temperature (bottom) comparing the nudged 100 km model run with the successful 120 and 135 km lid model runs.

to an appropriate thermospheric model, such as the Drag Temperature Model (DTM) developed by Bruinsma (2015), which spans the 120–1500 km range. This coupling is a goal of the Space Weather Atmosphere Models and Indices (SWAMI) project – see http://swami-h2020.eu/project-swami/. At an absolute minimum, the extended UM will therefore need to run up to 120 km. However, a merging region between the two models would be advantageous. Ideally, we would like to raise the upper boundary as high as possible to give a large merging region between the two models, however the globally uniform temperature structure in the current nudged model means it has a limited ability to represent latitudinal and longitudinal variability, which becomes more significant with increasing altitude in the lower thermosphere. Therefore we present model runs with 120 and 135 km upper boundary heights.

The 1.5 km resolution would be preferable due to its ability to resolve finer scale features in the model fields. However, on extension of the model upper boundary with this resolution, the nudged model could not be run for even short periods without becoming unstable even whilst using the stability mechanisms discussed in Section 2.2. Further additions to the model will be required to allow stable runs with this resolution at higher altitudes, such as more complete radiation and chemistry schemes.

We therefore use the 3 km resolution to extend the model upper boundary. We saw that this resolution still resolves some finer scale features as well as needing no additional stability mechanisms for the 100 km run. In fact, the 3 km resolution will give four vertical levels per scale height above around 120 km, and so this resolution is sufficient to accurately capture waves as the upper boundary is extended higher into the thermosphere.

5.2.1 120 and 135 km model lid

We now extend the 102 km, 94 level configuration to accommodate the new model lid heights.

For the 120 km lid this results in adding six more 3 km levels to give a 100 level configuration going up to exactly 120 km. For the 135 km lid this results in adding eleven more 3 km levels to give a 105 level configuration going up to exactly 135 km.

With these configurations, and the nudging implemented as in Section 4.1, the model does not initially run successfully. This is to be expected as greater wind speeds are observed at greater heights. Thus, as in the 1.5 km resolution setup, we adjust the halo region and sponge layer to combat these issues, and observe the following results:

- 120 km
  - Without the extended halo region, a stable run is achieved with $\bar{\mu} = 0.6\ \mathrm{s}^{-1}$;
  - With the extended halo region, a stable run is achieved with $\bar{\mu} = 0.2\ \mathrm{s}^{-1}$.
- 135 km
  - Without the extended halo region, a stable run cannot be achieved even when $\bar{\mu}$ is adjusted;
  - With the extended halo region, a stable run is achieved with $\bar{\mu} = 0.4\ \mathrm{s}^{-1}$.

It is evident therefore that the extended halos help considerably in preventing the model from crashing due to large instantaneous meridional wind speeds, without degrading the solution. We therefore use the extended halo runs for comparison. We compare the 3 km resolution 100 km lid climatologies presented in Section 5.1.1 (column 1) with the climatologies for both the 120 km (column 2) and 135 km (column 3) lids. Climatologies for December are shown in Figure 18 and for June in Figure 19.

With the modifications to the halo region and sponge layer we are able to achieve stable model runs with an extended upper boundary. In these figures we observe increasing variability from expected fields as the upper boundary increases; however we stress that the focus here is on attaining a stable model. This is an encouraging first step towards a whole atmosphere model, and it remains to add the physical parameterizations necessary to improve the realism of the fields at these heights.

In particular, strong unrealistic easterlies (cf. Figs. 5a and 6a of Liu et al., 2010) and vertical upwelling are evident at the equator in the upper levels of the model. These move upwards and strengthen as the upper boundary is raised. Thus, these features appear to be related to the placement of the upper boundary and as a result of the model specification rather than through realistic mechanisms. We do see the appearance of the westerly summer-time mesospheric jet at around 90 km. However, it is unclear as to whether this is realistic or also an artefact of the placement of the upper boundary.

More realistic damping mechanisms such as molecular viscosity and diffusion have been developed by Griffin & Thuburn (2018). This offers a route to model stability at higher levels which is preferable to ever stronger applications of the model sponge layer. This type of damping becomes important above around 130 km as the molecular diffusion timescale becomes shorter than the time scale for wave growth. As the UM upper boundary is raised to greater heights, it is envisaged that this will replace the current UM sponge layer detailed in Section 2.2.

It is evident therefore that the model still requires several additions before being able to produce realistic dynamics in the MLT. Consequent development of the extended UM will be able to build on the success of the nudging scheme and add the necessary physics to approach realistic simulation of the mesosphere and lower thermosphere.

6 Conclusions and future work

The Met Office's UM with an extended upper boundary of 100 km was tested and it was discovered that high wind speeds near the poles were causing the model to crash. On investigation of the radiative forcing, it was found that the LTE approximation made in the radiation scheme was leading to unphysical forcing in the MLT. This was the leading factor in causing model instabilities with an extended upper boundary.

A NLTE radiation scheme was not available at the time of performing this research. Thus, a nudging scheme was successfully implemented to replace the radiation scheme above 70 km. This scheme uses relaxation to push the temperature field from the dynamics of the model towards the prescribed temperature profile given in Figure 8. With this in place, the large winds evident from initial model runs disappeared and the extended

UM was stabilised with a 100 km upper boundary. This key result provides a valuable developmental tool to further extend the model's capabilities in the MLT.

To this end, the model vertical resolution and upper boundary height were then scrutinised. On changing the vertical resolution with a fixed 100 km lid, the use of the 3 km resolution provided a stable run with no additional changes necessary, whereas use of the 1.5 km resolution required an increase to the vertical damping coefficient and halo parameter. The model fields produced for both resolutions were in keeping with the original nudged model and additional detail was evident, particularly in the case of the 1.5 km resolution.

On extending the upper boundary however, the 1.5 km resolution made the model unstable. As commented, the 3 km resolution is in fact sufficient to provide four vertical levels per scale height above 120 km in any case, which allows vertically propagating waves to be resolved in the MLT. Thus the 3 km resolution was favoured for experiments to raise the upper boundary height. Successful, stable model runs were performed when the lid was raised to both 120 and 135 km, but an increase in the vertical damping coefficient and halo parameter was necessary. Figure 16 shows that scale height increases with altitude throughout the thermosphere, making the requirement for a 1.5 km or a 3 km vertical resolution too stringent. Future work will include experiments which use coarser vertical resolution in the thermosphere that match the increasing scale height.

Importantly, the various model configurations were all stable with the use of the nudging scheme and adjustment of the various pre-existing stability mechanisms. This is an encouraging first step towards the development of a whole atmosphere UM.

While the model showed some signs of realistic physics, the difference when compared to data was still significant. However, this is to be expected given the simplification of physics used here. In fact, the purpose of the implementation of the nudging scheme was as a developmental tool; to prove that a stable model run was possible with an extended model lid and to provide a base for further model extensions.

It is now the task to further develop the physics, chemistry and dynamics within the model to gradually replace the nudging to climatology used here. With this a more thorough comparison to data can be carried out, looking at more complex atmospheric features such as tides.

In particular, work will be carried out to introduce a NLTE radiation scheme to provide realistic heating in the model (see Jackson et al., 2020, for initial results), as well as introduce molecular viscosity and diffusion to provide a more realistic sponge layer at the upper boundary. This will make good progress into appropriately capturing realistic dynamics in the mesosphere and lower thermosphere in the Met Office's UM.

Acknowledgements. MJG and CJB are supported by a NERC GW4+ Doctoral Training Partnership studentship from the Natural Environment Research Council [NE/L002434/1] and are thankful for the collaborative support of the Met Office, UK. DJG and DRJ received funding for this work from the European Unions Horizon 2020 research and innovation programme under grant agreement No. 7776287. The editor thanks two anonymous reviewers for their assistance in evaluating this paper.

References

Akmaev RA. 2011. Whole atmosphere modeling: Connecting terrestrial and space weather. *Rev Geophys* **49(4)**: https://doi.org/10.1029/2011RG000364.

Becker Erich, Vadas Sharon L. 2018. Secondary gravity waves in the winter mesosphere: Results from a high-resolution global circulation model. *J Geophys Res Atmos* **123(5)**: 2605–2627.

Bruinsma Sean. 2015. The DTM-2013 thermosphere model. *J Space Weather Space Clim* **5**: A1.

Chamberlain JW and Hunten DM. 1987. Theory of planetary atmospheres. An introduction to their physics and chemistry. *Int Geophys Ser* **36**: 481.

COESA. 1976. *U.S. Standard Atmosphere 1976*, Vol. 40, US Government Printing Office, Washington, DC, 56 p.

Cullen MJP. 1993. The unified forecast/climate model. *Meteorol Mag* **122(1449)**: 81–94.

Davies T, Cullen MJP, Malcolm AJ, Mawson MH, Staniforth A, White AA, Wood N. 2005. A new dynamical core for the Met Office's global and regional modelling of the atmosphere. *Quart J Roy Meteor Soc: A Journal of the Atmospheric Sciences, Applied Meteorology And Physical Oceanography* **131(608)**: 1759–1782.

Edwards JM, Slingo A. 1996. Studies with a flexible new radiation code. I: Choosing a configuration for a large-scale model. *Quart J Roy Meteor Soc* **122(531)**: 689–719.

Fleming EL, Chandra S, Barnett JJ, Corney M. 1990. Zonal mean temperature, pressure, zonal wind and geopotential height as functions of latitude. *Adv Space Res* **10(12)**: 11–59.

Fomichev VI, Ogibalov VP, Beagley SR. 2004. Solar heating by the near-IR CO_2 bands in the mesosphere. *Geophys Res Lett* **31(21)**. https://doi.org/10.1029/2004GL020324.

Griffin DJ, Thuburn J. 2018. Numerical effects on vertical wave propagation in deep-atmosphere models. *Quart J Roy Meteor Soc* **144(711)**: 567–580.

Harry Gabriel. 2015. Stabilising and Validating the Met Office's Unified Model with 100 and 120 km Ceilings. *Master's thesis*. University of Bath.

Hedin AE, Biondi MA, Burnside RG, Hernandez G, Johnson RM, et al. 1991. Revised global model of thermosphere winds using satellite and ground-based observations. *J Geophys Res Space Phys* **96(A5)**: 7657–7688.

Immel TJ, Sagawa E, England SL, Henderson SB, Hagan ME, Mende SB, Frey HU, Swenson CM, Paxton LJ. 2006. Control of equatorial ionospheric morphology by atmospheric tides. *Geophys Res Lett* **33**, **(15)**. https://doi.org/10.1029/2006GL026161.

Ineson S, Scaife AA, Knight JR, Manners JC, Dunstone NJ, Gray LJ, Haigh JD. 2011. Solar forcing of winter climate variability in the Northern Hemisphere. *Nature Geosci* **4(11)**: 753.

Jackson DR, Fuller-Rowell TJ, Griffin DJ, Griffith MJ, Kelly CW, Marsh DR, Walach M-T. 2019. Future directions for whole atmo-sphere modelling: Developments in the context of space weather. *Space Weather* **17**: 1342–1350. https://doi.org/10.1029/2019SW002267

Jackson DR, Bruinsma S, Negrin S, Stolle C, Budd CJ, et al. 2020. The Space Weather Atmosphere Models and Indices (SWAMI) Project: Overview and first results. *J Space Weather Space Clim*, this issue. https://doi.org/10.1051/swsc/2020019.

Liu H-L, Foster BT, Hagan ME, McInerney JM, Maute A, et al. 2010. Thermosphere extension of the whole atmosphere community climate model. *J Geophys Res Space Phys* **115**: A12.

Marsh DR, Garcia RR, Kinnison DE, Boville BA, Sassi F, Solomon SC, Matthes K. 2007. Modeling the whole atmosphere response to solar cycle changes in radiative and geomagnetic forcing. *J Geophys Res Atmos* **112**: D23.

Morgenstern O, Braesicke P, O'Connor FM, Bushell AC, Johnson CE, Osprey SM, Pyle JA. 2009. Evaluation of the new UKCA climate-composition model – Part 1: The stratosphere. *Geosci Model Dev* **2(1)**: 43–57. https://doi.org/10.5194/gmd-2-43-2009.

O'Connor FM, Johnson CE, Morgenstern O, Abraham NL, Braesicke P, et al. 2014. Evaluation of the new UKCA climate-composition model – Part 2: The Troposphere. *Geosci Model Dev* **7(1)**: 41–91.

Päivärinta S-M, Seppälä A, Andersson ME, Verronen PT, Thölix L, Kyrölä E. 2013. Observed effects of solar proton events and sudden stratospheric warmings on odd nitrogen and ozone in the polar middle atmosphere. *J Geophys Res Atmos* **118(12)**: 6837–6848.

Rivest C, Staniforth A, Robert A. 1994. Spurious resonant response of semi-Lagrangian discretizations to orographic forcing: Diagnosis and solution. *Mon Weather Rev* **122(2)**: 366–376.

Schwartz MJ, Lambert A, Manney GL, Read WG, Livesey NJ, et al. 2008. Validation of the Aura Microwave Limb Sounder temperature and geopotential height measurements. *J Geophys Res Atmos* **113(D15)**.

Seppälä A, Randall CE, Clilverd MA, Rozanov E, Rodger CJ. 2009. Geomagnetic activity and polar surface air temperature variability. *J Geophys Res Atmos* **114**: A10.

Shepherd MG, Liu G, Shepherd GG. 2006. Mesospheric semiannual oscillation in temperature and nightglow emission. *J Atmos Sol Terr Phys* **68(3–5)**: 379–389.

Song I-S, Chun H-Y, Jee G, Kim S-Y, Kim J, Kim Y-H, Taylor MA. 2018. Dynamic initialization for whole atmospheric global modeling. *J Adv Model Earth Syst* **10(9)**: 2096–2120.

Swinbank R, Ortland DA. 2003. Compilation of wind data for the Upper Atmosphere Research Satellite (UARS) reference atmosphere project. *J Geophys Res Atmos* **108**: D19.

Tóth G, Sokolov IV, Gombosi TI, Chesney DR, Clauer CR, et al. 2005. Space Weather Modeling Framework: A new tool for the space science community. *J Geophys Res Space Phys* **110**: A12.

Telford PJ, Braesicke P, Morgenstern O, Pyle JA. 2008. Technical Note: Description and assessment of a nudged version of the new dynamics Unified Model. *Atmos Chem Phys* **8(6)**: 1701–1712.

Thuburn J, Staniforth A. 2004. Conservation and linear Rossby-mode dispersion on the spherical C grid. *Mon Weather Rev* **132(2)**: 641–653.

Walters D, Baran A, Boutle I, Brooks M, Earnshaw P, et al. 2017. The Met Office Unified Model Global Atmosphere 7.0/7.1 and JULES Global Land 7.0 configurations. *Geosci Model Dev Discuss* **2017**: 1–78.

Warner CD, McIntyre ME. 2001. An ultrasimple spectral parameterization for nonorographic gravity waves. *J Atmos Sci* **58(14)**: 1837–1857.

Waters JW, Froidevaux L, Harwood RS, Jarnot Robert F, et al. 2006. The earth observing system microwave limb sounder (EOS MLS) on the Aura satellite. *IEEE Trans Geosci Remote Sens* **44(5)**: 1075–1092.

Wood N, Staniforth A, White A, Allen T, Diamantakis M, et al. 2014. Mohamed and others. An inherently mass-conserving semi-implicit semi-Lagrangian discretization of the deep-atmosphere global non-hydrostatic equations. *Quart J Roy Meteor Soc* **140(682)**: 1505–1520.

Yue X, Schreiner WS, Pedatella NM, Kuo Y-H. 2016. Characterizing GPS radio occultation loss of lock due to ionospheric weather. *Space Weather* **14(4)**: 285–299.

Cite this article as: Griffith MJ, Jackson DR, Griffin DJ & Budd CJ 2020. Stable extension of the unified model into the mesosphere and lower thermosphere. *J. Space Weather Space Clim.* **10**, 19.

5.2. Conclusions

We present work describing the successful development of a stable extension to the Unified Model, with consequent testing with an increased vertical resolution and further increased upper boundary height.

The initial focus was on a rigorous analysis of the fields produced from the Extended Unified Model (ExUM). This revealed abnormally large wind speeds at the summer poles. Investigating further showed that this was caused by erroneous heating from the radiation scheme caused by the assumption of LTE in the MLT – an assumption which breaks down at around 65 km.

With a non-LTE radiation scheme still in development at the time of performing this research, an interim solution of relaxation to an analytic climatological temperature profile is used to give realistic atmospheric temperatures in the MLT. Adding this to the model gave a stabilised model with an upper boundary of 100 km.

Increasing the vertical resolution to 3 km in the MLT gave a run which remained stable with a 100 km lid, but which required increases to the vertical damping coefficient and model haloes for an upper boundary of both 120 km and 135 km. However, stable runs were still achieved. With a 1.5 km resolution, a stable run was achieved with a 100 km lid with increases to the vertical damping coefficient and model haloes. However, stable runs were not possible with 120 km and 135 km upper boundaries and a 1.5 km vertical resolution in the MLT.

Upon the introduction of a non-LTE radiation scheme in the model, it is reasonable to perform a first case study of the winds and atmospheric tides produced by the new ExUM to validate the model output in the MLT. The best way to do this is via a comparison to observations, and meteor radar observations are particularly robust in the MLT. In the following chapter, we perform a detailed comparison of winds and tides in the ExUM with those observed by meteor radar.

Chapter 6

Winds and Tides of the Extended Unified Model in the Mesosphere and Lower Thermosphere Validated with Meteor Radar Observations

In this chapter, we perform a first case study of the winds and tides from the newly Extended Unified Model produced in Chapter 5 and validate them with meteor radar observations in the 80-100 km region. This joint work was produced with Shaun M. Dempsey, David R. Jackson, Tracy Moffat-Griffin and Nicholas J. Mitchell and was published in *Annales Geophysicae* as an open access publication (Griffith et al., 2021).

6.1. Outline of the Article

We compare winds and tides of the Extended Unified Model with winds and tides from meteor radar observations. The ExUM used here now includes the non-LTE radiation scheme which improves the accuracy of the model in the MLT and gives a more accurate temperature distribution at the mesopause. This also produces a reversal in the wind direction in this region which was not previously seen, and this improvement makes a comparison with observations appropriate. Otherwise the model is unchanged from Chapter 5.

We use meteor radar observations of winds and tides in the region of 80-100 km over two radar stations – Rothera (68° S, 68° W) and Ascension Island (8° S, 14° W). These locations are chosen to study tides in two very different tidal regimes – the equatorial regime, where the diurnal (24 hour) tide dominates, and the polar regime, where the semi-diurnal (12 hour) tide dominates. The availability of radar data at both sites means that 2006 is the year chosen for the study.

The data from both the model and observations then undergo the same treatment. For both, we have hourly-sampled time profiles for both the zonal and meridional wind fields for the whole of the year considered. From these model fields we first compute background wind fields for each month by meaning over all values within a month. As well as this, we compute composite days for each month. The composite day is a representation of an average day over the course of a given month. Each one is an average for each hour of the day over the course of the month, at each height in the 80-100 km range, and with the monthly mean background winds removed. With this composite day, the atmospheric tidal amplitudes and phases are then calculated for each month by fitting a sinusoidal function with diurnal and semi-diurnal frequency to this composite day using a curve fitting algorithm, i.e., we fit a function of the form

$$f(x) = A\sin(2\pi x/24) + B\sin(2\pi x/24),$$

for the diurnal tide, and a function of the form

$$f(x) = A\sin(2\pi x/12) + B\sin(2\pi x/12),$$

for the semi-diurnal tide. The value of $\sqrt{A^2 + B^2}$ then gives the wave's amplitude. The tidal phases can also then be calculated using $\tan^{-1}(B/A)$ and give the Local

Time at which the tide first reached its maximum value for a particular component.

These values for wind and tidal properties are then compared with observations to form the results section of the work, where the differences and similarities seen are described. We observe notable discrepancies in the background winds in the polar regime, with the winds in the ExUM austral summer stronger than observed, and in austral winter the winds are in the wrong direction – they are westward rather than eastward. In the equatorial regime, several key characteristics such as the semiannual variation are reproduced, but there remain significant differences in the detail. The tidal amplitudes and phases are generally in good agreement with those observed at both locations and for both components. Many key qualitative features are reproduced such as the large diurnal and small semi-diurnal amplitudes in the equatorial regime; and the large semi-diurnal and small diurnal amplitudes in the polar regime.

In Section 4, these similarities and differences are discussed. In particular, we focus on the incorrect wind direction seen in the austral winter in the polar regime. The study of Becker and Vadas (2018) showed that the in situ generation of non-primary gravity waves is key to obtaining eastward mean winds in this region through the breaking of large amplitude gravity waves with significant eastward momentum fluxes. The ExUM, in common with nearly all GCMs, does not include these gravity wave sources. To analyse the USSP further, we perform a run with this scheme removed which corrects the wind direction in austral winter, but leads to incorrect winds in austral summer.

Appendix 6B: Statement of Authorship

This declaration concerns the article entitled:			
Winds and Tides of the Extended Unified Model in the Mesosphere and Lower Thermosphere Validated with Meteor Radar Observations			
Publication status (tick one) **Draft manuscript** ☐ **Submitted** ☐ **In review** ☐ **Accepted** ☐ **Published** ☒			
Publication details (reference)	Journal: Annales Geophysicae Authors: Matthew J. Griffith, Shaun M. Dempsey, David R. Jackson, Tracy Moffat-Griffin, Nicholas J. Mitchell		
Copyright status (tick the appropriate statement) I hold the copyright for this material ☒ Copyright is retained by the publisher, but I have been given permission to replicate the material here ☐			
Candidate's contribution to the paper (provide details, and also indicate as a percentage)	The bulk of the work for this article was performed by the author of the thesis (80%). The formulation of ideas and design of methodology was performed primarily by Nicholas J. Mitchell and the author of this thesis (50%) The radar observations were obtained by Tracy Moffat-Griffin and Nicholas J. Mitchell.The post-processing of this data was performed by Shaun M. Dempsey. The bulk of the presentation of the content was performed by the author of the thesis (90%). The author's contribution in particular was in performing the model runs for comparison with meteor radar data; performing the tidal analysis on the model and radar data; preparation of all figures; and leading the authoring of the manuscript with some contribution from all authors, in particular Nick Mitchell.		
Statement from Candidate	This paper reports on original research I conducted during the period of my Higher Degree by Research candidature.		
Signed	Matthew J. GRIFFITH	**Date**	06/08/2021

Last update: Feb 2019

Ann. Geophys., 39, 487–514, 2021
https://doi.org/10.5194/angeo-39-487-2021

Annales Geophysicae
Open Access
EGU

Winds and tides of the Extended Unified Model in the mesosphere and lower thermosphere validated with meteor radar observations

Matthew J. Griffith[1], Shaun M. Dempsey[2], David R. Jackson[3], Tracy Moffat-Griffin[4], and Nicholas J. Mitchell[2,4]

[1]Department of Mathematical Sciences, University of Bath, Claverton Down, Bath, BA2 7AY, UK
[2]Department of Electronic & Electrical Engineering, University of Bath, Claverton Down, Bath, BA2 7AY, UK
[3]Met Office, Fitzroy Rd, Exeter, EX1 3PB, UK
[4]British Antarctic Survey, High Cross, Madingley Rd, Cambridge, CB3 0ET, UK

Correspondence: Matthew J. Griffith (mjg41@bath.ac.uk)

Received: 15 January 2021 – Discussion started: 29 January 2021
Revised: 11 April 2021 – Accepted: 10 May 2021 – Published: 10 June 2021

Abstract. The mesosphere and lower thermosphere (MLT) is a critical region that must be accurately reproduced in general circulation models (GCMs) that aim to include the coupling between the lower and middle atmosphere and the thermosphere. An accurate representation of the MLT is thus important for improved climate modelling and the development of a whole atmosphere model. This is because the atmospheric waves at these heights are particularly large, and so the energy and momentum they carry is an important driver of climatological phenomena through the whole atmosphere, affecting terrestrial and space weather. The Extended Unified Model (ExUM) is the recently developed version of the Met Office's Unified Model which has been extended to model the MLT. The capability of the ExUM to model atmospheric winds and tides in the MLT is currently unknown. Here, we present the first study of winds and tides from the ExUM. We make a comparison against meteor radar observations of winds and tides from 2006 between 80 and 100 km over two radar stations – Rothera (68° S, 68° W) and Ascension Island (8° S, 14° W). These locations are chosen to study tides in two very different tidal regimes – the equatorial regime, where the diurnal (24 h) tide dominates, and the polar regime, where the semi-diurnal (12 h) tide dominates. The results of this study illustrate that the ExUM is capable of reproducing atmospheric winds and tides that capture many of the key characteristics seen in meteor radar observations, such as zonal and meridional wind maxima and minima, the increase in tidal amplitude with increasing height, and the decrease in tidal phase with increasing height. In particular, in the equatorial regime some essential characteristics of the background winds, tidal amplitudes and tidal phases are well captured but with significant differences in detail. In the polar regime, the difference is more pronounced. The ExUM zonal background winds in austral winter are primarily westward rather than eastward, and in austral summer they are larger than observed above 90 km. The ExUM tidal amplitudes here are in general consistent with observed values, but they are also larger than observed values above 90 km in austral summer. The tidal phases are generally well replicated in this regime. We propose that the bias in background winds in the polar regime is a consequence of the lack of in situ gravity wave generation to generate eastward fluxes in the MLT. The results of this study indicate that the ExUM has a good natural capability for modelling atmospheric winds and tides in the MLT but that there is room for improvement in the model physics in this region. This highlights the need for modifications to the physical parameterization schemes used in the model in this region – such as the non-orographic spectral gravity wave scheme – to improve aspects such as polar circulation. To this end, we make specific recommendations of changes that can be implemented to improve the accuracy of the ExUM in the MLT.

Published by Copernicus Publications on behalf of the European Geosciences Union.

1 Introduction

Atmospheric solar tides are global-scale oscillations of the atmosphere. They are primarily forced by solar heating of water vapour and ozone in the troposphere and stratosphere, by the release of latent heat in deep tropospheric convection or by planetary-scale non-linear interactions. The tides can ascend to the mesosphere and lower thermosphere (MLT) where they reach very large amplitudes and often dominate the motion field. Observations have revealed that the largest-amplitude tidal modes in the MLT are the 12 h semi-diurnal and 24 h diurnal tides. Tides of higher frequency are usually of much smaller amplitudes. Generally, the semi-diurnal tide maximizes at high latitudes, whereas the diurnal tide maximizes at low latitudes (Mitchell et al., 2002; Davis et al., 2013).

The tides can have significant fluxes of energy and momentum and so play a critical role in coupling the lower atmosphere and the thermosphere–ionosphere system. For example, tidal winds act to filter the field of atmospheric gravity waves (GWs), modulating the gravity wave momentum fluxes and the consequent forcing of the global atmospheric circulation (e.g. Fritts and Alexander, 2003). The temperature tides are believed to be an important source of the variability of polar mesospheric clouds, because tidal perturbations of temperature modulate the cloud ice crystal population (e.g. Fiedler et al., 2005). Tidal signatures propagate upwards from the MLT into the thermosphere, where the divergence of tidal momentum and heat fluxes can drive zonal wind changes of more than $30\,\mathrm{m\,s^{-1}}$ in the lower thermosphere and influence the transport of chemical species (e.g. Jones et al., 2014). Tides are also generated in situ in the thermosphere from the dissipation of GWs caused by deep convection, primarily in the Intertropical Convergence Zone (ITCZ) (Vadas et al., 2014). These thermospheric tides cause perturbations of neutral and plasma densities in the E- and F-regions of the ionosphere and so modulate the ionospheric wind dynamo (e.g. Oberheide et al., 2009; Yiğit and Medvedev, 2015; Liu, 2016). They can also change the total electron content (TEC) distributions, with the consequence of potentially modifying the conditions for seeding of equatorial plasma bubbles in the F-region. The significant zonal wavenumber-four structure in the equatorial ionosphere is thought to arise from the modulation of the E-region winds by a non-migrating diurnal tide (e.g. England et al., 2006).

The tides include both migrating and non-migrating modes. The migrating modes are sun-synchronous, propagate westwards, have zonal wavenumbers equal to the number of cycles of the tide per day and are directly excited by the insolation of solar radiation. In contrast, the non-migrating modes are not sun-synchronous, can propagate both eastwards or westwards, and have zonal wavenumbers not equal to the number of cycles of the tide per day. The non-migrating modes can be excited by strong non-linear interaction between migrating tides and planetary waves that generate so-called "secondary waves", including the non-migrating tidal modes (e.g. Teitelbaum and Vial, 1991; Beard et al., 1999; Palo et al., 2007; Pancheva et al., 2002). The tides and waves of the MLT consequently form a strongly coupled system, and at any point in the atmosphere the tides are a superposition of both migrating and non-migrating modes.

A striking feature of atmospheric tides is their variability on a wide range of timescales. For instance, tidal amplitudes and phases have been observed to have a strong seasonal variability (e.g. Mitchell et al., 2002; Davis et al., 2013). This has been proposed to result from phenomena including wave–mean-flow interactions and/or source variations and refraction/reflection (e.g. McLandress, 2002; Riggin et al., 2003; Riggin and Lieberman, 2013). Intra-seasonal variability is also observed. For example, variability of Arctic semi-diurnal tides has been shown to be well correlated with the amplitude of planetary wavenumber 1 at Antarctic latitudes, indicating significant inter-hemispheric coupling (Smith et al., 2007). At inter-annual timescales, tidal amplitudes and phases have been observed to vary in response to solar variability, the El Niño Southern Oscillation, sudden stratospheric warmings, the tropical Madden–Julian oscillation and the stratospheric quasi-biennial oscillation (QBO) (e.g. Christiansen et al., 2016).

At timescales of less than 30 d, the tides are observed to exhibit great variability, and amplitudes are frequently observed to fluctuate from day to day by up to about 300 % (e.g. Dempsey et al., 2021; Vitharana et al., 2019). This "tidal weather" has been proposed to have causes that include (i) variations in the background winds through which the tides must propagate, (ii) variations in tidal forcing resulting from solar variability and/or fluctuations in the distribution of water vapour and stratospheric ozone (e.g. Pancheva and Mitchell, 2004; Lieberman et al., 2004), and (iii) non-linear interactions with planetary waves that generate secondary waves that then beat with the primary tide, modulating its amplitude (e.g. Teitelbaum and Vial, 1991; Beard et al., 1999; Palo et al., 2007).

There is now considerable scientific interest in developing so-called "high-top" general circulation models (GCMs) that span the lower, middle and upper atmosphere, capturing vertical coupling processes via internal waves such as gravity waves and tides (e.g. Yiğit et al., 2016). These models are an important element in attempts to develop operational space-weather forecasting able to include the contributions to the variability of the thermosphere and ionosphere, as well as in the development of whole atmosphere models (e.g. Jackson et al., 2019; Liu, 2016; Akmaev, 2011). We summarize some of the recent key non-mechanistic high-top GCMs below:

1. The Whole Atmosphere Model (WAM; Akmaev et al., 2008; Fuller-Rowell et al., 2008) is an extended version of the U.S. National Weather Service Numerical Weather Prediction model, spanning the surface to

around 600 km. Focusing on the neutral atmosphere, WAM is able to represent well the mean state and tides in the thermosphere (e.g. Lieberman et al., 2013, show good agreement with diurnal and time mean Challenging Mini Satellite Payload winds).

2. The Whole Atmosphere Community Climate Model with thermosphere and ionosphere extension (WACCM-X; Liu et al., 2010, 2018a) is an extended version of the National Center for Atmospheric Research's WACCM, which itself can run up to 145 km (e.g. Garcia et al., 2007). It has a similar altitude range to WAM. Liu et al. (2018a) show that in WACCM-X the amplitudes and seasonal variations of atmospheric tides in the MLT are in good agreement with observations.

3. The extended Canadian Middle Atmosphere Model (eCMAM; Beagley et al., 2000) is an extended version of the standard CMAM with an upper boundary at a pressure level of 2×10^{-7} hPa. eCMAM was developed to examine the nature of the physics and dynamical processes in the MLT without the artificial effects of a sponge layer, which can have the unfortunate effect of modifying the circulation in the model in an unrealistic fashion (Fomichev et al., 2002). Dempsey et al. (2021) show that eCMAM generally reproduces observed diurnal tidal amplitudes in the polar regime well, and Davis et al. (2013) show that eCMAM is generally good in the equatorial regime with a trend of overestimating meridional amplitudes.

4. The Ground-to-topside model of the Atmosphere and Ionosphere for Aeronomy (GAIA; Fujiwara and Miyoshi, 2010; Jin et al., 2012, and references therein) combines three independent models: a whole atmosphere GCM, an ionosphere model and an electrodynamics model. GAIA also has a similar altitude range to WAM. Jin et al. (2012) show the ability of GAIA to model the impact of a sudden stratospheric warming (SSW) on migrating tides and the associated ionospheric response, with in general good agreement shown with Sounding of the Atmosphere using Broadband Emission and Constellation Observing System for Meteorology, Ionosphere, and Climate observations.

5. The Hamburg Model of the Neutral and Ionized Atmosphere (HAMMONIA; Schmidt et al., 2006; Meraner and Schmidt, 2016) is an extended version of MAECHAM5 (Giorgetta et al., 2006; Manzini et al., 2006), taking the upper boundary to approximately 250 km. The extended model includes important radiative and dynamical processes of the upper atmosphere and is coupled to a chemistry module containing 48 compounds.

6. The upper-atmosphere extension of ICON (Borchert et al., 2019) extends the standard ICON model so that model upper boundaries can be placed in the lower thermosphere. This includes a switch over to deep-atmosphere dynamics, as well as an implementation of an upper-atmosphere physics package based on that implemented by Schmidt et al. (2006) in HAMMONIA.

7. The Entire Atmosphere Global Model (EAGLE; Klimenko et al., 2019) combines the HAMMONIA neutral atmosphere model with the Global Self-consistent Model of the Thermosphere, Ionosphere, Protonosphere (GSM TIP) (Bessarab et al., 2012; Korenkov et al., 2012). The model includes radiative heating due to absorption of extreme solar UV, non-LTE (local thermodynamic equilibrium) treatment of the radiative cooling, molecular diffusion, ion drag, and simplified ion chemistry with which to treat the impact of precipitating energetic particles. Klimenko et al. (2019) show that the model successfully reproduces neutral temperature and total electron content (TEC) observations.

8. The HI Altitude Mechanistic General Circulation Model (HIAMCM; Becker and Vadas, 2020) is an extension of the high-resolution Kühlungsborn Mechanistic general Circulation Model (KMCM) extended to around 450 km. The model includes simplified but nevertheless explicit representations of the relevant components of an atmospheric climate model, and it is labelled "mechanistic" due its use of some idealized methods and the lack of a chemistry scheme. It is a high-resolution gravity-wave-resolving model, resolving horizontal wavelengths down to 165 km. Becker and Vadas (2020) showed that this GCM is unique in reproducing the travelling atmospheric disturbance (TAD) hotspot observed over the wintertime Southern Andes (e.g. Park et al., 2014; Trinh et al., 2018).

9. The Coupled Middle Atmosphere Thermosphere-2 (CMAT-2; Yiğit et al., 2009) GCM is an extension of the three-dimensional Coupled Thermosphere-Ionosphere-Plasmasphere model (CTIP; Millward et al., 1996) to an upper boundary of 300–500 km, depending on the solar activity. It uses a non-linear spectral GW parameterization of Yiğit et al. (2008) to study the propagation of a broad spectrum of GWs from the lower atmosphere to the thermosphere. Yiğit et al. (2021) found that accounting for latitudinal variations in the GW source appreciably improves simulations.

10. The University of Leipzig Middle and Upper Atmosphere Model (MUAM; Pogoreltsev, 2007; Pogoreltsev et al., 2007; Suvorova and Pogoreltsev, 2011) extends from the lower atmosphere up to 160 km. In a recent study by Lilienthal et al. (2020) with this GCM on the interaction of GW and terdiurnal tides they found

a strong dependence of tidal amplitude on the induced GW drag, generally being larger when GW drag is increased, whilst the overall strength of the GW source level momentum flux had a relatively small impact on the zonal mean climatology.

11. The whole atmosphere Kyushu GCM (Miyoshi and Fujiwara, 2008; Miyoshi and Yiğit, 2019) extends the pre-existing Kyushu GCM (Miyahara et al., 1993) up to 450 km. Miyoshi and Yiğit (2019) found that GW drag in the thermosphere significantly decelerates the mean zonal wind and plays an important role in the momentum budget, making a GW parameterization accounting for thermospheric processes essential for a coarse-grid whole atmosphere GCM.

In the context of these existing models, the Extended Unified Model (ExUM; Griffith et al., 2020) described in Sect. 2.1 extends the standard UM (Unified Model) (Walters et al., 2019) to the lower thermosphere. It is a model which does not make the hydrostatic assumption and uses the deep-atmosphere equations of motion making it particularly suitable for modelling atmospheric tides. As well as this, a non-LTE radiation scheme has been added so that the radiation scheme is physically appropriate up to 90 km (see Jackson et al., 2020), and after this the temperature is nudged towards an analytical profile – see Sect. 2.1 or Griffith et al. (2020) for more details.

Throughout these models and studies, tides have an important role in coupling the lower and upper atmosphere and it is important that tides are accurately represented. However, it is widely recognized that tides in the MLT remain challenging to model (e.g. Baldwin et al., 2019). In particular, model biases remain in both the seasonal variability of tides and their short-term variability at timescales of less than a month (e.g. Dempsey et al., 2021).

As well as tides, it is important that the deposition of momentum by subgrid-scale non-orographic GWs is also accurately represented in models through parameterization, due to their appreciable impact on atmospheric flow and tides in the MLT (e.g. Yiğit and Medvedev, 2017; Yiğit et al., 2009; Miyahara and Forbes, 1991). Yiğit and Medvedev (2017) discuss extensively the influence of parameterized small-scale GWs on the migrating diurnal tide. They show that GWs play an important role for the diurnal tide in the MLT region. They found that the GW effects on the thermal tide can be appropriately captured in a coarse-grid GCM provided that a GW parameterization, (i) considers a broad spectrum of harmonics, (ii) properly describes their propagation, and (iii) correctly accounts for the physics of wave breaking/saturation. Yiğit et al. (2021) suggest that smaller-than-measured GW fluxes have to be used at the source level in the lower atmosphere in order to reproduce the observed circulation in the middle atmosphere.

In this study, we test the ability of the ExUM to model diurnal and semi-diurnal tides by comparing the seasonal variation of these tides in the model to observations of zonal and meridional winds made in the mesosphere and lower thermosphere by two meteor radars. The two radars are at very different latitudes: one at the polar Antarctic site of Rothera (68° S, 68° W) and the other at Ascension Island (8° S, 14° W) in the equatorial Atlantic Ocean. The Rothera radar samples a latitude where the semi-diurnal tide is known to reach very large amplitudes but where the diurnal tide is small. In contrast, the Ascension Island radar samples a region where the diurnal tide is known to reach large amplitudes but the semi-diurnal tide is small. We use measurements of winds, tidal amplitudes, tidal phases and their seasonal variability as tests of the model's ability to accurately represent these tides.

The meteor radars are particularly well suited for this task, because they can make continuous reliable measurements at the heights of 80–100 km where the tidal modes reach large amplitude but where other ground-based radar measurement techniques, such as MF radar, may be subject to significant biases (e.g. Wilhelm et al., 2017). In fact, a recent study by Stober et al. (2021) examined the mean winds, diurnal and semi-diurnal tidal amplitudes and phases, and their associated momentum fluxes obtained from meteor radar data at six Southern Hemisphere locations (midlatitude to polar). They found that the results agreed reasonably well with Becker and Vadas (2018), thereby pointing to secondary GWs and vertical coupling as a mechanism by which GWs transfer energy and momentum to higher altitudes under wintertime conditions.

This study is organized as follows. In Sect. 2 we describe the development of the ExUM version used in this study and the meteor radar observations used to provide the observational "ground truth". In Sect. 3 we present the seasonal variability of background winds and diurnal and semi-diurnal tides in the ExUM and in observations, highlighting areas of agreement and disagreement. Finally, in Sects. 4 and 5 we place our results in the context of other tidal studies and consider how they can guide future development of the ExUM.

2 Model development and meteor radar observations

2.1 The Extended Unified Model

The Met Office's Unified Model (UM) is a GCM modelling the weather and climate of the atmosphere. It is split into two main sections: the first contains the *dynamical core*, which describes atmospheric dynamics by numerically solving the Euler equations of motion governing atmospheric flow, and the second is made up of *physical parameterizations*, which attempt to describe parts of atmospheric physics not captured by the governing equations, such as solar radiation and subgrid-scale GWs (see e.g. Walters et al., 2019, for an idea on the formulation of the Unified Model).

The current dynamical core (ENDGame; Wood et al., 2014) solves the non-hydrostatic, fully compressible deep-atmosphere equations of motion on a rotating sphere using a semi-implicit semi-Lagrangian formulation. The primary prognostic variables used are the three-dimensional wind components, virtual dry potential temperature[1], Exner function of pressure[2] and dry density, whilst moisture prognostics are advected as free tracers. The discretized equations are solved using an iterative implicit method – more details of which can also be found in Wood et al. (2014).

For the purposes of this case study, the horizontal resolution is fixed at 1.25° N × 1.875° E – or the so-called N96 resolution.[3]

The vertical resolution is extended from the 85-level 85 km configuration of the standard UM using the model implementation of Griffith et al. (2020). This gives the aforementioned ExUM which builds on the standard model to extend the working height of the UM into the lower thermosphere. The work makes it possible for the Unified Model to run in a stable manner with an upper boundary at 100, 120 and 135 km, with promising initial results.

Griffith et al. (2020) investigated the cause of an instability in the previously unstable ExUM. Through a thorough and systematic diagnostic evaluation of both the dynamical core and physical parameterizations used in the model, the root cause of the instability was identified – the radiation scheme. The assumption of local thermodynamic equilibrium (LTE[4]) used in the model is no longer valid on extension of the upper boundary of the model. To enable further testing without the need to completely re-engineer the existing radiation scheme – a significant undertaking – an interim solution of relaxation or nudging of the temperature field to climatological values was used. This scheme was engineered in Griffith et al. (2020), and more details can be found therein. With this addition, a stable ExUM implementation was successfully achieved with upper boundary heights of 100, 120 and 135 km. The 120 and 135 km implementations did, however, require additional stability modifications such as an increase in the value of the vertical damping coefficient. The primary impact of the damping coefficient is to reduce the magnitude of instantaneous vertical velocities approaching the upper boundary which can lead to model instabilities. The damping coefficient is therefore chosen as the minimal value so that the model can run in a stable manner (for more details on the specifics of the vertical damping used and the implementations for the 120 and 135 km upper boundary please see Griffith et al. (2020) – in particular, Sect. 2.2, Fig. 1 and Sect. 5.2 therein). Also, the nudging temperature profile used is globally uniform, and so the latitudinal variation in temperature was difficult to attain – for example, the summertime polar mesopause minimum was present but not realistically captured. However, in this initial research the focus was to produce a stable extension of the UM rather than to focus on precisely capturing realistic climatology. Thus, for this stability analysis, a simple and approximate climatological nudging temperature profile was used, which successfully showed that the model could run in a stable manner into the mesosphere and lower thermosphere (MLT).

Following this research, the radiation scheme was extended to include non-LTE effects and the model temperature now contains the appropriate realistic forcing up to around 90 km. This work is detailed by Jackson et al. (2020). The improvement to the summertime polar mesopause minimum and consequent improvement in the wind fields can be seen in Fig. 1.

Above around 90 km, the lack of appropriate high atmosphere chemistry and consequent heating via exothermic reactions means that the temperature profile cannot be assumed to be accurate. Given this lack of appropriate chemistry, the relaxation or nudging scheme must still be used above 90 km and is in place for our simulation. This pushes the model temperature towards a globally uniform temperature field, which can be seen for this region in Fig. 2.

In summary, this results in an ExUM which differs from the standard General Atmosphere (GA) 7.0 configuration of the UM (as described in Walters et al., 2019) in the following ways:

1. The model chemistry scheme is entirely switched off – the development of a chemistry scheme appropriate for the MLT is currently a work in progress.
2. Atmospheric aerosols are switched off and ozone background files are switched on.
3. The model upper boundary is raised from the standard 85 km to a height of 100 km.
4. The forcing from the radiation scheme now includes non-LTE effects, which means it is physically realistic up to 90 km.
5. The temperature field above 90 km is nudged towards the prescribed climatological temperature profile – this accounts for the lack of the chemistry scheme.

With this, the model is now sufficiently mature to ask the following question. Are the wind fields produced by the new

[1]The potential temperature θ is the temperature that an unsaturated parcel of dry air would have if brought adiabatically and reversibly from its initial state to a standard pressure, p_0, typically 1000 hPa. The virtual dry potential temperature is then the theoretical potential temperature of dry air that would have the same density as moist air.

[2]The Exner function Π can be viewed as non-dimensionalized pressure and has the useful relationship that the absolute temperature $T = \theta\Pi$.

[3]The integer N represents the maximum number of zonal 2 grid-point waves that can be represented – thus N96 can represent 96 such waves.

[4]The condition under which matter emits radiation based on its intrinsic properties and its temperature, uninfluenced by the magnitude of any incident radiation.

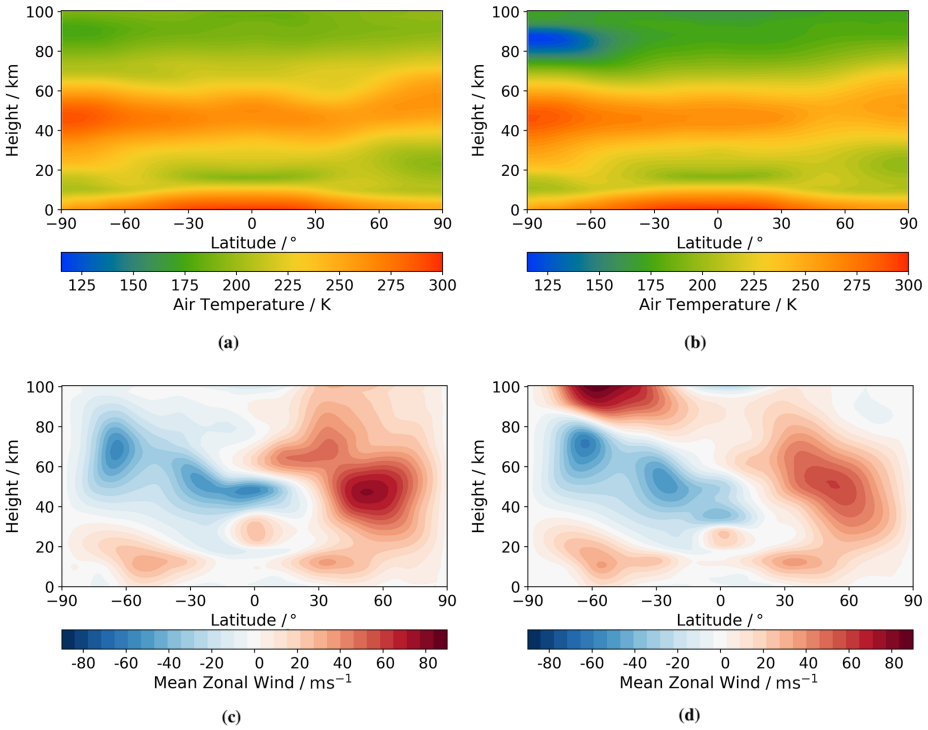

Figure 1. Latitude–height zonal-mean monthly-mean climatologies in December comparing **(a)** ExUM temperature before with **(b)** ExUM temperature after the non-LTE implementation. Also compared is **(c)** ExUM zonal (u) wind before with **(d)** ExUM zonal (u) wind after the non-LTE implementation. The more accurate modelling of the summertime polar mesopause minimum is evident upon introduction of the non-LTE radiation scheme with consequent effect on the modelled winds in the MLT.

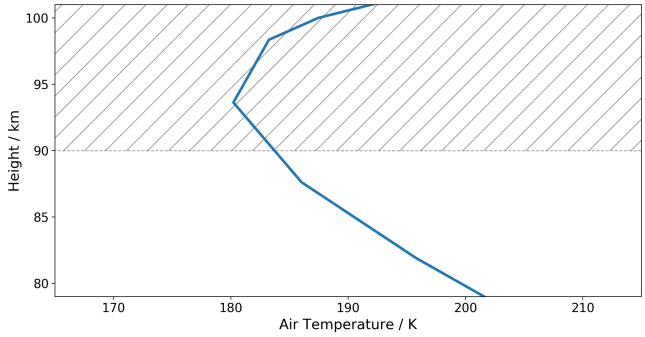

Figure 2. Nudging temperature profile over the region of interest sampled on model levels (80–100 km). Shading indicates the height above which this nudging profile is used in the ExUM model run.

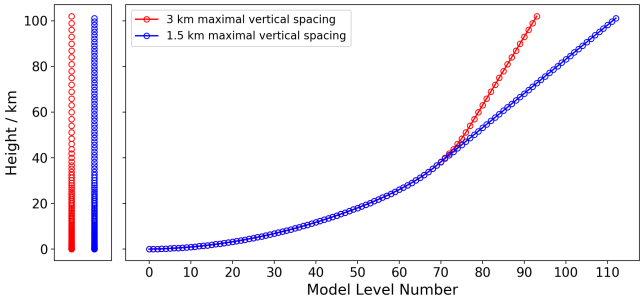

Figure 3. Vertical level sets for the 3 km maximal vertical spacing (red) and the 1.5 km maximal vertical spacing (blue).

ExUM physically realistic in the mesosphere and lower thermosphere? In this research, we answer this question by performing an initial case study comparing ExUM wind fields and tides to corresponding fields from meteor radar observations.

To begin this case study, we use the work of Griffith et al. (2020) to educate the choice of vertical resolution. The possibilities for a 100 km model upper boundary are the 94-level and 113-level configurations. These are based on the assumption of having a maximum vertical level depth of 3 and 1.5 km, respectively. These depths are based on the atmospheric scale height $H = RT/g$ and give two and four vertical model levels per scale height, respectively. These level sets can be seen in Fig. 3.

The 94-level configuration requires no changes to the model's vertical damping coefficient (see Griffith et al., 2020, for more details on the vertical damping coefficient), whereas the 113-level configuration requires a 6-fold increase in the vertical damping coefficient used – which can have the undesirable effect of modifying the general circulation in an unrealistic manner (e.g. Fomichev et al., 2002). As well as this, over the two chosen radar locations, the vertical wavelength

is typically around 20 km in the MLT (e.g. Davis et al. (2013) Table 1 for Ascension Island and Dempsey et al. (2021) Table 1 for Rothera). The resolution of the radar observations is also 3 km in the vertical, and this is the resolution used in the MLT in other models such as WACCM and eCMAM (described previously).

Therefore, the 94-level configuration is chosen for this study, which has a 3 km vertical resolution in the MLT. It avoids the use of the larger value for the vertical damping coefficient, matches up well with the resolution of the meteor radar observations as well as appropriately resolving wave scales for both radar locations.

Given the above choice of resolution, a choice of start date is required. This is guided by the availability of radar observations and this is discussed in Sect. 2.2 – with 2006 being the year chosen.

The model runs are then all initialized using the same operational analysis from 1 September 2005 at 00:00 UTC. This allows the model to settle after the initialization – known as the spin-up period of the model. Following this, climatological data (rather than year-dependent data) are used to force background fields such as atmospheric ozone. This choice was made primarily due to the unavailability of year-dependent forcing for the recently developed ExUM (such as that used in more developed models like WACCM-X e.g. Liu et al., 2018b). The primary focus of this work is to provide a first-look at the atmospheric tides present in the model, and we perform a first comparison of those tides with observations in order to justify that the core dynamics and physics of the model is sound. Differences seen here can then be used to educate future development.

The output attained from the model consists of hourly-sampled time profiles for both zonal and meridional wind fields for the whole of the model year considered – this high cadence is used so that diurnal and semi-diurnal frequencies can be accurately resolved. For simplicity, we only show results for a single simulation, but multiple simulations were performed to verify these results leading to the same conclusions. From these model fields, we compute monthly-mean background wind fields and composite days for each month. Each composite day gives an average for each hour of the day over the course of the month at each height in the 80–100 km range being considered. The atmospheric tidal amplitudes and phases are then calculated for each month by fitting a sinusoidal function to this composite day using a curve-fitting algorithm.

2.2 The meteor radars

We will compare the ExUM winds and tides to those measured by meteor radars. Meteor radars are well suited for wind and tidal studies because they can make continuous, reliable measurements of zonal and meridional winds at the heights of 80–100 km where tidal amplitudes reach large values (e.g. Dempsey et al., 2021). In this particular case, we consider observations made by two commercially produced all-sky "SKiYMET" radars. One such radar is sited at Rothera (68° S, 68° W) in the Antarctic, a latitude where we expect the semi-diurnal tide to dominate. The other is sited on Ascension Island (8° S, 14° W) in the equatorial Atlantic, a latitude where we expect the diurnal tide to dominate. The two radars both use the commercially produced all-sky SKiYMET system making their measurements directly comparable. A description of the SKiYMET radar can be found in Hocking et al. (2001). The availability of radar observations for both sites is shown in Fig. 4.

From this, it can be seen that the radars were simultaneously operational with the fewest interruptions throughout 2006, and so we use data from that year in our analysis.

The time series of winds recorded by the radars were analysed to determine tidal amplitudes and phases for the diurnal and semi-diurnal tides. The method employed is essentially a standard least-squares fitting method common in tidal analysis. The particular implementation used here is that described by Dempsey et al. (2021). In this, for each month a composite day of zonal and meridional hourly winds was constructed. A least-squares fit of sinusoidal oscillations with periods of 24, 12, 8 and 6 h, corresponding to the tides, was then made for each month and each component at each height. The result of this analysis is a monthly vector mean estimate of the amplitude and phase of each tide at heights from 79–101 km in both the zonal and meridional components (we will not consider the 8 and 6 h tides further in this study). These observed tides can then be compared to those predicted by the ExUM for the two sites.

3 Results

In this section, we present the ExUM winds and tides for the latitudes of Rothera and Ascension Island and compare them to the observations made by the two radars. We begin by presenting, in Fig. 5, examples of the ExUM zonal and meridional hourly winds for April 2006. These wind fields are typical of those produced in the MLT by the model and are shown to illustrate the general features of the model results. The figure presents winds for the locations of both Ascension Island and Rothera.

The figure reveals wind fields dominated by tidal modes of large amplitude. As expected, at the Antarctic location of Rothera the semi-diurnal tide dominates, whereas at the equatorial location of Ascension Island the diurnal tide dominates. The ExUM tidal amplitudes display some short-term variability and on occasion reach values in excess of $150\,\mathrm{m\,s^{-1}}$. At the location of Ascension Island the ExUM diurnal tidal amplitudes actually decrease slightly at heights above about 90 km. For both locations and in both the zonal and meridional components, there is a clear descent of the phase fronts with increasing time, corresponding to upwardly propagating tides. These tidal oscillations are superposed on

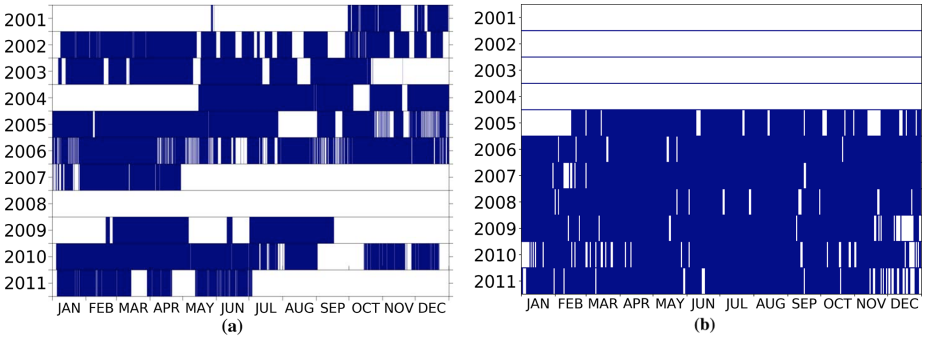

Figure 4. Availability of meteor radar observations for **(a)** Ascension Island (from Davis et al., 2013) and **(b)** Rothera. This motivates the choice of 2006 as the year for comparison.

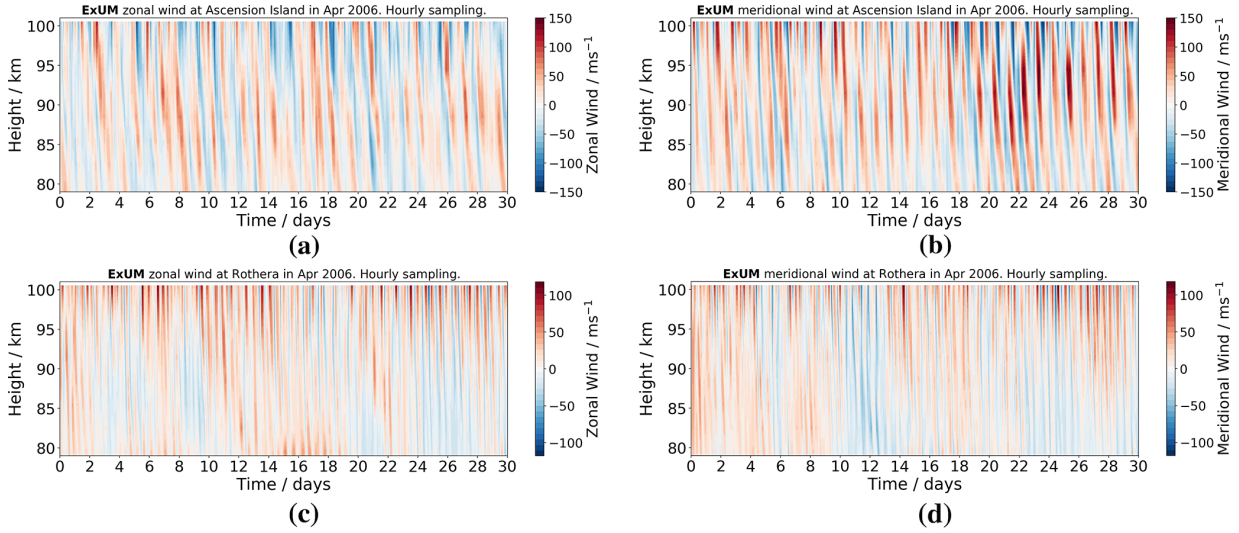

Figure 5. ExUM time–height wind contours from the 94-level model configuration in April 2006. At Ascension Island for the **(a)** zonal (u) and **(b)** meridional (v) components. Similarly at Rothera for the **(c)** zonal (u) and **(d)** meridional (v) components.

background wind fields that themselves display variation in height and time. Before we consider the variability of the tides in more detail, we will thus consider the ExUM's zonal and meridional background winds at the two locations, examine how they vary throughout the year and compare them to the radar observations. All months will be referred to by their three-letter abbreviation in lists for brevity.

3.1 Mean winds

The monthly-mean zonal and meridional winds for Ascension Island are presented in Fig. 6 and those for Rothera in Fig. 7. In each case we also present the corresponding monthly-mean winds observed by the respective radar. The zero-wind line in the figures is indicated by a dashed black line.

Firstly, we consider the equatorial site of Ascension Island. The ExUM monthly-mean zonal winds clearly exhibit the well-known mesospheric semi-annual oscillation, with wind maxima in January and June and minima in April and October. The amplitude of this semi-annual behaviour reduces at the upper heights in the figure and is largely absent at heights above about 95 km. The corresponding zonal winds observed by the radar also display a semi-annual cycle, but the height and time regions of westward winds (negative zonal wind) are rather more extensive than those of the ExUM, with an interval of westward winds being observed to last from January–May which is not well reproduced by the model. Further, the maximum monthly-mean observed wind speeds are about double those in the ExUM, with observed wind speeds reaching about $40\,\mathrm{m\,s^{-1}}$ at heights near 90 km in June and $-40\,\mathrm{m\,s^{-1}}$ at heights near 80 km in January. Nevertheless, the ExUM reproduces the general semi-annual pattern of zonal winds.

The corresponding monthly-mean meridional winds in the ExUM at heights below about 95 km display a seasonal pattern with northward winds present from about November–May and southward winds at other times. At heights above about 95 km, the meridional winds are southward through-

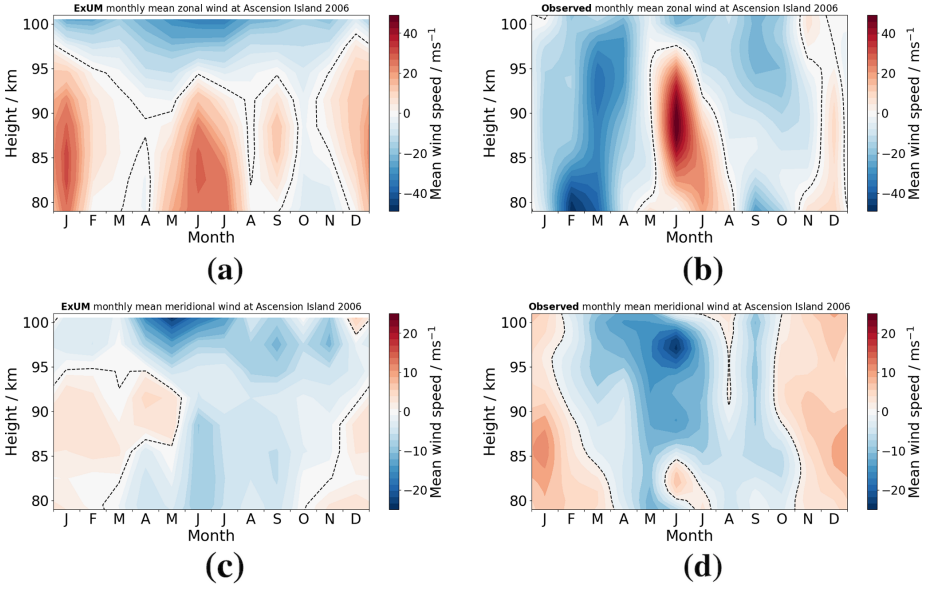

Figure 6. Time–height monthly-mean wind contours at Ascension Island in 2006 comparing **(a)** ExUM zonal wind with **(b)** observed zonal wind and **(c)** ExUM meridional wind with **(d)** observed meridional wind. The dashed black line represents the zero-wind line. Colour bars are kept consistent left to right for comparison.

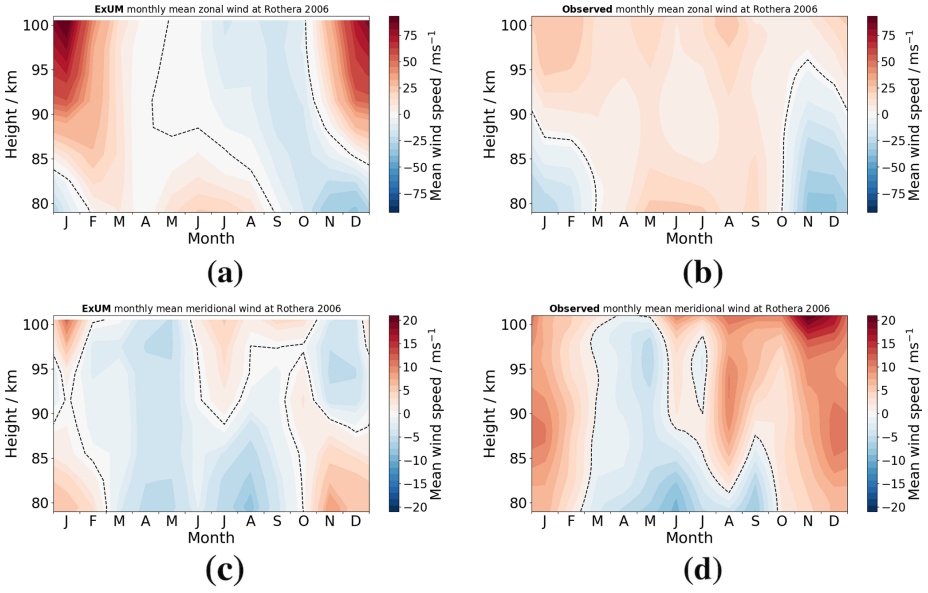

Figure 7. Time–height monthly-mean wind contours at Rothera in 2006 comparing **(a)** ExUM zonal wind with **(b)** observed zonal wind and **(c)** ExUM meridional wind with **(d)** observed meridional wind. The dashed black line represents the zero-wind line. Colour bars are kept consistent left to right for comparison.

out most of the year. The absolute wind speeds are generally much less than the zonal wind speeds and are mostly less than about $5\,\mathrm{m\,s^{-1}}$, although the strongest meridional winds occur at the upper heights in May/June when the southward winds reach about $15\,\mathrm{m\,s^{-1}}$. The observed meridional winds over Ascension Island display a generally similar seasonal variation to that of the ExUM. However, the observed wind speeds are slightly larger throughout most of the year, and the region of strongest southward flow in June/July extends to lower heights than in the ExUM.

In summary, comparing the ExUM and observed winds for Ascension Island, we see that some essential features are well captured and that the semi-annual variation is reproduced. However, there remain some notable differences in detail. This is particularly notable in February/March when the observed strong westward winds are not well reproduced.

Secondly, we consider the monthly-mean wind fields at the location of Rothera. Here, the ExUM zonal wind is predominantly eastward from November–May (i.e. through summer and into autumn) and reverses to be westward from July–October. The austral summer months exhibit a strong wind shear with velocities increasing from about $-20\,\mathrm{m\,s^{-1}}$ at heights of 80 km to more than $75\,\mathrm{m\,s^{-1}}$ at heights of 100 km. The radar observations from Rothera reveal rather smaller absolute wind speeds in austral summer with values ranging from about $-25\,\mathrm{m\,s^{-1}}$ at heights of 80 km to about $25\,\mathrm{m\,s^{-1}}$ at heights of 100 km – significantly less than predicted by the ExUM. The observed winds in winter are noticeably different from those of the ExUM. In particular, the observed winds are eastwards at all heights from March–October and reach speeds of more than $20\,\mathrm{m\,s^{-1}}$, whereas the ExUM yields westward winds at heights above about 85 km with speeds reaching $-20\,\mathrm{m\,s^{-1}}$ for most of these months. This is probably the most notable difference between the winds of the ExUM and those observed by the radars.

The ExUM meridional winds at the location of Rothera exhibit a seasonally reversing pattern with southward flow at all heights in March–June and regions of northward flow in the other months. In the austral summer months of November/December, there are southward winds at heights above about 90 km and northward winds below that height. The radar observations of meridional winds over Rothera reveal a broadly similar pattern of winds to those of the ExUM from January–August, although with rather stronger northward winds in January/February. However, in August–December the observed winds are rather different from those of the ExUM. In particular, the observed winds are almost entirely northward at all heights and actually reach the largest values measured in December, whereas the ExUM winds are actually southwards in November/December at heights above about 90 km.

In summary, comparing the ExUM and observed winds for Rothera, we see that some aspects of the seasonal variation of the observed winds are reproduced well in the ExUM, particularly below 85 km. However, there is a notable difference in that the observed zonal winds are eastwards in austral winter at all heights, whereas in the ExUM they are westwards except at the lowest heights. As well as this, the magnitude of the ExUM winds above 90 km in austral summer is also significantly larger than that observed. We will consider possible explanations for these differences in Sect. 4.

3.2 Diurnal tides

We now proceed to a more detailed comparison of the diurnal and semi-diurnal tidal amplitudes and phases in the ExUM at the two locations to those observed by the radars. As with the winds, we will consider monthly-mean properties, because they provide a test of the model's ability to reproduce the seasonal variation of the atmosphere.

Monthly-mean tidal amplitudes and phases at heights of 80–100 km were calculated as described in Sect. 2 for both the ExUM results and the radar observations.

3.2.1 Amplitudes

For the location of Ascension Island, the zonal and meridional amplitude components are presented in Fig. 8.

In each panel of the figures, the amplitudes predicted by the ExUM are plotted alongside the meteor radar observations. The shaded regions denote the standard deviation from the curve-fitting algorithm, and the black bars indicate the standard deviation from the mean of the measured amplitudes across the month.

Considering the monthly-mean ExUM results, we see that the ExUM tidal amplitudes in most months increase from values of about $10–20\,\mathrm{m\,s^{-1}}$ at heights near 80 km to about $20–40\,\mathrm{m\,s^{-1}}$ at heights of 100 km. However, in January and March the amplitudes do not increase across this height range. The zonal and meridional amplitudes are generally similar but not exactly the same. For instance, in May and November the meridional amplitudes are notably larger than the zonal amplitudes. In fact, the largest amplitudes in the ExUM occur in May when the meridional component amplitude at a height of 100 km exceeds $50\,\mathrm{m\,s^{-1}}$.

The corresponding observed tides display a generally similar behaviour, with amplitudes at the lower heights typically being in the range $10–20\,\mathrm{m\,s^{-1}}$ and increasing to larger values at the upper heights, except in January and December when the amplitudes remain approximately constant with height.

In terms of agreement between ExUM and observed amplitudes, the agreement tends to be better for the zonal components than for the meridional components, and in general the agreement is best at lower altitudes. For the zonal components, excellent agreement is observed in the majority of months. May is the biggest exception, which differs from the observed amplitude by $20–30\,\mathrm{m\,s^{-1}}$ in the worst case. Otherwise, deviations from observed amplitudes are around $10–20\,\mathrm{m\,s^{-1}}$ at most. Looking more closely at their relative magnitudes, the ExUM zonal amplitudes are often greater than or equal to the observed amplitudes up to 90 km and then less than or equal to the observed amplitudes above 90 km. For the meridional components, excellent agreement is observed in January, July, August and October. The months of September, November and December are reasonable with deviations of around $10–20\,\mathrm{m\,s^{-1}}$. However, the ExUM amplitudes differ notably (by around $30\,\mathrm{m\,s^{-1}}$) in the other 5 months. Looking more closely at their relative magnitudes, the amplitudes are similar between the two for January, April, July–September and October; the ExUM amplitudes are smaller in February and March and are larger in May, June, November and December.

Next, we will consider the equivalent monthly-mean diurnal tidal amplitudes at Rothera, which are shown in Fig. 9.

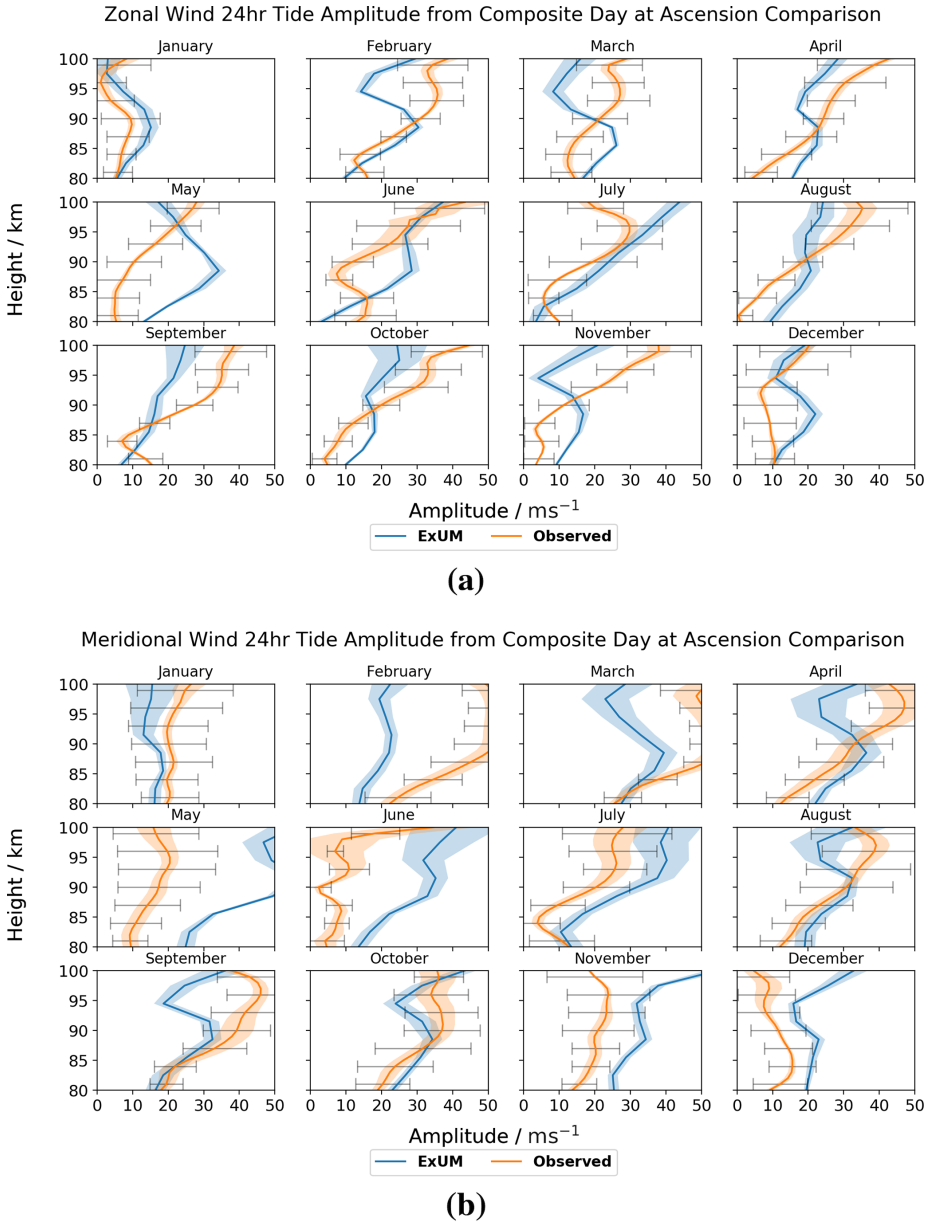

Figure 8. Amplitudes for each month as a function of height for the **(a)** zonal (u) and **(b)** meridional (v) components of the diurnal tide at Ascension Island. The shaded regions denote the standard deviation from the curve-fitting algorithm, and the black bars indicate the standard deviation from the mean of the measured amplitudes across the month. Both the amplitudes from the model (blue) and meteor radar (orange) are plotted.

Once more, we first consider the ExUM amplitudes. The zonal and meridional components are of similar, small, magnitude for all months. For the majority of months, the amplitudes remain roughly constant with increasing height; however, some growth of amplitude with increasing height is observed for November–February. Maximal amplitudes of ca. 20 m s^{-1} are seen in January for both the zonal and meridional components.

Secondly, we consider the observed amplitudes. These also have zonal and meridional components which are of similar, small, magnitude for all months. The amplitude remains roughly constant with increasing height in all cases. Maximal amplitudes of ca. 15 and ca. 20 m s^{-1} are observed for the November zonal component and the December meridional component, respectively.

In terms of agreement between ExUM and observed amplitudes, the agreement is excellent across all months for both zonal and meridional components. The magnitudes are similar for both components for all months.

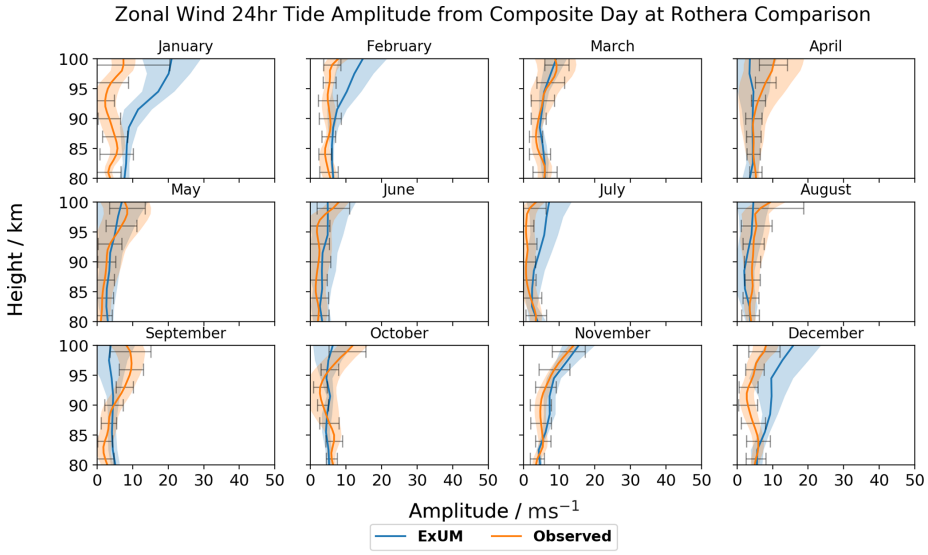

(a)

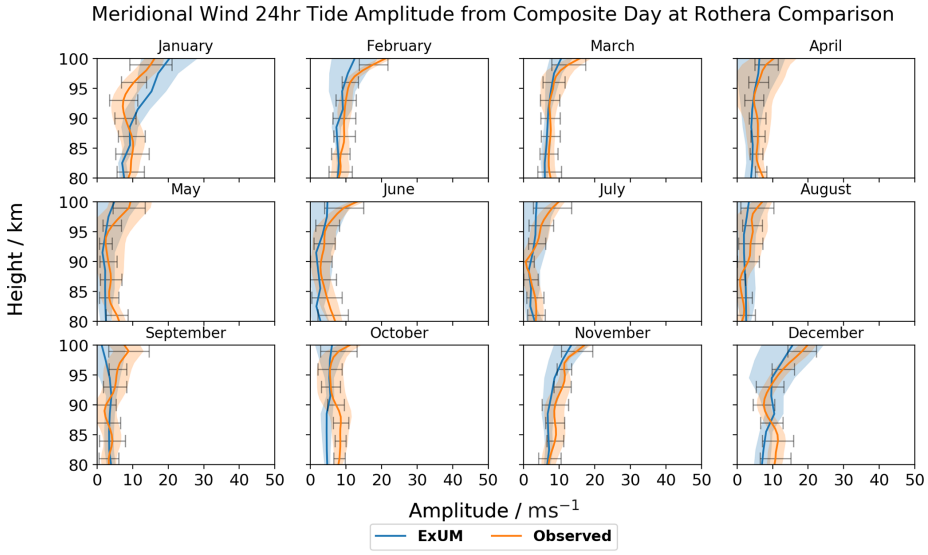

(b)

Figure 9. Amplitudes for each month as a function of height for the **(a)** zonal (u) and **(b)** meridional (v) components of the diurnal tide at Rothera. The shaded regions denote the standard deviation from the curve-fitting algorithm, and the black bars indicate the standard deviation from the mean of the measured amplitudes across the month. Both the amplitudes from the model (blue) and meteor radar (orange) are plotted.

3.2.2 Phases

The tidal phases are defined as the local time at which the tidal wind first reaches a maximum value for a particular component. Phases were calculated for zonal and meridional components for both the ExUM and observed winds at both Ascension Island and Rothera. As with the amplitudes, we present figures on which we plot both the ExUM tidal phases and the observed tidal phases.

The monthly diurnal tidal phases are presented for both the zonal and meridional wind components at Ascension Island in Fig. 10.

Firstly, we consider the ExUM phases. The ExUM meridional phases are consistent in leading their zonal counterparts, by around 4–8 h. A smooth decrease in phase with increasing height is observed for the majority of months indicative of upwardly propagating tides. In the zonal component, a lesser decrease with increasing height (namely, a

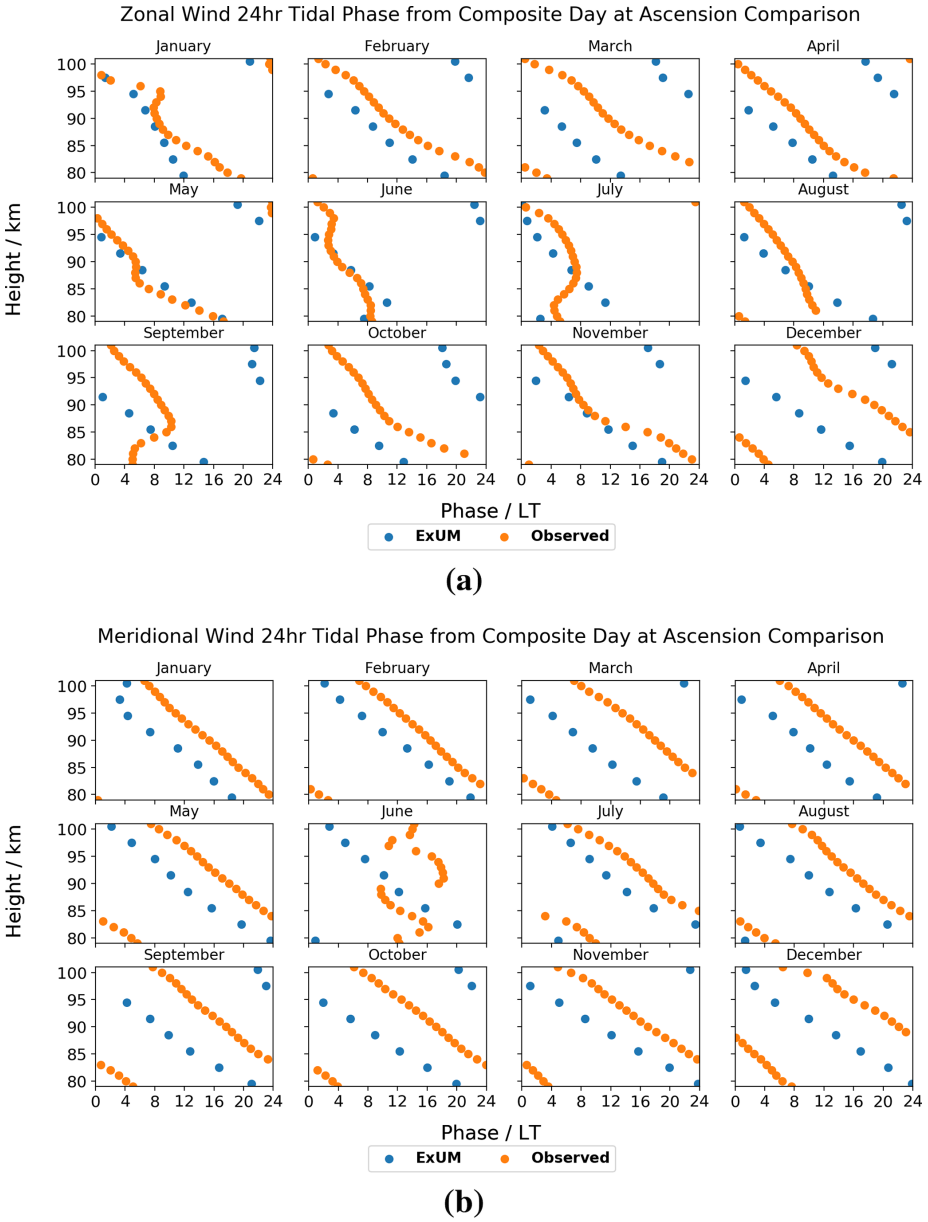

Figure 10. Phases for each month as a function of height for the **(a)** zonal (u) and **(b)** meridional (v) components of the diurnal tide at Ascension Island. Both the phases from the model (blue) and meteor radar (orange) are plotted.

steeper phase gradient) is seen at high altitudes in August–November.

Secondly, we consider the observed phases. As with the modelled phases, the observed meridional phases consistently lead the observed zonal phases by around 2–8 h, with June being the only exception where the observed meridional component is anomalous. This is to be expected given the lack of observations in June (see Fig. 4). June is also the only exception to a smooth decrease in phase with increasing height in the meridional component. In the zonal component, a decrease in phase with increasing height is observed in the majority of months, with the exceptions being at lower altitudes.

In terms of agreement between ExUM and observed phases, qualitative agreement in the characteristics of the phases is in general excellent across both components in all months. In terms of a quantitative comparison, for the zonal component, in several cases the ExUM phase is in excellent agreement, such as in January, May, June and November. However, in other months the observed phase leads the ExUM phase by 4–8 h, and the observed phases often have a steeper slope with height indicative of longer vertical wavelengths. For the meridional component, the observed phase

leads the ExUM phase by 4–10 h in all months, but the phase slope is similar between ExUM and observed phases for all months.

Next, the monthly diurnal tidal phases are presented for both the zonal and meridional wind components at Rothera in Fig. 11. It should be noted that the amplitudes for many months are small, and so caution must be taken in drawing conclusions from the corresponding phases. Nevertheless, we can look for qualitative features.

Again, we firstly consider the ExUM phases. The ExUM meridional phases are once more consistent in leading their zonal counterparts. In both components the phases remain roughly constant with increasing height for the majority of the year.

Secondly, we consider the observed phases. As with the modelled phases, the observed meridional phases consistently lead the observed zonal phases, with July being the only exception. In the zonal component, a general trend of decrease in phase with increasing height is seen in the majority of months, with the exceptions being at higher altitudes. In the meridional component, for most months the phase is roughly constant with increasing height, with a weak decrease in phase with increasing height observed in some months. July is again the exception where an increase in phase with increasing height is observed for lower altitudes.

In terms of agreement between ExUM and observed phases, the agreement is better for the meridional component, which is on the whole very good. For the zonal component, in several cases the ExUM phase is in excellent agreement, such as in February, March and October–December. However, in other months the ExUM phase leads the observed phase by 4–10 h, and the observed phases in general have a decreasing slope with increasing height, which is not apparent in the ExUM phases which on the whole have constant phase slope. For the meridional component, the agreement is in general excellent across the majority of months, with the roughly constant phase slope mirrored. The agreement is worse for May–July where the ExUM phase leads the observed phase by up to 10 h.

To summarize, this first comparison is indicative of the ExUM's strong ability to capture the diurnal tidal phases and amplitudes, with order of magnitude and qualitative agreement across many of the diagnostics considered, with no specific tuning necessary. Core qualitative features are reproduced – large amplitudes at Ascension Island compared with small amplitudes at Rothera, a general increase in amplitude with height, a general decrease in phase with height; the meridional tide component exceeding the zonal component, and the meridional phases leading their zonal counterparts.

The differences observed in amplitude do not follow a clear trend, but often the accuracy of the amplitudes in comparison with observed values is in general better at lower altitudes, and more differences were seen towards the upper heights of the model. The modelled phases systematically lead the observed phases by around 4–10 h. Where differences in phase gradient are evident, at Ascension Island, the observed phase gradients are often steeper than that seen in the ExUM and at Rothera; the ExUM phase gradients are generally vertical, which is not always the case in observations.

3.3 Semi-diurnal tides

We now proceed to a detailed comparison of tidal amplitudes and phases for the semi-diurnal tide, from both the ExUM and meteor radar observations at both locations.

Monthly-mean tidal amplitudes and phases at heights of 80–100 km were calculated as described in Sect. 2 for both the ExUM results and the radar observations.

3.3.1 Amplitudes

In each panel of the figures, the amplitudes predicted by the ExUM are plotted alongside the meteor radar observations. The shaded regions denote the standard deviation from the curve-fitting algorithm, and the black bars indicate the standard deviation from the mean of the measured amplitudes across the month.

The monthly semi-diurnal tidal amplitudes are presented for the zonal and meridional wind components at Ascension Island in Fig. 12.

Firstly, we consider the ExUM amplitudes. The ExUM meridional amplitudes are, for the majority of months, greater than or equal to the corresponding zonal amplitudes, particularly above 90 km. October does not fit this trend: the zonal component is larger than the meridional component and again more so above 90 km. Growth of amplitude with increasing height is observed for the majority of months in the ExUM meridional amplitudes, and the amplitudes remain roughly constant with increasing height for the ExUM zonal amplitudes. The months which do not follow this pattern are September–December, where the opposite is true; namely, the zonal amplitudes grow with increasing height, whereas the meridional amplitudes remain roughly constant with increasing height. The largest amplitudes of ca. $59\,\mathrm{m\,s^{-1}}$ are observed when looking more closely at the meridional components in June.

Secondly, we consider the observed amplitudes. We note that these amplitudes have meridional components which are greater than or equal to their zonal counterparts. In particular, October–December have similar amplitudes in both components. The observed zonal amplitudes on the whole remain constant with increasing height, with a slight increase evident in January, June and August. The meridional amplitudes remain roughly constant with increasing height for May and October–February and grow with increasing height for March, April and June–August. The largest amplitudes of ca. $42\,\mathrm{m\,s^{-1}}$ are observed when looking more closely at the meridional components in June.

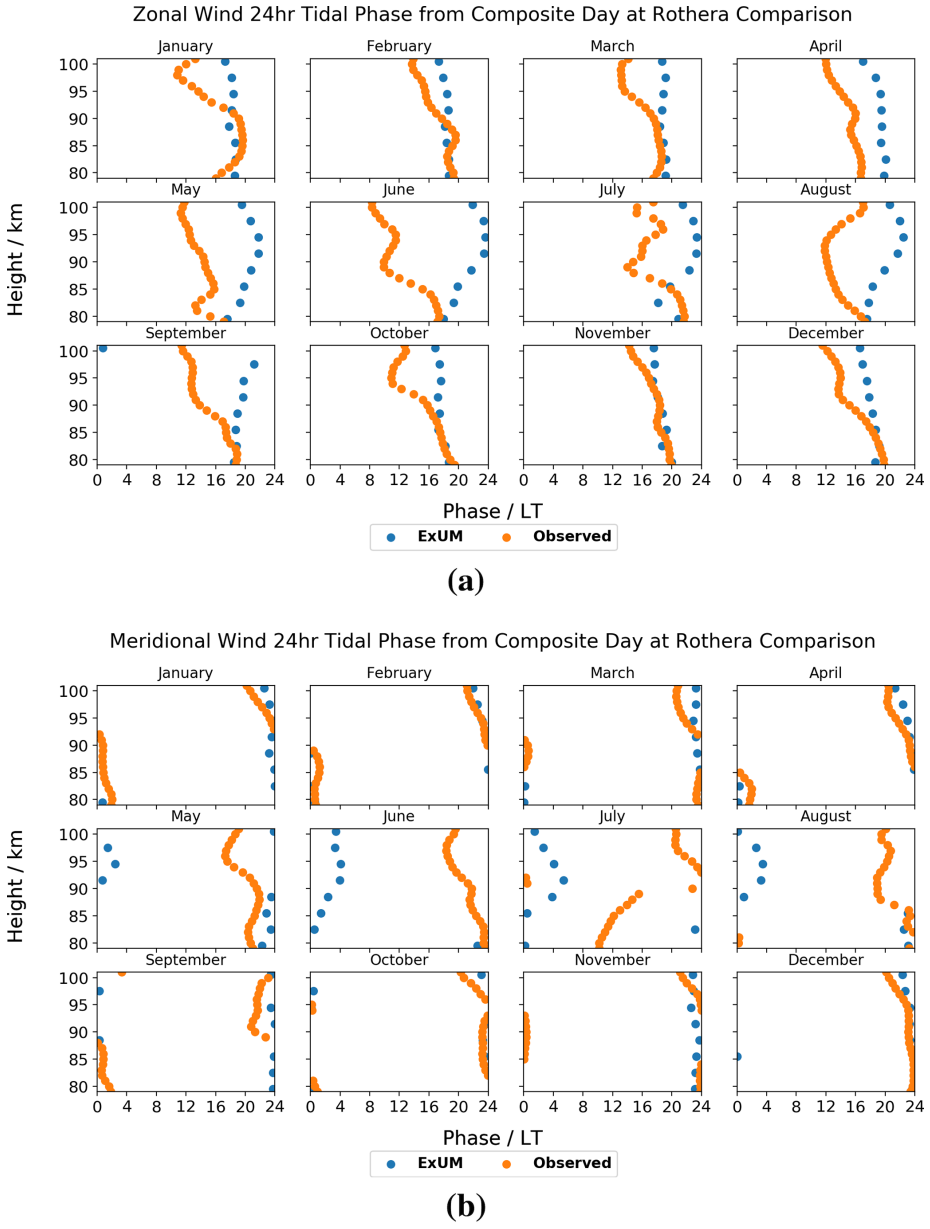

Figure 11. Phases for each month as a function of height for the **(a)** zonal (u) and **(b)** meridional (v) components of the diurnal tide at Rothera. Both the phases from the model (blue) and meteor radar (orange) are plotted.

In terms of agreement between ExUM and observed amplitudes, the agreement is excellent and is marginally better for the zonal components in comparison with the meridional components and in general is best at lower altitudes. For the zonal components, excellent agreement is observed in the majority of months. October is the biggest exception, which differs from the observed amplitude by 20–30 $\mathrm{m\,s^{-1}}$ at 100 km. Otherwise, deviations from observed amplitudes are around 5–15 $\mathrm{m\,s^{-1}}$. Looking more closely at their relative magnitudes, the ExUM zonal amplitudes are similar to observed amplitudes in the majority of cases but tend to be larger where the amplitudes do differ. For the meridional components, excellent agreement is observed once more in the majority of months. January and August are the main exceptions, with deviations of around 20 $\mathrm{m\,s^{-1}}$ at higher altitudes, but still show excellent agreement below 90 km. Otherwise the difference is minimal at 5–10 $\mathrm{m\,s^{-1}}$. Looking more closely at their relative magnitudes, the amplitudes are once more similar between the two, with the ExUM amplitudes again larger where they differ.

Next, the monthly semi-diurnal tidal amplitudes are presented for the zonal and meridional wind components at Rothera in Fig. 13.

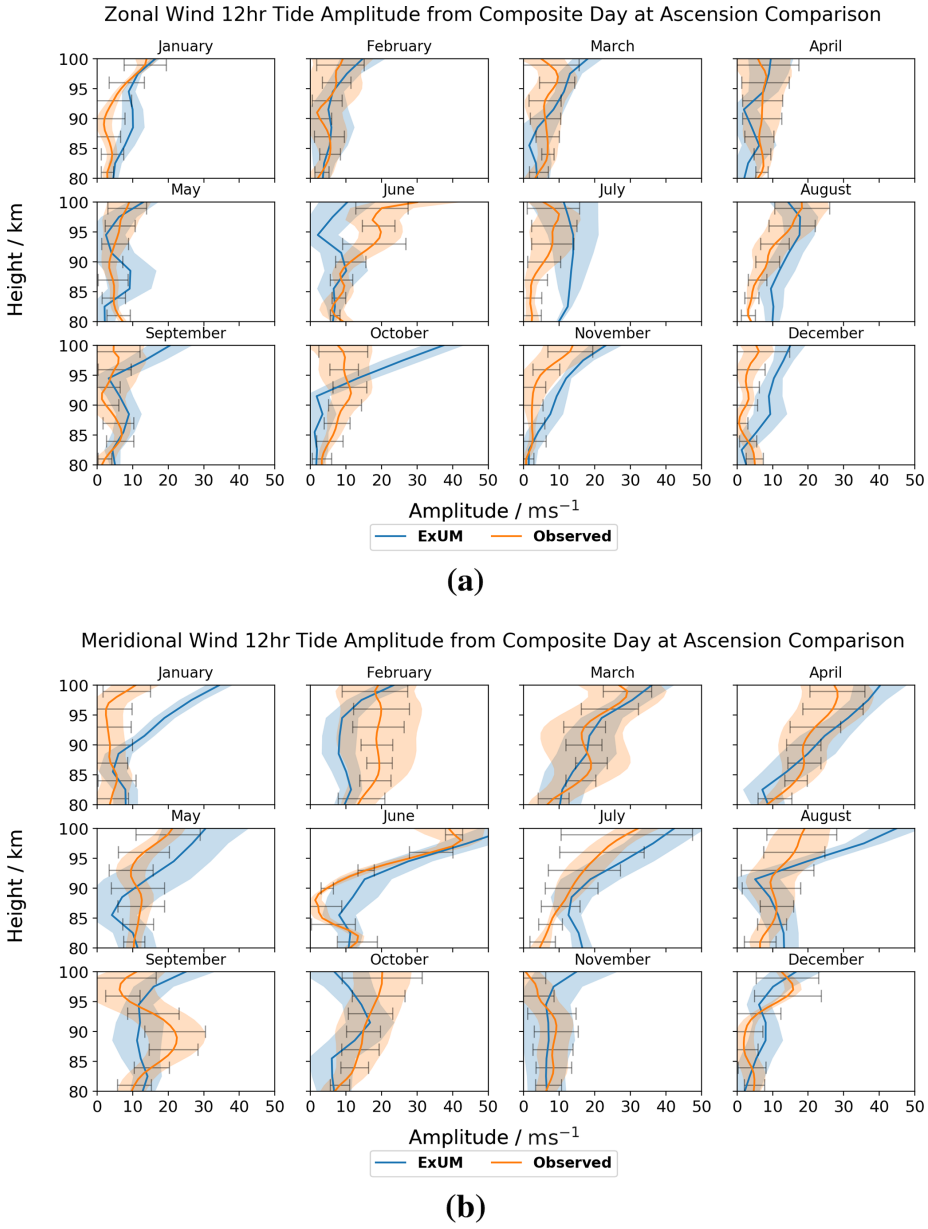

Figure 12. Amplitudes for each month as a function of height for the **(a)** zonal (u) and **(b)** meridional (v) components of the semi-diurnal tide at Ascension Island. The shaded regions denote the standard deviation from the curve-fitting algorithm, and the black bars indicate the standard deviation from the mean of the measured amplitudes across the month. Both the amplitudes from the model (blue) and meteor radar (orange) are plotted.

Once more, we first consider the ExUM amplitudes. The ExUM amplitudes are of very similar magnitude across both components – therefore, we will summarize them both simultaneously. The growth of amplitude with height is evident across nearly all months, with March being the only exception. We observe the largest amplitudes of ca. 40 m s^{-1} in December/January.

Secondly, we consider the observed amplitudes. The observed amplitudes are also of very similar magnitude across both components. The amplitudes exhibit growth with increasing height in March–May and less clearly so in August–October. For the remaining 6 months, the amplitude remains roughly constant with increasing height. The largest amplitudes of ca. 35 m s^{-1} are apparent in April.

In terms of agreement between ExUM and observed amplitudes, the agreement is mirrored for both the zonal and meridional components. Excellent agreement is observed in the majority of months with the best agreement in general at lower altitudes. December–March show the largest deviations of around 10–20 m s^{-1} at higher altitudes. Other-

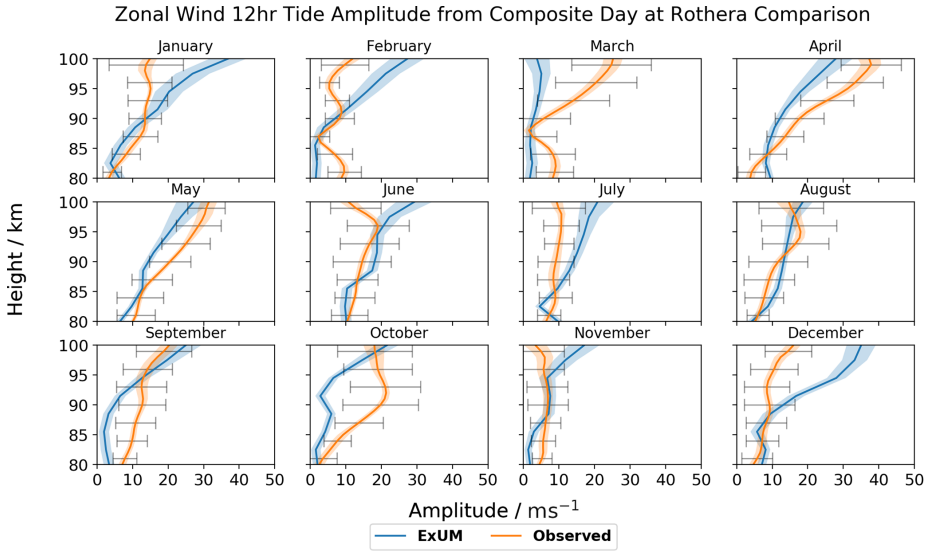

(a)

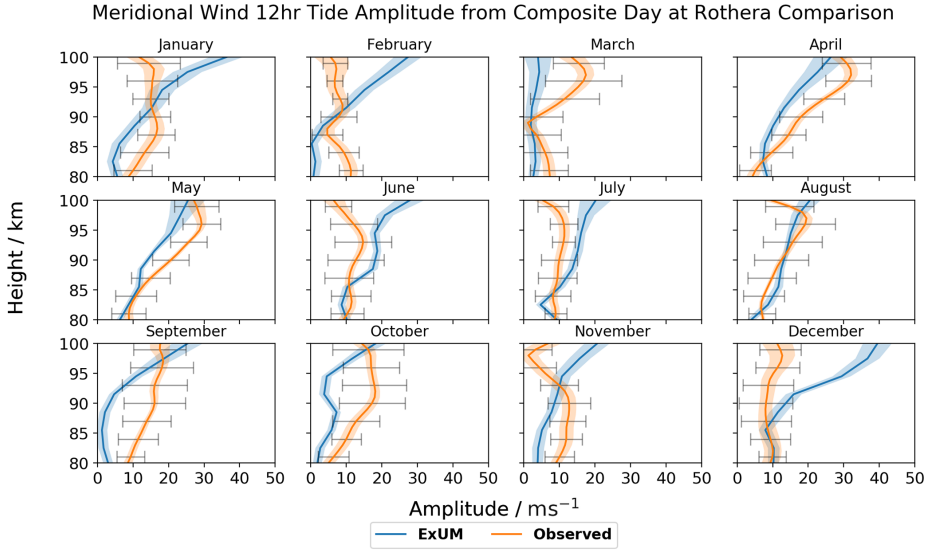

(b)

Figure 13. Amplitudes for each month as a function of height for the **(a)** zonal (u) and **(b)** meridional (v) components of the semi-diurnal tide at Rothera. The shaded regions denote the standard deviation from the curve-fitting algorithm, and the black bars indicate the standard deviation from the mean of the measured amplitudes across the month. Both the amplitudes from the model (blue) and meteor radar (orange) are plotted.

wise, the agreement is excellent with deviations of around 5–10 m s^{-1}. Looking more closely at their relative magnitudes, in general the amplitudes are similar. In the few cases they do differ, no obvious trend is apparent – for some months the ExUM amplitudes are larger, and for others they are smaller.

3.3.2 Phases

Along with the amplitudes, the monthly semi-diurnal tidal phases (namely, the hours of peak amplitude) were also calculated for zonal and meridional components for both the ExUM and observed winds at both Ascension Island and Rothera. Once more the phases predicted by the ExUM are plotted alongside those predicted by the meteor radar observations.

The monthly semi-diurnal tidal phases are presented for both the zonal and meridional wind components at Ascension Island in Fig. 14. It should be noted that the amplitudes for many months are small, and so caution must be taken in drawing conclusions from the corresponding phases. Nevertheless, we can as before look for qualitative features.

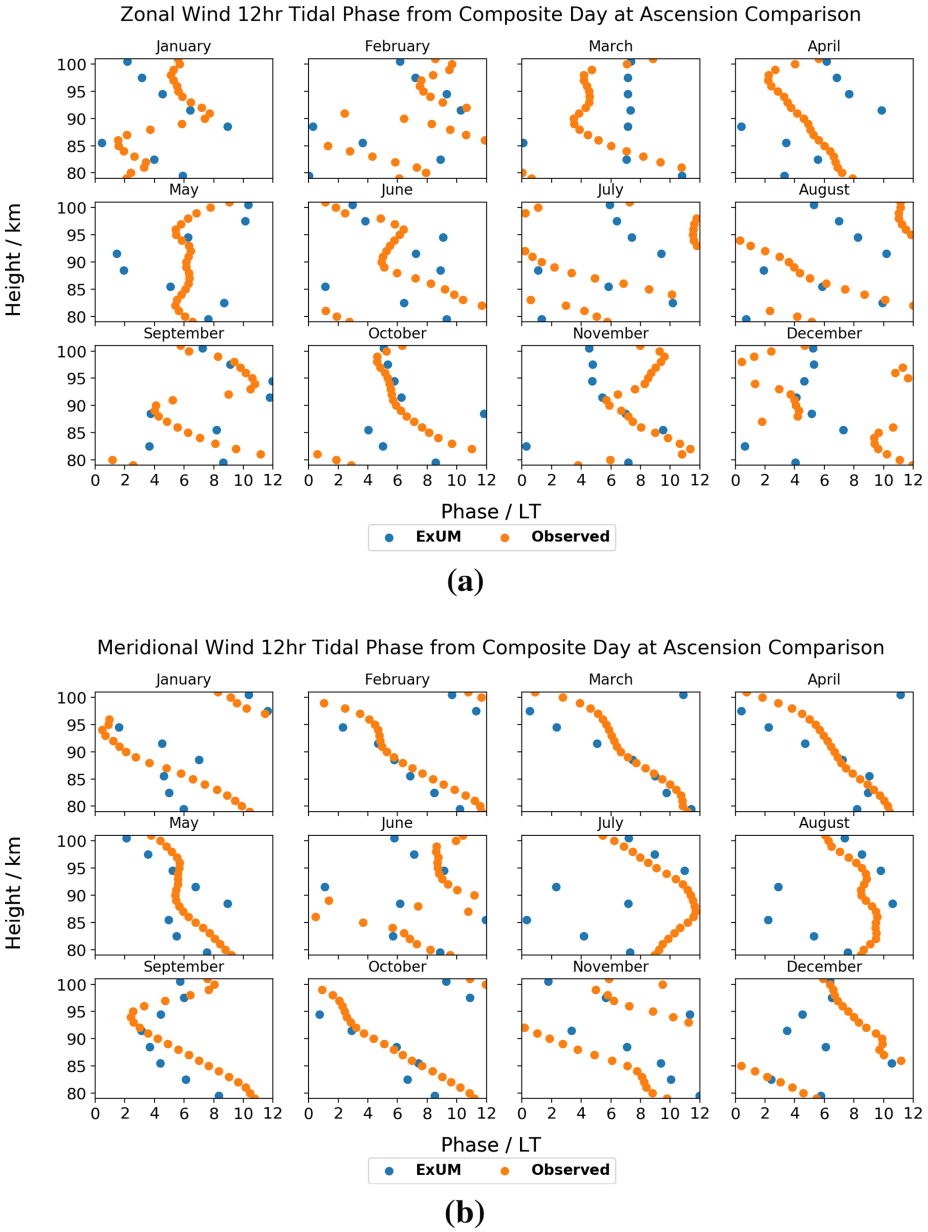

Figure 14. Phases for each month as a function of height for the **(a)** zonal (u) and **(b)** meridional (v) components of the semi-diurnal tide at Ascension Island. Both the phases from the model (blue) and meteor radar (orange) are plotted.

Firstly, we consider the ExUM phases. The ExUM meridional phases in general lead their zonal counterparts. A decrease in phase with increasing height is observed for the majority of months indicative of upwardly propagating tides; however, it is worth noting that the corresponding phase gradient is much shallower than that seen for the phases of the diurnal tide, and thus indicative of a shorter vertical wavelength. In the zonal component in March, November and December, the phase becomes roughly constant with increasing height at high altitudes, and May shows an increase in phase with increasing height also above 90 km.

Secondly, we consider the observed phases. Contrary to the modelled phases, it is not at all obvious that there is a trend between the observed zonal and meridional phases. In general, the trend of decrease in phase with increasing height is apparent in the majority of months for both components. However, other trends are observed. In the zonal component, the months of March, May, June and October all have heights for which the phase remains roughly constant with increasing height. January, May, September and November exhibit an increase in phase with increasing height at various heights. In the meridional component, there are fewer exceptions to the general trend of a decrease in phase with

increasing height. May/June have periods of constant phase with increasing height at around 95 km, and September exhibits an increase in phase with increasing height also around 95 km.

In terms of agreement between ExUM and observed phases, the agreement is in general better for the meridional component which is excellent for many months, such as January–April, October and November, but has larger differences in July–August. It is interesting to note that the model matches some of the less expected behaviour such as the increase in phase with increasing height above 90 km in September; however, the observed amplitudes are fairly small here. For the zonal component, the agreement tends to be good at best, in months such as January, September and October. Again it is interesting that some more complex features are well captured in September. The roughly constant phase with increasing height is also captured in March but is out of phase by around 2–3 h. This characteristic is repeated in many other months, such as July–August; namely, the correct qualitative behaviour is seen, but they are out of phase by 2–6 h. However, in other months the ExUM phases do not match those observed, in particular in November and December. In general though, the agreement is good and the trend of a more shallow decrease in phase with increasing height is mirrored between the ExUM and observed phases.

Next, the monthly semi-diurnal tidal phases are presented for the zonal and meridional wind components at Rothera in Fig. 15.

Again, we firstly consider the ExUM phases. The ExUM meridional phases are once more consistent in leading their zonal counterparts, by around 2–6 h. Apart from this phase shift, the zonal and meridional components are practically identical across all months. The phases exhibit a general trend of decrease with increasing height. This decrease is steeper in some months than others; for example, compare February/March (where it is shallow) with September/November (where it is steeper). This is indicative of varying vertical wavelength throughout the year but of consistently upwardly propagating tides.

Secondly, we consider the observed phases. As with the modelled phases, the observed meridional phases consistently lead the observed zonal phases by around 3–6 h. They also share the property that, apart from this phase shift, the zonal and meridional components are very similar across the majority of months. A general trend of decrease in the observed phase with increasing height is seen. The observed phases also exhibit a variety of phase gradients, with shallower gradients in March and October, and steeper gradients in June–September, for example.

In terms of agreement between ExUM and observed phases, the agreement on the whole is very good and is marginally better for the zonal component. The amount that the meridional component leads the zonal component is on the whole consistent across both phases. For the zonal component, in several cases the ExUM phase is in excellent agreement, such as in January, March, June, August and September, with a reasonably consistent phase gradient between the two. For several months, the main difference is that the observed phases have a steeper slope with increasing height (such as in May–July), indicative of longer vertical wavelengths. For the meridional component, it is a similar story in comparison with the zonal component; January, March, June, August and September show excellent agreement on the whole, and a steeper phase slope is seen in the observed phases in May–July. The agreement is, however, slightly worse between 80 and 90 km in March and September. In both components, February and November are less similar and show several qualitative differences. In general though, agreement is good with little phase shift between ExUM and observed phases with general trends such as the decrease in phase with increasing height well captured.

To summarize, the ExUM results capture some of the characteristic features of the observed diurnal and semi-diurnal tidal amplitudes and phases across many of the diagnostics considered, with no specific tuning beforehand. Key qualitative features are reproduced, including large diurnal amplitudes at Ascension Island (particularly in the zonal component) and large semi-diurnal amplitudes at Rothera, a general increase in amplitude with height, a general decrease in phase with height (indicating upward propagation), a similar magnitude for zonal and meridional components, and meridional phases that lead their zonal counterparts.

In the particular case of the semi-diurnal amplitudes, notable differences between the ExUM and the radar observations are often more pronounced at the greater heights.

Finally, the ExUM semi-diurnal phases systematically lead the observed phases by around 2–6 h at Ascension Island. Where differences in phase gradient are evident, the observed phase gradients are often slightly steeper than those seen in the ExUM at both locations, indicating that tidal vertical wavelengths in the ExUM are slightly shorter than observed.

4 Discussion

The results presented above reveal that there are many aspects of the background winds and the diurnal and semi-diurnal tides in the ExUM that agree well with observations made in the MLT by the meteor radars at the two sites. However, there are also a number of notable differences or biases. Here we will discuss the possible origins of these biases and consider how the ExUM might be developed in future to reduce them. Note that the focus of our discussion will be on the ExUM's representation of background winds and tides and how they compare to the observations. More complete investigations of the observed winds and tides themselves over these locations and discussions of how they compare to other observational studies can be found in Davis et al.

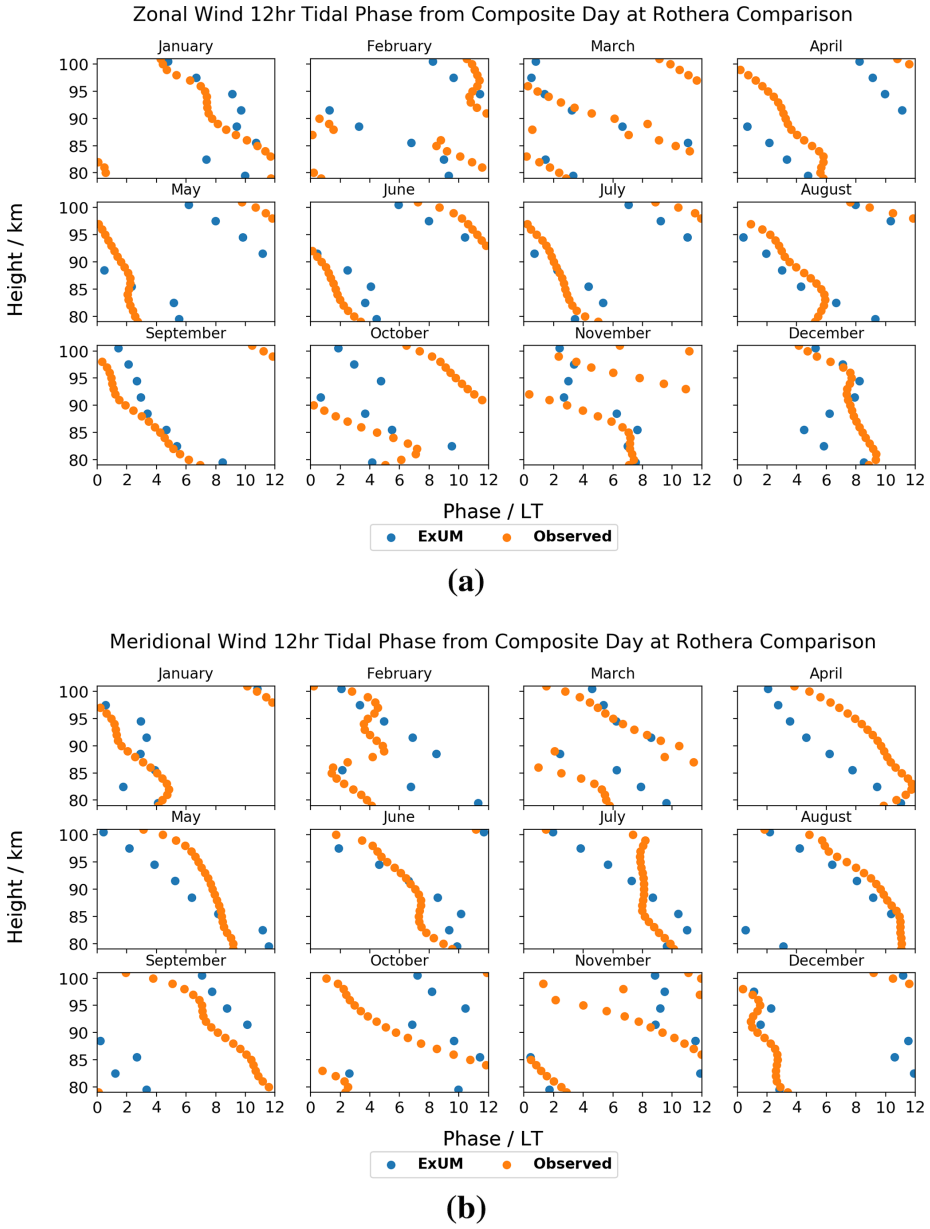

Figure 15. Phases for each month as a function of height for the **(a)** zonal (u) and **(b)** meridional (v) components of the semi-diurnal tide at Rothera. Both the phases from the model (blue) and meteor radar (orange) are plotted.

(2013) for Ascension Island and Sandford et al. (2010) and Dempsey et al. (2021) for Rothera.

4.1 Monthly-mean winds

The most striking difference between the ExUM's monthly-mean zonal and meridional winds in the MLT and those observed by the radars occurs in two regimes: (i) the Antarctic during austral summer, when the ExUM zonal winds at the upper heights are much stronger than observed over Rothera, and (ii) the Antarctic during austral winter, when the observations reveal eastward winds at all heights from March to October, but the ExUM predicts westward winds commencing in April; that is, the observed winds are actually in the opposite direction to those predicted by the ExUM.

The first of these differences most likely arises from the gravity wave parameterizations used in the ExUM, which are not yet tuned for the high-latitude MLT and so may give rise to unrealistically high mean-flow accelerations. However, the second difference is particularly striking, because the existence of any eastward winds in the polar winter MLT is unexpected since the strong eastward winds of the underlying winter stratosphere will have removed (by critical-level filtering) all ascending GWs with eastwards phase velocities

and momentum flux – leaving no such waves to dissipate in the MLT where they could force eastward winds.

Recently, an explanation for the existence of such eastward winds in the polar winter MLT has been proposed in the modelling study of Becker and Vadas (2018). These authors suggest that non-primary GWs are generated in situ over the Southern Andes in winter, either by non-linear instabilities or by the local body forces from the temporally and spatially localized wave drag resulting from the breaking of large-amplitude mountain (orographic) GWs. These non-primary GWs may include waves which have significant eastward momentum fluxes and which are excited at heights above levels where they would otherwise be removed by the critical-level filtering of eastward winds. When such eastward waves reach the MLT and themselves dissipate, their eastward momentum may then force eastward mean winds. However, Becker and Vadas (2018) did not have available zonal wind measurements from the austral winter MLT and so could not investigate further. In this context we also note that the MLT winds over Rothera for 2005–2009 reported by Sandford et al. (2010) also included eastward winds in winter. Further, the recent study by Stober et al. (2021) which considered the observations from six high southern-latitude radars for the year 2019 also reported wintertime eastward winds over all stations. The results we have presented here suggest that their predicted eastward winds do indeed occur, and so our observations are not in disagreement with the work of Becker and Vadas (2018) and suggest that non-primary gravity waves may play a key role in the circulation of the Antarctic MLT (cf. Becker and Vadas, 2020).

The ExUM, in common with nearly all GCMs, does not include gravity wave sources above the troposphere and so cannot produce an eastward forcing of the polar winter MLT since any eastward propagating waves in the model will be filtered out by critical levels before reaching the MLT. Therefore, the ExUM cannot produce the observed eastward winds. This limitation may well explain the lack of eastward polar winter winds also found in other GCMs which launch gravity waves from the surface only, including WACCM-X, eCMAM, MUAM and other high atmosphere models.

This bias in the ExUM indicates that further work is required on the GW forcing and parameterization for the MLT, with particular reference to in situ GW and non-primary GW generation (e.g. Becker and Vadas, 2018, 2020). In this context, it is worth noting that the non-orographic ultra-simple spectral parameterization (USSP) (Warner and McIntyre, 2001) used in the ExUM was designed, and primarily tuned, to obtain more realistic stratospheric features such as the quasi-biennial oscillation (QBO) rather than to give appropriate forcing in the MLT (Scaife et al., 2002).

The USSP scheme treats non-orographic gravity waves with non-zero phase speeds which are unable to be resolved by the model. This is important as the model has too coarse a resolution to represent large portions of the gravity wave spectrum. The approach used is that of Warner and McIntyre (2001) with further modifications (Scaife et al., 2002) to launch an unsaturated spectrum from a level close to the surface and to impose a homogeneous (location invariant) total vertical flux of horizontal wave pseudo-momentum. The spectrum uses a characteristic vertical wavelength peak of 4.3 km and parameterizes vertical wavelengths up to a maximum of 20 km. The amplitude of the spectrum is chosen to give momentum deposition and, hence, a QBO in the model that is realistic. For comparison with other parameterizations, a typical value of the total launch flux in all four directions is $6.6 \times 10^{-3}\,\mathrm{kgm^{-1}s^{-1}}$.

The scheme also includes the frictional heating due to gravity wave dissipation and consequent loss of kinetic energy (see Sect. 3.5 of Walters et al., 2019, for more details), but it does not include ionospheric heating effects such as ion drag. The inclusion of GW heating is important as previous studies, for example, by Medvedev and Klaassen (2003), Yiğit and Medvedev (2009) and Hickey et al. (2011) have shown that GWs produce localized, and occasionally very strong, heating and cooling, which certainly plays an important role in the MLT. However, the scheme does not have a latitudinally varying GW spectrum. Yiğit et al. (2021) showed that implementing this type of scheme can have a significant impact on middle atmosphere circulation, which can therefore have an important effect on the diurnal tides. Therefore, this addition will be a priority in future development of the USSP for the MLT.

To further investigate and demonstrate the role of GWs in forcing the winds of the MLT in the ExUM, we examined the time series of monthly-mean zonal and meridional gravity wave tendencies from the spectral scheme over the course of 2006. This is presented in Fig. 16.

It is evident from the tendencies in the figure that, as expected, the spectral GW scheme is the dominant driver of the MLT winds. This highlights the need for improvements and modifications in the scheme in the MLT if it is to produce the observed winds. We tested the impact of the USSP on the ExUM MLT winds by simply turning off the USSP scheme. With the USSP off, we attain the monthly-mean background winds at Rothera as shown in Fig. 17.

It can be seen from the figure that the ExUM winds with the USSP turned off now more closely resemble those observed over Rothera in austral summer (January–February and November–December). However, the austral winter worsens in comparison which illustrates that a spectral gravity wave scheme is certainly necessary for the MLT with this horizontal resolution. This highlights the limitations of the GWs parameterized by the USSP and suggests that improvements to the parameterization scheme are necessary to cope with GWs in the MLT – with particular focus on in situ gravity wave generation and non-primary (e.g. secondary) GWs which have been shown to also give the observed eastward winds (Becker and Vadas, 2018).

We also place these results in the context of the recent publication of Miyoshi and Yiğit (2019). They used the

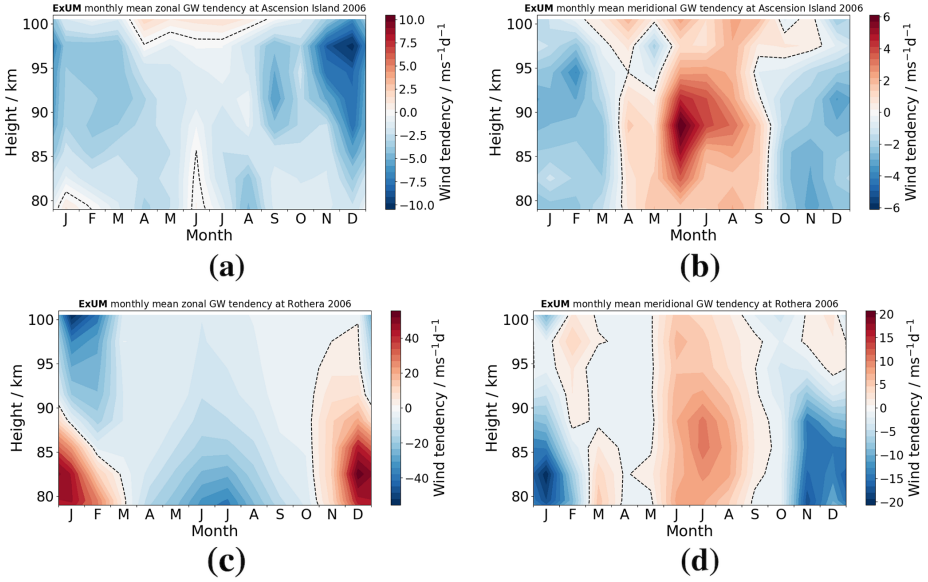

Figure 16. ExUM time–height gravity wave tendency contours in 2006. At Ascension Island for the **(a)** zonal (u) and **(b)** meridional (v) components. Similarly at Rothera for the **(c)** zonal (u) and **(d)** meridional (v) components.

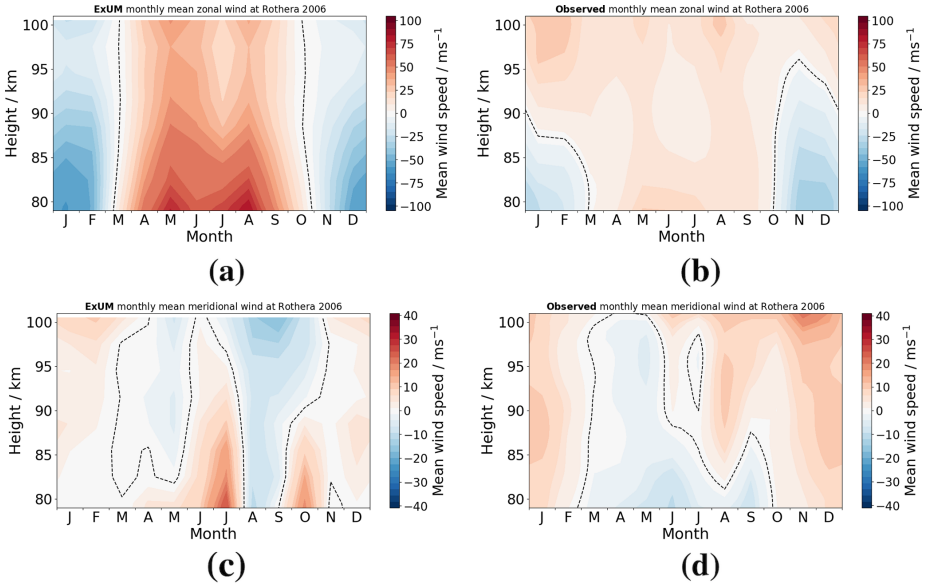

Figure 17. Time–height monthly-mean wind contours at Rothera in 2006 comparing **(a)** ExUM zonal wind without the USSP with **(b)** observed zonal wind and **(c)** ExUM meridional wind without the USSP with **(d)** observed meridional wind. The dashed black line represents the zero-wind line. Colour bars are kept consistent left to right for comparison.

Kyushu GCM and incorporated the non-linear spectral GW scheme of Yiğit et al. (2008). They showed that the non-orographic subgrid-scale GWs attenuate the migrating semi-diurnal solar-tide (SW2) amplitude for solstice conditions in the lower thermosphere and modify the latitudinal structure of the SW2 above a 150 km height. On inspection of the amplitudes of the semi-diurnal tide produced by the model with the USSP off at the two locations considered (not shown), it is also clear that the USSP acts to attenuate the semi-diurnal tidal amplitudes under solstice conditions, typically by around 20 m s^{-1} at a height of 100 km (primarily in June–September).

4.2 Diurnal and semi-diurnal tides

The results presented above for the tides show that the ExUM captures many of the main features of both diurnal and semi-diurnal tides at Ascension Island and Rothera. However, the

semi-diurnal tide at Ascension Island and the diurnal tide at Rothera reach only small amplitudes in both the ExUM and the observations, and so the model biases may not be meaningful. We will therefore restrict our discussion to the larger-amplitude tides that dominate the motion field at each location – that is, the diurnal tide at Ascension Island and the semi-diurnal tide at Rothera.

In the case of the diurnal tide over Ascension Island, the ExUM tidal amplitudes are in most months in good agreement with the observations and increase with height in a manner similar to that observed. However, there are differences in amplitude of greater than $20\,\mathrm{m\,s^{-1}}$ at some heights in some months in one or both components. This is particularly apparent in February, May and June in the meridional component.

In the case of the semi-diurnal tide over Rothera, the ExUM amplitudes are again generally in reasonable agreement with those observed, but there are some months where the ExUM amplitudes are rather larger than observed (January and December at the upper heights) or smaller than observed (September and October at the lower heights).

At Ascension Island, the diurnal tidal phases have gradients (vertical wavelengths) that are in excellent agreement with the observations, although the absolute values of phase in the ExUM in most months lead the observed phases by about 3–4 h. This systematic difference may, in part, reflect the accumulated phase difference over several cycles of the (short vertical wavelength) tide as it propagates from its sources at lower heights if there is a mismatch between the model vertical wavelength and that of the tide in the real atmosphere.

In the case of the semi-diurnal tide at Rothera, the phases are less well defined than is the case at Ascension Island. Indeed, in some months the vertical profile of tidal phase has a complicated structure without a uniform gradient across the height range considered. This is evident in both the ExUM results and the observations and is notable in, for example, the zonal phases in February and July. This behaviour may result from a superposition of different tidal modes across the height range considered. However, there are also months where the ExUM and observed tidal phases are in good agreement (for example, the meridional phases in February or October).

Considering both of the large-amplitude tides, we see that there are times and heights of good agreement and times and heights where the agreement is less good. These biases may be a consequence of the simplified globally uniform temperature nudging profile and the monthly fixed ozone background files used in this preliminary version of the ExUM. A move to a scheme with more realistic variation of temperature with latitude and season may therefore further improve tidal amplitudes in the ExUM. More fundamentally, however, this globally uniform nudging scheme needs to be replaced with molecular viscosity and diffusion (e.g. Griffin and Thuburn, 2018) as well as an improved chemistry scheme which will add the appropriate heating from exothermic reactions that is important throughout the thermosphere.

Yiğit and Medvedev (2017) and Miyoshi and Yiğit (2019) reported the migrating diurnal and semi-diurnal tidal amplitudes, respectively, and their interaction with GWs using the GW scheme of Yiğit et al. (2008). The diurnal tidal amplitudes in Yiğit and Medvedev (2017) in September of 10–$30\,\mathrm{m\,s^{-1}}$ in the zonal component and 10–$50\,\mathrm{m\,s^{-1}}$ in the meridional component agree reasonably with those observed in ExUM, where we see values of 10–$30\,\mathrm{m\,s^{-1}}$ in the zonal component and 15–$45\,\mathrm{m\,s^{-1}}$ in the meridional component. The semi-diurnal amplitudes in Miyoshi and Yiğit (2019) in June of 10–$30\,\mathrm{m\,s^{-1}}$ in the zonal component also agree with those observed in the ExUM, where we see values of 10–$30\,\mathrm{m\,s^{-1}}$ in the zonal component.

Dempsey et al. (2021) investigated diurnal and semi-diurnal tides over Rothera in the WACCM model and diurnal tides only in the eCMAM model. They also compared their results with meteor radar observations, but their study considered only the year 2009 and so is not directly comparable to the results presented here for 2006. Nevertheless, the broad seasonal characteristics of the tides can be compared and some differences noted between the model results. Here we will again restrict our considerations to the large-amplitude semi-diurnal tide at Rothera, since the amplitude of the diurnal tide at this site is small in both models and observations.

The semi-diurnal tide predicted by both WACCM and the ExUM has monthly-mean amplitudes of ca. 5–$10\,\mathrm{m\,s^{-1}}$ at heights of 80 km, which is generally comparable to the amplitudes revealed by the radar observations. However, above that height, although WACCM amplitudes increased with increasing height, they did so much less than is the case in the ExUM results presented here. In fact, the WACCM semi-diurnal tidal amplitudes exceeded $20\,\mathrm{m\,s^{-1}}$ at a height of 100 km in only 2 months in summer (November and December). In several months this matched well to the observations, but in other months it was rather smaller than observed at the upper heights (March through to September). This contrasts with the much larger amplitudes evident in the ExUM at a height of 100 km, which we have shown are in the range 20–$40\,\mathrm{m\,s^{-1}}$ in all months except March and which in some months significantly exceeds the observed amplitudes (e.g. January and December). Inter-annual variability in tidal amplitude prevents a direct comparison, but it seems likely from this that semi-diurnal tidal amplitudes in the ExUM exceed those of WACCM at heights approaching 100 km – at least in some months.

The WACCM results presented by Dempsey et al. (2021) also included estimates of monthly-mean tidal phase as a function of height and indicated a good agreement in the phase gradients (i.e. vertical wavelength) between WACCM and observations in some summer and winter months (particularly, January, February, May–August and December) but less good agreement around the equinoxes. Similar be-

haviour is apparent in our ExUM results, although again, in some months the agreement is less good, e.g. meridional phases in May and July which suggest longer vertical wavelengths in the ExUM than observed.

Davis et al. (2013) investigated both diurnal and semi-diurnal tides over Ascension Island using data from the same meteor radar used in our study. They also compared their observations to results from both WACCM and eCMAM. However, they presented their results as averages for the entire interval 2002–2011 and so, again, the results are not directly comparable with those we report here. We will thus again restrict our comments to consideration of the broad seasonal characteristics of the large-amplitude diurnal tide at Ascension Island, since the amplitude of the semi-diurnal tide at this site is small in both models and observations.

In general, Davis et al. (2013) showed that eCMAM tended to overestimate the meridional amplitudes of the diurnal tide over Ascension Island, whereas WACCM tended to underestimate them. The differences were not so large in the case of the zonal component amplitudes. Both models predicted larger amplitudes at the upper heights considered. In contrast, the results we have presented here show that the monthly-mean ExUM diurnal tidal amplitudes are not systematically larger or smaller than those observed but from month to month can vary and be either larger or smaller.

Estimates of monthly-mean tidal phase as a function of height and corresponding vertical wavelengths were also presented by Davis et al. (2013) for WACCM and eCMAM. Both models predicted tidal phases and vertical wavelengths with good agreement to the radar observations around the equinoxes but with less good agreement in the summer and winter months (particularly eCMAM which predicted much shorter diurnal zonal vertical wavelengths than are observed in summer). The ExUM generally does well in predicting the diurnal tidal phases and phase gradients (i.e. vertical wavelength) but with some small differences in summer months.

5 Conclusions

We have presented the first study demonstrating the ability of the newly Extended Unified Model (ExUM) to capture the background winds and the atmospheric tides of the MLT. We have detailed the changes made to the model which allowed these investigations, including (i) the addition of a non-LTE radiation scheme and (ii) the relaxation to a climatological temperature profile above 90 km. We tested the predicted winds and tides in the ExUM by comparing them to the tides observed by SKiYMET meteor radars at characteristic Antarctic and equatorial latitudes where we expect the diurnal and semi-diurnal tides, respectively, to dominate. We used data from 2006 and for each month determined monthly-mean tidal amplitudes and phases.

Despite the simplified nature of this initial development of the ExUM, the model produces diurnal and semi-diurnal tides that display many characteristics of the observed tides. In particular, the monthly-mean amplitudes and vertical phase gradients are in reasonably good agreement with the observations in most months and at most heights. It is still true that in some months and at some heights the predicted tidal amplitudes can differ significantly from those observed. Given that the comparison of winds described above highlights limitations in the ExUM's gravity wave parameterization, it may well be that this also impacts the model's tides and accounts for some of the differences.

1. The equatorial background MLT winds predicted by the ExUM capture some essential features well – the observed pattern of semi-annual variation is reproduced. However, there are several months where there are notable quantitative differences in the detail, e.g. February/March.

2. The polar background MLT winds predicted by the ExUM have some notable differences from those observed. Most striking are that (i) the winds in the ExUM in austral summer are stronger than observed, and (ii) the observed eastward winds in austral winter are not reproduced in the model, which actually predicts westward winds.

3. We have proposed that these eastward winds in the real atmosphere are forced by the fluxes of non-primary GWs generated when large-amplitude orographic GWs break in the upper stratosphere or mesosphere, as suggested in the modelling study of Becker and Vadas (2018). These discrepancies between the model predictions and the observations highlight the limitations of gravity wave parameterizations that only launch waves from near the surface.

4. The equatorial tidal amplitudes predicted by the ExUM are generally in good agreement with observations. Key qualitative features are reproduced, including large diurnal amplitudes and small semi-diurnal amplitudes, a general increase in amplitude with height, and the meridional tide component exceeding the zonal component.

5. The polar tidal amplitudes are generally good and also reproduce many of the qualitative features mentioned above. However, the ExUM noticeably overestimates the tidal amplitudes at the summer solstice. This is the height and time when the ExUM zonal winds are larger than those observed and we therefore propose the anomalous tidal amplitudes may be a consequence of these zonal winds.

6. The tidal phases of the larger tides have vertical phase gradients which are in very good agreement with observations. Key features are replicated including a general decrease in phase with height and the meridional phases

leading their zonal counterparts. A difference in phase is commonly seen but is expected given the ground-level source of parameterized GWs.

It is necessary for high-top models to reproduce these key features which are critical for deep coupling models as we strive towards more accurate models in the MLT. Further, we have suggested details for future work and parts of the model for future development. From this, we recommend two improvements to deal with the problems seen in the polar MLT: firstly the tuning of the spectral GW scheme to correct the wind direction in polar winter and secondly reducing the magnitude of winds around 95 km in polar summer (which may in turn address the overly large tidal amplitudes observed in polar summer). These improvements pave the way for the development of a whole atmosphere UM in the near future.

In summary, we have demonstrated that even with relaxation to a relatively simplified temperature field and the use of monthly ozone background files, the ExUM can produce tides with many of the features observed, highlighting its usefulness for future tidal studies. Further, we have suggested that the ExUM's gravity wave parameterization needs to be revised in light of what we infer to be the existence in the real atmosphere of significant fluxes of GWs not launched from the surface.

Code availability. The Unified Model code is provided courtesy of the UK Met Office and is subject to copyright.

Data availability. The Rothera and Ascension Island meteor radar data used in this study are provided by Mitchell (2019a, b). The model data are produced by the UK Met Office's Unified Model, copyright UK Met Office.

Author contributions. The experimental concept and design of methodology was performed by MJG and NJM. The Rothera meteor radar is operated by British Antarctic Survey (with principal investigator TMG). The radar data analysis was performed by SMD. The interpretation of results was performed by MJG, SMD, DRJ, TMG and NJM. The final authorship of article and preparation of figures was performed by MJG.

Competing interests. The authors declare that they have no conflict of interest.

Acknowledgements. Matthew J. Griffith, Nicholas J. Mitchell and Shaun M. Dempsey are thankful for the support of the University of Bath, the NERC GW4+ Doctoral Training Partnership studentship from the Natural Environment Research Council, and the support of the UK Met Office in collaboration with David R. Jackson. Tracy Moffat-Griffin is also thankful for the support of the Natural Environment Research Council. We are grateful to Chris Budd for helpful comments on an earlier version of this article.

Financial support. This research has been supported by the University of Bath (grant no. NE/L002434/1), the Horizon 2020 Framework Programme, H2020 European Institute of Innovation and Technology (SWAMI (grant no. 776287)), and the Natural Environment Research Council (grant nos. NE/R001391/1 and NE/R001235/1).

Review statement. This paper was edited by Gunter Stober and reviewed by two anonymous referees.

References

Akmaev, R.: Whole atmosphere modeling: Connecting terrestrial and space weather, Rev. Geophys., 49, RG4004, https://doi.org/10.1029/2011rg000364, 2011.

Akmaev, R. A., Fuller-Rowell, T., Wu, F., Forbes, J., Zhang, X., Anghel, A., Iredell, M., Moorthi, S., and Juang, H.-M.: Tidal variability in the lower thermosphere: Comparison of Whole Atmosphere Model (WAM) simulations with observations from TIMED, Geophys. Res. Lett., 35, L03810, https://doi.org/10.1029/2007gl032584, 2008.

Baldwin, M. P., Birner, T., Brasseur, G., Burrows, J., Butchart, N., Garcia, R., Geller, M., Gray, L., Hamilton, K., Harnik, N., Hegglin, M. I., Langematz, U., Robock, A., Sato, K., and Scaife, A. A.: 100 Years of Progress in Understanding the Stratosphere and Mesosphere, Meteor. Mon., 59, 27.1–27.62, https://doi.org/10.1175/AMSMONOGRAPHS-D-19-0003.1, 2019.

Beagley, S. R., McLandress, C., Fomichev, V. I., and Ward, W. E.: The extended Canadian middle atmosphere model, Geophys. Res. Lett., 27, 2529–2532, https://doi.org/10.1029/1999gl011233, 2000.

Beard, A., Mitchell, N., Williams, P., and Kunitake, M.: Non-linear interactions between tides and planetary waves resulting in periodic tidal variability, J. Atmos. Sol.-Terr. Phy., 61, 363–376, https://doi.org/10.1016/s1364-6826(99)00003-6, 1999.

Becker, E. and Vadas, S. L.: Secondary gravity waves in the winter mesosphere: Results from a high-resolution global circulation model, J. Geophys. Res.-Atmos., 123, 2605–2627, https://doi.org/10.1002/2017jd027460, 2018.

Becker, E. and Vadas, S. L.: Explicit Global Simulation of Gravity Waves in the Thermosphere, J. Geophys. Res.-Space, 125, e2020JA028 034, https://doi.org/10.1029/2020ja028034, 2020.

Bessarab, F., Korenkov, Y. N., Klimenko, M., Klimenko, V., Karpov, I., Ratovsky, K., and Chernigovskaya, M.: Modeling the effect of sudden stratospheric warming within the thermosphere–ionosphere system, J. Atmos. Sol.-Terr. Phy., 90, 77–85, https://doi.org/10.1016/j.jastp.2012.09.005, 2012.

Borchert, S., Zhou, G., Baldauf, M., Schmidt, H., Zängl, G., and Reinert, D.: The upper-atmosphere extension of the ICON general circulation model (version: ua-icon-1.0), Geosci. Model Dev., 12, 3541–3569, https://doi.org/10.5194/gmd-12-3541-2019, 2019.

Christiansen, B., Yang, S., and Madsen, M. S.: Do strong warm ENSO events control the phase of the stratospheric QBO?, Geophys. Res. Lett., 43, 10–489, https://doi.org/10.1002/2016GL070751, 2016.

Davis, R. N., Du, J., Smith, A. K., Ward, W. E., and Mitchell, N. J.: The diurnal and semidiurnal tides over Ascension Island (8° S, 14° W) and their interaction with the stratospheric quasi-biennial oscillation: studies with meteor radar, eCMAM and WACCM, Atmos. Chem. Phys., 13, 9543–9564, https://doi.org/10.5194/acp-13-9543-2013, 2013.

Dempsey, S., Hindley, N., Moffat-Griffin, T., Wright, C., Smith, A., Du, J., and Mitchell, N.: Winds and Tides of the Antarctic Mesosphere and Lower Thermosphere: One Year of Meteor-Radar Observations Over Rothera (68° S, 68° W) and Comparisons with WACCM and eCMAM, J. Atmos. Sol.-Terr. Phy., 212, 105 510, https://doi.org/10.1016/j.jastp.2020.105510, 2021.

England, S., Dobbin, A., Harris, M., Arnold, N., and Aylward, A.: A study into the effects of gravity wave activity on the diurnal tide and airglow emissions in the equatorial mesosphere and lower thermosphere using the Coupled Middle Atmosphere and Thermosphere (CMAT) general circulation model, J. Atmos. Sol.-Terr. Phy., 68, 293–308, https://doi.org/10.1016/j.jastp.2005.05.006, 2006.

Fiedler, J., Baumgarten, G., and von Cossart, G.: Mean diurnal variations of noctilucent clouds during 7 years of lidar observations at ALOMAR, Ann. Geophys., 23, 1175–1181, https://doi.org/10.5194/angeo-23-1175-2005, 2005.

Fomichev, V., Ward, W. E., Beagley, S., McLandress, C., McConnell, J., McFarlane, N., and Shepherd, T.: Extended Canadian Middle Atmosphere Model: Zonal-mean climatology and physical parameterizations, J. Geophys. Res.-Atmos., 107, ACL 9-1–ACL 9-14, https://doi.org/10.1029/2001jd000479, 2002.

Fritts, D. C. and Alexander, M. J.: Gravity wave dynamics and effects in the middle atmosphere, Rev. Geophys., 41, 1003, https://doi.org/10.1029/2001RG000106, 2003.

Fujiwara, H. and Miyoshi, Y.: Morphological features and variations of temperature in the upper thermosphere simulated by a whole atmosphere GCM, Ann. Geophys., 28, 427–437, https://doi.org/10.5194/angeo-28-427-2010, 2010.

Fuller-Rowell, T. J., Akmaev, R. A., Wu, F., Anghel, A., Maruyama, N., Anderson, D. N., Codrescu, M. V., Iredell, M., Moorthi, S., Juang, H. M., and Hou, Y. T.: Impact of terrestrial weather on the upper atmosphere, Geophys. Res. Lett., 35, L09808, https://doi.org/10.1029/2007gl032911, 2008.

Garcia, R., Marsh, D., Kinnison, D., Boville, B., and Sassi, F.: Simulation of secular trends in the middle atmosphere, 1950–2003, J. Geophys. Res.-Atmos., 112, D09301, https://doi.org/10.1029/2006jd007485, 2007.

Giorgetta, M., Manzini, E., Roeckner, E., Esch, M., and Bengtsson, L.: Climatology and forcing of the quasi-biennial oscillation in the MAECHAM5 model, J. Climate, 19, 3882–3901, https://doi.org/10.1175/jcli3830.1, 2006.

Griffin, D. and Thuburn, J.: Numerical effects on vertical wave propagation in deep-atmosphere models, Q. J. Roy. Meteor. Soc., 144, 567–580, https://doi.org/10.1002/qj.3229, 2018.

Griffith, M. J., Jackson, D. R., Griffin, D. J., and Budd, C. J.: Stable extension of the unified model into the mesosphere and lower thermosphere, J. Space Weather Spac., 10, 19, https://doi.org/10.1051/swsc/2020018, 2020.

Hickey, M., Walterscheid, R., and Schubert, G.: Gravity wave heating and cooling of the thermosphere: Sensible heat flux and viscous flux of kinetic energy, J. Geophys. Res.-Space, 116, A12326, https://doi.org/10.1029/2011ja016792, 2011.

Hocking, W., Fuller, B., and Vandepeer, B.: Real-time determination of meteor-related parameters utilizing modern digital technology, J. Atmos. Sol.-Terr. Phy., 63, 155–169, https://doi.org/10.1016/s1364-6826(00)00138-3, 2001.

Jackson, D. R., Fuller-Rowell, T. J., Griffin, D. J., Griffith, M. J., Kelly, C. W., Marsh, D. R., and Walach, M.-T.: Future Directions for Whole Atmosphere Modelling: Developments in the context of space weather, Space Weather, 17, 1342–1350, https://doi.org/10.1029/2019sw002267, 2019.

Jackson, D. R., Bruinsma, S., Negrin, S., Stolle, C., Budd, C. J., Gonzalez, R. D., Down, E., Griffin, D. J., Griffith, M. J., Kervalishvili, G. and Arenillas, D. L.: The Space Weather Atmosphere Models and Indices (SWAMI) Project: Overview and first results, J. Space Weather Spac., 10, 18, https://doi.org/10.1051/swsc/2020019, 2020.

Jin, H., Miyoshi, Y., Pancheva, D., Mukhtarov, P., Fujiwara, H., and Shinagawa, H.: Response of migrating tides to the stratospheric sudden warming in 2009 and their effects on the ionosphere studied by a whole atmosphere-ionosphere model GAIA with COSMIC and TIMED/SABER observations, J. Geophys. Res.-Space, 117, A10323, https://doi.org/10.1029/2012ja017650, 2012.

Jones Jr., M., Forbes, J., Hagan, M., and Maute, A.: Impacts of vertically propagating tides on the mean state of the ionosphere-thermosphere system, J. Geophys. Res.-Space, 119, 2197–2213, https://doi.org/10.1002/2013ja019744, 2014.

Klimenko, M. V., Klimenko, V. V., Bessarab, F. S., Sukhodolov, T. V., Vasilev, P. A., Karpov, I. V., Korenkov, Y. N., Zakharenkova, I. E., Funke, B., and Rozanov, E. V.: Identification of the mechanisms responsible for anomalies in the tropical lower thermosphere/ionosphere caused by the January 2009 sudden stratospheric warming, J. Space Weather Spac., 9, A39, https://doi.org/10.1051/swsc/2019037, 2019.

Korenkov, Y. N., Klimenko, V. V., Klimenko, M. V., Bessarab, F. S., Korenkova, N. A., Ratovsky, K. G., Chernigovskaya, M. A., Shcherbakov, A. A., Sahai, Y., Fagundes, P. R., and De Jesus, R.: The global thermospheric and ionospheric response to the 2008 minor sudden stratospheric warming event, J. Geophys. Res.-Space, 117, A10309, https://doi.org/10.1029/2012ja018018, 2012.

Lieberman, R., Oberheide, J., Hagan, M., Remsberg, E., and Gordley, L.: Variability of diurnal tides and planetary waves during November 1978–May 1979, J. Atmos. Sol.-Terr. Phy., 66, 517–528, https://doi.org/10.1016/j.jastp.2004.01.006, 2004.

Lieberman, R., Akmaev, R., Fuller-Rowell, T., and Doornbos, E.: Thermospheric zonal mean winds and tides revealed by CHAMP, Geophys. Res. Lett., 40, 2439–2443, https://doi.org/10.1002/grl.50481, 2013.

Lilienthal, F., Yiğit, E., Samtleben, N., and Jacobi, C.: Variability of Gravity Wave Effects on the Zonal Mean Circulation and Migrating Terdiurnal Tide as Studied with the Middle and Upper Atmosphere Model (MUAM2019) Using a Whole Atmosphere Nonlinear Gravity Wave Scheme, Frontiers in Astronomy and Space Sciences, 7, 588956, https://doi.org/10.3389/fspas.2020.588956, 2020.

Liu, H.-L.: Variability and predictability of the space environment as related to lower atmosphere forcing, Space Weather, 14, 634–658, https://doi.org/10.1002/2016SW001450, 2016.

Liu, H. L., Foster, B. T., Hagan, M. E., McInerney, J. M., Maute, A., Qian, L., Richmond, A. D., Roble, R. G., Solomon, S. C., Garcia, R. R., and Kinnison, D.: Thermosphere extension of the whole atmosphere community climate model, J. Geophys. Res.-Space, 115, A12302, https://doi.org/10.1029/2010JA015586, 2010.

Liu, H. L., Bardeen, C. G., Foster, B. T., Lauritzen, P., Liu, J., Lu, G., Marsh, D. R., Maute, A., McInerney, J. M., Pedatella, N. M., and Qian, L.: Development and validation of the Whole Atmosphere Community Climate Model with thermosphere and ionosphere extension (WACCM-X 2.0), J. Adv. Model. Earth Sy., 10, 381–402, https://doi.org/10.1002/2017ms001232, 2018a.

Liu, J., Liu, H., Wang, W., Burns, A. G., Wu, Q., Gan, Q., Solomon, S. C., Marsh, D. R., Qian, L., Lu, G., and Pedatella, N. M.: First results from the ionospheric extension of WACCM-X during the deep solar minimum year of 2008, J. Geophys. Res.-Space, 123, 1534–1553, https://doi.org/10.1002/2017ja025010, 2018b.

Manzini, E., Giorgetta, M., Esch, M., Kornblueh, L., and Roeckner, E.: The influence of sea surface temperatures on the northern winter stratosphere: Ensemble simulations with the MAECHAM5 model, J. Climate, 19, 3863–3881, https://doi.org/10.1175/jcli3826.1, 2006.

McLandress, C.: The seasonal variation of the propagating diurnal tide in the mesosphere and lower thermosphere. Part I: The role of gravity waves and planetary waves, J. Atmos. Sci., 59, 893–906, https://doi.org/10.1175/1520-0469(2002)059<0893:tsvotp>2.0.co;2, 2002.

Medvedev, A. and Klaassen, G.: Thermal effects of saturating gravity waves in the atmosphere, J. Geophys. Res.-Atmos., 108, ACL 4-1–ACL 4-18, https://doi.org/10.1029/2002jd002504, 2003.

Meraner, K. and Schmidt, H.: Transport of nitrogen oxides through the winter mesopause in HAMMONIA, J. Geophys. Res.-Atmos., 121, 2556–2570, https://doi.org/10.1002/2015jd024136, 2016.

Millward, G., Moffett, R., Quegan, S., and Fuller-Rowell, T.: A coupled thermosphere-ionosphere-plasmasphere model (CTIP), Solar-Terrestrial Energy Program: Handbook of Ionospheric Models, edited by: Schunk, R. W., 239–279, Cent. for Atmos. and Space Sci., Utah State Univ., Logan, Utah, available at: https://www.bc.edu/content/dam/bc1/offices/ISR/SCOSTEP/Multimedia/other/ionospheric-models.pdf (last access: 8 June 2021), 1996.

Mitchell, N. J.: University of Bath: Rothera Skiymet Meteor Radar data (2005–present), Centre for Environmental Data Analysis, available at: https://catalogue.ceda.ac.uk/uuid/aa44e02718fd4ba49cefe36d884c6e50 (last access: 8 June 2021), 2019a.

Mitchell, N. J.: University of Bath: Ascension Island Skiymet Meteor Radar data (2001–2012), Centre for Environmental Data Analysis, available at: https://catalogue.ceda.ac.uk/uuid/0d05cf74e17f49c2b7c5cd02faa59291 (last access: 8 June 2021), 2019b.

Mitchell, N., Pancheva, D., Middleton, H., and Hagan, M.: Mean winds and tides in the Arctic mesosphere and lower thermosphere, J. Geophys. Res.-Space, 107, SIA 2-1–SIA 2-14, https://doi.org/10.1029/2001ja900127, 2002.

Miyahara, S. and Forbes, J. M.: Interactions between gravity waves and the diurnal tide in the mesosphere and lower thermosphere, J. Meteorol. Soc. Jpn. Ser. II, 69, 523–531, https://doi.org/10.2151/jmsj1965.69.5_523, 1991.

Miyahara, S., Yoshida, Y., and Miyoshi, Y.: Dynamic coupling between the lower and upper atmosphere by tides and gravity waves, J. Atmos. Terr. Phys., 55, 1039–1053, https://doi.org/10.1016/0021-9169(93)90096-h, 1993.

Miyoshi, Y. and Fujiwara, H.: Gravity waves in the thermosphere simulated by a general circulation model, J. Geophys. Res.-Atmos., 113, D01101, https://doi.org/10.1029/2007jd008874, 2008.

Miyoshi, Y. and Yiğit, E.: Impact of gravity wave drag on the thermospheric circulation: implementation of a nonlinear gravity wave parameterization in a whole-atmosphere model, Ann. Geophys., 37, 955–969, https://doi.org/10.5194/angeo-37-955-2019, 2019.

Oberheide, J., Forbes, J., Häusler, K., Wu, Q., and Bruinsma, S.: Tropospheric tides from 80 to 400 km: Propagation, interannual variability, and solar cycle effects, J. Geophys. Res.-Atmos., 114, D00I05, https://doi.org/10.1029/2009jd012388, 2009.

Palo, S., Forbes, J., Zhang, X., Russell III, J., and Mlynczak, M.: An eastward propagating two-day wave: Evidence for nonlinear planetary wave and tidal coupling in the mesosphere and lower thermosphere, Geophys. Res. Lett., 34, L07807, https://doi.org/10.1029/2006gl027728, 2007.

Pancheva, D., Merzlyakov, E., Mitchell, N. J., Portnyagin, Y., Manson, A. H., Jacobi, C., Meek, C. E., Luo, Y., Clark, R. R., Hocking, W. K., and MacDougall, J.: Global-scale tidal variability during the PSMOS campaign of June–August 1999: interaction with planetary waves, J. Atmos. Sol.-Terr. Phy., 64, 1865–1896, https://doi.org/10.1016/s1364-6826(02)00199-2, 2002.

Pancheva, D. V. and Mitchell, N. J.: Planetary waves and variability of the semidiurnal tide in the mesosphere and lower thermosphere over Esrange (68° N, 21° E) during winter, J. Geophys. Res.-Space, 109, A08307, https://doi.org/10.1029/2004ja010433, 2004.

Park, J., Lühr, H., Lee, C., Kim, Y. H., Jee, G., and Kim, J.-H.: A climatology of medium-scale gravity wave activity in the midlatitude/low-latitude daytime upper thermosphere as observed by CHAMP, J. Geophys. Res.-Space, 119, 2187–2196, https://doi.org/10.1002/2013ja019705, 2014.

Pogoreltsev, A.: Generation of normal atmospheric modes by stratospheric vacillations, Izv. Atmos. Ocean. Phy+., 43, 423–435, https://doi.org/10.1134/s0001433807040044, 2007.

Pogoreltsev, A., Vlasov, A., Fröhlich, K., and Jacobi, C.: Planetary waves in coupling the lower and upper atmosphere, J. Atmos. Sol.-Terr. Phy., 69, 2083–2101, https://doi.org/10.1016/j.jastp.2007.05.014, 2007.

Riggin, D., Meyer, C., Fritts, D., Jarvis, M., Murayama, Y., Singer, W., Vincent, R., and Murphy, D.: MF radar observations of seasonal variability of semidiurnal motions in the mesosphere at high northern and southern latitudes, J. Atmos. Sol.-Terr. Phy., 65, 483–493, https://doi.org/10.1016/s1364-6826(02)00340-1, 2003.

Riggin, D. M. and Lieberman, R. S.: Variability of the diurnal tide in the equatorial MLT, J. Atmos. Sol.-Terr. Phy., 102, 198–206, https://doi.org/10.1016/j.jastp.2013.05.011, 2013.

Sandford, D. J., Beldon, C. L., Hibbins, R. E., and Mitchell, N. J.: Dynamics of the Antarctic and Arctic mesosphere and lower thermosphere – Part 1: Mean winds, Atmos. Chem. Phys., 10, 10273–10289, https://doi.org/10.5194/acp-10-10273-2010, 2010.

Scaife, A., Butchart, N., Warner, C., and Swinbank, R.: Impact of a spectral gravity wave parameterization on the stratosphere in the Met Office Unified Model, J. Atmos. Sci., 59, 1473–1489, https://doi.org/10.1175/1520-0469(2002)059<1473:ioasgw>2.0.co;2, 2002.

Schmidt, H., Brasseur, G., Charron, M., Manzini, E., Giorgetta, M., Diehl, T., Fomichev, V., Kinnison, D., Marsh, D., and Walters, S.: The HAMMONIA chemistry climate model: Sensitivity of the mesopause region to the 11-year solar cycle and CO_2 doubling, J. Climate, 19, 3903–3931, https://doi.org/10.1175/jcli3829.1, 2006.

Smith, A. K., Pancheva, D. V., Mitchell, N. J., Marsh, D. R., Russell III, J. M., and Mlynczak, M. G.: A link between variability of the semidiurnal tide and planetary waves in the opposite hemisphere, Geophys. Res. Lett., 34, L07809, https://doi.org/10.1029/2006gl028929, 2007.

Stober, G., Janches, D., Matthias, V., Fritts, D., Marino, J., Moffat-Griffin, T., Baumgarten, K., Lee, W., Murphy, D., Kim, Y. H., Mitchell, N., and Palo, S.: Seasonal evolution of winds, atmospheric tides, and Reynolds stress components in the Southern Hemisphere mesosphere–lower thermosphere in 2019, Ann. Geophys., 39, 1–29, https://doi.org/10.5194/angeo-39-1-2021, 2021.

Suvorova, E. and Pogoreltsev, A.: Modeling of nonmigrating tides in the middle atmosphere, Geomagn. Aeronomy+., 51, 105–115, https://doi.org/10.1134/s0016793210061039, 2011.

Teitelbaum, H. and Vial, F.: On tidal variability induced by nonlinear interaction with planetary waves, J. Geophys. Res.-Space, 96, 14169–14178, https://doi.org/10.1029/91ja01019, 1991.

Trinh, Q. T., Ern, M., Doornbos, E., Preusse, P., and Riese, M.: Satellite observations of middle atmosphere–thermosphere vertical coupling by gravity waves, Ann. Geophys., 36, 425–444, https://doi.org/10.5194/angeo-36-425-2018, 2018.

Vadas, S., Liu, H.-L., and Lieberman, R.: Numerical modeling of the global changes to the thermosphere and ionosphere from the dissipation of gravity waves from deep convection, J. Geophys. Res.-Space, 119, 7762–7793, https://doi.org/10.1002/2014ja020280, 2014.

Vitharana, A., Zhu, X., Du, J., Oberheide, J., and Ward, W. E.: Statistical Modeling of Tidal Weather in the Mesosphere and Lower Thermosphere, J. Geophys. Res.-Atmos., 124, 9011–9027, https://doi.org/10.1029/2019jd030573, 2019.

Walters, D., Baran, A. J., Boutle, I., Brooks, M., Earnshaw, P., Edwards, J., Furtado, K., Hill, P., Lock, A., Manners, J., Morcrette, C., Mulcahy, J., Sanchez, C., Smith, C., Stratton, R., Tennant, W., Tomassini, L., Van Weverberg, K., Vosper, S., Willett, M., Browse, J., Bushell, A., Carslaw, K., Dalvi, M., Essery, R., Gedney, N., Hardiman, S., Johnson, B., Johnson, C., Jones, A., Jones, C., Mann, G., Milton, S., Rumbold, H., Sellar, A., Ujiie, M., Whitall, M., Williams, K., and Zerroukat, M.: The Met Office Unified Model Global Atmosphere 7.0/7.1 and JULES Global Land 7.0 configurations, Geosci. Model Dev., 12, 1909–1963, https://doi.org/10.5194/gmd-12-1909-2019, 2019.

Warner, C. and McIntyre, M.: An ultrasimple spectral parameterization for nonorographic gravity waves, J. Atmos. Sci., 58, 1837–1857, https://doi.org/10.1175/1520-0469(2001)058<1837:auspfn>2.0.co;2, 2001.

Wilhelm, S., Stober, G., and Chau, J. L.: A comparison of 11-year mesospheric and lower thermospheric winds determined by meteor and MF radar at 69° N, Ann. Geophys., 35, 893–906, https://doi.org/10.5194/angeo-35-893-2017, 2017.

Wood, N., Staniforth, A., White, A., Allen, T., Diamantakis, M., Gross, M., Melvin, T., Smith, C., Vosper, S., Zerroukat, M., and Thuburn, J.: An inherently mass-conserving semi-implicit semi-Lagrangian discretization of the deep-atmosphere global non-hydrostatic equations, Q. J. Roy. Meteor. Soc., 140, 1505–1520, https://doi.org/10.1002/qj.2235, 2014.

Yiğit, E. and Medvedev, A. S.: Heating and cooling of the thermosphere by internal gravity waves, Geophys. Res. Lett., 36, L14807, https://doi.org/10.1029/2009gl038507, 2009.

Yiğit, E. and Medvedev, A. S.: Internal wave coupling processes in Earth's atmosphere, Adv. Space Res., 55, 983–1003, https://doi.org/10.1016/j.asr.2014.11.020, 2015.

Yiğit, E. and Medvedev, A. S.: Influence of parameterized small-scale gravity waves on the migrating diurnal tide in Earth's thermosphere, J. Geophys. Res.-Space, 122, 4846–4864, https://doi.org/10.1002/2017ja024089, 2017.

Yiğit, E., Aylward, A. D., and Medvedev, A. S.: Parameterization of the effects of vertically propagating gravity waves for thermosphere general circulation models: Sensitivity study, J. Geophys. Res.-Atmos., 113, D19106, https://doi.org/10.1029/2008jd010135, 2008.

Yiğit, E., Medvedev, A. S., Aylward, A. D., Hartogh, P., and Harris, M. J.: Modeling the effects of gravity wave momentum deposition on the general circulation above the turbopause, J. Geophys. Res.-Atmos., 114, D07101, https://doi.org/10.1029/2008jd011132, 2009.

Yiğit, E., Knížová, P. K., Georgieva, K., and Ward, W.: A review of vertical coupling in the Atmosphere–Ionosphere system: Effects of waves, sudden stratospheric warmings, space weather, and of solar activity, J. Atmos. Sol.-Terr. Phy., 141, 1–12, https://doi.org/10.1016/j.jastp.2016.02.011, 2016.

Yiğit, E., Medvedev, A. S., and Ern, M.: Effects of Latitude-Dependent Gravity Wave Source Variations on the Middle and Upper Atmosphere, Frontiers in Astronomy and Space Sciences, 7, 614018, https://doi.org/10.3389/fspas.2020.614018, 2021.

6.2. Conclusions

The addition of a non-LTE radiation scheme was detailed and the monthly mean background winds and tidal amplitudes and phases produced by the ExUM are compared rigorously with meteor radar observations between 80 and 100 km.

The results of this work indicate that the ExUM has a good inherent capability to capture background winds and tides in the MLT, despite the use of relaxation to a relatively simplified global temperature field and the use of monthly ozone background fields. However, there were significant differences in the detail with the background winds, particularly in the polar regime, with the ExUM winds primarily westward in austral winter compared to observed eastward winds.

The gravity wave parameterisation used in the model does not include the in-situ generation of non-primary gravity waves, and model runs with the USSP off indicate that the scheme is not providing appropriate forcing in the MLT. To this end, development and redesign of the gravity wave schemes for use in the MLT is clearly necessary. This work is beyond the scope of this PhD, but what can be done is to gain further insight into how these schemes should be developed and recommend further studies to improve their capability – we approach this topic in the next Chapter, where we perform an analysis of migrating and non-migrating modes in the model.

Chapter 7

Analysis of Migrating and Non-Migrating Tides of the Extended Unified Model in the Mesosphere and Lower Thermosphere

In this chapter, we perform a first analysis of non-migrating tides in the Extended Unified Model as well as examining the latitudinal and short-term variability of the migrating modes. This uses and builds on the stable ExUM initially produced in Chapter 5, and modified in Chapter 6. This joint work was produced with Nicholas J. Mitchell and has been submitted to *Annales Geophysicae* as an open access publication.

7.1. Outline of the Article

We analyse the modelled temperature, zonal wind and meridional wind fields produced by the model, and extract the tidal perturbations of these fields. With this, we obtain a detailed analysis of the broad spectrum of spatial and temporal modes of atmospheric tides present in the model. We present the first results illustrating the non-migrating (not sun-following) tidal modes present in the model, and also show the latitudinal and short-term variation of both migrating and non-migrating modes.

We begin with an introduction to atmospheric tides and the drivers of both migrating and non-migrating tides. Further, we detail other high-top models and important aspects for modelling in the MLT such as a non-orographic gravity wave parameterisation scheme.

We then present the developments made to the ExUM, building on those in Chapter 6, such as a nudging scheme which now varies with month and latitude, as well as an improved vertical resolution, which becomes coarser with increased height to reflect the increase in vertical wavelengths/scale height in the thermosphere, as suggested in Chapter 5.

Following this, the results of the tidal analysis using the ExUM with these new developments are presented. We provide an initial exploration of the model fields, looking at instantaneous tidal perturbations for the three model fields considered. We then restrict our attention to the latitudes considered previously (Rothera (68° S) and Ascension Island (8° S)), and look at how the instantaneous tidal variations vary with height as well as the non-migrating modes present at each of these two locations. Finally, we present the latitudinal and short-term variation for both the migrating and non-migrating components at a height of 95 km for modelled temperature, zonal wind and meridional wind.

In Section 4, we discuss how the fields produced by the ExUM compare with other studies of migrating and non-migrating tides using a combination of models and observational datasets. To aid this discussion, we also take a closer look at the eastward propagating diurnal tide with zonal wavenumber 3, examining the change in its magnitude with increasing height.

Appendix 6B: Statement of Authorship

This declaration concerns the article entitled:			
Analysis of Migrating and Non-Migrating Tides of the Extended Unified Model in the Mesosphere and Lower Thermosphere			
Publication status (tick one) **Draft manuscript** ☐ **Submitted** ☐ **In review** X **Accepted** ☐ **Published** ☐			
Publication details (reference)	Journal: Annales Geophysicae Authors: Matthew J. Griffith, Nicholas J. Mitchell		
Copyright status (tick the appropriate statement) I hold the copyright for this material X — Copyright is retained by the publisher, but I have been given permission to replicate the material here ☐			
Candidate's contribution to the paper (provide details, and also indicate as a percentage)	The bulk of the work for this article was performed by the author of the thesis (80%). The formulation of ideas for this paper was performed by the author of this thesis. The research direction for this paper was dictated by the author of this thesis. The design of methodology was led by the author of this thesis (75%). The bulk of the presentation of the content was performed by the author of the thesis (90%). The author's contribution in particular was in performing the model runs for comparison with meteor radar data; implementing improvements to the model's nudging scheme and vertical level set; performing the non-migrating tidal analysis on the model data; preparation of all figures; and leading the authoring of the manuscript with some contribution from Nicholas J. Mitchell.		
Statement from Candidate	This paper reports on original research I conducted during the period of my Higher Degree by Research candidature.		
Signed	Matthew J. GRIFFITH	**Date**	06/08/2021

Last update: Feb 2019

Analysis of Migrating and Non-Migrating Tides of the Extended Unified Model in the Mesosphere and Lower Thermosphere

Matthew J. Griffith[1] and Nicholas J. Mitchell[2,3]

[1]Department of Mathematical Sciences, University of Bath, Claverton Down, Bath, BA2 7AY, UK.
[2]Department of Electronic & Electrical Engineering, University of Bath, Claverton Down, Bath, BA2 7AY, United Kingdom.
[3]British Antarctic Survey, High Cross, Madingley Rd, Cambridge, CB3 0ET, United Kingdom.

Correspondence: Matthew Griffith (M.J.Griffith@bath.ac.uk)

Abstract. Atmospheric tides play a key role in coupling the lower, middle and upper atmosphere/ionosphere. The tides reach large amplitudes in the Mesosphere and Lower Thermosphere (MLT) where they can have significant fluxes of energy and momentum and so strongly influence the coupling and dynamics. The tides must therefore be accurately represented in Global Circulation Models (GCMs) that seek to model the coupling of atmospheric layers and impacts on the ionosphere. The tides consist of both migrating (sun-following) and non-migrating (not sun-following) components, both of which have important influences on the atmosphere. The Extended Unified Model (ExUM) is a recently developed version of the Met Office's GCM (the Unified Model) which has been extended to include the MLT. Here, we present the first in-depth analysis of migrating and non-migrating modes in the ExUM. We show that the ExUM produces both non-migrating and migrating tides in the MLT of significant amplitude across a rich spectrum of spatial and temporal modes. The dominant non-migrating modes in the MLT are found to be the DE3, DW2 and DW3 in the diurnal tide and the S0, SW1 and SW3 in the semidiurnal tide. These modes can have monthly mean amplitudes at a height of 95 km as large as 35 ms^{-1}/10 K. All the non-migrating modes exhibit a strong seasonal variability in amplitude and significant short-term variability is evident. Both the migrating and non-migrating modes exhibit notable variation with latitude. For example, the temperature and wind diurnal tides maximise at low latitudes and the semidiurnal tides include maxima at high latitudes. Our results demonstrate the capability of the ExUM for modelling atmospheric migrating and non-migrating tides and lay the foundation for its future development into a whole atmosphere model. To this end, we make specific recommendations on further developments which would improve the capability of the model.

1 Introduction

Atmospheric solar thermal tides are global-scale oscillations with a period exactly equal to one day or an integer fraction of one day. The solar thermal tides (hereafter, simply "tides") are excited primarily by the diurnal cycle in the solar heating of water vapour and ozone in the troposphere and stratosphere and the release of latent heat in deep tropospheric convection.

As the tides propagate upwards from their source regions their amplitudes increase because of the decreasing atmospheric gas density. In the mesosphere and lower thermosphere region (MLT) at heights of 80 - 100 km the tides cause large fluctuations in winds, temperature, density and many other atmospheric parameters, including airglow emissions, ice-particle concentrations

and trace-species densities etc. Tidal amplitudes in the MLT can exceed several 10s of m/s and they are often the largest-amplitude fluctuations of the MLT's field of waves and tides.

Observations have revealed that the largest-amplitude tides in the MLT are the 24-hour diurnal and 12-hour semidiurnal tides. Generally, the semidiurnal tide is observed to reach maximum amplitudes at high latitudes near about 60°N/60°S but has small amplitudes at low latitudes, whereas the diurnal tide reaches maximum amplitudes at low latitudes but has much smaller amplitudes at middle and high latitudes (Mitchell et al., 2002; Davis et al., 2013; Mukhtarov et al., 2009; Pancheva et al., 2010).

The importance of tides lies in the key role they play in coupling the lower, middle and upper atmosphere/ionosphere (see reviews by Smith, 2012; Yiğit and Medvedev, 2015; Liu, 2016; Yiğit et al., 2016). For instance, the tidal winds modulate the fluxes of gravity waves (GWs) and so influence the wave forcing of the general circulation (e.g., Fritts and Alexander, 2003). The energy and momentum deposited by tides can cause a substantial warming of the MLT and a downward displacement of, and reduction in, the gravity-wave momentum transfer (wave drag) in the upper mesosphere (Becker, 2017). Tidal temperature fluctuations can cause variability in the occurrence of polar mesospheric clouds (Fiedler et al., 2005). The tides propagate upwards from the MLT into the thermosphere where they can modulate the ionospheric wind dynamo (e.g., Oberheide et al., 2009; Yiğit and Medvedev, 2015; Liu, 2016). The tides may also mediate the ionospheric response to sudden stratospheric warmings (e.g., Goncharenko et al., 2010).

An important distinction is between the migrating (sun-synchronous) tides and the non-migrating (not-sun-synchronous) tides. Here we will use the standard notation to identify the different tidal modes. In this, a mode is identified as either D or S to denote that it has diurnal or semidiurnal period; E or W to denote eastward or westward propagation and s = 0, 1, 2, 3... to denote its zonal wavenumber. A DW1 tide is thus a diurnal, westward propagating tide of wavenumber 1, an SE2 tide is a semidiurnal, eastward propagating tide of wavenumber 2 and a D0 or S0 is a standing diurnal or semidiurnal oscillation, respectively, with no zonal propagation or variation in phase (also known as a "breathing" mode).

The migrating diurnal and semidiurnal modes are thus the DW1 and SW2 modes, respectively, that propagate westwards at sun-synchronous phase speeds and have zonal wavenumbers equal to the number of cycles of the tide per day. These tides are directly excited by the heating of the atmosphere by solar radiation. In contrast, the non-migrating tides are thought to be excited primarily by either i) longitudinal (land/sea) differences in the release of latent heat from deep tropospheric convection at tropical latitudes or ii) non-linear interactions between stationary planetary waves of zonal wavenumber 1 and the migrating tides. The latent-heat forcing is believed to primarily excite the diurnal modes DE1, DE2, DE3, DW2, DW5, D0 and the semidiurnal modes SW1, SE2, SW3 and SW6 (Forbes et al., 2003, 2007, 2008; Oberheide et al., 2006; Hagan and Forbes, 2002, 2003; Ekanayake et al., 1997; Oberheide et al., 2006). The non-linear interactions are thought to excite primarily the diurnal D0 and DW2 modes and the SW1 and SW3 modes (Hagan and Roble, 2001; Angelats i Coll and Forbes, 2002; Forbes and Wu, 2006; Murphy et al., 2009).

Tides propagating from the MLT into the thermosphere may drive significant modulation of F-region ionospheric density (see review by England, 2012). In general, although the migrating tides may produce strong day/night ionospheric variations, it is the non-migrating tides that can produce longitudinal variations in the ionosphere. These latter tides can modulate F-region

ionospheric density through mechanisms including i) electrodynamic coupling to the E-region dynamo, ii) plasma advection along geomagnetic field lines and iii) the modulation of photochemical equilibrium. Of particular note is that the conspicuous wavenumber-four structures observed in low-latitude total electron content have been suggested to result from a modulation of F-region density by a spectrum of non-migrating tidal modes (particularly DE3) (Hagan et al., 2007; Forbes et al., 2008).

The important role of the tides in atmospheric coupling means that they must be represented accurately in models intending to span the lower, middle and upper atmosphere/ionosphere. However, it is recognised that there are major aspects of tides that remain challenging to model and that the causes of tidal variability remain uncertain (e.g., Smith et al., 2007; Baldwin et al., 2019). In particular, model biases remain in both the seasonal variability of tides and their short-term variability at time scales of less than a month (e.g., Dempsey et al., 2021; Chang et al., 2012; Hagan and Forbes, 2002; Oberheide et al., 2011; Ortland and Alexander, 2006).

Understanding the sources, propagation, variability and impacts of non-migrating tides is therefore crucial in attempts to investigate and model the coupling of atmospheric layers and the ionosphere. However, observational studies of non-migrating tides are limited by inherent difficulties in resolving the various migrating and non-migrating tidal modes. For instance, there have been extensive ground-based observations made of tides in the MLT, in many cases made by meteor or MF radars (e.g., Murphy et al., 2007; Davis et al., 2013; Hibbins et al., 2019; Liu et al., 2020; Pancheva et al., 2021; Dempsey et al., 2021; Griffith et al., 2021). These radar observations usually offer excellent height and time resolution and are well suited to studies of tidal variability on time scales ranging from the day-to-day to the decadal - but observations made from a single site yield only the amplitudes, phases and vertical wavelengths of the superposition of migrating and non-migrating tides and cannot resolve the observed tidal oscillations into individual modes.

In contrast, satellite instruments can make global observations, but are often limited by the need for the satellite to precess through local time in order to resolve the various nonmigrating modes. This limits the time resolution of the measurements such that, for instance, in many studies of non-migrating tides, TIMED/SABER measurements have an effective time resolution of about 60 days (e.g., Forbes et al., 2008) and UARS/HRDI and UARS/MLS have time resolutions of about 30 days (e.g., Forbes et al., 2003; Forbes and Wu, 2006).

These limitations in the ability of ground-based and satellite observations to resolve non-migrating tides mean that models must play an important role in efforts to understand their nature and variability.

"High-top" General Circulation Models (GCMs), which cover height ranges from the ground to the upper atmosphere, have considerable utility in the study of vertical coupling processes (e.g. Yiğit et al., 2016; Pogoreltsev et al., 2007; Akmaev, 2011). Such models play an important part in attempts to capture the variability of the thermosphere and ionosphere for space weather-forecasting, as well as in producing Whole Atmosphere Models (e.g., Jackson et al., 2019; Liu, 2016; Akmaev, 2011; Fritts et al., 2008).

A summary of several of the recent key non-mechanistic "high-top" GCMs is given in Griffith et al. (2021). Here, we simply note that a number of such models exist including the following, i) The Whole Atmosphere Model (WAM; Akmaev et al., 2008; Fuller-Rowell et al., 2008); ii) The Whole Atmosphere Community Climate Model with thermosphere and ionosphere extension (WACCM-X; Liu et al., 2010, 2018); iii) The extended Canadian Middle Atmosphere Model (eCMAM; Beagley

et al., 2000); iv) The Ground-to-topside model of the Atmosphere and Ionosphere for Aeronomy (GAIA; Fujiwara and Miyoshi, 2010; Jin et al., 2012, and references therein); v) The Hamburg Model of the Neutral and Ionized Atmosphere (HAMMONIA; Schmidt et al., 2006; Meraner and Schmidt, 2016); vi) The upper-atmosphere extension of ICON (Borchert et al., 2019); vii) The Entire Atmosphere GLobal model (EAGLE; Klimenko et al., 2019); viii) The HI Altitude Mechanistic General Circulation Model (HIAMCM; Becker and Vadas, 2020); ix) The Coupled Middle Atmosphere Thermosphere-2 (CMAT-2; Yiğit et al., 2009); x) The University of Leipzig Middle and Upper Atmosphere Model (MUAM; Pogoreltsev, 2007; Pogoreltsev et al., 2007; Suvorova and Pogoreltsev, 2011); and xi) The whole atmosphere Kyushu GCM (Miyoshi and Fujiwara, 2008; Miyoshi and Yiğit, 2019).

Several other models are also relevant in studies of tides and coupling. These include, i) The NCAR Thermosphere Ionosphere Mesosphere Electrodynamics General Circulation Model (TIME-GCM; Roble and Ridley, 1994; Hagan and Roble, 2001; Yamashita et al., 2010); ii) The linear mechanistic Global Wave Scale Model (GWSM; Hagan et al., 1999; Hagan and Forbes, 2002); and, iii) The Climatological Tidal Model of the Thermosphere (CTMT; Oberheide et al., 2011).

In the context of these various "high-top" models, the new Extended Unified Model (ExUM; Griffith et al., 2020, 2021) extends the standard UM (Unified Model) (Walters et al., 2017) to the lower thermosphere. The model itself and its development for the lower thermosphere is described further in Sect. 2.1, but we highlight here that the ExUM does not make the hydrostatic assumption and uses the deep-atmosphere equations of motion, making it a good candidate for modelling atmospheric tides.

Griffith et al. (2021) investigated the ability of the ExUM to reproduce the observed winds and diurnal and semidiurnal tides of the MLT and compared them with meteor-radar observations at characteristic equatorial and polar locations (Ascension Island (8°S, 14°W) and Rothera (68°S, 68°W), respectively). The study demonstrated that, although there are biases in the model tidal fields, they nevertheless capture many essential features of the observed tides. However, Griffith et al. (2021) did not decompose the model tidal fields into migrating and non-migrating components, nor did they examine the latitudinal structure of the tides beyond the two locations considered.

It is also worth introducing here the importance of deposition of momentum by sub-grid scale non-orographic GWs, which must be accurately captured in parameterization schemes because of their important impact on tides in the MLT (e.g., Yiğit and Medvedev, 2017; Yiğit et al., 2009; Miyahara and Forbes, 1991). For example, Yiğit and Medvedev (2017) provide an extensive discussion into the influence of parameterized small-scale GWs on the migrating diurnal tide. The gravity-wave scheme used in the ExUM is detailed in Sect. 2.

Here we present the first use of the new ExUM to investigate the variability and latitudinal structure of tides in the MLT – the region where tidal amplitudes become large. We ask the following scientific questions: i) what are the characteristics of the combined migrating and non-migrating tidal modes in the MLT of the new ExUM? ii) what is the contribution of individual migrating and non-migrating modes at the high and low latitudes where the semidiurnal and diurnal modes, respectively, are believed dominant? iii) how do the various tidal modes in the ExUM compare with those observed? and iv) what improvements can be suggested to be made in the ExUM to increase its ability to model tides in the MLT?

In Sect. 2 we describe the development of the ExUM version used. In Sect. 3 we present details of the principal non-migrating diurnal and semidiurnal tides and investigate the latitudinal and short-term variability of both the migrating and non-migrating

tides. As with Griffith et al. (2021), we use the characteristic equatorial and polar latitudes of Ascension Island (8°S) and Rothera (68°S). Finally, in Sect. 4 and Sect. 5 we place our results in the context of other tidal studies and consider how our results can guide future development of the ExUM.

2 Model development

2.1 The Extended Unified Model

The General Circulation Model (GCM) employed by the UK Met Office is the Unified Model (UM), which models both climate and weather forecast time scales with a unified approach. The model consists of two main parts – atmospheric dynamics and atmospheric physics. The former involves solving the Euler equations of motion governing atmospheric flow, and contains the *dynamical core* of the model; the latter attempts to make up for atmospheric physics not captured or resolved by the model dynamics, such as solar radiation and sub-grid scale GWs through *physical parameterizations* – see Walters et al. (2017) for more information on the complete formulation of the UM and Wood et al. (2014) for more information on the model dynamics.

The horizontal resolution is fixed at $1.25°$ N$\times 1.875°$ E and the vertical resolution is extended above the 85-level, 85 km standard UM configuration to a 100-level, 120 km configuration detailed below. Given the lack of modelled ionospheric effects such as ion drag in this model, we only consider fields up to around 110 km. This yields the previously mentioned Extended Unified Model which extends the working height of the standard UM into the lower thermosphere – initial work to perform this extension is discussed in Griffith et al. (2020). Following this research, the radiation scheme was extended to include non-LTE effects and the model temperature now contains the appropriate realistic forcing up to around 90 km. This work is detailed by Jackson et al. (2020) and discussed further in Griffith et al. (2021).

Latent heat release in the model is captured primarily through the UM convection schemes and associated large-scale cloud and cloud fraction schemes (see Sect. 2.5, 3.6.2 and 3.7 of Walters et al. (2017) for a more detailed description of the parameterizations used).

The ExUM uses the non-orographic Ultra Simple Spectral Parameterization (USSP) of Warner and McIntyre (2001). The USSP scheme treats non-orographic GWs with non-zero phase speeds which are unable to be resolved by the model. The approach used is that of Warner and McIntyre (2001) with further modifications (Scaife et al., 2002) to launch an unsaturated spectrum from a level close to the surface and to impose a homogeneous (location invariant) total vertical flux of horizontal wave pseudomomentum. The spectrum uses a characteristic vertical wavelength peak of 4.3 km and parameterizes vertical wavelengths up to a maximum of 20 km. The amplitude of the spectrum is chosen to give momentum deposition and, hence, a Quasi-Biennial Oscillation (QBO) in the model that is realistic. For comparison with other parameterizations, a typical value of the total launch flux in all four directions is $6.6\times10^{-3}\,\mathrm{kgm^{-1}s^{-1}}$.

The inclusion of thermal effects is also important in the MLT (e.g., Yiğit and Medvedev, 2009; Medvedev and Klaassen, 2003; Hickey et al., 2011), and the USSP includes frictional heating due to gravity wave dissipation, and consequent loss of kinetic energy (see Walters et al. (2017) for more details), but does not include ionospheric heating effects such as ion drag.

The aptitude of the USSP for use in the MLT and steps for its future development will be discussed in light of the results of this study.

Above around 90 km, the lack of appropriate high atmosphere chemistry and consequent heating via exothermic reactions means that the model temperature values cannot be assumed to be accurate. Given this lack of appropriate chemistry, a relaxation or nudging scheme to a climatological temperature field is used above 90 km (this scheme was first developed in Griffith et al. (2020) and more details can be found therein). Previously, as in Griffith et al. (2021), the temperature profile used in the nudging scheme was globally uniform, and so latitudinal variation in the MLT was only very weak, e.g. the summertime polar mesopause minimum was observed but not captured in a realistic manner. Thus, following this research, it was deemed that a more realistic temperature profile would be beneficial for the accuracy of the model in the MLT. To this end, the globally uniform temperature profile is replaced in this study with a temperature profile which varies by month and season, and with a varying mesopause height. This analytic temperature profile was calculated using a least-squares curve fitting algorithm, fitting to temperatures from the Committee on Space Research (COSPAR) International Reference Atmosphere (CIRA) (Fleming et al., 1990). Whilst this is an old data set, it gives a good climatological representation of atmospheric temperature up to 120 km. As well as this, the temperature profile produced for the nudging scheme only need provide an approximate representation of the atmospheric state.

To produce the analytic temperature profile $T_{\text{nudge}}(t, \phi, z)$ – a function of month (t), latitude (ϕ) and height (z) – we first fit a function T_{min} of month (t) and latitude (ϕ) to the minimum temperature value in the CIRA data found at the mesopause. The fit is of the form

$$T_{\text{min}}(t, \phi) = a_{\text{T}} + b_{\text{T}} \cos\left(\frac{2\pi}{12}\,|t-6|\right) \cos\left(\frac{\pi}{2} + \frac{2\pi}{360}\phi\right).$$

We then fit a function z_{min} of month (t) and latitude (ϕ) to the height (in metres) at which this mesopause temperature minimum occurs in the CIRA data. This results in an analytic profile for the height of the mesopause. The fit is of the form

$$z_{\text{min}}(t, \phi) = a_{\text{z}} + b_{\text{z}} \cos\left(\frac{2\pi}{12}\,|t-6|\right) \cos\left(\frac{\pi}{2} + \frac{2\pi}{360}\phi\right)$$

In summary, we now have an analytic expression for both the temperature at the mesopause and the height of the mesopause as a function of month and latitude. Fitting the parameters to the CIRA data yields $a_{\text{T}} = 178.45$, $b_{\text{T}} = 25.73$, $a_{\text{z}} = 94065.91$ and $b_{\text{z}} = 4561.23$. We compare the use of these analytic profiles with the CIRA data in Figures 1 and 2.

It can be seen that the analytic function gives a reasonable fit to the measured temperatures for the purposes of the nudging scheme – the analytic expression remains relatively simple and we avoid overfitting.

From this, the height dependence can be created. The temperature lapses linearly to the mesopause temperature minimum from below, and then a power law fit is used above the mesopause up to the current model lid at 120 km. Namely, at a height z above the mesopause, we fit a function of the form

$$T_{\text{nudge}}(t, \phi, z) = T_{\text{min}}(t, \phi) + \Gamma_{\text{thermo}} \left(z - z_{\text{min}}(t, \phi)\right)^{k}.$$

This fit yields parameters $\Gamma_{\text{thermo}} = 4.03 \times 10^{-9}$ and $k = 2.41$. The zonal mean monthly mean variation in height above the mesopause can be seen in Figure 3. We observe a very good fit and the necessity of the power law fit is clearly demonstrated.

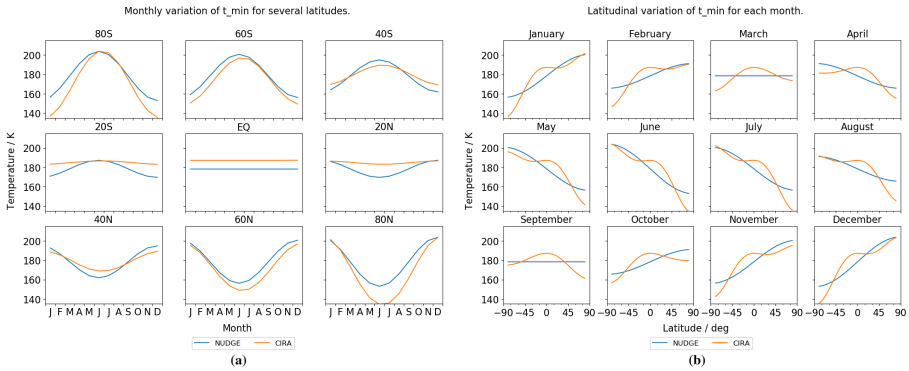

Figure 1. Variation of the fitted mesopause temperature profile $T_{\min}$ for **(a)** several latitudes as a function of month, and **(b)** all months as a function of latitude. The fitted function gives a reasonable fit for the purposes of the nudging scheme.

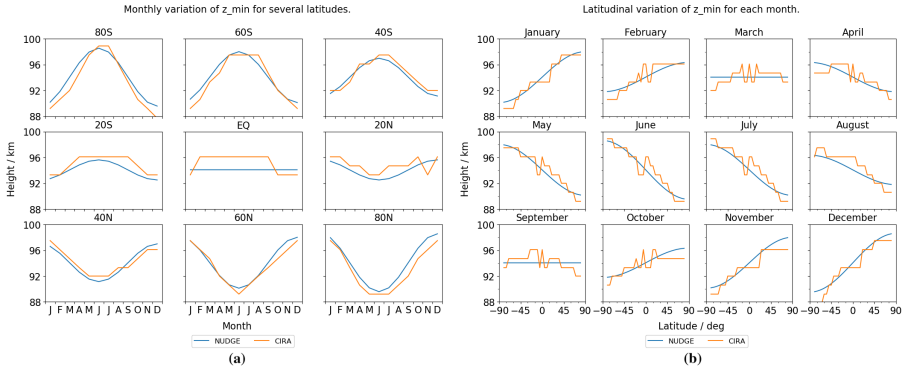

Figure 2. Variation of the fitted mesopause height profile $z_{\min}$ for **(a)** several latitudes as a function of month, and **(b)** all months as a function of latitude. The fitted function gives a reasonable fit for the purposes of the nudging scheme.

To summarise, this results in an ExUM which differs from the standard General Atmosphere (GA) 7.0 configuration of the UM (as described in Walters et al., 2017) in the following ways:

1. The model chemistry scheme is entirely switched off – the development of a chemistry scheme appropriate for the MLT is currently a work in progress.
2. Atmospheric aerosols are switched off and ozone background files are switched on.
3. The model upper boundary is raised from the standard 85 km to a height of 120 km.
4. The forcing from the radiation scheme now includes non-LTE effects which means it is physically realistic up to 90 km.
5. The temperature field above 90 km is nudged towards the prescribed monthly and latitudinally varying climatological temperature profile – this accounts for the lack of the chemistry scheme.

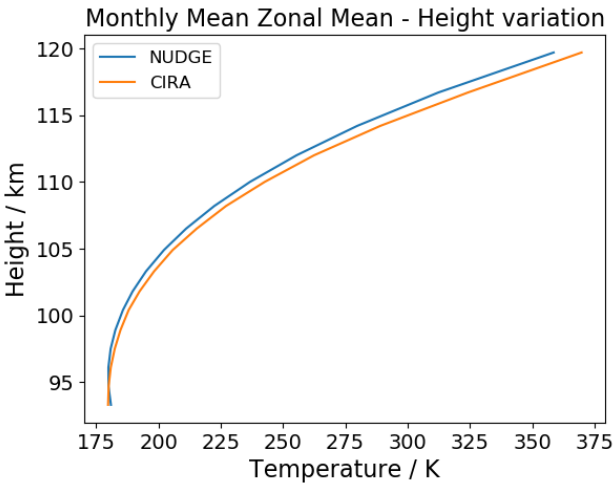

Figure 3. Variation of the zonal-mean monthly-mean fitted nudging profile with height.

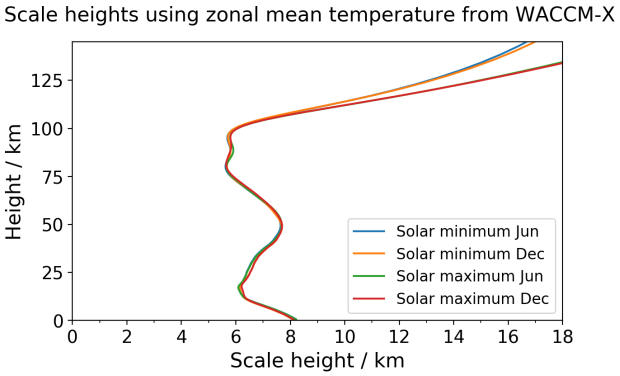

Figure 4. Atmospheric scale heights calculated using WACCM-X temperatures to give a baseline.

We now describe the vertical level set used. The implementation builds on that used in Griffith et al. (2020) and Griffith et al. (2021). We move away from the fixed vertical level depth above the mesopause used previously, and instead use the atmospheric scale height to construct the vertical level set. This allows physically important vertical wave scales to be captured appropriately whilst relieving the numerical instabilities which can come from a fine vertical level set (e.g., Griffin and Thuburn, 2018; Griffith et al., 2020).

The implementation is as follows. The atmospheric scale height $H = RT/g$ is calculated for summer/winter conditions at both solar maximum and solar minimum using WACCM-X temperature values (e.g., Liu et al., 2010, 2018). This gives a reasonable baseline from which to calculate the vertical level set (see Figure 4).

From this analysis, we decide to use zonal mean solar minimum conditions to create the vertical level set. This yields a vertical resolution which can capture wave scales appropriately throughout the solar cycle without the stringent condition

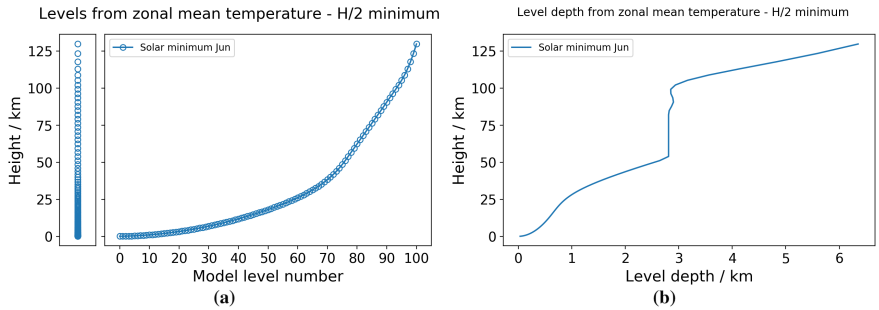

Figure 5. (a) Vertical level set and **(b)** corresponding level depths produced using the new implementation. The vertical level depth can be seen to be capped up to the mesopause, and then increase with increase in temperature going up through the thermosphere.

imposed by using zonal minimum temperatures. With an upper boundary at 120 km the effects of using the solar minimum temperature do not have much impact on the value of the scale height used, but with this condition in place the vertical level set can remain consistent when the upper boundary of the model is extended further into the thermosphere.

The vertical level depth remains the same as in the standard UM (namely increasing exponentially with increasing height from the lower boundary of the model), until the vertical depth reaches the value determined by the minimum value of $H/2$ found at the mesopause - we use $H/2$ to give a vertical 2 grid-point per scale height structure. At this point, we fix the vertical level depth at this value until the mesopause is reached.

Above the mesopause, the vertical level depth increases again with increasing height, and we use the value of $H/2$ to define each level depth. Namely, we add on a vertical level of depth $H/2$, read off the value of $H/2$ at the new atmospheric height reached, and then add on a vertical level with this depth, and so on. Thus, the vertical level depths gradually become larger and larger as the model reaches higher into the thermosphere. The levels and vertical level depths produced by this method can be seen in Figure 5.

This completes specification of the model. The model runs are then all initialised using the same operational analysis from 1 September 2000 at 00 UTC. This allows the model to settle after the initialisation – known as the spin-up period of the model. Following this, climatological data is used to force background fields such as atmospheric ozone. Thus, we primarily examine climatological fields in this study – the main focus of this work is to provide a closer look at the migrating and non-migrating modes of atmospheric tides present in the model.

An example of the climatological temperatures, zonal (u) winds and meridional (v) winds are provided for equinox and solstice conditions in Figure 6. The variation in the height of the mesopause can be clearly seen in the modelled temperature field. There are also still biases that exist in the model, such a summer wind reversal at middle latitudes which is at a lower altitude than expected and seasonal wind biases as discussed in Griffith et al. (2021). However, the goal of this paper is to provide an initial insight into the migrating and non-migrating tides present in the model and to educate improvements which can be made to correct these biases for future versions of the model.

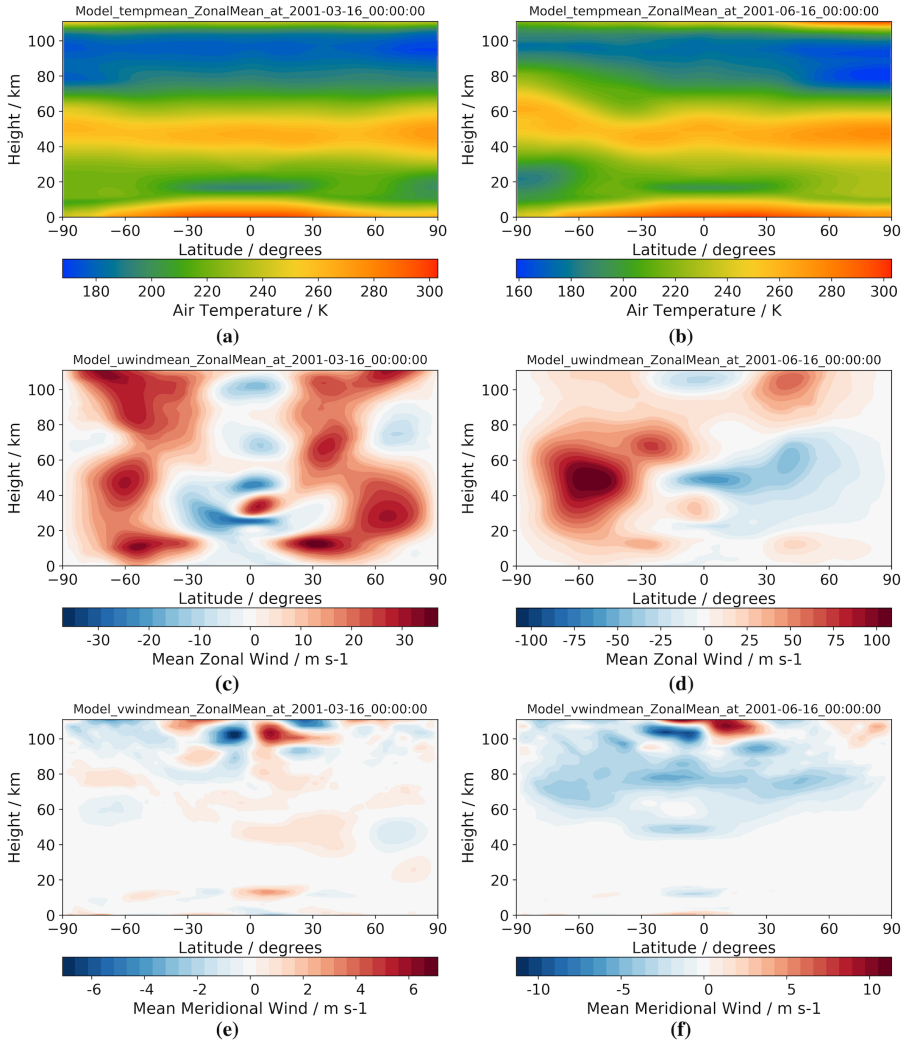

Figure 6. Latitude-height plot showing zonal-mean monthly-mean fields for equinox (March) conditions for **(a)** temperature, **(c)** zonal (u) winds and **(e)** meridional (v) winds, and for solstice (June) conditions also for **(b)** temperature, **(d)** zonal (u) winds and **(f)** meridional (v) winds.

The output attained from the model consists of hourly-sampled time profiles for temperature and both zonal and meridional wind fields for the whole of the model year considered – this high cadence is used so that diurnal and semidiurnal frequencies can be accurately resolved. For simplicity, we only show results for a single simulation, but multiple simulations were performed to verify these results leading to the same conclusions. From these model fields, we compute several diagnostics to examine the properties of the tides produced by the model. We first extract the tidal perturbations by removing the mean from the model fields. We then decompose these tidal perturbations into diurnal and semidiurnal components in time, as well

as several components in space. More precisely, we decompose the tidal perturbations by fitting a function of the form

$$F(t,\lambda) = A_0 + \sum_{i=1}^{2}\sum_{j=-6}^{6} A_{ij}\cos\left(it\frac{2\pi}{24} + j\lambda\frac{2\pi}{360} - \phi_{ij}\right),$$

for a given model field F varying in time (hours) and longitude (degrees). The amplitude of each component is then given by A_{ij} with ϕ_{ij} the corresponding phase.

3 Results

In this section, we present the ExUM migrating and non-migrating tides. We first look at instantaneous tidal perturbations as a function of latitude and height for the first day of January. Here, we look at the total migrating and non-migrating components, without decomposition into separate spatial modes. This provides some initial insight into the tidal properties of the modelled temperature, zonal and meridional wind fields as a superposition of all spatial modes.

Following this, we restrict our attention to two latitudes, an equatorial latitude at 8°S, and a polar latitude at 68°S. We choose these latitudes to examine two key regimes, namely the equatorial regime, where the migrating diurnal tide is dominant; and the polar regime, where the migrating semidiurnal tide is dominant. Numerous observational studies have been performed at these latitudes (e.g. the studies performed using meteor radar at Ascension Island and Rothera by Davis et al. (2013) and Dempsey et al. (2021)) as well as the previous ExUM study by Griffith et al. (2021). For both these regimes, we first examine their variation with height using instantaneous tidal amplitudes as a function of longitude and height. Following this, we decompose the non-migrating portion of the tidal perturbations into its various spatial modes using the fit described above on a 30-day sliding window. The plots for both the diurnal and semidiurnal temporal frequency and for the three model variables considered then highlights the variation in amplitude of each spatial mode over the course of the year.

Having studied tidal properties at two latitudes, we then wish to examine the latitudinal properties of the modelled tides, to observe how amplitudes vary as a function of latitude. Again we decompose the tidal perturbations into their various spatial modes and analyse how these vary as a function of latitude for both the diurnal and semidiurnal temporal frequencies and for the three model variables considered.

Finally, we return our attention to the equatorial and polar latitudes investigated previously to look at the short term variation in the tidal amplitudes of some of the dominant migrating and non-migrating modes over the course of the year. We investigate this short term variability by calculating the amplitudes with a 24-hour sliding window and compare it to the standard 30-day sliding window used previously. This is to gain an insight into the "tidal weather" present in the model, which has been a recent topic of interest in the analysis of the MLT (e.g., Vitharana et al., 2019).

3.1 An initial exploration of model fields

We begin with an initial exploration of the model fields examined in this study – namely temperature, zonal (u) winds and meridional (v) winds. We fix a height of 95 km and plot instantaneous tidal perturbations from the modelled fields along with their decomposition into migrating and non-migrating components at 00UT on 1st January. These can be seen in Figure 7.

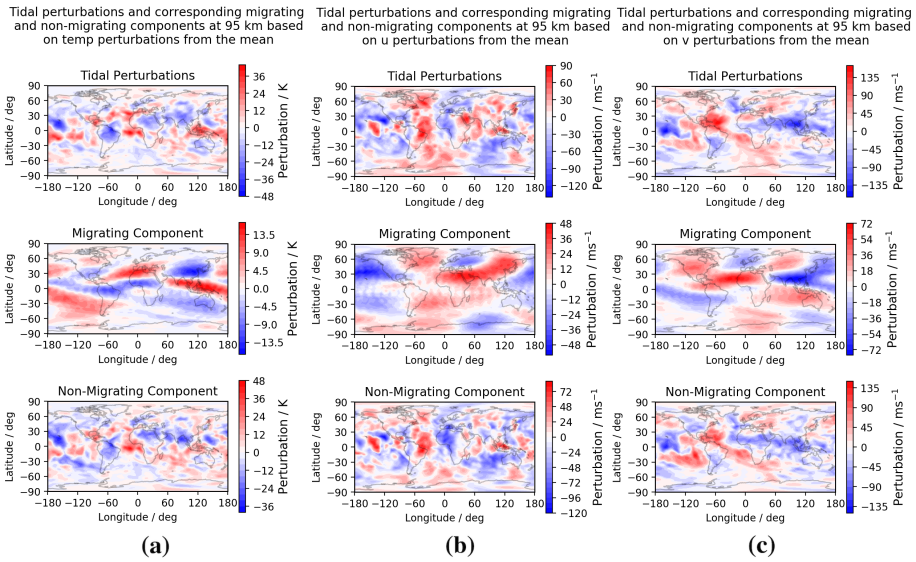

Figure 7. Longitude-latitude snapshot at 00UT on the first day of January of tidal perturbations at 95 km for **(a)** temperature, **(b)** zonal (u) winds and **(c)** meridional (v) winds. The equatorial DW1 tide and polar SW2 tide can be seen as the primary components of the migrating tide, with a superposition of several zonal wavenumbers apparent in the non-migrating components.

Of note is the size of the instantaneous tidal perturbations, which reach nearly 50 K in the modelled temperature field and around 140 ms^{-1} in the modelled winds.

The decomposition of these fields into migrating and non-migrating components reveals a migrating component that has a clear dominance in the DW1 component at equatorial latitudes, with a transition to a dominant SW2 component apparent on moving to polar latitudes. The non-migrating component is of significant magnitude – up to nearly 50 K in temperature and 140 ms^{-1} in wind – and it is clear that it makes up a large portion of the tidal perturbation. The irregular nature of these fields indicate a superposition of several zonal wavenumbers and a need for further investigation – particularly given their large magnitude.

To this end, we examine the zonal wavenumber structure of the non-migrating tide in both an equatorial and polar regime in the following sections.

3.2 Equatorial regime

Firstly, we examine the height structure of the instantaneous tidal perturbations and corresponding migrating and non-migrating components of the model fields in the equatorial regime. Again we consider 00UT on 1st January. These can be seen in Figure 8.

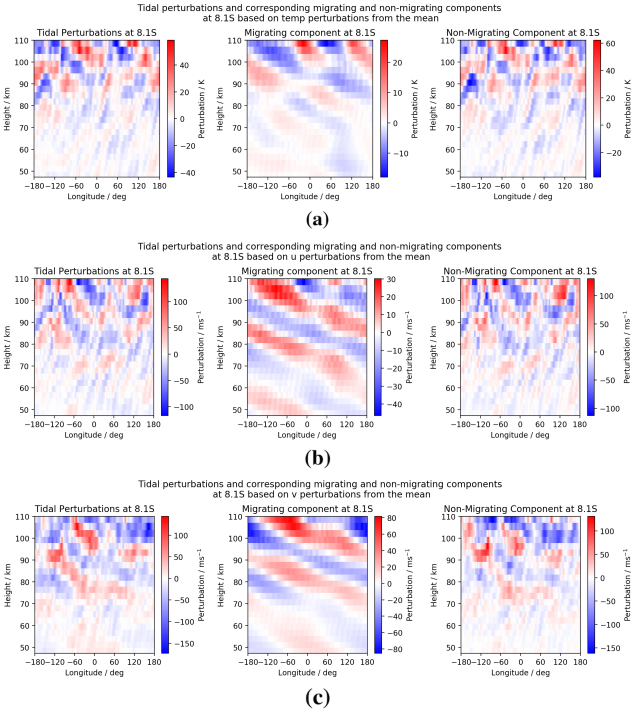

Figure 8. Longitude-height snapshot at 00UT on the first day of January at the equatorial latitude of Ascension Island ($8^{\circ}\mathrm{S}$) of tidal perturbations for **(a)** temperature, **(b)** zonal (u) winds and **(c)** meridional (v) winds. The equatorial DW1 tide can be seen as the primary component of the migrating tide, with some presence of the SW2 tide in temperature. A superposition of several zonal wavenumbers is apparent in the non-migrating components.

Once more the amplitudes of the non-migrating component can be seen to contribute significantly to the overall tidal field – with magnitudes of up to 60 K in the temperature field and 170 ms^{-1} in the wind fields. Amplitudes of the tides can be seen to increase with increasing height which is consistent with the decrease in atmospheric density.

The migrating component of the temperature field appears to be dominated by the SW2 component above 60 km. In the wind fields, the migrating component is clearly dominated by the DW1 component at all heights. In all fields, the slope of the phase fronts is shallow indicative of a short vertical wavelength.

The non-migrating component is once more irregular but some structure can be seen, in particular a zonal wavenumber 3 structure around 90 km. In general the slope of the phase fronts appears to be steeper indicative of longer vertical wavelengths than those seen in the migrating component.

We now once more focus on a height of 95 km and decompose the non-migrating tidal field into its zonal wavenumber components using the method described in Sect. 2.1. With this we will be able to see which zonal wavenumbers are the dominant contributors to the non-migrating tide. We plot both diurnal and semidiurnal temporal frequencies in the equatorial

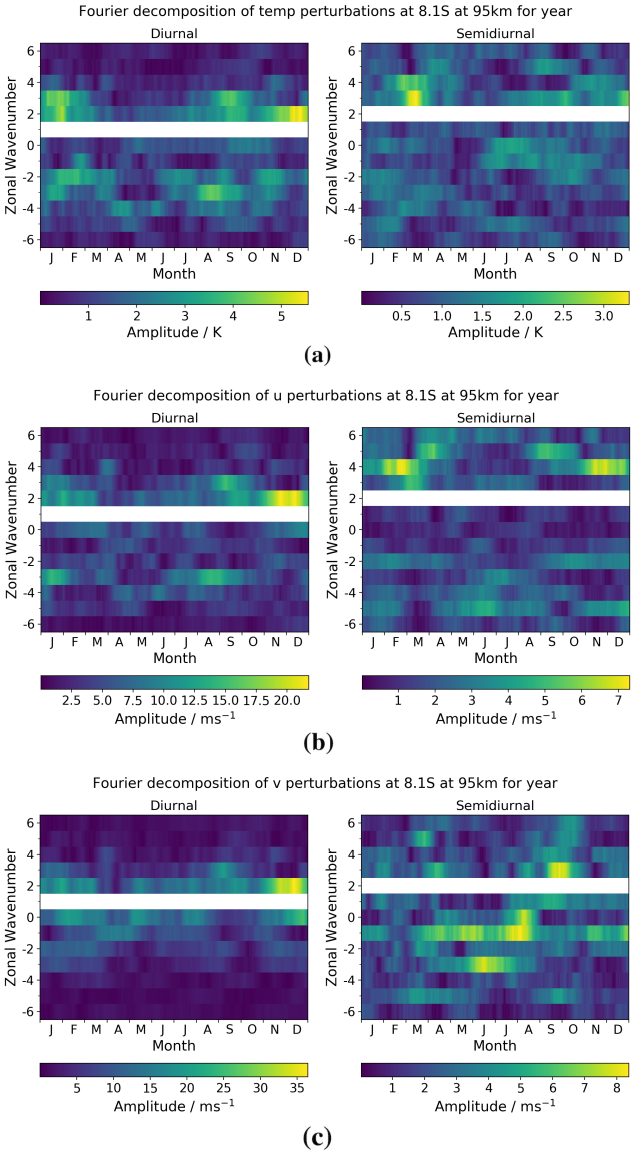

Figure 9. Diurnal and semidiurnal tidal amplitudes as a function of month and zonal wavenumber at the equatorial latitude of Ascension Island (8°S) for **(a)** temperature, **(b)** zonal (u) winds and **(c)** meridional (v) winds. The dominant migrating tidal component is removed in each case for clarity.

regime for each zonal wavenumber across the year in Figure 9. We use a 30-day sliding average window centred on a given day.

The first feature of note is that the maximal amplitude of the diurnal tide is always larger than that of the semidiurnal tide in this equatorial regime. This is consistent with what is expected at an equatorial latitude where the diurnal tide should dominate.

The magnitude of the semidiurnal tide in temperature is around 60% of that seen for the diurnal tide, which has a maximal amplitude of 5.5 K. In the zonal wind, the magnitude of the semidiurnal tide is around a third of that seen in the diurnal tide – which has a maximal amplitude of 22 ms^{-1} – and in the meridional wind the semidiurnal tide is roughly a quarter of the observed diurnal tide, which has a maximal amplitude of 36 ms^{-1}.

We now focus on the modelled temperature field. In the diurnal component, we observe the largest non-migrating tidal amplitudes in the DW2 component, with a maximal peak of 5.5 K in December with amplitudes of 4 - 5 K also seen in January. Other non-migrating diurnal tidal amplitudes of note are the DW3, which has maximal amplitudes of 4 - 5 K in January and September; the DE2, which has maximal amplitudes of 4 - 5 K in January/February; and the DE3 which has maximal amplitudes of 4 - 5 K in January and August. In the semidiurnal component, magnitudes are generally small, but peaks are seen in the SW3 and SW4 tides, which have maximal amplitudes of around 3 K in March.

Moving to the modelled zonal winds, in the diurnal component, the largest non-migrating tidal amplitudes are once more in the DW2 component. We observe a maximal peak of around 22 ms^{-1} occurring in November/December. Other non-migrating diurnal components of notable magnitude are the DW3, which peaks at around 15 ms^{-1}, and the DE3 which peaks in January and August with a value of around 15 ms^{-1}. In the semidiurnal component, again magnitudes are small, but we observe maximal amplitudes in the SW4 tidal component of around 7 ms^{-1} in February/March and November/December. The SW5 component is also present, with maximal values of around 6 ms^{-1} in March/April and September.

Finally, we examine the modelled meridional winds. In the diurnal component maximal amplitudes of around 36 ms^{-1} are seen in the DW2 component, occurring in November/December. Other tidal components of note are the "breathing" D0 component, which maximises with an amplitude of 25 - 30 ms^{-1} in December; and the DW3 component where we see a peak value of around 25 ms^{-1} in September. In the semidiurnal component – which are of relatively small magnitude – we observe maximal amplitudes of around 8 ms^{-1} spread across a number of components: the SW3 which peaks in September/October; the S0 which peaks in August; the SE1 which sustains larger values from April through to August; and the SE3 component which peaks in June.

In summary, the tidal properties in the equatorial tidal regime for i) modelled temperature, ii) modelled zonal wind and iii) modelled meridional wind are as follows:

- The instantaneous fields show maximal perturbation magnitudes at high altitudes of i) 60 K, ii) 140 ms^{-1} and iii) 170 ms^{-1}.
- The maximal amplitude of the diurnal non-migrating tidal components is always larger than that of the semidiurnal tide.
- The DW2 component is the dominant diurnal non-migrating component across all fields, with maximal amplitudes of i) 5.5 K, ii) 22 ms^{-1} and iii) 36 ms^{-1}. The DE3, DE2 and DW3 components are other components with notable magnitudes.
- The semidiurnal non-migrating components are small across the board, but relatively we see the largest magnitudes in i) SW3 & SW4, ii) SW4 & SW5 and iii) SE3, SE1, S0 & SW3.

We perform a brief comparison with observations to place these results in the context of measured values. SABER values represent satellite measurements of temperature and TIDI & UARS values represent satellite measurements of wind – see Sect. 4 for more details. The magnitude of the migrating component is similar to observed values with some differences. Values of up to 22 ms^{-1} are seen in SABER equatorial temperatures in Forbes et al. (2008) at 100 km, compared to ExUM values of around 15 ms^{-1}. In terms of wind, values of up to 40 ms^{-1} and 70 ms^{-1} are seen in TIDI equatorial zonal and meridional winds (respectively) in Wu et al. (2008a) at 95 km, compared to ExUM values of around 30 ms^{-1} and 70 ms^{-1}. A notable equatorial DW2 with smaller DE2 and DE3 components is also observed in TIDI equatorial zonal and meridional winds in Oberheide et al. (2006), however they only observe maximal values of around 12 ms^{-1} and 18 ms^{-1} at 95 km compared to ExUM values of 22 ms^{-1} and 36 ms^{-1} for the zonal and meridional wind respectively. Finally, notable meridional equatorial SW4 zonal and SW3 meridional tidal components are also seen in TIDI equatorial zonal and meridional winds in Oberheide et al. (2007) at 95 km, however they also observe a notable SW1 meridional component which is not clear in the ExUM values. A notable SW3 meridional component is also seen in UARS equatorial meridional winds in Angelats i Coll and Forbes (2002).

Having examined the non-migrating tidal components in the equatorial regime, we now move on to the polar regime, where we expect the semidiurnal tide to dominate.

3.3 Polar regime

We now perform the same analysis in the polar regime. We again first examine the height structure of the instantaneous tidal perturbations and corresponding migrating and non-migrating components of the model fields in this regime. We consider 00UT on 1st January. These can be seen in Figure 10.

The magnitude of the tidal perturbations is smaller in the polar regime than in the equatorial regime. It remains clear that the non-migrating component makes up a significant portion of the tidal field – up to almost 20 K in the temperature field and up to 120 ms^{-1} in the wind fields. Again, the amplitudes of the tides increase with increasing height as the density decreases.

The migrating component of the temperature field is small, particularly when compared to the equatorial regime. It appears to be dominated by the DW1 component, less clearly so towards the top of the model where it is clear several components are superposed. In the instantaneous wind fields, there is a transition from a dominant DW1 component to a dominant SW2 component around 90 to 100 km. The slope of the phase fronts is steeper when compared with the equatorial regime, indicative of longer vertical wavelengths at this polar latitude.

The non-migrating component is again a superposition of many wavenumbers, but several finer wave structures can be seen. In particular around 90 - 95 km where we observe what appear to be zonal wave number 4 and 5 structures. There appear to be phase fronts indicating both westward and eastward propagation, as expected in non-migrating tides. The plots of the non-migrating component again highlight the need to decompose the field into its zonal wavenumber structure to provide a better picture on the zonal wavenumbers present in the model fields.

We now once more focus on a height of 95 km and decompose the non-migrating tidal field into its zonal wavenumber components using the method described in 2.1. We plot both diurnal and semidiurnal temporal frequencies in the equatorial

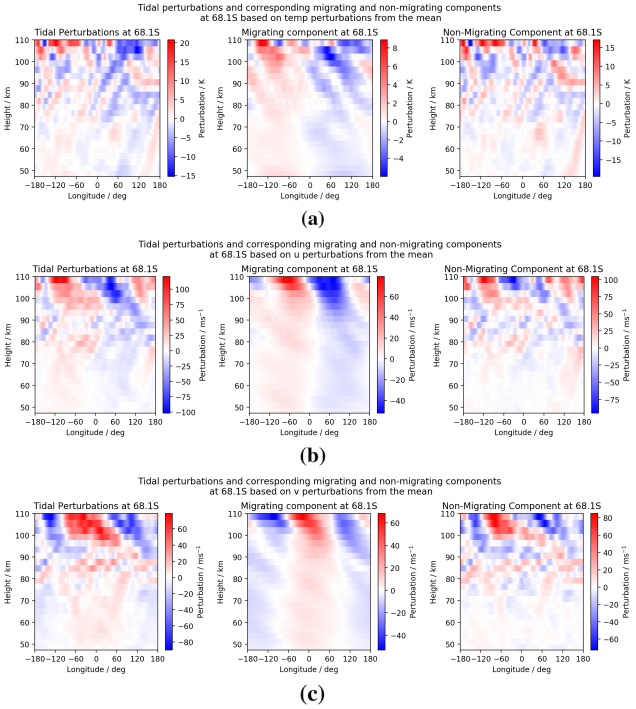

Figure 10. Longitude-height snapshot at 00UT on the first day of January at the polar latitude of Rothera (68°S) of tidal perturbations for **(a)** temperature, **(b)** zonal (u) winds and **(c)** meridional (v) winds. The equatorial DW1 tide can be seen as the primary component of the migrating tide at lower altitudes, with a switch to a dominant SW2 component occurring around 95 - 100 km in the wind fields and the temperature field becoming irregular. A superposition of several zonal wavenumbers is apparent in the non-migrating components.

regime for each zonal wavenumber across the year in Figure 9. We use a 30-day sliding average window centred on a given day.

We observe that, as expected, the maximal amplitude of the semidiurnal tide is always larger than that of the diurnal tide in this polar regime. The magnitude of the diurnal tide in temperature is around 40% of that seen in the semidiurnal tide – it is worth noting that both have small magnitude however, with a maximal amplitude of around 1.6 K in the semidiurnal component. The zonal wind has a diurnal component which is around 20% of the observed semidiurnal tidal amplitude, which maximises at around 14 ms^{-1}. Finally, the meridional wind has a diurnal component which is roughly 10% of the observed semidiurnal tidal amplitude, which maximises at around 13 ms^{-1}.

We comment first on the modelled temperature field. The magnitudes are small across both components, and therefore we will not place too much weight on observations made here. We see maximal amplitudes of around 1.6 K in the "breathing" S0 component in April/May and of around 0.6 K in the "breathing" D0 component in October.

The wind fields have larger magnitude. In the modelled zonal winds, we observe the largest non-migrating tidal amplitudes in the SW1 component, with a maximal value of around 14 ms^{-1} occurring in August/September and with larger values of

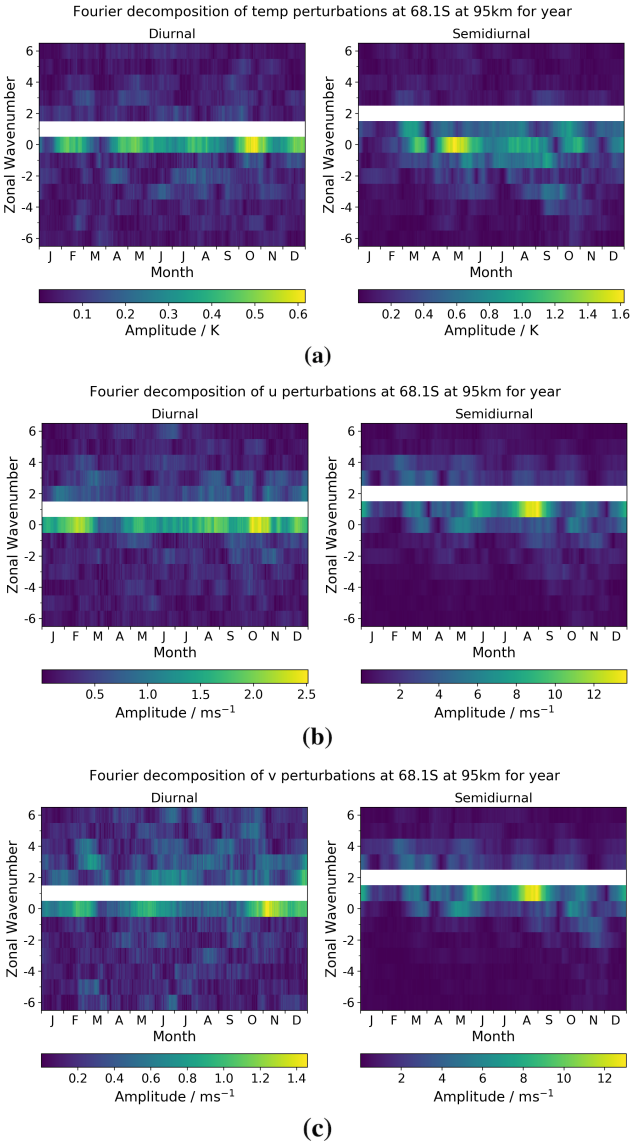

Figure 11. Diurnal and semidiurnal tidal amplitudes as a function of month and zonal wavenumber at the polar latitude of Rothera (68°S) for **(a)** temperature, **(b)** zonal (u) winds and **(c)** meridional (v) winds. The dominant migrating tidal component is removed in each case for clarity.

around 10 ms^{-1} also seen in May/June. Other notable non-migrating semidiurnal amplitudes are the "breathing" S0 component which peaks at around 8 ms^{-1} in May and October. The diurnal component has small magnitude, and the largest values of around 2.5 ms^{-1} are seen in the "breathing" D0 component in February and October.

Finally, we focus on the modelled meridional winds. The largest non-migrating tidal amplitude of around 13 ms^{-1} is seen in the SW1 component in August/September, with large values of around 10 ms^{-1} seen in June. There are once more some

larger values observed in the "breathing" S0 component also, with maximal values of around 8 ms^{-1} occurring in May and October. Again, the diurnal component has small magnitudes, with maximal amplitudes of around 1.4 ms^{-1} observed in the "breathing" D0 component in November.

In summary, the tidal properties in the polar tidal regime for i) modelled temperature, ii) modelled zonal wind and iii) modelled meridional wind are as follows:

- The instantaneous fields show maximal perturbation magnitudes at high altitudes of i) 20 K, ii) 120 ms^{-1} and iii) 90 ms^{-1}.
- The maximal amplitude of the semidiurnal non-migrating tidal components is always larger than that of the diurnal tide.
- The SW1 component is the dominant semidiurnal non-migrating component across the wind fields, with the values in the temperature field being generally small. We observe maximal amplitudes of i) 1.0 K, ii) 14 ms^{-1} and iii) 10 ms^{-1}. The "breathing" S0 component also has notable magnitudes across all fields.
- The diurnal non-migrating components are small across the board, but relatively we see the largest magnitudes in the D0 component in all fields.

We perform a brief comparison with observations to place these results in the context of measured values. The magnitude of the migrating component is similar to observed values. Values of 30 - 40 ms^{-1} are seen in UARS polar meridional winds in Angelats i Coll and Forbes (2002) at 95 km, compared to ExUM values of around 30 ms^{-1}. A notable SW1 polar meridional tidal component is also seen in UARS winds in Angelats i Coll and Forbes (2002). However, the values observed at 95 km are closer to 4 ms^{-1} and values closer to 10 ms^{-1} (as seen in the ExUM at 95 km) are only observed at 105 - 110 km. However, the polar SW1 component of TIDI polar zonal and meridional winds reported in Wu et al. (2011) at 95 km are up to 12 ms^{-1} in both the zonal and meridional components, in keeping with the values seen in the ExUM. Finally, the non-migrating components of the TIDI polar zonal winds reported in Wu et al. (2008b) show notable DE3, DE2, DE1, D0 and DW2 magnitudes (around 12 ms^{-1}) which we do not observe in the ExUM at polar latitudes.

We now have a good grasp of the dominant non-migrating tidal components in two key regimes – at an equatorial and polar latitude. We now wish to get a better understanding of how the components of the tide vary with latitude, and so we examine this in the following section.

3.4 Latitudinal dependence

Here, we extract the latitudinal dependence of the tides, by examining the amplitudes of the spatial modes as a function of latitude for each month of the year. We include the migrating mode in this analysis, and remove zonal wavenumber 5 and 6 – which are generally small – to help with visualisation. In Figure 12 we plot the diurnal tidal amplitudes for the spatial modes considered for each month. In Figure 13 we repeat the analysis but for the semidiurnal tidal amplitudes.

We first turn our attention to the modelled temperature field. We observe maximal tidal amplitudes of around 16 K. Looking at the migrating (DW1) component, we see a clear three-peak structure, with the largest peak observed at the equator and the

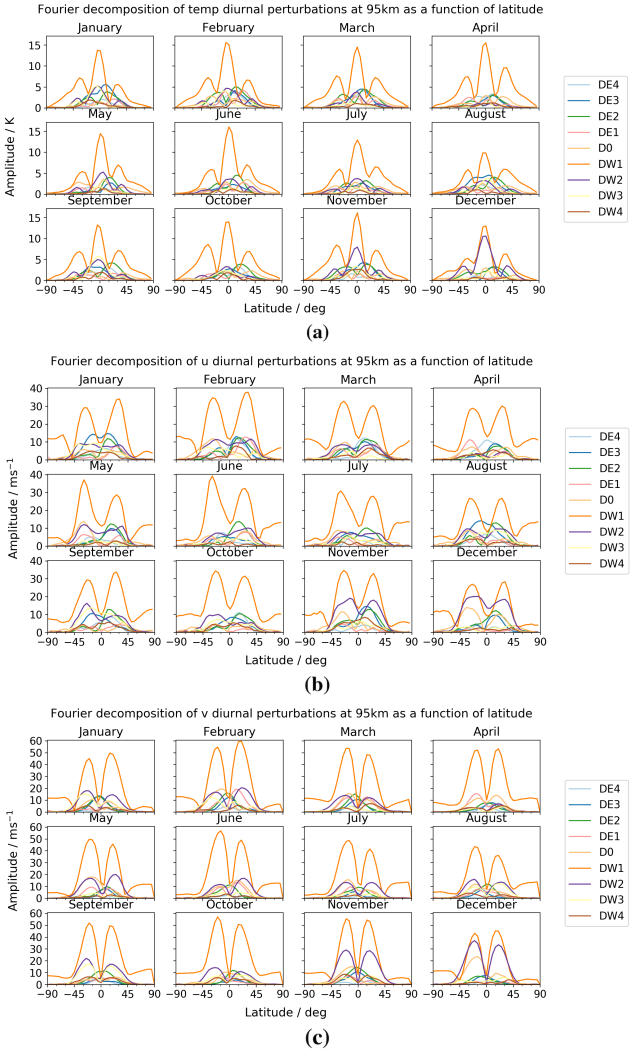

Figure 12. Latitude-amplitude plot of diurnal tidal amplitudes across the year for **(a)** temperature, **(b)** zonal (u) winds and **(c)** meridional (v) winds.

two smaller peaks at latitudes of approximately 30°S and 30°N. We observe maximal amplitudes in June and November with a pronounced minimum in August. Looking at the non-migrating components, we observe that the DW2 component is by far the largest with amplitudes of up to around 11 K at the equator in December where it is nearly as large as the diurnal migrating component. It also has large amplitudes in November of 7 - 8 K and in May and September when it reaches around 5 K at the equator. We also observe that it has a similar three peak structure. Other large components of note are the DE3, DE2 and DW3 components. The DE3 generally has a one peak structure in a 20°S to 20°N band around the equator which reaches a maximal amplitude of around 5 K in January and August. The DE2 generally has a two peak structure with these peaks occurring at the minima of the DW1 component at around 25°S and 25°N, and with maximum amplitudes of around 5 K in February and

June. Finally, the DW3 component generally has a three peak structure in line with the structure observed in the migrating component. We see maximal amplitudes of this component of around 5 K in January and September.

We focus now on the modelled zonal winds, where we observe maximal tidal amplitudes of around 40 ms^{-1}. In the migrating (DW1) component, we see a clear two peak structure with large peaks at approximately 20 - 30°S and 25 - 30°N with a minimum at the equator. Some increase towards the south pole is evident in the austral spring/summer period (October, November, December, January, February). Maximal amplitudes occur in February, June and October/November, whilst minimal amplitudes occur in April and August. Turning our attention to the non-migrating components, we once more observe a dominant DW2 component with amplitudes up to around 20 ms^{-1} in December matching that of the diurnal migrating tide. In general it also has the same two peak structure as the migrating mode. The DW2 is large in November also reaching around 20 ms^{-1}, and in May and September where it reaches 10 - 15 ms^{-1}. Many other non-migrating components also have large amplitudes in different months of the year. The DE4 maximises at 12 ms^{-1} at around 15°N in March/April and October. The DE3 maximises at around 17 ms^{-1} in the region of 15°S to 15°N in January and November. The DE2 reaches values of around 15 ms^{-1} at 15°N for a large part of the year. The DE1 maximises at around 12 ms^{-1} at 30°S in April and at 30°N in January. The "breathing" D0 mode reaches a value of 15 ms^{-1} at around 30°S in February, May and December. Finally, the DW3 component maximises at around 15 ms^{-1} at around 15°S in September.

Finally we look at the modelled meridional winds. These have the largest maximal amplitudes seen so far of around 60 ms^{-1}. The migrating (DW1) component shows a similar clear two peak structure to that observed in the zonal wind, with the peaks similarly located around 20°S and 20°N with a pronounced minimum at the equator. Again, some increase is seen towards the south pole in the austral spring/summer period but it is relatively less pronounced when compared to the zonal wind. The maximal amplitudes also follow the same monthly pattern as the zonal winds; we see maxima in February, June and October and minima in Apr/May and August. Looking at the non-migrating components, the DW2 is again dominant, follows a two peak structure and has maximal amplitude in December of around 40 ms^{-1} comparable with the amplitude of the diurnal migrating component. The DW2 is also large in November with a maximal amplitude around 30 ms^{-1}, and through much of the rest of the year with amplitudes near 20 ms^{-1} (it is at its smallest in April with amplitudes below 10 ms^{-1}). Many other non-migrating components are also large as was observed with the zonal winds. The DE3 generally has a one peak structure maximising at the equator with values around 15 ms^{-1} in January. The DE2 has a similar one peak structure with maximal values of 15 ms^{-1} at the equator in January, February, March and November. The DE1 reaches values of 16 ms^{-1} at 15°S in April and 20 ms^{-1} at 15°N in February. The "breathing" D0 mode maximises at 15°S with a value of 19 ms^{-1} in February and with a value of 22 ms^{-1} in December. Finally, the DW3 generally has a two peak structure maximising around 20°S and 20°N with values of 15 ms^{-1} in January and August and 18 ms^{-1} in September.

Having performed an in depth analysis of the diurnal tidal components, we now look at the variation of the semidiurnal tidal components with latitude, presented in Figure 13.

We first focus on the modelled temperature field, where we see maximal tidal amplitudes of around 11 K which are less than those seen in the diurnal migrating component. In the migrating (SW2) component, we generally observe a three peak structure - occasionally one of the peaks breaks down leaving a two peak structure remaining. The central peak generally

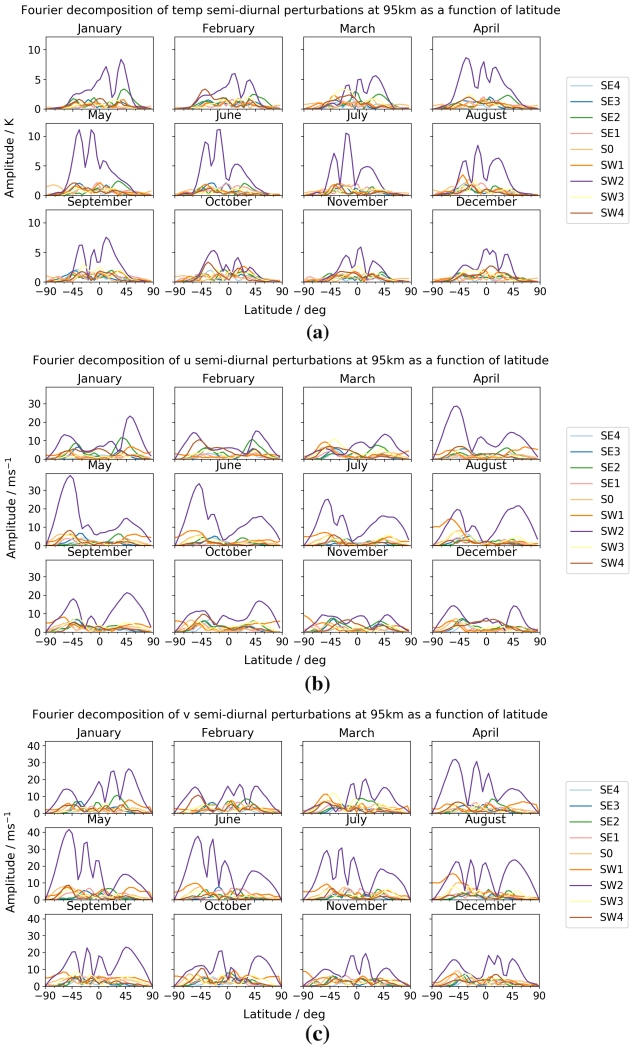

Figure 13. Latitude-amplitude plot of semidiurnal tidal amplitudes across the year for **(a)** temperature, **(b)** zonal (u) winds and **(c)** meridional (v) winds.

occurs between 10°S and 10°N with the left and right peaks occurring approximately 30° north or south of the central peak. We observe maximal amplitudes in May/June/July and minimal amplitudes in October/November/December. Turning our attention to the non-migrating semidiurnal tidal components, there is no clear largest component. The SE2, SW1, SW3 and SW4 components represent the largest of the non-migrating components. The SE2 has maximal amplitudes of 3 - 4 K around 40°N for most of the first half of the year. Peak amplitudes of around 3 - 4 K are also seen for the SW1 component at 40°S in August; and for the SW3 component at 20°S in March. Finally, the SW4 component reaches values of 4 K at 40°S in February and at around 30°S in October.

We now look at the modelled zonal winds. We observe maximal tidal amplitudes of around 40 ms^{-1}, which are similar to those seen in the diurnal migrating component. Looking at the migrating (SW2) component, we generally see a two peak structure, but a third smaller peak often occurs between these peaks. Generally, the two largest peaks occur at approximately 50°S and 50°N and there is often a third peak between these occurring anywhere between 30°S and 30°N. Maximal amplitudes are seen in May/June, with minimal amplitudes in November/December. In general the peak amplitude at 50°S is greater than or equal to the peak amplitude observed at 50°N. Now looking at the non-migrating components, again there is no outright largest non-migrating tide. As in the temperature field, the SE2, SW1, SW3 and SW4 have the largest amplitudes. The SE2 tends to have a two peak structure with maximal values at 40°S and 40°N. It maximises with values of 10 ms^{-1} at these latitudes in January/February. The SW1 component tends to peak towards the south pole. It has maximal amplitudes at 60°S, with a value of 10 ms^{-1} in March and 15 ms^{-1} in August. The SW3 reaches a peak value of around 10 ms^{-1} at around 40°S in March. Finally, the SW4 component maximises with a value of 10 ms^{-1} at 50°S in February and at 40°S in October.

Finally, we analyse the modelled meridional winds. We observe maximal tidal amplitudes similar to those seen in the zonal winds of around 40 ms^{-1} making them smaller than those seen in the diurnal migrating component. The migrating (SW2) component generally has a four peak structure with the two outer peaks centred around approximately 50°S and 50°N and the two central peaks moving to the north and south of the equator about 25 degrees apart. The tide has maximal amplitudes around May/June and has minimal amplitudes in November/December. Looking at the non-migrating components, again there is no clear dominant component and the SE2, SW1, SW3 and SW4 all have notable magnitudes. The SE2 component maximises at 30°N in June with a value of 10 ms^{-1}. Similar to the zonal wind SW1 component, the SW1 component here also has its largest amplitudes towards the south pole. We observe maximal amplitudes of 18 ms^{-1} at around 55°S in August. The SW3 component peaks at 13 ms^{-1} in March at 40°S. Finally the SW4 component has a maximal amplitude of 13 ms^{-1} seen in February at 50°S, and values of 10 ms^{-1} seen at 50°S in May and at 45°S in October.

In summary, the tidal properties as a function of latitude for i) modelled temperature, ii) modelled zonal wind and iii) modelled meridional wind are as follows:

- Maximal diurnal tidal amplitudes are i) 16 K, ii) 40 ms^{-1} and iii) 60 ms^{-1}, which are produced by the migrating (DW1) component.
- The diurnal migrating component has a i) three peak, ii) & iii) two peak structure.
- The dominant diurnal non-migrating component is the DW2 component across all fields with maximal amplitudes of i) 11 K, ii) 20 ms^{-1} and iii) 40 ms^{-1}. Other components of notable magnitude are the i) DE3, DE2 & DW3, ii) & iii) DE3, DE2, DE1, D0 & DW3.
- Maximal semidiurnal tidal amplitudes are i) 11 K, ii) 40 ms^{-1} and iii) 40 ms^{-1}, which are produced by the migrating (SW2) component.
- In general, the semidiurnal migrating component has a i) three peak, ii) two peak and iii) four peak structure.

– The dominant non-migrating semidiurnal components are the SE2, SW1, SW3 and SW4 components across all fields, with maximal amplitudes of i) 4 K, ii) 15 ms^{-1} and iii) 18 ms^{-1}.

We have now detailed the variation in diurnal and semidiurnal tidal amplitudes with latitude for the various spatial modes considered. It is now worthwhile to consider variation on a finer time scale – namely short term variability – which we focus on for the final section of our analysis.

3.5 Short term variability

Here we perform an analysis of the short term variability present in the amplitude of the tidal components. This is primarily to investigate the magnitude of such perturbations. To do this, we apply the analysis to a 30-day sliding window, and contrast it with that from a 1-day sliding window. In Figure 14, we present the variability in the migrating and some of the larger non-migrating tidal components across the course of the year within the two regimes we considered previously – namely an equatorial and a polar latitude. The bold line represents the value from the 30-day sliding window, and the faded line represents the value obtained using the 1-day sliding window.

We first analyse the modelled temperature field. Looking at the migrating modes (DW1 and SW2) in the equatorial regime, we see maximal amplitudes of around 15 K. We observe a peak in DW1 amplitudes in January/February of around 8 K with short term variation of up to 4 K throughout the year (i.e. at least a 50% variation). The SW2 component here peaks at a maximal value of around 12 K in May/June with short term variation of up to 3 K throughout the year (i.e. at least a 25% variation). In general the SW2 has larger amplitudes in April to September (equatorial Spring/Summer) with smaller amplitudes in October to March (equatorial Autumn/Winter). The migrating modes in the polar regime are relatively small throughout the year for both components with little short term variation. We focus on a subset of the non-migrating modes which have larger magnitudes within each of the two regimes, with peak values of around 12 K. In the equatorial regime, we focus on the DE3, DW2 and DW3 tidal components. The DE3 peaks in January and August with values around 4 K, with short term variation up to 5 K throughout the year (i.e. short term variation of 125%). The DW2 has maximal values in January and December of around 5 K with short term variation up to to 5 K throughout the year (i.e. short term variation of around 100%). Finally, the DW3 peaks in January/February and September with values around 5 K and with short term variation of up to 7 K – the largest short term variation seen of 140%. The non-migrating modes in the polar regime are also relatively small – perhaps the only point of note is the short term variation in the "breathing" S0 component which varies by up to 1 K, or around a 75% variation.

We now turn our attention to the modelled zonal winds. First focusing on the migrating modes (DW1 and SW2) in the equatorial regime, we observe maximal amplitudes of around 35 ms^{-1}. Looking at the DW1 component, we see peak amplitudes of around 30 ms^{-1} in March/April and October/November, with short term variation of up to 12 ms^{-1}, or a 40% variation. The SW2 component peaks in April/May with amplitudes of around 12 ms^{-1} with short term variation of up to 5 ms^{-1}, or around a 40% variation. In the polar regime, we observe larger amplitudes than those seen in the temperature field. The dominant SW2 component peaks in April/May with a value of 28 ms^{-1}, with short term variation of up to 10 ms^{-1}, or around a 35% variation.

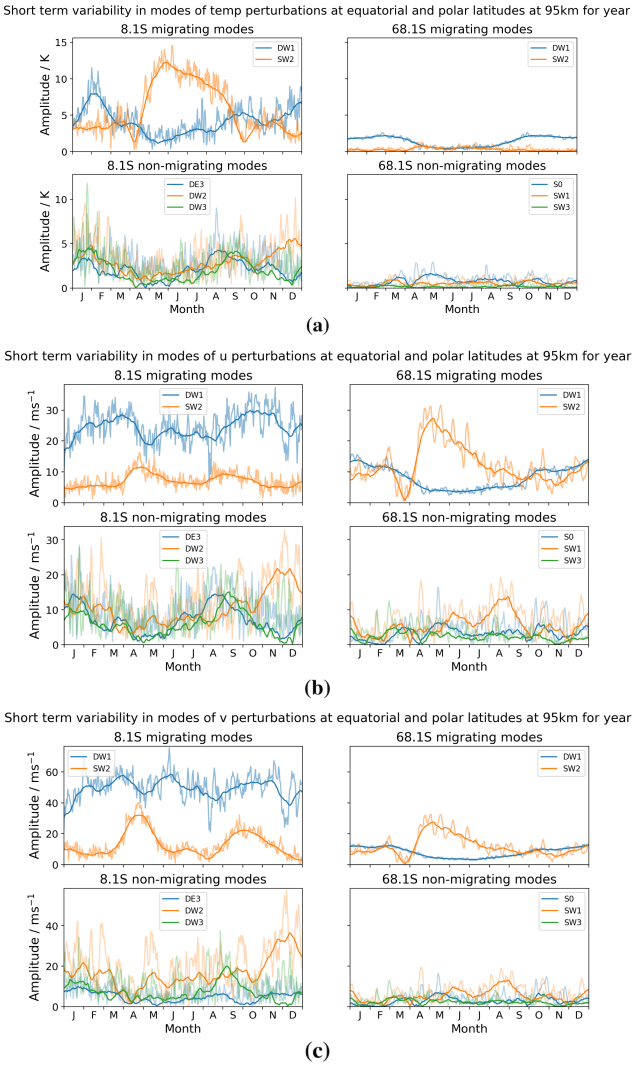

Figure 14. Tidal amplitudes as a function of time for the latitudes of 8°S and 68°S showing the short term variability of the migrating and largest non-migrating tidal components over the course of the year for **(a)** temperature, **(b)** zonal (u) winds and **(c)** meridional (v) winds. The bold line represents the value from the 30-day sliding window, and the faded line represents the value obtained using the 1-day sliding window.

535 It is notable that this large peak amplitude follows near zero amplitude values in the preceding month. The DW1 component in the polar regime has maximal values of 12 ms^{-1} in January and December with short term variation of around 3 ms^{-1}, or a 25% variation. The amplitudes seem to experience a six month low in April through September, following by a six month high from October through March which is also observed to a lesser extent in the temperature field. Moving to the non-migrating components, we observe maximal amplitudes similar to those seen in the migrating components of around 35 ms^{-1}. We again
540 focus on the DE3, DW2 and DW3 components in the equatorial regime. The DE3 peaks in January and August with values

around 14 ms^{-1}, with short term variation of up to 12 ms^{-1}, or around a 85% variation. These peaks line up with the peaks in the temperature field seen previously. The DW2 has maximal values of 20 ms^{-1} observed in November/December with large short term variation of up to 20 ms^{-1}, or a 100% variation. Finally, the DW3 peaks in January and September with values of 10 and 14 ms^{-1} respectively. The short term variation seen here is some of the largest seen in the zonal winds, with variation up to 18 - 19 ms^{-1}, or around a 130% variation. Finally, we look at the non-migrating component in the polar regime, and focus on the S0, SW1 and SW3 components. The "breathing" S0 component peaks with values of 6 ms^{-1} in May with large short term variation of up to 10 ms^{-1} or around 165%. The SW1 component has maximal values in August/September of around 12 ms^{-1} with large short term variation of up to 15 ms^{-1} or 125%. The SW3 component peaks around February/March/April with values of around 5 ms^{-1}, and again with large short term variation of around 7 - 8 ms^{-1}, or around 150%.

Finally we come to the modelled meridional winds. In the migrating modes (DW1 and SW2) we observe a very similar pattern to the migrating modes seen in the zonal wind field, with similar amplitudes in the polar regime, but with almost double the amplitude in the equatorial regime, giving maximal amplitudes of around 70 ms^{-1}. The DW1 component in the equatorial regime has the same March/April and October/November peak seen in the zonal winds, with amplitudes here of around 60 and 55 ms^{-1} respectively. In the meridional winds we also see larger values in June of near 60 ms^{-1}. The short term variation seen is up to 20 ms^{-1}, or around 33% of the base value. The SW2 component has more pronounced peaks in April/May and September/October (the equinoxes) than the zonal winds, with values of 30 ms^{-1} and 20 ms^{-1} respectively. Short term variation occurs up to a value of 10 ms^{-1}, or around a 33 - 50% variation. Moving on to the migrating modes in the polar regime, as noted previously these have very similar structure and magnitude to the migrating components seen in the zonal winds and so we refer the reader to this analysis. The non-migrating modes see maximal amplitudes of around 60 ms^{-1}, which is similar to the maximal amplitude seen in the migrating components. In the equatorial regime we again focus on the DE3, DW2 and DW3 components. The DE3 component has consistently smaller amplitudes than those seen in the corresponding component in the zonal winds, with amplitudes always less than 10 ms^{-1}. The short term variation is still pronounced however with a magnitude of up to 10 ms^{-1}, or over a 100% variation. The DW2 component has a very similar structure to that seen in the zonal winds, but with almost double the magnitude, peaking in November/December with a value of 38 ms^{-1}. We observe short term variation of up to 22 ms^{-1}, or a variation of nearly 60%. Finally, coming to the DW3 component, we see a similar structure to that seen in the zonal wind, but with a larger peak in August/September of around 20 ms^{-1}, and a slightly larger peak in January/February of around 14 ms^{-1}. Short term variation seen here is at most 15 - 20 ms^{-1}, or around a 100% variation in general. We now approach the non-migrating tidal components in the polar regime, and again focus on the S0, SW1 and SW3 components. As with the migrating components in the polar regime, these have very similar structure and magnitude to that seen in the zonal wind non-migrating components and so we refer the reader to this analysis.

In summary, the tidal properties considering short term variability for i) modelled temperature, ii) modelled zonal wind and iii) modelled meridional wind are as follows:

- Maximal amplitudes of the migrating components in the equatorial regime are, for DW1, i) 8 K, ii) 30 ms^{-1} and iii) 60 ms^{-1}, and for SW2, i) 12 K, ii) 12 ms^{-1} and iii) 30 ms^{-1}.

- Maximal amplitudes of the migrating components in the polar regime are, for DW1, i) <5 K, ii) 12 ms^{-1} and iii) 12 ms^{-1}, and for SW2, i) <5 K, ii) 28 ms^{-1} and iii) 28 ms^{-1}.

- Short term variation or "tidal weather" in the migrating components can lead to a percentage variation of up to i) 50%, ii) 40% and iii) 50%.

- Maximal amplitudes of the non-migrating components considered in the equatorial regime are i) 5 K, ii) 20 ms^{-1} and iii) 38 ms^{-1}.

- Maximal amplitudes of the non-migrating components considered in the polar regime are i) <5 K, ii) 12 ms^{-1} and iii) 12 ms^{-1}.

- Short term variation or "tidal weather" in the diurnal non-migrating components considered can lead to a percentage variation of up to i) 140%, ii) 130% and iii) 100%.

- Short term variation or "tidal weather" in the semidiurnal non-migrating components considered can lead to a percentage variation of up to i) 75%, ii) 165% and iii) 165%.

This completes our analysis of the migrating and non-migrating tidal modes observed in the modelled temperature, zonal and meridional wind fields from the Extended Unified Model, and we proceed to put these results in the context of other modelling and observational studies in the discussion which follows.

4 Discussion

In the results presented above, we observe significant magnitude and structure in the components of both the migrating and non-migrating modes across the range of diagnostics considered. Here, we place these results in the context of other modelling and observational studies of migrating and non-migrating tides and discuss the similarities and differences observed. Note that there a large number of diagnostics which could be considered for such multi-dimensional data. Thus we must naturally restrict the discussion to a limited subsection of the data, but one which is representative of the phenomena observed in the ExUM. For observational data, we use both meteor radar data and satellite observations. The zonal and meridional wind measurements used are from a High Resolution Doppler Imager (HRDI) aboard the Upper Atmosphere Research Satellite (UARS) as well as a Doppler Imager (TIDI) aboard the NASA Thermosphere, Ionosphere, Mesosphere, Energetics and Dynamics (TIMED) explorer. Temperature measurements used are from the Sounding of the Atmosphere using Broadband Emission Radiometry (SABER) also aboard the TIMED explorer.

We consider the studies of Miyoshi et al. (2017), who used an atmosphere-ionosphere coupled model to investigate non-migrating atmospheric tides; Hagan and Forbes (2002), who used the linear mechanistic Global Wave Scale Model (GWSM) to investigate migrating and non-migrating tides in the MLT; Oberheide et al. (2011), who presented results from the Climatological Tidal Model of the Thermosphere (CTMT) from 80 - 400 km; Hibbins et al. (2019), who made observations using meteor radar wind data from the Super Dual Auroral Radar Network (SuperDARN) in the Northern Hemisphere, at around

$60^{\circ}\mathrm{N}$ and at around 95 km; Chang et al. (2012), who compared ground-based observations of equinox diurnal tide wind fields from the first CAWSES Global Tidal Campaign with results from five commonly used models; Pokhotelov et al. (2018), who compared meteor-radar observations made in Germany and Norway to the Kühlungsborn Mechanistic Circulation Model (KMCM); Dempsey et al. (2021), who compared meteor-radar observations at Rothera to the Whole Atmosphere Community Climate Model (WACCM) and the Extended Canadian Middle Atmosphere Model (eCMAM); Ortland and Alexander (2006), who compared observations of the diurnal tide from TIDI and UARS winds and SABER temperatures against a linear mechanistic tide model; Iimura et al. (2010), who provided an assessment of non-migrating semidiurnal tides present in TIDI wind measurements; Oberheide et al. (2006, 2007), who also examined non-migrating diurnal and semidiurnal tides in TIDI wind measurements; Wu et al. (2008a,b, 2011), who examined migrating and non-migrating diurnal and semidiurnal tides in TIDI wind measurements; Angelats i Coll and Forbes (2002), who examined both migrating and non-migrating semidiurnal tides in UARS meridional winds; Huang and Reber (2004), who examined both migrating and non-migrating diurnal and semidiurnal tides in UARS wind measurments; Zhang et al. (2006) & Forbes et al. (2008), who presented both migrating and non-migrating diurnal and semidiurnal tides in SABER temperature measurements; and Li et al. (2015), who presented DE3 and SE2 tidal components from SABER temperature measurements.

4.1 Non-Migrating modes

We focus first on the non-migrating modes produced by the ExUM and discuss these in the context of other studies of non-migrating modes in the MLT.

4.1.1 The DE3

Given the importance of the DE3 in producing the wavenumber 4 structures observed in low-latitude total electron content in the ionosphere (Forbes et al., 2008), we first focus on this non-migrating mode. We shall summarise the results observed in previous modelling and observational studies, and then compare with the results from the ExUM.

Miyoshi et al. (2017) considered the temperature field, and found that the DE3 was the largest of all non-migrating tidal components in the MLT (peaking around 17 K amplitude at 110 km at the equator)(however at 80 km a maximal amplitude of 3 K is observed at 20S and 20N). Hagan and Forbes (2002) obtained a DE3 component of 30 K amplitude at 115 km compared to a 17 K observed amplitude. Oberheide et al. (2011) observed, in September at 100 km, a zonal wind DE3 with maximal amplitude at the equator of around 18 - 20 ms^{-1}, no meridional wind DE3 component, and a temperature DE3 component with maximal amplitude around the equator of around 9 K. Finally, the zonal wind field was also investigated at 90 km. The non-migrating components vanish on moving down to 90 km, i.e. the DE3 component seen previously disappears.

Considering the ExUM fields at 95 km, the DE3 component has a maximal amplitude of around 5 K in the temperature field, 17 ms^{-1} in the zonal wind field and 15 ms^{-1} in the meridional wind field. It would also be informative to consider the DE3 component produced in the ExUM at different model heights. We therefore plot this in Figure 15.

In the temperature field, we see a distinct increase in the amplitude of the DE3 component with increasing height. We see peak value of around 10 K at 107 km and a value of 4 - 5 K in September at 100 km. Whilst it is not inconceivable that the DE3

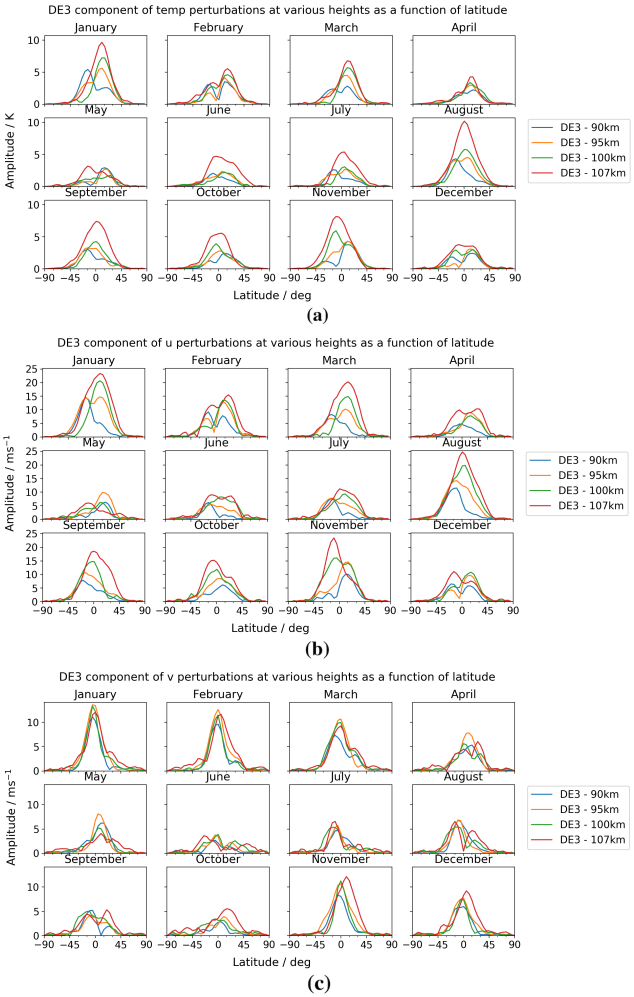

Figure 15. Latitude-amplitude plot of DE3 tidal amplitudes at various heights across the year for **(a)** temperature, **(b)** zonal (u) winds and **(c)** meridional (v) winds.

component could have maximal amplitudes of 17 K at 115 km, this component appears to be slightly underestimated in the modelled temperature field. In the zonal wind field, we also observe a distinct increase of the DE3 amplitude with increasing height. It reaches amplitudes of around 16 ms^{-1} at 100 km in September, but has values up to around 20 ms^{-1} in other months. These values are comparable to those seen in CTMT. Unlike CTMT however, the DE3 component is generally smaller at 90 km, but certainly does not disappear at this altitude. Finally, the meridional wind field is, in contrast to CTMT, non-zero at 100 km. It does not appear to greatly increase with increasing height, and actually peaks with amplitudes around 15 ms^{-1} in January at 95 km.

Finally, we focus on a more detailed comparison with observational results and how they compare with the ExUM DE3 tidal fields produced.

In temperature, the satellite observations come from SABER. Forbes et al. (2008) observed DE3 amplitudes at 95 km in August/September of 6 - 8 K at around $10^{\circ}\mathrm{S}$ and decaying either side of this latitude. Maximal values of 12 K are observed at the same latitude at 105 - 110 km. There is a transition from a two peak structure at lower altitudes (76 km) to a single peak structure at higher altitudes (116 km) with this single peak structure having maximal values in August/September, with near zero values over equatorial winter. Zhang et al. (2006) and Li et al. (2015) echo these results. In comparison to the fields produced by the ExUM, the latitudinal structure is well captured with a transition from a two peak to single peak structure apparent with increasing altitude. The peak magnitudes are also fairly similar for the heights considered, although the ExUM perhaps slightly underestimates the DE3 component at the upper heights of the model. However it is the seasonal dependence that is the major discrepancy. A peak value is seen in August, but the peak persists for months such as November and January where small or zero values are seen in the SABER observations.

The zonal wind is provided by satellite observations from TIDI and UARS. Oberheide et al. (2006) observed DE3 amplitudes at 95 km with maximal amplitudes of 14 ms^{-1} in August/September at (or just south of) the equator, growing to 18 ms^{-1} at around 100 - 105 km. There is a pronounced period of maximal amplitudes from July to September occurring with a single peak structure, with minimal amplitudes in December/January/February and May/June, often with a two peak structure. Wu et al. (2008b) echo these results, but with slightly larger values of 16 ms^{-1} at 95 km growing to around 25 ms^{-1} at around 105 km. Huang and Reber (2004) also echo these results, but with larger values again of 20 ms^{-1} at 95 km. In comparison to the fields produced by the ExUM, the peak values in August are more in keeping with Huang and Reber (2004), but are generally similar to the other studies considered. The increase in amplitude with increasing height and the latitudinal structure are also reproduced, with a single peak structure seen in months with large amplitudes, and a two peak structure often seen in months with smaller amplitudes. However, once more the seasonal dependence is the major discrepancy. Larger values are seen in August/September, with smaller values in May and June, but large values are seen in January - March where much smaller values are seen in TIDI and UARS measurements.

The meridional wind field is also provided by satellite observations from TIDI and UARS. Oberheide et al. (2006) observed DE3 amplitudes at 95 km with maximal amplitudes of 10 ms^{-1} in January/February at the equator, which do not grow further with increasing height. Maximal amplitudes are generally in November, December and January to April, with smaller amplitudes for the rest of the year, and with a year round single peak structure. Wu et al. (2008b) and Huang and Reber (2004) both echo these results. In comparison to the fields produced by the ExUM, we see that the ExUM DE3 meridional component has amplitudes which are slightly larger than those observed, peaking around 15 ms^{-1}. However the latitudinal single peak structure, the seasonal structure and lack of significant increase with increasing height are all features which are also produced by the modelled meridional wind.

Ultimately then, whilst some differences do exist between the ExUM and other models and observational studies, it is notable that the DE3 component is of significant magnitude for all diagnostics considered, and is in fact one of the larger components of the motion field.

4.1.2 Other non-migrating modes

We move our attention to other non-migrating modes found in the studies introduced above.

Miyoshi et al. (2017) found other components of note in the diurnal non-migrating tides are the DE2, DW2 and D0 with amplitudes of around 7 K in the 90 - 100 km region. Hagan and Forbes (2002) found that the DE3 also generates DW5, SW6 and SE2 via zonal wavenumber 4 interactions and DW2, D0, SW3 and SW1 via zonal wavenumber 1 interactions. The DW2 was around 5 K which was comparable with observed values. The study of Oberheide et al. (2011) using the CTMT (introduced above) in September at 100 km observed some spread from DW1 to D0 and DW2 in the zonal wind, with amplitudes around 10 ms^{-1}. The meridional wind also has D0 and DW2 components with amplitudes around 10 ms^{-1}. Finally, the temperature field sees amplitudes spread from the DW1 to the DW2 component with amplitudes around 6 - 7 K.

Considering the ExUM temperature field at 95 km, the DW2 is the largest of all non-migrating components, peaking around 11 K at the equator. The DE2 and DW3 reach maximal amplitudes around 5 K, whilst other components remain below 5 K. The ExUM is consistent with the studies considered in that it reproduces a large DW2 component, with magnitudes of around 5 K in September at 95 km consistent with values observed in CTMT at 100 km. The DE2 magnitude is also similar to that observed by Miyoshi et al. (2017), but we do not see magnitudes above 5 K in the D0 or DW5 components. In the wind fields at 95 km in September, the DW2 peaks around 20 ms^{-1}, larger than that observed in CTMT, whereas the D0 has peak amplitudes around 5 ms^{-1}, smaller than that seen in CTMT.

Miyoshi et al. (2017) observed that the SW3 was the largest of all the semidiurnal non-migrating components in MLT (around 8 K at 110 km). Other components of note are the SE2 and SW1 with amplitudes of around 6 K at 110 km. Hibbins et al. (2019) found that, in general, the semidiurnal tide was dominated by the SW2 (migrating) component with smaller contributions from SW1 and SW3 especially around the equinoxes. They found that the semidiurnal components maximised in the autumn equinox, with a secondary wintertime maximum. Iimura et al. (2010) demonstrated that a non-migrating SW1 is clearly present in the MLT horizontal winds in the Northern Hemisphere, maximizing around 60°N in late spring/early summer. In addition, an SW3 and weaker S0 component were also evident in the lower thermosphere. The study of Oberheide et al. (2011) using the CTMT (introduced above) in September at 100 km observed some spread of the SW2 component in the zonal wind into the SW1 and SW3 components, with maximal amplitudes around 10 - 14 ms^{-1}. These components disappeared at 90 km. There are no notable non-migrating semidiurnal components in the meridional wind or temperature fields.

Considering the ExUM temperature field at 95 km, the SE2, SW1, SW3 and SW4 all have similar magnitudes of around 3 - 4 K, with the peak SW3 values occurring at the equinoxes. These values are not inconsistent with the values observed by Miyoshi et al. (2017) at 110 km. In the zonal wind field at 95 km, the SE2, SW1, SW3 and SW4 are again the larger components with values around 10 ms^{-1}. These larger semidiurnal components are in general similar to the observations of Hibbins et al. (2019) and Iimura et al. (2010). The seasonal dependence is less obvious, but at around 60°N, the SW1 component appears to be at its largest in April. The SW1 and SW3 components in the ExUM are consistent with those observed by Oberheide et al. (2011). However, we also observe significant semidiurnal non-migrating components in the meridional wind which are not seen in their study, with values around 15 ms^{-1}.

Finally, we focus on a more detailed comparison with observational results and how they compare with the other ExUM non-migrating tidal fields produced. We generally look at the DW2 and the SW1 to limit the discussion.

Forbes et al. (2008) observed DW2 tidal amplitudes in temperature at 96 km peaking at 7 K in a single peak at the equator around November/December. The tide persists from September to February and is near zero for the rest of the year. In comparison, the ExUM has slightly larger peak amplitudes of 11 K at 95 km in December, and in general a three peak structure centred on the equator is evident (akin to the migrating tide) rather than a single peak at the equator. The seasonal dependence is generally well replicated, but with non-zero values persisting for much of the year.

Oberheide et al. (2006) observed DW2 tidal amplitudes in zonal wind at 95 km peaking at 12 ms^{-1} in September at 25 - 30°S, generally occurring with a two peak structure either side of the equator. Larger magnitudes are observed from September to February with smaller amplitudes for the rest of the year. Wu et al. (2008b) includes higher latitudes, and observed larger peak amplitudes of up to 20 ms^{-1} which occur in April/July at around 50°S with the smaller two peak structure replicated in some months. Huang and Reber (2004) also observe larger peak amplitudes of 16 ms^{-1} occurring in July/September at around 40°S. In comparison, the ExUM DW2 tide peaks with amplitudes around 20 ms^{-1} at 95 km in November/December at 25 - 30°S and 25 - 30°N. Thus the two peak structure is replicated in latitude but with larger amplitudes than those observed. As well as this, the modelled DW2 does not have larger amplitudes at higher latitudes. The seasonal dependence is also not well replicated, with small amplitudes in April and July. However larger amplitudes through the latter part of the year are generally seen. Looking at the SW1 zonal tide at 95 km, Wu et al. (2011) observed maximal amplitudes around 18 ms^{-1} in November/December/January at 70 - 90°S. Values of around 9 ms^{-1} persist for much of the rest of the year at high southerly latitudes. In comparison, the ExUM also has an SW2 which is large at high southerly latitudes, but with maximal values of 10 - 15 ms^{-1}. The seasonal dependence is also not replicated with the largest values occurring in March and August.

Oberheide et al. (2006) observed DW2 tidal amplitudes in meridional wind at 95 km peaking at 18 ms^{-1} in February and September at 20 - 25°S, occurring with a two peak structure either side of the equator as in the zonal tide. The meridional tide also has larger magnitudes from September to February with smaller amplitudes for the rest of the year. Huang and Reber (2004) echo these results, as do Wu et al. (2008b), but with larger maximal amplitudes of around 25 ms^{-1} observed. In comparison, the ExUM DW2 tide has a much larger peak amplitude of around 40 ms^{-1} in December. The seasonal dependence is reasonably well replicated with the biggest discrepancy being the large values in May which are not seen to this extent in observations. The two peak latitudinal structure is well replicated. Looking at the SW1 meridional tide at 95 km, Oberheide et al. (2007) observes peak amplitudes of around 8 ms^{-1} in January/February at around 45°S. Huang and Reber (2004) observed similarly large values in February at around 40°S. Wu et al. (2011) and Angelats i Coll and Forbes (2002) include higher latitudes. Wu et al. (2011) observe peak amplitudes of 15 - 18 ms^{-1} in December at 70 - 90°S. Generally largest amplitudes are seen in October to January at high southern latitudes, with amplitudes up to 9 ms^{-1} observed in February to September at high northern latitudes. Angelats i Coll and Forbes (2002) observes similar latitudinal and seasonal structure, but with smaller peak southern latitude amplitudes of around 10 ms^{-1}. In comparison, the ExUM has a similar peak magnitude of around 16 ms^{-1} at high southern latitudes, but this is observed in August rather than December and thus the seasonal dependence is not well replicated. Amplitudes of around 9 ms^{-1} are seen at high northern latitudes in April and May which are consistent with observations.

The ExUM results here reinforce the conclusions of the studies above, that there are significant amplitudes present across several non-migrating modes. Generally latitudinal structure is well replicated but it is the seasonal structure which is the major discrepancy between the modelled non-migrating tides and observations.

4.2 Migrating modes

We now focus on the migrating tidal modes produced by the ExUM and discuss these results in the context of other studies of migrating modes in the MLT.

Chang et al. (2012) observed that the models resolved the expected bimodal structure with tropical peaks associated with the diurnal migrating tide. Zonal wind amplitudes at 90 km ranged from around 50 ms^{-1} in GWSM and eCMAM to around 25 ms^{-1} in WACCM3 and to around 10 ms^{-1} in TIME-GCM. In meridional wind, amplitudes at 90 km ranged from 70 - 80 ms^{-1} in GWSM and ECMAM to 30 ms^{-1} in WACCM3 and to 15 ms^{-1} in TIME-GCM. Peak amplitudes in WACCM3 were found to occur around 15°S and 15°N whereas in GSWM and ECMAM peaks occurred around 25°S and 25°N. At 22°N, the 95 km zonal wind diurnal amplitudes increased to 65 ms^{-1} in GSWM, decreased to 40 ms^{-1} in ECMAM and increased to 40 ms^{-1} in WACCM3. The 95 km meridional wind diurnal amplitudes increased to 100 ms^{-1} in GSWM, and remained roughly constant in ECMAM and WACCM. Day to day variability or "tidal weather" was not overly present in the models used, but radar observations showed variations in zonal wind diurnal amplitudes from around 5 ms^{-1} up to as much as 40 ms^{-1} over a 5 day period at latitudes around peak tidal amplitudes, and variations in meridional wind diurnal amplitudes from around 15 ms^{-1} up to as much as 80 ms^{-1}.

In comparison with these results, the ExUM also yields a two-peaked structure in the equinox diurnal tide winds fields with peaks in the tropics. The zonal wind component of this tide at 95 km peaks at 30-35 ms^{-1} in equinox conditions, whereas the meridional wind component has peak amplitudes around 50-55 ms^{-1}. In both cases, the peaks are observed around 20 - 30°S and 20 - 30°N. This peak location is therefore closer to GSWM and ECMAM than WACCM3. Both wind components of the diurnal amplitudes observed in the ExUM fall between those observed in GSWM and ECMAM (which are larger) and those observed by WACCM3 and TIME-GCM (which are smaller), which suggests that the tidal magnitudes produced by the ExUM are at least reasonably consistent with other high-top models. The ExUM amplitudes are taken at 95 km whereas the others are taken at 90 km so some caution must be taken in drawing too many conclusions. However, it is worth noting that the values observed at 22°N by Chang et al. (2012) at 95 km also lead to the same conclusions when comparing with the ExUM amplitudes. Finally, the short term variability in zonal wind diurnal amplitudes varies from around 15 ms^{-1} up to as much as 35 ms^{-1} around the September equinox, with the meridional wind varying from around 30 ms^{-1} up to as much as 60 ms^{-1} around the September equinox. This amount of variation was not observed in the models used, and it is encouraging that the ExUM produces short term variation which is similar in magnitude to that seen in the radar observations presented in the study.

We now consider the migrating tides produced by CTMT in the study of Oberheide et al. (2011) (introduced above) in September at 100 km. In terms of the diurnal migrating tides, the zonal wind showed a two peak DW1 structure at 30°S and 30°N, with maximal amplitude of 16 - 18 ms^{-1}. The meridional wind showed a two peak DW1 structure at 20°S and 20°N, with maximal amplitude of 26 ms^{-1}. The temperature field showed a three peak DW1 structure with the largest peak at the

equator and two smaller peaks at 40°S and 40°N. The equatorial peak has a maximal amplitude of 15 K, whilst the smaller peaks have maximal amplitudes around 6 - 7 K. Moving to the semidiurnal migrating tides, the zonal wind showed a two peak SW2 structure at 50 - 60°S and 40°N (as well as some larger values observed between 20 - 30°S) with a maximal amplitude of 28 ms^{-1}. The meridional wind has a four peak structure, with two larger peaks at 50 - 60°S and 40°N, and smaller peaks at 20 - 30°S and 0 - 10°N. The larger peaks have amplitude around 25 - 30 ms^{-1} whilst the smaller peaks have amplitudes around 20 ms^{-1}. Finally the temperature field showed a three peak SW2 structure, with the largest peak at 20°N with smaller peaks at 40°S and 10°S. The largest peak at 20°N has 13 K amplitude, whilst the smaller peaks have amplitudes around 7 - 10 K.

We again must be cautious in drawing too many conclusions in the comparison with ExUM fields taken at 95 km, but we can at least get some idea of the broad features of the modelled tides. The location of each peak is very similar in the zonal and meridional diurnal amplitudes, with maximal amplitudes around half that seen in the ExUM in both cases. The three peak temperature structure concurs with that seen in the ExUM, with similar magnitudes observed for each of the three peaks. The location of the peaks in temperature is about 10 degrees closer to the equator in ExUM compared to CTMT. Looking at the semidiurnal migrating tides, the ExUM zonal wind maximal amplitude is around 40 ms^{-1} in September, around 10 ms^{-1} larger than that seen in CTMT. The two peak structure is replicated in the ExUM, with the third smaller peak around 15°S being similar to the larger values seen in CTMT between 20 - 30°S. The ExUM meridional wind maximal amplitude is around 20 ms^{-1} in September, which is slightly less than that seen in CTMT. The four peak structure is also observed in the ExUM, with peaks at similar locations. Finally, the three peak structure is also observed in the ExUM temperature field in September, with the peaks in similar locations to those seen in CTMT, but with smaller magnitudes - the northmost peak is at around 7 K with the two other peaks at around 5 - 6 K.

Ortland and Alexander (2006) placed a particular focus on tuning the Gravity Wave (GW) forcing to best reflect the diurnal tide structure, rather than to focus the tuning on matching observed mean wind and temperature structure as is standard practice. They observed diurnal meridional wind amplitudes at 95 km with similar latitudinal structure to that observed in the ExUM. The peak magnitudes are on the whole slightly larger in TIDI and their tidal model, ranging from 60 - 80 ms^{-1}, whereas we observe values around 50 ms^{-1} in the ExUM in March. The conclusions when comparing the diurnal temperature amplitude at 95 km are similar. A similar latitudinal structure is observed but with peak magnitudes on the whole slightly larger in SABER and their tidal model – around 20 K – than those observed in ExUM – around 15 K – in March.

Whilst the focus of our study is not on the development of the GW parameterization (the focus is rather to provide a detailed decomposition of the migrating and non-migrating modes produced by the ExUM), it is nevertheless pertinent to discuss aspects of the GW parameterization here to aid future development. Particularly in the context of studies such as Ortland and Alexander (2006) and Yiğit et al. (2021).

As noted in Sect. 2, the ExUM uses the non-orographic Ultra Simple Spectral Parameterization (USSP) of Warner and McIntyre (2001), and includes frictional heating due to gravity wave dissipation, and consequent loss of kinetic energy (see Walters et al. (2017) for more details).

Ortland and Alexander (2006) found that the inclusion of GW forcing tuned for tidal structure acted to narrow the peak location by around 5 degrees. It was noted that the overall effects of gravity wave momentum forcing is highly dependent

on the chosen gravity wave parameterization and chosen source spectrum. Yiğit et al. (2021) showed that implementing a latitudinally varying GW source spectrum can have a significant impact on middle atmosphere circulation, which can therefore have an important effect on the diurnal tides.

It has also been recently suggested that in-situ GW generation above the troposphere and non-primary (e.g. secondary) GW parameterization is necessary to obtain polar winter eastward winds in the MLT (Becker and Vadas, 2018, 2020) which is missing from current high-top models (e.g. Dempsey et al. (2021) in the context of WACCM and ECMAM, and Griffith et al. (2021) in the context of ExUM).

Therefore, to improve the capability of the ExUM in the MLT we recommend further studies to investigate i) the impact on the middle atmosphere mean flow structure of tuning the parameters of the USSP to produce the correct tidal structure in the MLT; ii) the appropriate latitudinal and azimuthal variation in the source spectrum of the USSP for gravity wave parameterization in the MLT; iii) the impact of such a latitudinally and azimuthally varying source spectrum on the tidal structure in the MLT as well as on the mean wind and temperatures in the middle atmosphere; iv) the impact of GW heating on tidal amplitudes in the MLT; and v) the impact of in-situ and non-primary GW generation on modelled winds and tides in the MLT.

Finally, we focus on a more detailed comparison with observational results and how they compare with the ExUM migrating tidal fields produced.

The meteor-radar observations discussed in Pokhotelov et al. (2018), show northern hemisphere semidiurnal zonal and meridional wind tidal amplitudes with values larger than 40 ms^{-1}, which we do not observe in the fields produced by the ExUM. However, the meteor-radar observations discussed in Dempsey et al. (2021), show southern hemisphere semidiurnal zonal and meridional wind amplitudes of 20 - 40 ms^{-1}, which is in keeping with the values seen in the southern hemisphere in the ExUM. It should be noted that interannual variability is currently not included in the modelled values, which could account for some of the differences observed with this study.

Satellite observations are primarily from SABER for temperature, and UARS and TIDI for winds, as introduced above. Focusing first on temperature, the study of Forbes et al. (2008) observes a DW1 at 100 km with strong three-peak structure centred on the equator with the outer peaks around 30°S and 30°N in March to May, with amplitudes around 20 K. This becomes weaker in other parts of the year with values closer to 10 - 15 K with a pronounced low around January. The SW2 at 100 km has a less clear latitudinal structure, but there tend to be maxima either side of the equator in bands from 10 - 30°N and 5 - 40°S, with the southerly peak in May to July and the northerly peak around January to March with values around 15 K. The study of Zhang et al. (2006) shows similar seasonal and latitudinal variation, but with amplitudes of 10 - 15 K for the diurnal migrating tide and 5 - 10 K for the semidiurnal migrating tide at 95 km. In comparison to the fields produced by the ExUM, we see a strikingly similar latitudinal structure in DW1 tide and a reasonably similar structure in the SW2 tide. The peak magnitudes are also similar with values of 10 - 15 K for the ExUM DW1 tide and 5 - 10 K for the ExUM SW2 tide. In the SW2 tide the seasonal variation is also similar, however it is the seasonal structure in the DW1 tide where there is the largest discrepancy. We observe peak values in the ExUM occurring in June and November with lows around August. It should be noted that the seasonal variation is significantly less pronounced, with the equatorial peak varying only between lows of 10 K and highs of 16 K. It is perhaps the case that improved seasonal forcing is therefore necessary in the ExUM.

Looking at observations of zonal winds, Wu et al. (2008a) observed peak values in the DW1 tide from TIDI at 95 km at around 30 - 40°S and 30 - 40°N with values of 60 and 40 ms^{-1} respectively. These peak values tend to occur around April, but with larger values up to 40 ms^{-1} seen throughout the year. Wu et al. (2011) observed peak values in the SW2 tide from TIDI at 95 km at around 50 - 70°S and 50 - 70°N with peak values around 30 - 40 ms^{-1}. The southern hemisphere peaks occur around April and December, whereas the northern hemisphere peaks occur around January and August. Huang and Reber (2004) observe peak values in the DW1 tide from UARS at 95 km which are slightly more equatorward, but with similar maximal amplitudes and a pronounced peak in March/April, with much lower values throughout the rest of the year. In comparison to the fields produced by the ExUM, the latitudinal structure is well reproduced, with similar, but often smaller, peak magnitudes in both the DW1 and SW2 tide. The pronounced peak in March/April is not seen in the ExUM DW1 tide, with little variation over the course of the year. We see much more variation in the SW2 tide, with the May peak in the southern hemisphere and January/August/September peak in the northern hemisphere not too dissimilar to observations. It is once more the seasonal structure of the DW1 that represents the largest discrepancy.

For the meridional winds, Wu et al. (2008a) observed peak values in the DW1 tide from TIDI at 95 km at around 20°S and 20°N with values around 60 - 70 ms^{-1} in March and September/October. Wu et al. (2011) observed peak values in the SW2 tide from TIDI at 95 km at around 50 - 70°S and 50 - 70°N as in the zonal wind, with peak values around 40 ms^{-1}, and with smaller peaks also apparent at lower latitudes. We see peak values in the southern hemisphere in June and in the northern hemisphere in August/December/January. Angelats i Coll and Forbes (2002) observe similar latitudinal and seasonal structure in the SW2 tide from UARS, with slightly larger magnitudes of up to 50 ms^{-1} at 95 km. Huang and Reber (2004) observe peak values in the DW1 tide from UARS at 95 km in keeping with those observed by Wu et al. (2008a). In comparison to the fields produced by the ExUM, the latitudinal and seasonal structure as well as maximal amplitudes are very similar to observations, with no major discrepancies.

In summary, across all the tides considered, the ExUM results illustrate strong amplitude variation with latitude and month across the many components considered. There are small discrepancies in the latitudinal peak location of the modelled tides, as well as small discrepancies where tidal magnitudes are over/underestimated. However the largest discrepancy compared with observations appears to be the seasonal structure, which is only occasionally reproduced and often differs greatly from observed values. It is possible that a factor in this discrepancy in seasonal structure is the simplified radiation and chemistry implementation used – namely that the climatological temperature profile used only gives a simple approximation for monthly and latitudinal variation compared to real values, with no interannual variation; and the ozone background files used also only give a simple approximation for monthly and latitudinal variation compared to real values, also with no interannual variation. This study therefore reinforces that the details of the gravity wave parameterization and radiation/chemistry schemes are important in the MLT and this will be the focus of future model development.

5 Conclusions

In this study, we perform the first in-depth analysis of migrating and non-migrating modes present in the new Extended Unified Model. We have improved on the implementation of the ExUM used in Griffith et al. (2021) by i) using a monthly and latitudinally varying temperature profile above 90 km, and ii) using a vertical resolution based on atmospheric scale height so that physically important waves are captured. We investigate the instantaneous tidal perturbations and spatial wave number decomposition at two characteristic latitudes – that of Ascension Island near the equator where the diurnal wind tide dominates, and that of Rothera at polar latitudes, where the semidiurnal wind tide dominates. We characterise the latitudinal dependence of both the diurnal and semidiurnal tide, and their variability on shorter time scales at the equatorial and polar latitudes. The model thus proves to be a useful tool for investigating migrating and non-migrating modes. This is particularly useful given the difficulty in obtaining measurements of non-migrating modes.

Key results include:

1. The decomposition of the modelled temperature, zonal and meridional wind fields into migrating and non-migrating tides yields significant amplitudes across a rich spectrum of temporal and spatial modes.

2. The ExUM produces non-migrating modes of significant amplitude in the MLT. The DW2, DE3 and DW3 modes are dominant in the diurnal tide and the SW1, S0 and SW3 modes are dominant in the semidiurnal tide. These modes include those proposed as being key agents in thermosphere-ionosphere coupling e.g. those producing the wavenumber 4 structure in TEC in the ionosphere.

3. The migrating modes are in general consistent with those reported in other modelling and observational studies. The wind fields have a bimodal latitudinal structure with tropical peaks in amplitude in the case of the diurnal tide, and with an approximate bimodal structure with amplitude peaks at polar latitudes in the case of the semidiurnal tide. The temperature field latitudinal structure reveals a three peak structure centred on the equator.

4. The ExUM suggests there is significant short-term variability in the migrating and non-migrating modes – this is particularly important given the great difficulty of making experimental determinations of the short-term variability of non-migrating tides.

5. There is distinct growth in the DE3 amplitude with increasing height, from 90 km up to a height of around 105 km, where the model physics is still reasonably complete. This is an important observation given the suggested impact of the DE3 in driving ionospheric variability.

6. We have proposed specific future developments of the model to improve the accuracy and physical completeness of the ExUM in the MLT, with a particular focus on the parameterization of gravity waves and the development of radiation/chemistry schemes.

In summary, our results indicate the usefulness of the ExUM in modelling atmospheric migrating and non-migrating tides in the MLT and provide insight not only into further developments required for the ExUM, but for developments within the broader context of whole atmosphere modelling.

Code availability. The Unified Model code is provided courtesy of the UK Met Office and is subject to copyright.

Data availability. The model data is produced by the UK Met Office's Unified Model, copyright UK Met Office.

Author contributions. The experimental concept, design of methodology and interpretation of results was performed by Griffith and Mitchell. The final authorship of the manuscript and preparation of figures was performed by Griffith.

Competing interests. No competing interests are present.

Acknowledgements. MJG and NJM are supported by a NERC GW4+ Doctoral Training Partnership studentship from the Natural Environment Research Council [NE/L002434/1] and are thankful for the collaborative support of the Met Office, UK.

References

Akmaev, R.: Whole atmosphere modeling: Connecting terrestrial and space weather, Reviews of Geophysics, 49, https://doi.org/10.1029/2011rg000364, 2011.

Akmaev, R. A., Fuller-Rowell, T., Wu, F., Forbes, J., Zhang, X., Anghel, A., Iredell, M., Moorthi, S., and Juang, H.-M.: Tidal variability in the lower thermosphere: Comparison of Whole Atmosphere Model (WAM) simulations with observations from TIMED, Geophysical Research Letters, 35, https://doi.org/10.1029/2007gl032584, 2008.

Angelats i Coll, M. and Forbes, J.: Nonlinear interactions in the upper atmosphere: The s= 1 and s= 3 nonmigrating semidiurnal tides, Journal of Geophysical Research: Space Physics, 107, SIA 3–1 – SIA 3–15, https://doi.org/10.1029/2001ja900179, 2002.

Baldwin, M., Birner, T., Brasseur, G., Burrows, J., Butchart, N., Garcia, R., Geller, M., Gray, L., Hamilton, K., Harnik, N., Hegglin, M., Langematz, U., Robock, A., Sato, K., and Scaife, A.: 100 Years of Progress in Understanding the Stratosphere and Mesosphere, Meteorological Monographs, 59, 27.1–27.62, https://doi.org/10.1175/AMSMONOGRAPHS-D-19-0003.1, 2019.

Beagley, S. R., McLandress, C., Fomichev, V. I., and Ward, W. E.: The extended Canadian middle atmosphere model, Geophysical research letters, 27, 2529–2532, https://doi.org/10.1029/1999gl011233, 2000.

Becker, E.: Mean-flow effects of thermal tides in the mesosphere and lower thermosphere, Journal of Atmospheric Sciences, 74, 2043–2063, https://doi.org/10.1175/jas-d-16-0194.1, 2017.

Becker, E. and Vadas, S. L.: Secondary gravity waves in the winter mesosphere: Results from a high-resolution global circulation model, Journal of Geophysical Research: Atmospheres, 123, 2605–2627, https://doi.org/10.1002/2017jd027460, 2018.

Becker, E. and Vadas, S. L.: Explicit Global Simulation of Gravity Waves in the Thermosphere, Journal of Geophysical Research: Space Physics, 125, https://doi.org/10.1029/2020ja028034, 2020.

Borchert, S., Zhou, G., Baldauf, M., Schmidt, H., Zängl, G., and Reinert, D.: The upper-atmosphere extension of the ICON general circulation model (version: ua-icon-1.0), Geoscientific Model Development, 12, 3541–3569, https://doi.org/10.5194/gmd-12-3541-2019, 2019.

Chang, L., Ward, W., Palo, S., Du, J., Wang, D.-Y., Liu, H.-L., Hagan, M., Portnyagin, Y., Oberheide, J., Goncharenko, L., Nakamura, T., Hoffmann, P., Singer, W., Batista, P., Clemesha, B., Manson, A., Riggin, D., She, C.-Y., Tsuda, T., and Yuan, T.: Comparison of diurnal tide in models and ground-based observations during the 2005 equinox CAWSES tidal campaign, Journal of atmospheric and solar-terrestrial physics, 78, 19–30, https://doi.org/10.1016/j.jastp.2010.12.010, 2012.

Davis, R., Du, J., Smith, A., Ward, W., and Mitchell, N.: The diurnal and semidiurnal tides over Ascension Island (8° S, 14° W) and their interaction with the stratospheric quasi-biennial oscillation: studies with meteor radar, eCMAM and WACCM., Atmospheric Chemistry & Physics, 13, https://doi.org/10.5194/acp-13-9543-2013, 2013.

Dempsey, S., Hindley, N., Moffat-Griffin, T., Wright, C., Smith, A., Du, J., and Mitchell, N.: Winds and Tides of the Antarctic Mesosphere and Lower Thermosphere: One Year of Meteor-Radar Observations Over Rothera (68° S, 68° W) and Comparisons with WACCM and eCMAM., Journal of Atmospheric and Solar-Terrestrial Physics, 212, https://doi.org/10.1016/j.jastp.2020.105510, 2021.

Ekanayake, E., Aso, T., and Miyahara, S.: Background wind effect on propagation of nonmigrating diurnal tides in the middle atmosphere, Journal of Atmospheric and Solar-Terrestrial Physics, 59, 401–429, https://doi.org/10.1016/S1364-6826(96)00012-0, 1997.

England, S.: A review of the effects of non-migrating atmospheric tides on the Earth's low-latitude ionosphere, Space science reviews, 168, 211–236, https://doi.org/10.1007/s11214-011-9842-4, 2012.

Fiedler, J., Baumgarten, G., and Von Cossart, G.: Mean diurnal variations of noctilucent clouds during 7 years of lidar observations at ALOMAR, Annales Geophysicae, https://doi.org/10.5194/angeo-23-1175-2005, 2005.

Fleming, E. L., Chandra, S., Barnett, J., and Corney, M.: Zonal mean temperature, pressure, zonal wind and geopotential height as functions of latitude, Advances in Space Research, 10, 11–59, https://doi.org/10.1016/0273-1177(90)90386-e, 1990.

Forbes, J., Hagan, M., and Zhang, X.: Seasonal cycle of nonmigrating diurnal tides in the MLT region due to tropospheric heating rates from the NCEP/NCAR Reanalysis Project, Advances in Space Research, 39, 1347–1350, https://doi.org/10.1016/j.asr.2003.09.076, 2007.

Forbes, J., Zhang, X., Palo, S., Russell, J., Mertens, C., and Mlynczak, M.: Tidal variability in the ionospheric dynamo region, Journal of Geophysical Research: Space Physics, 113, https://doi.org/10.1029/2007ja012737, 2008.

Forbes, J. M. and Wu, D.: Solar tides as revealed by measurements of mesosphere temperature by the MLS experiment on UARS, Journal of the atmospheric sciences, 63, 1776–1797, https://doi.org/10.1175/jas3724.1, 2006.

Forbes, J. M., Zhang, X., Talaat, E. R., and Ward, W.: Nonmigrating diurnal tides in the thermosphere, Journal of Geophysical Research: Space Physics, 108, https://doi.org/10.1029/2002ja009262, 2003.

Fritts, D., Vadas, S., Riggin, D., Abdu, M., Batista, I., Takahashi, H., Medeiros, A., Kamalabadi, F., Liu, H.-L., Fejer, B., and Taylor, M.: Gravity wave and tidal influences on equatorial spread F based on observations during the Spread F Experiment (SpreadFEx), Annales Geophysicae, 26, 3235–3252, https://doi.org/10.5194/angeo-26-3235-2008, 2008.

Fritts, D. C. and Alexander, M. J.: Gravity wave dynamics and effects in the middle atmosphere, Reviews of geophysics, 41, https://doi.org/10.1029/2001RG000106, 2003.

Fujiwara, H. and Miyoshi, Y.: Morphological features and variations of temperature in the upper thermosphere simulated by a whole atmosphere GCM, in: Annales Geophysicae, vol. 28, pp. 427–437, Copernicus GmbH, https://doi.org/10.5194/angeo-28-427-2010, 2010.

Fuller-Rowell, T., Akmaev, R., Wu, F., Anghel, A., Maruyama, N., Anderson, D., Codrescu, M., Iredell, M., Moorthi, S., Juang, H., and Hou, Y.: Impact of terrestrial weather on the upper atmosphere, Geophysical Research Letters, 35, https://doi.org/10.1029/2007gl032911, 2008.

Goncharenko, L., Coster, A., Chau, J., and Valladares, C.: Impact of sudden stratospheric warmings on equatorial ionization anomaly, Journal of Geophysical Research: Space Physics, 115, https://doi.org/10.1029/2010ja015400, 2010.

Griffin, D. and Thuburn, J.: Numerical effects on vertical wave propagation in deep-atmosphere models, Quarterly Journal of the Royal Meteorological Society, 144, 567–580, https://doi.org/10.1002/qj.3229, 2018.

Griffith, M. J., Jackson, D. R., Griffin, D. J., and Budd, C. J.: Stable extension of the unified model into the mesosphere and lower thermosphere, Journal of Space Weather and Space Climate, 10, https://doi.org/10.1051/swsc/2020018, 2020.

Griffith, M. J., Dempsey, S. M., Jackson, D. R., Moffat-Griffin, T., and Mitchell, N. J.: Winds and Tides of the Extended Unified Model in the Mesosphere and Lower Thermosphere Validated with Meteor Radar Observations, Annales Geophysicae, 39, 1–28, https://doi.org/10.5194/angeo-39-487-2021, 2021.

Hagan, M. and Forbes, J.: Migrating and nonmigrating diurnal tides in the middle and upper atmosphere excited by tropospheric latent heat release, Journal of Geophysical Research: Atmospheres, 107, ACL 6–1 – ACL 6–15, https://doi.org/10.1029/2001jd001236, 2002.

Hagan, M. and Forbes, J. M.: Migrating and nonmigrating semidiurnal tides in the upper atmosphere excited by tropospheric latent heat release, Journal of Geophysical Research: Space Physics, 108, https://doi.org/10.1029/2002ja009466, 2003.

Hagan, M. and Roble, R.: Modeling diurnal tidal variability with the National Center for Atmospheric Research thermosphere-ionosphere-mesosphere-electrodynamics general circulation model, Journal of Geophysical Research: Space Physics, 106, 24 869–24 882, https://doi.org/10.1029/2001ja000057, 2001.

Hagan, M., Burrage, M. D., Forbes, J., Hackney, J., Randel, W., and Zhang, X.: GSWM-98: Results for migrating solar tides, Journal of Geophysical Research: Space Physics, 104, 6813–6827, https://doi.org/10.1029/1998JA900125, 1999.

Hagan, M., Maute, A., Roble, R., Richmond, A., Immel, T., and England, S.: Connections between deep tropical clouds and the Earth's ionosphere, Geophysical Research Letters, 34, https://doi.org/10.1029/2007gl030142, 2007.

Hibbins, R., Espy, P. J., Orsolini, Y., Limpasuvan, V., and Barnes, R.: SuperDARN observations of semidiurnal tidal variability in the MLT and the response to sudden stratospheric warming events, Journal of Geophysical Research: Atmospheres, 124, 4862–4872, https://doi.org/10.1029/2018jd030157, 2019.

Hickey, M., Walterscheid, R., and Schubert, G.: Gravity wave heating and cooling of the thermosphere: Sensible heat flux and viscous flux of kinetic energy, Journal of Geophysical Research: Space Physics, 116, https://doi.org/10.1029/2011ja016792, 2011.

Huang, F. T. and Reber, C. A.: Nonmigrating semidiurnal and diurnal tides at 95 km based on wind measurements from the High Resolution Doppler Imager on UARS, Journal of Geophysical Research: Atmospheres, 109, https://doi.org/10.1029/2003JD004442, 2004.

Iimura, H., Fritts, D., Wu, Q., Skinner, W., and Palo, S.: Nonmigrating semidiurnal tide over the Arctic determined from TIMED Doppler Interferometer wind observations, Journal of Geophysical Research: Atmospheres, 115, https://doi.org/10.1029/2009jd012733, 2010.

Jackson, D., Bruinsma, S., Negrin, S., Stolle, C., Budd, C., Gonzalez, R., Down, E., Griffin, D., Griffith, M., Kervalishvili, G., and Arenillas, D.: The Space Weather Atmosphere Models and Indices (SWAMI) Project: Overview and first results, Journal of Space Weather and Space Climate, 10, https://doi.org/10.1051/swsc/2020019, 2020.

Jackson, D. R., Fuller-Rowell, T. J., Griffin, D. J., Griffith, M. J., Kelly, C. W., Marsh, D. R., and Walach, M.-T.: Future directions for whole atmosphere modeling: Developments in the context of space weather, Space Weather, 17, 1342–1350, https://doi.org/10.1029/2019SW002267, 2019.

Jin, H., Miyoshi, Y., Pancheva, D., Mukhtarov, P., Fujiwara, H., and Shinagawa, H.: Response of migrating tides to the stratospheric sudden warming in 2009 and their effects on the ionosphere studied by a whole atmosphere-ionosphere model GAIA with COSMIC and TIMED/SABER observations, Journal of Geophysical Research: Space Physics, 117, https://doi.org/10.1029/2012ja017650, 2012.

Klimenko, M. V., Klimenko, V. V., Bessarab, F. S., Sukhodolov, T. V., Vasilev, P. A., Karpov, I. V., Korenkov, Y. N., Zakharenkova, I. E., Funke, B., and Rozanov, E. V.: Identification of the mechanisms responsible for anomalies in the tropical lower thermosphere/ionosphere caused by the January 2009 sudden stratospheric warming, Journal of Space Weather and Space Climate, 9, https://doi.org/10.1051/swsc/2019037, 2019.

Li, X., Wan, W., Ren, Z., Liu, L., and Ning, B.: The variability of nonmigrating tides detected from TIMED/SABER observations, Journal of Geophysical Research: Space Physics, 120, 10 793–10 808, https://doi.org/10.1002/2015JA021577, 2015.

Liu, G., Janches, D., Lieberman, R. S., Moffat-Griffin, T., Fritts, D. C., and Mitchell, N. J.: Coordinated Observations of 8-and 6-hr Tides in the Mesosphere and Lower Thermosphere by Three Meteor Radars Near 60° S Latitude, Geophysical Research Letters, 47, e2019GL086 629, https://doi.org/10.1029/2019GL086629, 2020.

Liu, H.-L.: Variability and predictability of the space environment as related to lower atmosphere forcing, Space Weather, 14, 634–658, https://doi.org/10.1002/2016SW001450, 2016.

Liu, H.-L., Foster, B., Hagan, M., McInerney, J., Maute, A., Qian, L., Richmond, A., Roble, R., Solomon, S., Garcia, R., and Kinnison, D.: Thermosphere extension of the whole atmosphere community climate model, Journal of Geophysical Research: Space Physics, 115, https://doi.org/10.1029/2010JA015586, 2010.

Liu, H.-L., Bardeen, C., Foster, B., Lauritzen, P., Liu, J., Lu, G., Marsh, D., Maute, A., McInerney, J., Pedatella, N., and Qian, L.: Development and validation of the Whole Atmosphere Community Climate Model with thermosphere and ionosphere extension (WACCM-X 2.0), Journal of Advances in Modeling Earth Systems, 10, 381–402, https://doi.org/10.1002/2017ms001232, 2018.

Medvedev, A. and Klaassen, G.: Thermal effects of saturating gravity waves in the atmosphere, Journal of Geophysical Research: Atmospheres, 108, ACL 4–1 – ACL 4–18, https://doi.org/10.1029/2002jd002504, 2003.

Meraner, K. and Schmidt, H.: Transport of nitrogen oxides through the winter mesopause in HAMMONIA, Journal of Geophysical Research: Atmospheres, 121, 2556–2570, https://doi.org/10.1002/2015jd024136, 2016.

Mitchell, N., Pancheva, D., Middleton, H., and Hagan, M.: Mean winds and tides in the Arctic mesosphere and lower thermosphere, Journal of Geophysical Research: Space Physics, 107, SIA 2–1 – SIA 2–14, https://doi.org/10.1029/2001ja900127, 2002.

Miyahara, S. and Forbes, J. M.: Interactions between gravity waves and the diurnal tide in the mesosphere and lower thermosphere, Journal of the Meteorological Society of Japan. Ser. II, 69, 523–531, https://doi.org/10.2151/jmsj1965.69.5_523, 1991.

Miyoshi, Y. and Fujiwara, H.: Gravity waves in the thermosphere simulated by a general circulation model, Journal of Geophysical Research: Atmospheres, 113, https://doi.org/10.1029/2007jd008874, 2008.

Miyoshi, Y. and Yiğit, E.: Impact of gravity wave drag on the thermospheric circulation: implementation of a nonlinear gravity wave parameterization in a whole-atmosphere model, Annales Geophysicae, 37, 955–969, https://doi.org/10.5194/angeo-37-955-2019, 2019.

Miyoshi, Y., Pancheva, D., Mukhtarov, P., Jin, H., Fujiwara, H., and Shinagawa, H.: Excitation mechanism of non-migrating tides, Journal of Atmospheric and Solar-Terrestrial Physics, 156, 24–36, https://doi.org/10.1016/j.jastp.2017.02.012, 2017.

Mukhtarov, P., Pancheva, D., and Andonov, B.: Global structure and seasonal and interannual variability of the migrating diurnal tide seen in the SABER/TIMED temperatures between 20 and 120 km, Journal of Geophysical Research: Space Physics, 114, https://doi.org/10.1029/2008JA013759, 2009.

Murphy, D., French, W., and Vincent, R.: Long-period planetary waves in the mesosphere and lower thermosphere above Davis, Antarctica, Journal of atmospheric and solar-terrestrial physics, 69, 2118–2138, https://doi.org/10.1016/j.jastp.2007.06.008, 2007.

Murphy, D., Aso, T., Fritts, D., Hibbins, R., McDonald, A., Riggin, D., Tsutsumi, M., and Vincent, R.: Source regions for Antarctic MLT non-migrating semidiurnal tides, Geophysical research letters, 36, https://doi.org/10.1029/2008gl037064, 2009.

Oberheide, J., Wu, Q., Killeen, T., Hagan, M., and Roble, R.: Diurnal nonmigrating tides from TIMED Doppler Interferometer wind data: Monthly climatologies and seasonal variations, Journal of Geophysical Research: Space Physics, 111, https://doi.org/10.1029/2005JA011491, 2006.

Oberheide, J., Wu, Q., Killeen, T., Hagan, M., and Roble, R.: A climatology of nonmigrating semidiurnal tides from TIMED Doppler Interferometer (TIDI) wind data, Journal of atmospheric and solar-terrestrial physics, 69, 2203–2218, https://doi.org/10.1016/j.jastp.2007.05.010, 2007.

Oberheide, J., Forbes, J., Häusler, K., Wu, Q., and Bruinsma, S.: Tropospheric tides from 80 to 400 km: Propagation, interannual variability, and solar cycle effects, Journal of Geophysical Research: Atmospheres, 114, https://doi.org/10.1029/2009jd012388, 2009.

Oberheide, J., Forbes, J., Zhang, X., and Bruinsma, S.: Climatology of upward propagating diurnal and semidiurnal tides in the thermosphere, Journal of Geophysical Research: Space Physics, 116, https://doi.org/10.1029/2011ja016784, 2011.

Ortland, D. A. and Alexander, M. J.: Gravity wave influence on the global structure of the diurnal tide in the mesosphere and lower thermosphere, Journal of Geophysical Research: Space Physics, 111, https://doi.org/10.1029/2005ja011467, 2006.

Pancheva, D., Mukhtarov, P., and Andonov, B.: Global structure, seasonal and interannual variability of the eastward propagating tides seen in the SABER/TIMED temperatures (2002–2007), Advances in space research, 46, 257–274, https://doi.org/10.5194/angeo-27-687-2009, 2010.

Pancheva, D., Mukhtarov, P., Hall, C., Smith, A., and Tsutsumi, M.: Climatology of the short-period (8-h and 6-h) tides observed by meteor radars at Tromsø and Svalbard, Journal of Atmospheric and Solar-Terrestrial Physics, 212, 105 513, https://doi.org/10.1016/j.jastp.2020.105513, 2021.

Pogoreltsev, A.: Generation of normal atmospheric modes by stratospheric vacillations, Izvestiya, Atmospheric and Oceanic Physics, 43, 423–435, https://doi.org/10.1134/s0001433807040044, 2007.

Pogoreltsev, A., Vlasov, A., Fröhlich, K., and Jacobi, C.: Planetary waves in coupling the lower and upper atmosphere, Journal of Atmospheric and Solar-Terrestrial Physics, 69, 2083–2101, https://doi.org/10.1016/j.jastp.2007.05.014, 2007.

Pokhotelov, D., Becker, E., Stober, G., and Chau, J. L.: Seasonal variability of atmospheric tides in the mesosphere and lower thermosphere: meteor radar data and simulations, Annales Geophysicae, 36, 825–830, https://doi.org/10.5194/angeo-36-825-2018, 2018.

Roble, R. and Ridley, E.: A thermosphere-ionosphere-mesosphere-electrodynamics general circulation model (TIME-GCM): Equinox solar cycle minimum simulations (30–500 km), Geophysical Research Letters, 21, 417–420, https://doi.org/10.1029/93GL03391, 1994.

Scaife, A., Butchart, N., Warner, C., and Swinbank, R.: Impact of a spectral gravity wave parameterization on the stratosphere in the Met Office Unified Model, Journal of the atmospheric sciences, 59, 1473–1489, https://doi.org/10.1175/1520-0469(2002)059<1473:ioasgw>2.0.co;2, 2002.

Schmidt, H., Brasseur, G., Charron, M., Manzini, E., Giorgetta, M., Diehl, T., Fomichev, V., Kinnison, D., Marsh, D., and Walters, S.: The HAMMONIA chemistry climate model: Sensitivity of the mesopause region to the 11-year solar cycle and CO2 doubling, Journal of Climate, 19, 3903–3931, https://doi.org/10.1175/jcli3829.1, 2006.

Smith, A. K.: Global dynamics of the MLT, Surveys in Geophysics, 33, 1177–1230, https://doi.org/10.1007/s10712-012-9196-9, 2012.

Smith, A. K., Pancheva, D. V., Mitchell, N. J., Marsh, D. R., Russell III, J. M., and Mlynczak, M. G.: A link between variability of the semidiurnal tide and planetary waves in the opposite hemisphere, Geophysical research letters, 34, https://doi.org/10.1029/2006gl028929, 2007.

Suvorova, E. and Pogoreltsev, A.: Modeling of nonmigrating tides in the middle atmosphere, Geomagnetism and Aeronomy, 51, 105–115, https://doi.org/10.1134/s0016793210061039, 2011.

Vitharana, A., Zhu, X., Du, J., Oberheide, J., and Ward, W. E.: Statistical Modeling of Tidal Weather in the Mesosphere and Lower Thermosphere, Journal of Geophysical Research: Atmospheres, 124, 9011–9027, https://doi.org/10.1029/2019jd030573, 2019.

Walters, D., Baran, A., Boutle, I., Brooks, M., Earnshaw, P., Edwards, J., Furtado, K., Hill, P., Lock, A., Manners, J., Morcrette, C., Mulcahy, J., Sanchez, C., Smith, C., Stratton, R., Tennant, W., Tomassini, L., Van Weverberg, K., Vosper, S., Willett, M., Browse, J., Bushell, A., Dalvi, M., Essery, R., Gedney, N., Hardiman, S., Johnson, B., Johnson, C., Jones, A., Mann, G., Milton, S., Rumbold, H., Sellar, A., Ujiie, M., Whitall, M., Williams, K., and Zerroukat, M.: The Met Office Unified Model Global Atmosphere 7.0/7.1 and JULES Global Land 7.0 configurations, Geoscientific Model Development Discussions, 2017, 1–78, https://doi.org/10.5194/gmd-2017-291, https://www.geosci-model-dev.net/12/1909/2019/gmd-12-1909-2019.pdf, 2017.

Warner, C. and McIntyre, M.: An ultrasimple spectral parameterization for nonorographic gravity waves, Journal of the atmospheric sciences, 58, 1837–1857, https://doi.org/10.1175/1520-0469(2001)058<1837:auspfn>2.0.co;2, 2001.

Wood, N., Staniforth, A., White, A., Allen, T., Diamantakis, M., Gross, M., Melvin, T., Smith, C., Vosper, S., Zerroukat, M., and Thuburn, J.: An inherently mass-conserving semi-implicit semi-Lagrangian discretization of the deep-atmosphere global non-hydrostatic equations, Quarterly Journal of the Royal Meteorological Society, 140, 1505–1520, https://doi.org/10.1002/qj.2235, 2014.

Wu, Q., Ortland, D., Killeen, T., Roble, R., Hagan, M., Liu, H.-L., Solomon, S., Xu, J., Skinner, W., and Niciejewski, R.: Global distribution and interannual variations of mesospheric and lower thermospheric neutral wind diurnal tide: 1. Migrating tide, Journal of Geophysical Research: Space Physics, 113, https://doi.org/10.1029/2007JA012542, 2008a.

Wu, Q., Ortland, D., Killeen, T., Roble, R., Hagan, M., Liu, H.-L., Solomon, S., Xu, J., Skinner, W., and Niciejewski, R.: Global distribution and interannual variations of mesospheric and lower thermospheric neutral wind diurnal tide: 2. Nonmigrating tide, Journal of Geophysical Research: Space Physics, 113, https://doi.org/10.1029/2007JA012543, 2008b.

Wu, Q., Ortland, D., Solomon, S., Skinner, W., and Niciejewski, R.: Global distribution, seasonal, and inter-annual variations of mesospheric semidiurnal tide observed by TIMED TIDI, Journal of atmospheric and solar-terrestrial physics, 73, 2482–2502, https://doi.org/10.1016/j.jastp.2011.08.007, 2011.

Yamashita, C., Liu, H.-L., and Chu, X.: Responses of mesosphere and lower thermosphere temperatures to gravity wave forcing during stratospheric sudden warming, Geophysical Research Letters, 37, https://doi.org/10.1029/2009GL042351, 2010.

Yiğit, E. and Medvedev, A. S.: Heating and cooling of the thermosphere by internal gravity waves, Geophysical Research Letters, 36, https://doi.org/10.1029/2009gl038507, 2009.

Yiğit, E. and Medvedev, A. S.: Internal wave coupling processes in Earth's atmosphere, Advances in Space Research, 55, 983–1003, https://doi.org/10.1016/j.asr.2014.11.020, 2015.

Yiğit, E. and Medvedev, A. S.: Influence of parameterized small-scale gravity waves on the migrating diurnal tide in Earth's thermosphere, Journal of Geophysical Research: Space Physics, 122, 4846–4864, https://doi.org/10.1002/2017ja024089, 2017.

Yiğit, E., Medvedev, A. S., Aylward, A. D., Hartogh, P., and Harris, M. J.: Modeling the effects of gravity wave momentum deposition on the general circulation above the turbopause, Journal of Geophysical Research: Atmospheres, 114, https://doi.org/10.1029/2008jd011132, 2009.

Yiğit, E., Knížová, P. K., Georgieva, K., and Ward, W.: A review of vertical coupling in the Atmosphere–Ionosphere system: Effects of waves, sudden stratospheric warmings, space weather, and of solar activity, Journal of Atmospheric and Solar-Terrestrial Physics, 141, 1–12, https://doi.org/10.1016/j.jastp.2016.02.011, 2016.

Yiğit, E., Medvedev, A. S., and Ern, M.: Effects of Latitude-Dependent Gravity Wave Source Variations on the Middle and Upper Atmosphere, Frontiers in Astronomy and Space Sciences, 7, https://doi.org/10.3389/fspas.2020.614018, 2021.

Zhang, X., Forbes, J. M., Hagan, M. E., Russell III, J. M., Palo, S. E., Mertens, C. J., and Mlynczak, M. G.: Monthly tidal temperatures 20–120 km from TIMED/SABER, Journal of Geophysical Research: Space Physics, 111, https://doi.org/10.1029/2005JA011504, 2006.

7.2. Conclusions

Additions made to improve the ExUM in the MLT are detailed and the capability of the model to produce migrating and non-migrating tides with realistic magnitudes and latitudinal & short-term variability is examined by inter-comparison with other modelling and observational studies.

The results show that the ExUM produces migrating and non-migrating modes which are in general consistent with the other models and observational datasets considered. However, there is much variation even across the limited number of studies considered and following from the conclusions of Chapter 6, specific recommendations are made for the direction of further studies to improve modelling in the MLT, with a particular focus on the non-orographic gravity wave parameterisation used in the ExUM (the USSP).

In particular, we recommend further studies to investigate i) the impact on the middle atmosphere mean flow structure of tuning the parameters of the USSP to produce the correct tidal structure in the MLT; ii) the appropriate latitudinal and azimuthal variation in the source spectrum of the USSP for gravity wave parameterisation in the MLT; iii) the impact of such a latitudinally and azimuthally varying source spectrum on the tidal structure in the MLT as well as on the mean wind and temperatures in the middle atmosphere; iv) the impact of GW heating on tidal amplitudes in the MLT; and v) the impact of in-situ and non-primary GW generation on modelled winds and tides in the MLT.

Chapter 8

Final Conclusions and Outlook

In this thesis, the overarching goal has been to produce a stable extension of the Met Office's Unified Model (UM) into the Mesosphere and Lower Thermosphere and validate the output against both observational datasets and other atmospheric models of this region. Thus, the work performed in this thesis describes the necessary steps for development of the novel stable extended Unified Model, as well as a first investigation into the realism of the model by comparison to both meteor radar observations and other modelling and observational studies. This provides a solid foundation for the development of a Whole Atmosphere Unified Model.

In Chapter 3, we give some context to the studies performed in the thesis. We provide preliminary background on atmospheric structure and the UM, discussing atmospheric layers, and the dynamical and physical components of the UM. We also refer to introductions to high-top models and to atmospheric tides performed in both Chapters 6 and 7. We conclude the introductory portion of the thesis with a commentary on whole atmosphere models in Chapter 4, which gives a useful insight into current whole atmosphere models, as well as important considerations in their development.

In Chapter 5, we produce the first stable extension of the UM with an upper boundary at 100 km. We performed a thorough and systematic investigation of the extended model, and found that the assumption of Local Thermodynamic Equilibrium (LTE) above 65 km was causing the observed high wind speeds and consequent instability in the model. Therefore, the influence of the radiation scheme is removed above this height and is replaced with a relaxation or "nudging" scheme. This pushes the model temperature above 65 km towards a globally uniform analytic temperature profile to yield realistic temperatures in the MLT whilst the non-LTE radiation scheme and appropriate chemistry schemes are under development. With this model configuration, a stable Extended UM (ExUM) was successfully produced, illustrating that this was the primary cause of model instability. This successful implementation then allowed testing of different upper boundary heights as well as different vertical resolutions for the MLT. Both 3 km and 1.5 km resolutions were used, based on 2 and 4 levels per atmospheric scale height respectively at the mesopause. The latter was found to require a significant increase to the vertical damping coefficient whilst the former remained stable with a 100 km lid. Upper boundaries at heights of 120 km and 135 km were trialled, with the 1.5 km being too unstable for raised upper boundaries. The 3 km resolution however produced stable runs with some increase to the vertical damping coefficient, and so it became the model configuration going forward.

In the second part of the thesis, we use the stable ExUM implementation from the first part of the thesis to provide a first analysis of the atmospheric fields produced by the model in the MLT, as well as implement some incremental updates to the model. In Chapter 6, we perform a first comparison of the winds and atmospheric tides produced by the ExUM with meteor radar observations between heights of 80 and 100 km. Additionally, a non-LTE radiation scheme developed at the Met Office is introduced to this version of the ExUM, which provides appropriate forcing up to 90 km, above which the nudging scheme is still used. The comparison is performed

in two key regimes, at an equatorial latitude (Ascension Island (8° S, 14° W)), where the diurnal (24 hour) tide dominates and a polar latitude (Rothera (68° S, 68° W)), where the semidiurnal (12 hour) tide dominates. The results illustrate that the ExUM has a good natural capability for modelling atmospheric winds and tides in the MLT, but that are some significant differences in the detail. For example, in the equatorial regime, some key characteristics are captured such as zonal & meridional wind minima and maxima, the increase in tidal amplitude with increasing height and the decrease in tidal phase which increasing height. However, in the polar regime, the ExUM zonal background winds in austral winter are primarily westward rather than eastward and in austral summer are larger than observed above 90 km. However, it is worth noting that this bias is also seen in other high-top models, and we propose that this is caused by the lack of in-situ gravity wave generation to generate eastward fluxes in the MLT. The globally uniform temperature relaxation profile is also clearly sub-optimal, and so we make specific recommendations of changes that can be implemented to improve the accuracy of the ExUM in the MLT.

Whilst the implementation of a more complex gravity wave parameterisation scheme is beyond the scope of this thesis, we can provide further insight into the spatial and temporal modes of atmospheric tides produced by the model in order to guide development of such a scheme. Moreover, we take the opportunity to make developments to the nudging scheme used in the model as well as to the vertical resolution used as the upper boundary of the model is pushed to greater heights. This goal provides the basis of the study in Chapter 7, where we perform a first investigation into the non-migrating (not sun-following) tides produced by the model as well as look at the latitudinal and short-term variation of both migrating and non-migrating tides. Model diagnostics of atmospheric temperature, zonal and meridional winds are investigated firstly at an equatorial and polar regime as in Chapter 6, looking at instantaneous tidal perturbations as well as the non-migrating modes at a height of 95 km. Following this, the latitudinal dependence of the migrating and non-migrating modes is investigated at 95 km. Finally, the short term variability of the migrating and largest non-migrating modes is investigated once more at equatorial and polar latitudes, and at 95 km. The results of the study show that the ExUM produces a rich spectrum of migrating and non-migrating modes which are reasonably consistent with other observational and modelling studies. In particular, the model reproduces large DE3, DW2 and DW3 non-migrating diurnal modes and large SW1 and SW3 non-migrating semidiurnal modes. The latitudinal structure of the migrating modes is also reproduced. For example, the diurnal tide in the zonal wind reproduces the expected bimodal structure with tropical peaks. Finally, the short term variability is also significant, fluctuating by up to 150% in the non-migrating modes – a property which is seen observationally but is not a common feature of current high-top atmospheric models. However, the general variability between studies illustrates that there is still more to do to improve the physics of the model in the MLT. We recommend further studies which can be performed to analyse the non-orographic gravity wave parameterisation scheme to provide a more complete model of the MLT.

The aim of the thesis was to develop a stable Extended Unified Model and validate its output based on other modelling studies and observational datasets in order to lay the foundation for a Whole Atmosphere Unified Model. Naturally, this process has led to further questions and directions for further study which have not been pursued. We describe some of the possibilities for future research in the following section.

8.1. Future Research

8.1.1 The effect of the horizontal resolution of the model on tidal modes

The studies of Chapters 6 and 7 raise the question as to what is missing from the model to account for the observed inaccuracies in the model fields, most notably the incorrect wind direction at polar latitudes in austral winter. It is likely that the parameterizations which account for unresolved atmospheric features are not including appropriate physical phenomena which are particularly important in the MLT, such as in-situ gravity wave generation. An approach to quantify this difference would be to run climate simulations at a much higher resolution to attempt to resolve the appropriate physics in the MLT. Appropriate resolutions would be the N216 or N512 resolutions available in the Unified Model, which give mid-latitude horizontal resolutions of around 60 km and 25 km respectively, compared to the N96 resolution with a mid-latitude horizontal resolution of around 135 km. This would determine whether an improved horizontal resolution rectifies model biases such as the incorrect wind direction mentioned above. As well as this, the information yielded from these experiments could be used to educate the development of parameterisation schemes for lower resolution runs. For example, the vertical wavenumber spectrum could be calculated from the high resolution model run and used to improve that used in the model's non-orographic gravity wave parameterisation scheme (USSP).

8.1.2 An improved non-orographic gravity wave parameterisation

Building on an examination of the model at higher horizontal resolutions and the results of Chapter 7, an in depth study of the model's GW parameterisation scheme (the USSP) would help quantify which aspects of the scheme need to be modified and which parts of the scheme require additional physical processes to be added. For example, Ortland and Alexander (2006) showed that tuning the parameters of the GW scheme for tidal structure in the MLT acted to narrow the location of the tropical peaks in the zonal wind diurnal tide by around 5 degrees. Yiğit et al. (2021) also showed that a latitudinally varying source spectrum can have a significant impact on middle atmosphere circulation with consequent effect on the diurnal tides.

Thus, an in depth study could answer questions such as: i) If the parameters of the USSP are tuned to produce the correct tidal structure in the MLT, is a realistic mean flow structure preserved?; ii) What latitudinal and azimuthal structure is helpful to produce the correct tidal structure in the MLT?; iii) If a latitudinally varying (and possibly azimuthally varying) source spectrum is used in the USSP, what impact does this have on the tidal structure and mean wind and temperatures?; iv) What is the impact of GW heating on tidal amplitudes in the MLT?; and v) Does adding in-situ and non-primary GW generation improve the modelled wind and hence tidal structures in high-top models?

8.1.3 The introduction of a realistic atmospheric sponge layer

The vertical damping coefficient was a necessary tool for model stability when approaching the upper boundary of the model in Chapter 5. However, this is an artificial "sponge" layer, and its inclusion was primarily to prevent numerical instabilities at the upper boundary caused by wave reflection off the upper boundary. A more natural solution is to use the physically realistic molecular viscosity and diffusion towards

the upper heights of the model, which act to naturally diffuse waves as they approach the upper boundary. An investigation of the molecular viscosity implementation was performed by Griffin (2016), and its implementation in a 1D vertical version of the dynamical core detailed in Griffin and Thuburn (2018). This showed promising stability improvements to the model even with a boundary raised up to 600 km. Inclusion of this in the current ExUM would act to give realistic damping as the upper boundary is reached and remove the need for an artificial sponge layer in future studies.

8.1.4 A Whole Atmosphere Unified Model: Coupling the ExUM to an ionosphere model

As well as improvements to the physical schemes and vertical damping near the upper boundary, above 110 km it becomes important to include the impacts of the ionisation of the atmosphere and hence transition from a model of the neutral atmosphere to an ionosphere model with an appropriate blending region. With an ExUM stable up to 170 km, the blending with an ionospheric model is feasible. The most feasible next step to this end would be to blend the ExUM with the Thermosphere-Ionosphere-Electrodynamics General Circulation Model (TIE-GCM; Qian et al., 2014) which simulates the thermosphere/ionosphere system with a lower boundary at 97 km. The work in this thesis provides a solid foundation for this blending with TIE-GCM and the subsequent development of a Met Office Whole Atmosphere model (MOWA) in the near future.

In summary, this thesis presents the necessary steps for the extension of the Met Office's Unified Model into the Mesosphere and Lower Thermosphere. We produced a stabilised model with a raised upper boundary, and compared the results with other modelling and observational studies in order to inform future development of the model in the MLT. In a broader context, the studies presented in this thesis demonstrate the challenges which must be overcome to produce a high-top atmospheric model, and the important atmospheric diagnostics which must be evaluated to give accurate model fields in the MLT and lay a solid foundation for a whole atmosphere model.

Bibliography

RA Akmaev. Whole atmosphere modeling: Connecting terrestrial and space weather. *Reviews of Geophysics*, 49(RG4004), 2011. doi:10.1029/2011rg000364.

RA Akmaev, TJ Fuller-Rowell, F Wu, JM Forbes, X Zhang, AF Anghel, MD Iredell, S Moorthi, and H-M Juang. Tidal variability in the lower thermosphere: Comparison of Whole Atmosphere Model (WAM) simulations with observations from TIMED. *Geophysical Research Letters*, 35(L03810), 2008. doi:10.1029/2007gl032584.

M Angelats i Coll and JM Forbes. Nonlinear interactions in the upper atmosphere: The s=1 and s=3 nonmigrating semidiurnal tides. *Journal of Geophysical Research: Space Physics*, 107(A8):SIA 3–1 – SIA 3–15, 2002. doi:10.1029/2001ja900179.

A Arakawa and VR Lamb. Computational design of the basic dynamical processes of the UCLA general circulation model. *Methods in computational physics*, 17:173–265, 1977. doi:10.1016/b978-0-12-460817-7.50009-4.

MP Baldwin, LJ Gray, TJ Dunkerton, K Hamilton, PH Haynes, WJ Randel, JR Holton, MJ Alexander, I Hirota, T Horinouchi, DBA Jones, JS Kinnersley, C Marquardt, K Sato, and M Takahashi. The quasi-biennial oscillation. *Reviews of Geophysics*, 39(2):179–229, 2001. doi:10.1029/1999rg000073.

MP Baldwin, T Birner, G Brasseur, J Burrows, N Butchart, R Garcia, M Geller, L Gray, K Hamilton, N Harnik, MI Hegglin, U Langematz, A Robock, K Sato, and AA Scaife. 100 years of progress in understanding the stratosphere and mesosphere. *Meteorological Monographs*, 59:27.1–27.62, 2019. doi:10.1175/AMSMONOGRAPHS-D-19-0003.1.

SR Beagley, C McLandress, VI Fomichev, and WE Ward. The extended Canadian Middle Atmosphere Model. *Geophysical research letters*, 27(16):2529–2532, 2000. doi:10.1029/1999gl011233.

AG Beard, NJ Mitchell, PJS Williams, and M Kunitake. Non-linear interactions between tides and planetary waves resulting in periodic tidal variability. *Journal of Atmospheric and Solar-Terrestrial Physics*, 61(5):363–376, 1999. doi:10.1016/s1364-6826(99)00003-6.

E Becker. Mean-flow effects of thermal tides in the mesosphere and lower thermosphere. *Journal of Atmospheric Sciences*, 74(6):2043–2063, 2017. doi:10.1175/jas-d-16-0194.1.

E Becker and SL Vadas. Secondary gravity waves in the winter mesosphere: Results from a high-resolution global circulation model. *Journal of Geophysical Research: Atmospheres*, 123 (5):2605–2627, 2018. doi:10.1002/2017jd027460.

E Becker and SL Vadas. Explicit global simulation of gravity waves in the thermosphere. *Journal of Geophysical Research: Space Physics*, 125(10), 2020. doi:10.1029/2020ja028034.

T Benacchio and N Wood. Semi-implicit semi-Lagrangian modelling of the atmosphere: a Met Office perspective. *Communications in Applied and Industrial Mathematics*, 7(3):4–25, 2016. doi:10.1515/caim-2016-0020.

FS Bessarab, Yu N Korenkov, MV Klimenko, VV Klimenko, IV Karpov, KG Ratovsky, and MA Chernigovskaya. Modeling the effect of sudden stratospheric warming within the thermosphere–ionosphere system. *Journal of atmospheric and solar-terrestrial physics*, 90: 77–85, 2012. doi:10.1016/j.jastp.2012.09.005.

S Borchert, G Zhou, M Baldauf, H Schmidt, G Zängl, and D Reinert. The upper-atmosphere extension of the ICON general circulation model (version: ua-icon-1.0). *Geoscientific Model Development*, 12:3541–3569, 2019. doi:10.5194/gmd-12-3541-2019.

V Bothmer and IA Daglis. *Space weather: physics and effects*. Springer Science & Business Media, 2007.

JW Chamberlain and DM Hunten. Theory of planetary atmospheres. An introduction to their physics and chemistry. *International Geophysics Series*, 36:481, 1987. doi:10.1016/s0074-6142(08)x6046-2.

LC Chang, WE Ward, SE Palo, J Du, D-Y Wang, H-L Liu, ME Hagan, Y Portnyagin, J Oberheide, LP Goncharenko, T Nakamura, P Hoffmann, W Singer, P Batista, B Clemesha, AH Manson, DM Riggin, C-Y She, T Tsuda, and T Yuan. Comparison of diurnal tide in models and ground-based observations during the 2005 equinox CAWSES tidal campaign. *Journal of atmospheric and solar-terrestrial physics*, 78:19–30, 2012. doi:10.1016/j.jastp.2010.12.010.

JG Charney and NA Phillips. Numerical integration of the quasi-geostrophic equations for barotropic and simple baroclinic flows. *Journal of Meteorology*, 10(2):71–99, 1953. doi:10.1175/1520-0469(1953)010<0071:niotqg>2.0.co;2.

B Christiansen, S Yang, and MS Madsen. Do strong warm ENSO events control the phase of the stratospheric QBO? *Geophysical Research Letters*, 43(19):10489–10495, 2016. doi:10.1002/2016GL070751.

E Cordero, N Wood, and A Staniforth. Impact of semi-Lagrangian trajectories on the discrete normal modes of a non-hydrostatic vertical-column model. *Quarterly Journal of the Royal Meteorological Society*, 131(605):93–108, 2005. doi:10.1256/qj.04/34.

MJP Cullen. The unified forecast/climate model. *Meteorological Magazine*, 122(1449):81–94, 1993.

MJP Cullen. Alternative implementations of the semi-Lagrangian semi-implicit schemes in the ECMWF model. *Quarterly Journal of the Royal Meteorological Society*, 127(578):2787–2802, 2001. doi:10.1002/qj.49712757814.

U Das, WE Ward, CJ Pan, and SK Das. Migrating and non-migrating tides observed in the stratosphere from FORMOSAT-3/COSMIC temperature retrievals. *Annales Geophysicae*, 38(2):421–435, 2020. doi:10.5194/angeo-38-421-2020.

T Davies, MJP Cullen, AJ Malcolm, MH Mawson, A Staniforth, AA White, and N Wood. A new dynamical core for the Met Office's global and regional modelling of the atmosphere. *Quarterly Journal of the Royal Meteorological Society: A journal of the atmospheric sciences, applied meteorology and physical oceanography*, 131(608):1759–1782, 2005. doi:10.1256/qj.04.101.

RN Davis, J Du, AK Smith, WE Ward, and NJ Mitchell. The diurnal and semidiurnal tides over Ascension Island (8°S, 14°W) and their interaction with the stratospheric quasi-biennial oscillation: studies with meteor radar, eCMAM and WACCM. *Atmospheric Chemistry & Physics*, 13(18), 2013. doi:10.5194/acp-13-9543-2013.

SM Dempsey, NP Hindley, T Moffat-Griffin, CJ Wright, AK Smith, J Du, and NJ Mitchell. Winds and Tides of the Antarctic Mesosphere and Lower Thermosphere: One Year of Meteor-Radar Observations Over Rothera (68°S, 68°W) and Comparisons with WACCM and eCMAM. *Journal of Atmospheric and Solar-Terrestrial Physics*, 212(105510), 2021. ISSN 1364-6826. doi:10.1016/j.jastp.2020.105510.

JM Edwards and A Slingo. Studies with a flexible new radiation code. I: Choosing a configuration for a large-scale model. *Quarterly Journal of the Royal Meteorological Society*, 122 (531):689–719, 1996. doi:10.1002/qj.49712253107.

EMP Ekanayake, T Aso, and S Miyahara. Background wind effect on propagation of nonmigrating diurnal tides in the middle atmosphere. *Journal of Atmospheric and Solar-Terrestrial Physics*, 59(4):401–429, 1997. doi:10.1016/S1364-6826(96)00012-0.

SL England. A review of the effects of non-migrating atmospheric tides on the Earth's low-latitude ionosphere. *Space science reviews*, 168(1):211–236, 2012. doi:10.1007/s11214-011-9842-4.

SL England, A Dobbin, MJ Harris, NF Arnold, and AD Aylward. A study into the effects of gravity wave activity on the diurnal tide and airglow emissions in the equatorial mesosphere and lower thermosphere using the Coupled Middle Atmosphere and Thermosphere (CMAT) general circulation model. *Journal of atmospheric and solar-terrestrial physics*, 68(3-5):293–308, 2006. doi:10.1016/j.jastp.2005.05.006.

J Fiedler, G Baumgarten, and G Von Cossart. Mean diurnal variations of noctilucent clouds during 7 years of lidar observations at ALOMAR. *Annales Geophysicae*, 2005. doi:10.5194/angeo-23-1175-2005.

EL Fleming, S Chandra, JJ Barnett, and M Corney. Zonal mean temperature, pressure, zonal wind and geopotential height as functions of latitude. *Advances in Space Research*, 10(12): 11–59, 1990. doi:10.1016/0273-1177(90)90386-e.

VI Fomichev, WE Ward, SR Beagley, C McLandress, JC McConnell, NA McFarlane, and TG Shepherd. Extended Canadian Middle Atmosphere Model: Zonal-mean climatology and physical parameterizations. *Journal of Geophysical Research: Atmospheres*, 107:ACL 9–1 – ACL 9–14, 2002. doi:10.1029/2001jd000479.

VI Fomichev, VP Ogibalov, and SR Beagley. Solar heating by the near-IR CO2 bands in the mesosphere. *Geophysical research letters*, 31(21), 2004. doi:10.1029/2004gl020324.

JM Forbes and D Wu. Solar tides as revealed by measurements of mesosphere temperature by the MLS experiment on UARS. *Journal of the atmospheric sciences*, 63(7):1776–1797, 2006. doi:10.1175/jas3724.1.

JM Forbes, X Zhang, ER Talaat, and W Ward. Nonmigrating diurnal tides in the thermosphere. *Journal of Geophysical Research: Space Physics*, 108(A1), 2003. doi:10.1029/2002ja009262.

JM Forbes, ME Hagan, and X Zhang. Seasonal cycle of nonmigrating diurnal tides in the MLT region due to tropospheric heating rates from the NCEP/NCAR Reanalysis Project. *Advances in Space Research*, 39(8):1347–1350, 2007. doi:10.1016/j.asr.2003.09.076.

JM Forbes, X Zhang, S Palo, J Russell, CJ Mertens, and M Mlynczak. Tidal variability in the ionospheric dynamo region. *Journal of Geophysical Research: Space Physics*, 113(A02310), 2008. doi:10.1029/2007ja012737.

DC Fritts and MJ Alexander. Gravity wave dynamics and effects in the middle atmosphere. *Reviews of geophysics*, 41(1003), 2003. doi:10.1029/2001RG000106.

DC Fritts and PK Rastogi. Convective and dynamical instabilities due to gravity wave motions in the lower and middle atmosphere: Theory and observations. *Radio Science*, 20(6):1247–1277, 1985. doi:10.1029/RS020i006p01247.

DC Fritts, SL Vadas, DM Riggin, MA Abdu, IS Batista, H Takahashi, A Medeiros, F Kamalabadi, H-L Liu, BG Fejer, and MJ Taylor. Gravity wave and tidal influences on equatorial spread F based on observations during the Spread F Experiment (SpreadFEx). *Annales Geophysicae*, 26(11):3235–3252, 2008. doi:10.5194/angeo-26-3235-2008.

H Fujiwara and Y Miyoshi. Morphological features and variations of temperature in the upper thermosphere simulated by a whole atmosphere GCM. In *Annales Geophysicae*, volume 28, pages 427–437. Copernicus GmbH, 2010. doi:10.5194/angeo-28-427-2010.

TJ Fuller-Rowell, RA Akmaev, F Wu, A Anghel, N Maruyama, DN Anderson, MV Codrescu, M Iredell, S Moorthi, HM Juang, and YT Hou. Impact of terrestrial weather on the upper atmosphere. *Geophysical Research Letters*, 35(L09808), 2008. doi:10.1029/2007gl032911.

RR Garcia, DR Marsh, DE Kinnison, BA Boville, and Fabrizio Sassi. Simulation of secular trends in the middle atmosphere, 1950–2003. *Journal of Geophysical Research: Atmospheres*, 112(D09301), 2007. doi:10.1029/2006jd007485.

MA Geller, T Zhou, R Ruedy, I Aleinov, L Nazarenko, NL Tausnev, S Sun, M Kelley, and Y Cheng. New gravity wave treatments for GISS climate models. *Journal of climate*, 24(15): 3989–4002, 2011. doi:10.1175/2011jcli4013.1.

MA Giorgetta, E Manzini, E Roeckner, M Esch, and L Bengtsson. Climatology and forcing of the quasi-biennial oscillation in the MAECHAM5 model. *Journal of Climate*, 19(16): 3882–3901, 2006. doi:10.1175/jcli3830.1.

LP Goncharenko, AJ Coster, JL Chau, and CE Valladares. Impact of sudden stratospheric warmings on equatorial ionization anomaly. *Journal of Geophysical Research: Space Physics*, 115(A00G07), 2010. doi:10.1029/2010ja015400.

DJ Griffin. *Extension of a Non-Hydrostatic Dynamical Core into the Thermosphere*. PhD thesis, University of Exeter, 2016.

DJ Griffin and J Thuburn. Numerical effects on vertical wave propagation in deep-atmosphere models. *Quarterly Journal of the Royal Meteorological Society*, 144(711):567–580, 2018. doi:10.1002/qj.3229.

MJ Griffith and NJ Mitchell. Analysis of migrating and non-migrating tides of the Extended Unified Model in the mesosphere and lower thermosphere. *Annales Geophysicae*, 2021. doi:10.5194/angeo-2021-21.

MJ Griffith, DR Jackson, DJ Griffin, and CJ Budd. Stable extension of the Unified Model into the mesosphere and lower thermosphere. *Journal of Space Weather and Space Climate*, 10 (19), 2020. doi:10.1051/swsc/2020018.

MJ Griffith, SM Dempsey, DR Jackson, T Moffat-Griffin, and NJ Mitchell. Winds and tides of the Extended Unified Model in the mesosphere and lower thermosphere validated with meteor radar observations. *Annales Geophysicae*, 39(3):487–514, 2021. doi:10.5194/angeo-39-487-2021.

ME Hagan and JM Forbes. Migrating and nonmigrating diurnal tides in the middle and upper atmosphere excited by tropospheric latent heat release. *Journal of Geophysical Research: Atmospheres*, 107(D24):ACL 6–1 – ACL 6–15, 2002. doi:10.1029/2001jd001236.

ME Hagan and JM Forbes. Migrating and nonmigrating semidiurnal tides in the upper atmosphere excited by tropospheric latent heat release. *Journal of Geophysical Research: Space Physics*, 108(A2), 2003. doi:10.1029/2002ja009466.

ME Hagan and RG Roble. Modeling diurnal tidal variability with the National Center for Atmospheric Research thermosphere-ionosphere-mesosphere-electrodynamics general circulation model. *Journal of Geophysical Research: Space Physics*, 106(A11):24869–24882, 2001. doi:10.1029/2001ja000057.

ME Hagan, MD Burrage, JM Forbes, J Hackney, WJ Randel, and X Zhang. GSWM-98: Results for migrating solar tides. *Journal of Geophysical Research: Space Physics*, 104(A4): 6813–6827, 1999. doi:10.1029/1998JA900125.

ME Hagan, A Maute, RG Roble, AD Richmond, TJ Immel, and SL England. Connections between deep tropical clouds and the Earth's ionosphere. *Geophysical Research Letters*, 34 (20), 2007. doi:10.1029/2007GL030142.

G Harry. Stabilising and validating the Met Office's Unified Model with 100 and 120 km ceilings. Master's thesis, University of Bath, 2015.

AE Hedin, MA Biondi, RG Burnside, G Hernandez, RM Johnson, TL Killeen, C Mazaudier, JW Meriwether, JE Salah, RJ Sica, RW Smith, NW Spencer, VB Wickwar, and TS Virdi. Revised global model of thermosphere winds using satellite and ground-based observations. *Journal of Geophysical Research: Space Physics*, 96(A5):7657–7688, 1991. doi:10.1029/91ja00251.

RE Hibbins, PJ Espy, YJ Orsolini, V Limpasuvan, and RJ Barnes. SuperDARN observations of semidiurnal tidal variability in the MLT and the response to sudden stratospheric warming events. *Journal of Geophysical Research: Atmospheres*, 124(9):4862–4872, 2019. doi:10.1029/2018jd030157.

MP Hickey, RL Walterscheid, and G Schubert. Gravity wave heating and cooling of the thermosphere: Sensible heat flux and viscous flux of kinetic energy. *Journal of Geophysical Research: Space Physics*, 116(A12326), 2011. doi:10.1029/2011ja016792.

CO Hines. *The upper atmosphere in motion*. Wiley Online Library, 1974. doi:10.1029/gm018p0014.

WK Hocking, B Fuller, and B Vandepeer. Real-time determination of meteor-related parameters utilizing modern digital technology. *Journal of Atmospheric and Solar-Terrestrial Physics*, 63(2-3):155–169, 2001. doi:10.1016/s1364-6826(00)00138-3.

FT Huang and CA Reber. Nonmigrating semidiurnal and diurnal tides at 95 km based on wind measurements from the High Resolution Doppler Imager on UARS. *Journal of Geophysical Research: Atmospheres*, 109(D10110), 2004. doi:10.1029/2003JD004442.

H Iimura, DC Fritts, Q Wu, WR Skinner, and SE Palo. Nonmigrating semidiurnal tide over the Arctic determined from TIMED Doppler Interferometer wind observations. *Journal of Geophysical Research: Atmospheres*, 115(D06109), 2010. doi:10.1029/2009jd012733.

TJ Immel, E Sagawa, SL England, SB Henderson, ME Hagan, SB Mende, HU Frey, CM Swenson, and LJ Paxton. Control of equatorial ionospheric morphology by atmospheric tides. *Geophysical Research Letters*, 33(15), 2006. doi:10.1029/2006gl026161.

S Ineson, AA Scaife, JR Knight, JC Manners, NJ Dunstone, LJ Gray, and JD Haigh. Solar forcing of winter climate variability in the Northern Hemisphere. *Nature Geoscience*, 4(11): 753–757, 2011. doi:10.1038/ngeo1282.

DR Jackson, TJ Fuller-Rowell, DJ Griffin, MJ Griffith, CW Kelly, DR Marsh, and M-T Walach. Future directions for whole atmosphere modeling: Developments in the context of space weather. *Space Weather*, 17:1342–1350, 2019. doi:10.1029/2019SW002267.

DR Jackson, S Bruinsma, S Negrin, C Stolle, CJ Budd, RD Gonzalez, E Down, DJ Griffin, MJ Griffith, G Kervalishvili, and DL Arenillas. The Space Weather Atmosphere Models and Indices (SWAMI) Project: Overview and first results. *Journal of Space Weather and Space Climate*, 10(18), 2020. doi:10.1051/swsc/2020019.

D Janches, AW Yu, MA Krainak, C Gardner, B Kaifler, S Etemad, DC Fritts, SD Eckermann, RL Collins, ECM Dawkins, RS Lieberman, DR Marsh, G Liu, and W Jarvis. The Atmospheric Coupling and Dynamics Across the Mesopause (ACaDAMe) mission. *Advances in Space Research*, 64(10):1915–1925, 2019. doi:10.1016/j.asr.2019.07.012.

H Jin, Y Miyoshi, D Pancheva, P Mukhtarov, H Fujiwara, and H Shinagawa. Response of migrating tides to the stratospheric sudden warming in 2009 and their effects on the ionosphere studied by a whole atmosphere-ionosphere model GAIA with COSMIC and TIMED/SABER observations. *Journal of Geophysical Research: Space Physics*, 117 (A10323), 2012. doi:10.1029/2012ja017650.

M Jones Jr, JM Forbes, ME Hagan, and Astrid Maute. Impacts of vertically propagating tides on the mean state of the ionosphere-thermosphere system. *Journal of Geophysical Research: Space Physics*, 119(3):2197–2213, 2014. doi:10.1002/2013ja019744.

CW Kelly. *Chemistry and transport of layered phenomena in the mesosphere-lower thermosphere*. PhD thesis, University of Leeds, 2020.

MV Klimenko, VV Klimenko, FS Bessarab, TV Sukhodolov, PA Vasilev, IV Karpov, YN Korenkov, IE Zakharenkova, B Funke, and EV Rozanov. Identification of the mechanisms responsible for anomalies in the tropical lower thermosphere/ionosphere caused by the January 2009 sudden stratospheric warming. *Journal of Space Weather and Space Climate*, 9 (A39), 2019. doi:10.1051/swsc/2019037.

YN Korenkov, VV Klimenko, MV Klimenko, FS Bessarab, NA Korenkova, KG Ratovsky, MA Chernigovskaya, AA Shcherbakov, Y Sahai, PR Fagundes, and R De Jesus. The global thermospheric and ionospheric response to the 2008 minor sudden stratospheric warming event. *Journal of Geophysical Research: Space Physics*, 117(A10309), 2012. doi:10.1029/2012ja018018.

R Laprise. The Euler equations of motion with hydrostatic pressure as an independent variable. *Monthly weather review*, 120(1):197–207, 1992. doi:10.1175/1520-0493(1992)120<0197:TEEOMW>2.0.CO;2.

X Li, W Wan, Z Ren, L Liu, and B Ning. The variability of nonmigrating tides detected from TIMED/SABER observations. *Journal of Geophysical Research: Space Physics*, 120(12): 10793–10808, 2015. doi:10.1002/2015JA021577.

RS Lieberman, J Oberheide, ME Hagan, EE Remsberg, and LL Gordley. Variability of diurnal tides and planetary waves during November 1978–May 1979. *Journal of atmospheric and solar-terrestrial physics*, 66(6-9):517–528, 2004. doi:10.1016/j.jastp.2004.01.006.

RS Lieberman, RA Akmaev, TJ Fuller-Rowell, and E Doornbos. Thermospheric zonal mean winds and tides revealed by CHAMP. *Geophysical Research Letters*, 40(10):2439–2443, 2013. doi:10.1002/grl.50481.

F Lilienthal, E Yiğit, N Samtleben, and C Jacobi. Variability of Gravity Wave Effects on the Zonal Mean Circulation and Migrating Terdiurnal Tide as Studied with the Middle and Upper Atmosphere Model (MUAM2019) Using a Whole Atmosphere Nonlinear Gravity Wave Scheme. *Frontiers in Astronomy and Space Sciences*, 7(588956), 2020. doi:10.3389/fspas.2020.588956.

G Liu, D Janches, RS Lieberman, T Moffat-Griffin, DC Fritts, and NJ Mitchell. Coordinated observations of 8-and 6-hr tides in the Mesosphere and Lower Thermosphere by three meteor radars near 60°S Latitude. *Geophysical Research Letters*, 47(1), 2020. doi:10.1029/2019GL086629.

H-L Liu. Variability and predictability of the space environment as related to lower atmosphere forcing. *Space Weather*, 14(9):634–658, 2016. doi:10.1002/2016SW001450.

H-L Liu, BT Foster, ME Hagan, JM McInerney, A Maute, L Qian, AD Richmond, RG Roble, SC Solomon, RR Garcia, and D Kinnison. Thermosphere extension of the whole atmosphere community climate model. *Journal of Geophysical Research: Space Physics*, 115(A12302), 2010. doi:10.1029/2010JA015586.

H-L Liu, CG Bardeen, BT Foster, P Lauritzen, J Liu, G Lu, DR Marsh, A Maute, JM McInerney, NM Pedatella, and L Qian. Development and validation of the Whole Atmosphere Community Climate Model with thermosphere and ionosphere extension (WACCM-X 2.0). *Journal of Advances in Modeling Earth Systems*, 10(2):381–402, 2018a. doi:10.1002/2017ms001232.

J Liu, H-L Liu, W Wang, AG Burns, Q Wu, Q Gan, SC Solomon, DR Marsh, L Qian, G Lu, and NM Pedatella. First results from the ionospheric extension of WACCM-X during the deep solar minimum year of 2008. *Journal of Geophysical Research: Space Physics*, 123(2): 1534–1553, 2018b. doi:10.1002/2017ja025010.

M Majdzadeh and GP Klaassen. An analysis of the Hines and Warner–McIntyre–Scinocca nonorographic gravity wave drag parametrizations. *Quarterly Journal of the Royal Meteorological Society*, 145(722):2308–2334, 2019. doi:10.1002/qj.3559.

AH Manson, CE Meek, CM Hall, S Nozawa, NJ Mitchell, D Pancheva, W Singer, and P Hoffmann. Mesopause dynamics from the Scandinavian triangle of radars within the PSMOS-DATAR Project. *Annales Geophysicae*, 22(2):367–386, 2004. doi:10.5194/angeo-22-367-2004.

E Manzini, MA Giorgetta, M Esch, L Kornblueh, and E Roeckner. The influence of sea surface temperatures on the northern winter stratosphere: Ensemble simulations with the MAECHAM5 model. *Journal of climate*, 19(16):3863–3881, 2006. doi:10.1175/jcli3826.1.

DR Marsh, RR Garcia, DE Kinnison, BA Boville, F Sassi, SC Solomon, and K Matthes. Modeling the whole atmosphere response to solar cycle changes in radiative and geomagnetic forcing. *Journal of Geophysical Research: Atmospheres*, 112(D23306), 2007. doi:10.1029/2006jd008306.

NJ Mayne, I Baraffe, DM Acreman, C Smith, N Wood, DS Amundsen, J Thuburn, and DR Jackson. Using the UM dynamical cores to reproduce idealised 3D flows. *arXiv preprint arXiv:1310.6041*, 2013. doi:10.5194/gmdd-6-3681-2013.

C McLandress. The seasonal variation of the propagating diurnal tide in the mesosphere and lower thermosphere. Part I: The role of gravity waves and planetary waves. *Journal of the Atmospheric Sciences*, 59(5):893–906, 2002. doi:10.1175/1520-0469(2002)059<0893:tsvotp>2.0.co;2.

AS Medvedev and GP Klaassen. Parameterization of gravity wave momentum deposition based on nonlinear wave interactions: Basic formulation and sensitivity tests. *Journal of Atmospheric and Solar-Terrestrial Physics*, 62(11):1015–1033, 2000. doi:10.1016/s1364-6826(00)00067-5.

AS Medvedev and GP Klaassen. Thermal effects of saturating gravity waves in the atmosphere. *Journal of Geophysical Research: Atmospheres*, 108(4040):ACL 4–1 – ACL 4–18, 2003. doi:10.1029/2002jd002504.

T Melvin, M Dubal, N Wood, A Staniforth, and M Zerroukat. An inherently mass-conserving iterative semi-implicit semi-Lagrangian discretization of the non-hydrostatic vertical-slice equations. *Quarterly Journal of the Royal Meteorological Society: A journal of the atmospheric sciences, applied meteorology and physical oceanography*, 136(648):799–814, 2010. doi:10.1002/qj.603.

K Meraner and H Schmidt. Transport of nitrogen oxides through the winter mesopause in HAMMONIA. *Journal of Geophysical Research: Atmospheres*, 121(6):2556–2570, 2016. doi:10.1002/2015jd024136.

GH Millward, RJ Moffett, S Quegan, and TJ Fuller-Rowell. A coupled thermosphere-ionosphere-plasmasphere model (CTIP). *Solar-Terrestrial Energy Program: Handbook of Ionospheric Models, edited by R. W. Schunk*, pages 239–279, 1996. Available at `https://www.bc.edu/content/dam/bc1/offices/ISR/SCOSTEP/Multimedia/other/ionospheric-models.pdf`.

NJ Mitchell. University of Bath: Ascension Island Skiymet Meteor Radar data (2001-2012). Centre for Environmental Data Analysis, 2019a. Available at: `https://catalogue.ceda.ac.uk/uuid/0d05cf74e17f49c2b7c5cd02faa59291` (last access: 8 June 2021).

NJ Mitchell. University of Bath: Rothera Skiymet Meteor Radar data (2005-present). Centre for Environmental Data Analysis, 2019b. Available at: `https://catalogue.ceda.ac.uk/uuid/aa44e02718fd4ba49cefe36d884c6e50` (last access: 8 June 2021).

NJ Mitchell, D Pancheva, HR Middleton, and ME Hagan. Mean winds and tides in the Arctic mesosphere and lower thermosphere. *Journal of Geophysical Research: Space Physics*, 107: SIA 2–1 – SIA 2–14, 2002. doi:10.1029/2001ja900127.

S Miyahara and JM Forbes. Interactions between gravity waves and the diurnal tide in the mesosphere and lower thermosphere. *Journal of the Meteorological Society of Japan. Ser. II*, 69(5):523–531, 1991. doi:10.2151/jmsj1965.69.5_523.

S Miyahara, Y Yoshida, and Y Miyoshi. Dynamic coupling between the lower and upper atmosphere by tides and gravity waves. *Journal of atmospheric and terrestrial physics*, 55 (7):1039–1053, 1993. doi:10.1016/0021-9169(93)90096-h.

Y Miyoshi and H Fujiwara. Gravity waves in the thermosphere simulated by a general circulation model. *Journal of Geophysical Research: Atmospheres*, 113(D01101), 2008. doi:10.1029/2007jd008874.

Y Miyoshi and E Yiğit. Impact of gravity wave drag on the thermospheric circulation: Implementation of a nonlinear gravity wave parameterization in a whole-atmosphere model. *Annales Geophysicae*, 37(5):955–969, 2019. doi:10.5194/angeo-37-955-2019.

Y Miyoshi, D Pancheva, P Mukhtarov, H Jin, H Fujiwara, and H Shinagawa. Excitation mechanism of non-migrating tides. *Journal of Atmospheric and Solar-Terrestrial Physics*, 156:24–36, 2017. doi:10.1016/j.jastp.2017.02.012.

O Morgenstern, P Braesicke, FM O'Connor, AC Bushell, CE Johnson, SM Osprey, and JA Pyle. Evaluation of the new UKCA climate-composition model-Part 1: The stratosphere. *Geoscientific Model Development*, 2(1), 2009. doi:10.5194/gmdd-1-381-2008.

P Mukhtarov, D Pancheva, and B Andonov. Global structure and seasonal and interannual variability of the migrating diurnal tide seen in the SABER/TIMED temperatures between 20 and 120 km. *Journal of Geophysical Research: Space Physics*, 114(A02309), 2009. doi:10.1029/2008JA013759.

DJ Murphy, WJR French, and RA Vincent. Long-period planetary waves in the mesosphere and lower thermosphere above Davis, Antarctica. *Journal of atmospheric and solar-terrestrial physics*, 69(17-18):2118–2138, 2007. doi:10.1016/j.jastp.2007.06.008.

DJ Murphy, T Aso, DC Fritts, RE Hibbins, AJ McDonald, DM Riggin, M Tsutsumi, and RA Vincent. Source regions for Antarctic MLT non-migrating semidiurnal tides. *Geophysical research letters*, 36(9), 2009. doi:10.1029/2008gl037064.

J Oberheide, Q Wu, TL Killeen, ME Hagan, and RG Roble. Diurnal nonmigrating tides from TIMED Doppler Interferometer wind data: Monthly climatologies and seasonal variations. *Journal of Geophysical Research: Space Physics*, 111(A10S03), 2006. doi:10.1029/2005JA011491.

J Oberheide, Q Wu, TL Killeen, ME Hagan, and RG Roble. A climatology of nonmigrating semidiurnal tides from TIMED Doppler Interferometer (TIDI) wind data. *Journal of atmospheric and solar-terrestrial physics*, 69(17-18):2203–2218, 2007. doi:10.1016/j.jastp.2007.05.010.

J Oberheide, JM Forbes, K Häusler, Qian Wu, and SL Bruinsma. Tropospheric tides from 80 to 400 km: Propagation, interannual variability, and solar cycle effects. *Journal of Geophysical Research: Atmospheres*, 114(D00I05), 2009. doi:10.1029/2009jd012388.

J Oberheide, JM Forbes, X Zhang, and SL Bruinsma. Climatology of upward propagating diurnal and semidiurnal tides in the thermosphere. *Journal of Geophysical Research: Space Physics*, 116(A11306), 2011. doi:10.1029/2011ja016784.

FM O'Connor, CE Johnson, O Morgenstern, NL Abraham, P Braesicke, M Dalvi, GA Folberth, MG Sanderson, PJ Telford, A Voulgarakis, PJ Young, G Zeng, WJ Collins, and JA Pyle. Evaluation of the new UKCA climate-composition model–Part 2: The Troposphere. *Geoscientific Model Development*, 7(1):41–91, 2014. doi:10.5194/gmd-7-41-2014.

DA Ortland and MJ Alexander. Gravity wave influence on the global structure of the diurnal tide in the mesosphere and lower thermosphere. *Journal of Geophysical Research: Space Physics*, 111(A10S10), 2006. doi:10.1029/2005ja011467.

S-M Päivärinta, A Seppälä, ME Andersson, PT Verronen, L Thölix, and E Kyrölä. Observed effects of solar proton events and sudden stratospheric warmings on odd nitrogen and ozone in the polar middle atmosphere. *Journal of Geophysical Research: Atmospheres*, 118(12): 6837–6848, 2013. doi:10.1002/jgrd.50486.

SE Palo, JM Forbes, X Zhang, JM Russell III, and MG Mlynczak. An eastward propagating two-day wave: Evidence for nonlinear planetary wave and tidal coupling in the mesosphere and lower thermosphere. *Geophysical research letters*, 34(L07807), 2007. doi:10.1029/2006gl027728.

D Pancheva, E Merzlyakov, NJ Mitchell, Yu Portnyagin, AH Manson, C Jacobi, CE Meek, Y Luo, RR Clark, WK Hocking, and J MacDougall. Global-scale tidal variability during the PSMOS campaign of June–August 1999: interaction with planetary waves. *Journal of Atmospheric and Solar-Terrestrial Physics*, 64(17):1865–1896, 2002. doi:10.1016/s1364-6826(02)00199-2.

D Pancheva, N Mitchell, H Middleton, and H Muller. Variability of the semidiurnal tide due to fluctuations in solar activity and total ozone. *Journal of atmospheric and solar-terrestrial physics*, 65(1):1–19, 2003. doi:10.1016/S1364-6826(02)00084-6.

D Pancheva, P Mukhtarov, and B Andonov. Global structure, seasonal and interannual variability of the eastward propagating tides seen in the SABER/TIMED temperatures (2002–2007). *Advances in space research*, 46(3):257–274, 2010. doi:10.5194/angeo-27-687-2009.

D Pancheva, P Mukhtarov, C Hall, AK Smith, and M Tsutsumi. Climatology of the short-period (8-h and 6-h) tides observed by meteor radars at Tromsø and Svalbard. *Journal of Atmospheric and Solar-Terrestrial Physics*, 212(105513), 2021. doi:10.1016/j.jastp.2020.105513.

DV Pancheva and NJ Mitchell. Planetary waves and variability of the semidiurnal tide in the mesosphere and lower thermosphere over Esrange (68°N, 21°E) during winter. *Journal of Geophysical Research: Space Physics*, 109(A08307), 2004. doi:10.1029/2004ja010433.

J Park, H Lühr, C Lee, YH Kim, G Jee, and J-H Kim. A climatology of medium-scale gravity wave activity in the mid-latitude/low-latitude daytime upper thermosphere as observed by CHAMP. *Journal of Geophysical Research: Space Physics*, 119(3):2187–2196, 2014. doi:10.1002/2013ja019705.

NM Pedatella, AK Smith, and H-L Liu. Simulations of zonal mean gravity wave drag short-term variability in the southern hemisphere mesosphere. *Journal of Geophysical Research: Atmospheres*, 123(21):11849–11860, 2018. doi:10.1029/2018jd028306.

JMC Plane, W Feng, and ECM Dawkins. The mesosphere and metals: Chemistry and changes. *Chemical reviews*, 115(10):4497–4541, 2015. doi:10.1021/cr500501m.

AI Pogoreltsev. Generation of normal atmospheric modes by stratospheric vacillations. *Izvestiya, Atmospheric and Oceanic Physics*, 43(4):423–435, 2007. doi:10.1134/s0001433807040044.

AI Pogoreltsev, AA Vlasov, K Fröhlich, and C Jacobi. Planetary waves in coupling the lower and upper atmosphere. *Journal of Atmospheric and Solar-Terrestrial Physics*, 69(17-18): 2083–2101, 2007. doi:10.1016/j.jastp.2007.05.014.

D Pokhotelov, E Becker, G Stober, and JL Chau. Seasonal variability of atmospheric tides in the mesosphere and lower thermosphere: meteor radar data and simulations. *Annales Geophysicae*, 36(3):825–830, 2018. doi:10.5194/angeo-36-825-2018.

L Qian, AG Burns, BA Emery, B Foster, G Lu, A Maute, AD Richmond, RG Roble, SC Solomon, and W Wang. The NCAR TIE-GCM: A community model of the coupled thermosphere/ionosphere system. *Modeling the ionosphere-thermosphere system*, 201:73–83, 2014. doi:10.1002/9781118704417.ch7.

DM Riggin and RS Lieberman. Variability of the diurnal tide in the equatorial MLT. *Journal of Atmospheric and Solar-Terrestrial Physics*, 102:198–206, 2013. doi:10.1016/j.jastp.2013.05.011.

DM Riggin, CK Meyer, DC Fritts, MJ Jarvis, Y Murayama, W Singer, RA Vincent, and DJ Murphy. MF radar observations of seasonal variability of semidiurnal motions in the mesosphere at high northern and southern latitudes. *Journal of Atmospheric and Solar-Terrestrial Physics*, 65(4):483–493, 2003. doi:10.1016/s1364-6826(02)00340-1.

C Rivest, A Staniforth, and A Robert. Spurious resonant response of semi-Lagrangian discretizations to orographic forcing: Diagnosis and solution. *Monthly weather review*, 122(2): 366–376, 1994. doi:10.1175/1520-0493(1994)122<0366:SRROSL>2.0.CO;2.

RG Roble and EC Ridley. A thermosphere-ionosphere-mesosphere-electrodynamics general circulation model (TIME-GCM): Equinox solar cycle minimum simulations (30–500 km). *Geophysical Research Letters*, 21(6):417–420, 1994. doi:10.1029/93GL03391.

DJ Sandford, CL Beldon, RE Hibbins, and NJ Mitchell. Dynamics of the Antarctic and Arctic mesosphere and lower thermosphere–Part 1: Mean winds. *Atmos. Chem. Phys*, 10(21): 10273–10289, 2010. doi:10.5194/acp-10-10273-2010.

AA Scaife, N Butchart, CD Warner, and R Swinbank. Impact of a spectral gravity wave parameterization on the stratosphere in the Met Office Unified Model. *Journal of the atmospheric sciences*, 59(9):1473–1489, 2002. doi:10.1175/1520-0469(2002)059<1473:ioasgw>2.0.co;2.

H Schmidt, GP Brasseur, M Charron, E Manzini, MA Giorgetta, T Diehl, VI Fomichev, D Kinnison, Dan Marsh, and S Walters. The HAMMONIA chemistry climate model: Sensitivity of the mesopause region to the 11-year solar cycle and CO2 doubling. *Journal of Climate*, 19(16):3903–3931, 2006. doi:10.1175/jcli3829.1.

MJ Schwartz, A Lambert, GL Manney, WG Read, NJ Livesey, L Froidevaux, CO Ao, PF Bernath, CD Boone, RE Cofield, WH Daffer, BJ Drouin, EJ Fetzer, RA Fuller, RF Jarnot, JH Jiang, YB Jiang, BW Knosp, K KrÃ¼ger, J-LF Li, MG Mlynczak, S Pawson, JM Russell III, ML Santee, WV Snyder, PC Stek, RP Thurstans, AM Tompkins, PA Wagner, KA Walker, JW Waters, and DL Wu. Validation of the Aura Microwave Limb Sounder temperature and geopotential height measurements. *Journal of Geophysical Research: Atmospheres*, 113(D15S11), 2008. doi:10.1029/2007JD008783.

A Seppälä, CE Randall, Mark A Clilverd, Eugene Rozanov, and CJ Rodger. Geomagnetic activity and polar surface air temperature variability. *Journal of Geophysical Research: Space Physics*, 114(A10312), 2009. doi:10.1029/2008ja014029.

MG Shepherd, G Liu, and GG Shepherd. Mesospheric semiannual oscillation in temperature and nightglow emission. *Journal of atmospheric and solar-terrestrial physics*, 68(3-5):379–389, 2006. doi:10.1016/j.jastp.2005.02.029.

AK Smith. Global dynamics of the MLT. *Surveys in Geophysics*, 33(6):1177–1230, 2012. doi:10.1007/s10712-012-9196-9.

AK Smith, DV Pancheva, NJ Mitchell, DR Marsh, JM Russell III, and MG Mlynczak. A link between variability of the semidiurnal tide and planetary waves in the opposite hemisphere. *Geophysical research letters*, 34(L07809), 2007. doi:10.1029/2006gl028929.

I-S Song, H-Y Chun, G Jee, S-Y Kim, J Kim, Y-H Kim, and MA Taylor. Dynamic initialization for whole atmospheric global modeling. *Journal of Advances in Modeling Earth Systems*, 10 (9):2096–2120, 2018. doi:10.1029/2017ms001213.

G Stober, D Janches, V Matthias, D Fritts, J Marino, T Moffat-Griffin, K Baumgarten, W Lee, D Murphy, YH Kim, NJ Mitchell, and S Palo. Seasonal evolution of winds, atmospheric tides, and reynolds stress components in the southern hemisphere mesosphere–lower thermosphere in 2019. *Annales Geophysicae*, 39(1):1–29, 2021. doi:10.5194/angeo-39-1-2021.

EV Suvorova and AI Pogoreltsev. Modeling of nonmigrating tides in the middle atmosphere. *Geomagnetism and Aeronomy*, 51(1):105–115, 2011. doi:10.1134/s0016793210061039.

R Swinbank and DA Ortland. Compilation of wind data for the Upper Atmosphere Research Satellite (UARS) reference atmosphere project. *Journal of Geophysical Research: Atmospheres*, 108(D19), 2003. doi:10.1029/2002jd003135.

H Teitelbaum and F Vial. On tidal variability induced by nonlinear interaction with planetary waves. *Journal of Geophysical Research: Space Physics*, 96(A8):14169–14178, 1991. doi:10.1029/91ja01019.

PJ Telford, P Braesicke, O Morgenstern, and JA Pyle. Technical Note: Description and assessment of a nudged version of the new dynamics Unified Model. *Atmospheric Chemistry and Physics*, 8(6):1701–1712, 2008. doi:10.5194/acp-8-1701-2008.

C Temperton and A Staniforth. An efficient two-time-level semi-Lagrangian semi-implicit integration scheme. *Quarterly Journal of the Royal Meteorological Society*, 113(477):1025–1039, 1987. doi:10.1002/qj.49711347714.

J Thuburn and A Staniforth. Conservation and linear Rossby-mode dispersion on the spherical C grid. *Monthly weather review*, 132(2):641–653, 2004. doi:10.1175/1520-0493(2004)132<0641:calrdo>2.0.co;2.

G Tóth, IV Sokolov, TI Gombosi, DR Chesney, CR Clauer, DL De Zeeuw, KC Hansen, KJ Kane, WB Manchester, RC Oehmke, KG Powell, AJ Ridley, II Roussev, QF Stout, O Volberg, RA Wolf, S Sazykin, A Chan, B Yu, and J Kóta. Space weather modeling framework: A new tool for the space science community. *Journal of Geophysical Research: Space Physics*, 110(A12226), 2005. doi:10.1029/2005ja011126.

QT Trinh, M Ern, E Doornbos, P Preusse, and M Riese. Satellite observations of middle atmosphere–thermosphere vertical coupling by gravity waves. *Annales geophysicae*, 36(2): 425–444, 2018. doi:10.5194/angeo-36-425-2018.

T Tsuda, TE VanZandt, M Mizumoto, S Kato, and S Fukao. Spectral analysis of temperature and Brunt-Väisälä frequency fluctuations observed by radiosondes. *Journal of Geophysical Research: Atmospheres*, 96(D9):17265–17278, 1991. doi:10.1029/91JD01944.

United States Committee on Extension to the Standard Atmosphere (COESA). U.S. Standard Atmosphere 1976. *US Government Printing Office, Washington, DC*, 40:56, 1976.

SL Vadas, H-L Liu, and RS Lieberman. Numerical modeling of the global changes to the thermosphere and ionosphere from the dissipation of gravity waves from deep convection. *Journal of Geophysical Research: Space Physics*, 119(9):7762–7793, 2014. doi:10.1002/2014ja020280.

A Vitharana, X Zhu, J Du, J Oberheide, and WE Ward. Statistical modeling of tidal weather in the mesosphere and lower thermosphere. *Journal of Geophysical Research: Atmospheres*, 124(16):9011–9027, 2019. doi:10.1029/2019jd030573.

D Walters, A Baran, I Boutle, M Brooks, P Earnshaw, J Edwards, K Furtado, P Hill, A Lock, J Manners, C Morcrette, J Mulcahy, C Sanchez, C Smith, R Stratton, W Tennant, L Tomassini, K Van Weverberg, S Vosper, M Willett, J Browse, A Bushell, M Dalvi, R Essery, N Gedney, S Hardiman, B Johnson, C Johnson, A Jones, G Mann, S Milton, H Rumbold, A Sellar, M Ujiie, M Whitall, K Williams, and M Zerroukat. The Met Office Unified Model Global Atmosphere 7.0/7.1 and JULES Global Land 7.0 configurations. *Geoscientific Model Development*, 12(5):1909–1963, 2019. doi:10.5194/gmd-12-1909-2019.

CD Warner and ME McIntyre. An ultrasimple spectral parameterization for nonorographic gravity waves. *Journal of the atmospheric sciences*, 58(14):1837–1857, 2001. doi:10.1175/1520-0469(2001)058<1837:auspfn>2.0.co;2.

JW Waters, L Froidevaux, RS Harwood, RF Jarnot, HM Pickett, WG Read, PH Siegel, RE Cofield, MJ Filipiak, DA Flower, JR Holden, GK Lau, NJ Livesey, GL Manney, HC Pumphrey, ML Santee, DL Wu, DT Cuddy, RR Lay, MS Loo, VS Perun, MJ Schwartz, PC Stek, RP Thurstans, MA Boyles, KM Chandra, MC Chavez, Gun-Shing C, BV Chudasama, R Dodge, RA Fuller, MA Girard, JH Jiang, Yibo J, BW Knosp, RC LaBelle, JC Lam, KA Lee, D Miller, JE Oswald, NC Patel, DM Pukala, O Quintero, DM Scaff, W Van Snyder, MC Tope, PA Wagner, and MJ Walch. The earth observing system microwave limb sounder (EOS MLS) on the Aura satellite. *IEEE Transactions on Geoscience and Remote Sensing*, 44(5):1075–1092, 2006. doi:10.1109/TGRS.2006.873771.

S Wilhelm, G Stober, and JL Chau. A comparison of 11-year mesospheric and lower thermospheric winds determined by meteor and MF radar at 69°N. In *Annales Geophysicae*, volume 35, pages 893–906. Copernicus GmbH, 2017. doi:10.5194/angeo-35-893-2017.

N Wood, A Staniforth, A White, T Allen, M Diamantakis, M Gross, T Melvin, C Smith, S Vosper, M Zerroukat, and J Thuburn. An inherently mass-conserving semi-implicit semi-lagrangian discretization of the deep-atmosphere global non-hydrostatic equations. *Quarterly Journal of the Royal Meteorological Society*, 140(682):1505–1520, 2014. doi:10.1002/qj.2235.

Q Wu, DA Ortland, TL Killeen, RG Roble, ME Hagan, H-L Liu, SC Solomon, Jiyao Xu, WR Skinner, and RJ Niciejewski. Global distribution and interannual variations of mesospheric and lower thermospheric neutral wind diurnal tide: 1. Migrating tide. *Journal of Geophysical Research: Space Physics*, 113(A05308), 2008a. doi:10.1029/2007JA012542.

Q Wu, DA Ortland, TL Killeen, RG Roble, ME Hagan, H-L Liu, SC Solomon, Jiyao Xu, WR Skinner, and RJ Niciejewski. Global distribution and interannual variations of mesospheric and lower thermospheric neutral wind diurnal tide: 2. Nonmigrating tide. *Journal of Geophysical Research: Space Physics*, 113(A05309), 2008b. doi:10.1029/2007JA012543.

Q Wu, DA Ortland, SC Solomon, WR Skinner, and RJ Niciejewski. Global distribution, seasonal, and inter-annual variations of mesospheric semidiurnal tide observed by TIMED TIDI. *Journal of atmospheric and solar-terrestrial physics*, 73(17-18):2482–2502, 2011. doi:10.1016/j.jastp.2011.08.007.

C Yamashita, H-L Liu, and X Chu. Responses of mesosphere and lower thermosphere temperatures to gravity wave forcing during stratospheric sudden warming. *Geophysical Research Letters*, 37(9), 2010. doi:10.1029/2009GL042351.

E Yiğit and AS Medvedev. Heating and cooling of the thermosphere by internal gravity waves. *Geophysical Research Letters*, 36(L14807), 2009. doi:10.1029/2009gl038507.

E Yiğit and AS Medvedev. Internal wave coupling processes in Earth's atmosphere. *Advances in Space Research*, 55(4):983–1003, 2015. doi:10.1016/j.asr.2014.11.020.

E Yiğit and AS Medvedev. Influence of parameterized small-scale gravity waves on the migrating diurnal tide in Earth's thermosphere. *Journal of Geophysical Research: Space Physics*, 122 (4):4846–4864, 2017. doi:10.1002/2017ja024089.

E Yiğit, AD Aylward, and AS Medvedev. Parameterization of the effects of vertically propagating gravity waves for thermosphere general circulation models: Sensitivity study. *Journal of Geophysical Research: Atmospheres*, 113(D19106), 2008. doi:10.1029/2008jd010135.

E Yiğit, AS Medvedev, AD Aylward, P Hartogh, and MJ Harris. Modeling the effects of gravity wave momentum deposition on the general circulation above the turbopause. *Journal of Geophysical Research: Atmospheres*, 114(D07101), 2009. doi:10.1029/2008jd011132.

E Yiğit, PK Knížová, K Georgieva, and W Ward. A review of vertical coupling in the atmosphere–ionosphere system: Effects of waves, sudden stratospheric warmings, space weather, and of solar activity. *Journal of Atmospheric and Solar-Terrestrial Physics*, 141: 1–12, 2016. doi:10.1016/j.jastp.2016.02.011.

E Yiğit, AS Medvedev, and M Ern. Effects of latitude-dependent gravity wave source variations on the middle and upper atmosphere. *Frontiers in Astronomy and Space Sciences*, 7(614018), 2021. doi:10.3389/fspas.2020.614018.

X Yue, WS Schreiner, NM Pedatella, and Y-H Kuo. Characterizing GPS radio occultation loss of lock due to ionospheric weather. *Space Weather*, 14(4):285–299, 2016. doi:10.1002/2015sw001340.

X Zhang, JM Forbes, ME Hagan, JM Russell III, SE Palo, CJ Mertens, and MG Mlynczak. Monthly tidal temperatures 20–120 km from TIMED/SABER. *Journal of Geophysical Research: Space Physics*, 111(A10S08), 2006. doi:10.1029/2005JA011504.